DEVELOPMENT AND APPLICATIONS OF NOVEL NANOSTRUCTURES FROM GRAPHENE AND VIRAL BUILDING BLOCKS

By

KATE STOKES

A thesis submitted to

the University of Birmingham

for the degree of

DOCTOR OF ENGINEERING

Advanced Nanomaterials Structures and Applications Group

School of Chemical Engineering

College of Engineering and Physical Sciences

University of Birmingham

September 2024

ABSTRACT

GraPhage13 aerogels (GPA) are porous, ultra-low density nanocomposites fabricated through the self-assembly of graphene oxide (GO), a monolayer of carbon atoms with various oxygen-containing functional groups, and the filamentous bacteriophage M13. The cost-effective, scalable, and environmentally friendly production of GPA, combined with the ability to customise its properties through the functionalisation of GO and chemical and genetic modification of M13, makes GPA a highly promising material across a diverse range of industries, including healthcare, defence, and environmental monitoring.

This thesis presents a comprehensive investigation into GPA, focusing on the optimal chemical environment for its formation, the mechanism of its self-assembly, and its physical characterisation. A wide range of experimental techniques were employed, including microscopy and spectroscopy methods such as scanning electron microscopy (SEM), atomic force microscopy (AFM), Raman spectroscopy, ultraviolet-visible (UV-Vis) spectroscopy, and energy-dispersive X-ray (EDX) spectroscopy. Additional techniques included titrations, zeta potential analysis, dynamic vapour sorption (DVS), and electrical conductivity measurements. The resulting data were analysed using kinetic modelling, peak fitting, image analysis, and statistical evaluation, including the use of the Bayesian Information Criterion (BIC) to assess model accuracy.

Interactions between GO and M13 were found to be pH-dependent. In the range of pH 2–6, electrostatic repulsion is minimised, enabling their aggregation. The optimal GPA was generated by combining GO and M13 at pH 4.9. At lower pH values, M13 tends

to independently precipitate or suffer structural damage, while the increased electrostatic repulsion towards pH 6 reduces the probability of aggregation.

Examining its thermal properties, GPA demonstrated progressive structural changes upon heating, including partial reduction of GO, a decrease in stiffness, increased structural disorder, and the formation of fewer but larger pores.

Thermal characterisation revealed progressive structural changes with heating, including partial reduction of GO, decreased stiffness, increased disorder, and the formation of fewer but larger pores. GPA also demonstrated high hygroscopicity, with a water sorption capacity of 0.68 ± 0.02 g/g at 90% relative humidity, exhibiting stable and reversible behaviour. Ethanol uptake outperformed similar carbon-based materials, and although acetone uptake was lower, there is potential to improve and tune its sorption capacity for specific analytes through the functionalisation of GO and M13.

The electrical properties of GPA revealed its inherently insulating nature, with a low conductivity of 6.8 nS/cm. However, this was significantly enhanced through the incorporation of gold nanoparticles (AuNPs), increasing to 190 nS/cm with 20 nm AuNPs and up to 360 nS/cm with 5 nm AuNPs

Together, these findings lay a foundation for the integration of GPA into graphene-based devices. The tuneability and multifunctionality of GPA highlight its potential in applications such as chemical sensors, adsorbents, and energy storage systems.

ACKNOWLEDGEMENTS

I'd like to take the time to acknowledge the people without whom this would not have been possible.

Firstly, I would like to express my deepest gratitude to my academic supervisor, Professor Pola Goldberg Oppenheimer, for giving me the opportunity to complete my EngD in the Advanced Nanomaterials, Structures and Applications (ANMSA) group, and my industrial supervisor Henry White for enabling our collaboration with BAE Systems. Their guidance, support, and encouragement have been invaluable.

I would like to acknowledge the EPSRC and BAE Systems for providing the funding that enabled me to undertake this project. Additionally, I extend my thanks to the Centre of Doctoral Training (CDT) in Formulation Engineering for their financial support and the continuous opportunities they have provided.

I am incredibly grateful to my fellow members of the ANMSA group for their constant support, help, and endless supply of coffee and chocolate. I will miss you all.

Special thanks go to the School of Chemical Engineering, particularly the technical staff, for training me on numerous pieces of equipment and assisting whenever something inevitably went wrong!

I would also like to thank Professor Tim Dafforn and the Dafforn laboratories for providing the space, equipment, and training necessary for my biological samples.

I am deeply grateful to my collaborators, Dr. Paolo Passaretti and Dr. Yiwei Sun, for their invaluable contributions. They generously offered their time, expertise, and insights, engaging in thoughtful discussions on experimental ideas and providing

critical feedback on my paper drafts. I could not have asked for better collaborators, and I truly could not have accomplished this without their support. I wish them all the best in their future endeavours and sincerely hope that our paths cross again for future collaborations.

Outside of academic pursuits, I have been privileged to take part in numerous outreach activities. As the first in my immediate family to attend university, I understand how important outreach is in encouraging those from disadvantaged backgrounds to pursue university and careers in STEM. A massive thank you goes to science presenter Jon Wood and the National Outreach Officer for Discover Materials, Dr. Chris Hamlett, who provided me with so many opportunities to develop my own outreach workshops, help at science festivals, and run activities at school visits. It has meant a lot to me to be able to give back and hopefully inspire a future generation of scientists.

Finally, I'd like to thank my friends and family. Even though a lot of the time they have no idea what I actually do, their constant love and support have always helped push me through. In particular, I am deeply grateful to my incredible partner Tim, who has been unwavering in his support throughout, especially during moments when I doubted that this thesis would come together. I love you, and I could not have done this without you.

CONTENTS LISTING

LIST OF PUBLICATIONS

The following papers form the basis of this thesis:

- **K. Stokes**, Y. Sun, P. Passaretti, H. White, and P. G. Oppenheimer, “Unveiling the Sorption Properties of Graphene Oxide – M13 Bacteriophage Aerogels for Advanced Sensing and Environmental Applications”, [in publication].
- P. Passaretti, **K. Stokes**, J. Carter, Y. Sun, F. Cuozzo, A. G. R. Zanna, T. R. Dafforn, P. Goldberg Oppenheimer, “Characterisation, Modifications and Applications of the Filamentous Bacteriophage M13”, [in publication].
- **K. Stokes**, Y. Sun, J. L. Thomas, P. Passaretti, H. White, and P. Goldberg Oppenheimer, “Conductivity Optimisation of Graphene Oxide-M13 Bacteriophage Nanocomposites: Towards Graphene-Based Gas Micronano-sensors”, *Discover Nano*, vol. 19, p. 152, 2024, doi: 10.1186/s11671-024-04101-w
- **K. Stokes**, Y. Sun, H. Zhang, P. Passaretti, H. White, and P. Goldberg Oppenheimer, "Thermonanomechanics of Graphene Oxide-M13 Bacteriophage Nanocomposites -Towards Graphene-Based Nanodevices," *Carbon Trends,* vol. 15, p. 100343, 2024, doi: 10.1016/j.cartre.2024.100343
- **K. Stokes**, Y. Sun, P. Passaretti, H. White, and P. G. Oppenheimer, "Optimisation of Graphage13 Macro-Dispersibility via Understanding the pH-Dependent Ionisation During Self-Assembly: Towards the Manufacture of Graphene-Based Nanodevices," *Nanoscale* vol. 15, pp. 13304 - 13312, 2023, doi: 10.1039/d3nr00778b.

In addition, the following paper was published:

- **K. Stokes**, K. Clark, D. Odetade, M. Hardy, and P. G. Oppenheimer, "Advances in Lithographic Techniques for Precision Nanostructure Fabrication in Biomedical Applications," Discover Nano vol. 18 (153), 2023, doi: 10.1186/s11671-023-03938-x.

CONTENTS

LIST OF FIGURES

LIST OF TABLES

LIST OF ABBREVATIONS

1D One-dimensional

2D Two-dimensional

3D Three-dimensional

AFM Atomic force microscopy

BET Brunauer-Emmett-Teller

BIC Bayesian information criterion

BGA Biocomposite graphene-based aerogel

BRED Bacteriophage Recombineering of Electroporated DNA

CNTs Carbon nanotubes

CRISPR Clustered Regularly Interspaced Short Palindromic Repeats

CWA Chemical warfare agent

DIW Deionised water

DLR Dual-site Langmuir-Freundlich

DLVO Derjaguin-Landau-Verwey-Overbeek

dsDNA Double-stranded DNA

DVS Dynamic vapour sorption

EDX Energy dispersive x-ray

EMI Electromagnetic interference

F-D Force-distance

FWHM Full width half maximum

GA Graphene-based aerogel

GAB Guggenheim-Anderson-de Boer

GO Graphene oxide

GPA GraPhage13 aerogel

GPH GraPhage13 hydrogel

LO Longitudinal optical

LSPR Localised surface plasmon resonance

NB Nutrient broth

NPs Nanoparticles

NWs Nanowires

OCFGs Oxygen-containing functional groups

PCR Polymerase chain reaction

PEG Polyethylene glycol

PP Partial pressure

PSO Pseudo-second-order

rGO Reduced graphene oxide

rpm Revolutions per minute

SEM Scanning electron microscopy

SERS Surface-enhanced Raman spectroscopy

SNR Signal-to-noise ratio

SPR Surface plasmon resonance

ssDNA Single-stranded deoxyribonucleic acid

TO Transverse optical

UV-Vis Ultraviolet-visible

VOC Volatile organic compound

CHAPTER 1

INTRODUCTION

This chapter includes extracts from the following paper:

P. Passaretti, **K. Stokes**, J. Carter, Y. Sun, F. Cuozzo, A. G. R. Zanna, T. R. Dafforn and P. Goldberg Oppenheimer " Characterisation, Modifications and Applications of the Filamentous Bacteriophage M13." (in submission)

Author contributions – **P. Passaretti** and **K. Stokes** wrote the main manuscript text (**K. Stokes** wrote the sections included in this chapter). **P. Passaretti** prepared figures. **J. Carter**, **Y. Sun**, **F. Cuozzo**, and **A. G. R. Zanna** provided specific sections in the review and overall insights. **T. Dafforn** and **P. Goldberg Oppenheimer** provided supervision and funding acquisition for the study. **P. Passaretti** and **P. Goldberg Oppenheimer** edited the revised drafts. All authors reviewed the manuscript.

1.1 Introduction to Nanostructures

Nanostructures are materials with at least one dimension within the nanometre scale, typically between 1-100 nm (1 nm = 10^{-9} m) [1]. At this scale, quantum effects become significant, and the surface-to-volume ratio increases dramatically compared to their bulk counterparts, leading to enhancements in their mechanical, thermal, electrical, optical, and magnetic properties [2-5]. The unique properties of nanostructures offer a wide range of applications such as bioimaging, drug delivery, antimicrobial surfaces, sensors, and energy storage [6-9]. However, the translation of these advancements into practical applications necessitates fabrication methods capable of producing consistent nanostructures at a high throughput and low cost. Conventional top-down fabrication techniques, such as lithography, involve etching away a bulk material to generate structures with micronano-scale dimensions [10]. Although these methods enable the production of complex, high-resolution nanostructures, they often suffer from limitations such as high fabrication costs, prolonged processing times, and structural imperfections [11].

Alternatively, bottom-up fabrication takes advantage of physical and chemical interactions between atoms and molecules to generate nanostructures. By combining particles in solution and optimising conditions such as the pressure, temperature and pH, it is possible to manipulate the inter-particle interactions. This can initiate their self-assembly, whereby these building blocks spontaneously reorganise into a well-defined, ordered structure [12, 13]. These advantages have driven increasing levels of research into the self-assembly of a wide variety of atoms and molecules, exploring the chemical conditions required to initiate their interaction and understanding how these conditions control the resulting nanostructures [14, 15].

In particular, there has been significant interest in the self-assembly of nanostructures with biological building blocks, owing to their numerous advantages and unique properties. The wide range of biomolecules, such as DNA, proteins, peptides, viruses and enzymes, enable a diverse array of options for nanostructure assembly. These biomolecules often show higher reactivity compared to non-biological molecules and possess many functional groups, providing a variety of functionalities. Additionally, the reaction conditions required are typically less stringent, often occurring under ambient conditions, which reduces both the complexity and cost. The structure, chemistry, and dimensions of biomolecules can also be easily controlled, providing a versatile and cost-effective route to fabricate a wide range of tailorable, multifunctional nanostructures [16, 17].

The self-assembly of bionanocomposites, created by integrating nanomaterials with biological building blocks, is particularly advantageous as it combines the unique functionalities of both components. The biological elements contribute biocompatibility, biodegradability, and tuneable surface functional groups, while the embedded nanomaterials enhance chemical and mechanical properties [18, 19].

This thesis focuses on a bionanocomposites known as the GraPhage13 aerogel (GPA), generated through the self-assembly of graphene oxide (GO) and the filamentous virus M13 bacteriophage [20]. The following sections will introduce GO, M13 and GPA, followed by an exploration of GPA's potential applications, the challenges in its future industrial implementation, and an overview of the investigations presented in this thesis.

1.2 Graphene-Based Materials

1.2.1 Graphene and Graphene Oxide

Graphene is an atomic layer of sp^2-hybridised carbon atoms in a π-conjugated honeycomb structure (Figure 1.1a), first characterised by Novoselov and Geim in 2004 [18]. Since its discovery, graphene has gained significant interest within the scientific community for its exceptional properties. These include its remarkably high carrier mobility at room temperature, excellent electrical and thermal conductivity, high mechanical strength, large specific surface area, and high transparency [21-25]. These attributes position graphene as a versatile material with applications in various fields, such as sensors [26, 27], flexible electronics [28, 29], energy storage [30, 31], transparent conductive films [32, 33], and stealth technologies [34, 35].

However, the industrial integration and applications of graphene have been hindered by several factors. Its zero-band gap limits its use in semiconductor applications such as in optics and electronics, while its chemical inertness and hydrophobicity present challenges in its functionalisation. Moreover, scaling up the production of high-quality graphene is challenging, as various production methods introduce chemical variability and defects, limiting its reproducibility and functionality [36, 37].

Graphene derivatives offer a promising alternative for graphene-based devices. Graphene oxide (GO), like graphene, consists of an atomic layer of carbon atoms, but it also contains various oxygen-containing functional groups (OCFGs) such as carbonyl, carboxyl, hydroxyl, and epoxide groups (Figure 1.1b). These functional groups render GO hydrophilic, resulting in its ability to form stable dispersions in water, and increase its chemical reactivity [38]. While GO lacks the superior electrical

conductivity due to the disruption of the sp^2 lattice by the OCFGs, it can be reduced to form reduced graphene oxide (rGO), which exhibits a similar electrical conductivity to pristine graphene (Figure 1.1b) [39].

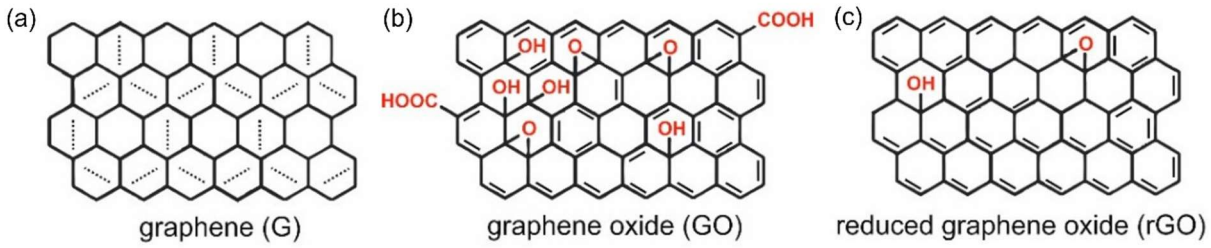

Figure 1.1: Graphene, graphene oxide and reduced graphene oxide structures

(a) Graphene is an atomic layer of sp^2 – hybridised carbon atoms in a honeycomb structure. **(b)** graphene oxide (GO) is graphene with oxygen-containing functional groups (OCFGs) **(c)** reduced graphene oxide (rGO) has less OCFGs than GO but more structural defects than graphene. Image adapted from [40].

1.2.2 Graphene-Based Aerogels

Another inherent limitation of graphene is its propensity to aggregate or undergo restacking due to strong van der Waals forces and π-π interactions. This diminishes its characteristics such as its high surface area, conductivity, and mechanical strength [41]. To maintain these properties, graphene-based derivatives can be assembled into 3D morphologies, such as ultralightweight porous structures known as aerogels. Graphene-based aerogels (GAs) possess a highly interconnected porous network and large surface area offering extensive contact areas for chemical reactions. These structures can also preserve the properties of graphene, such as its chemical stability, conductivity and mechanical strength [42]. As a result, GAs have found applications as catalysts [43, 44], biomedical sensors [45, 46], and supercapacitors [47, 48].

The fabrication of GAs typically begins with the production of hydrogels, which are 3D water-insoluble cross-linked porous networks [49]. GO is the increasingly becoming the graphene derivative of choice to generate these hydrogels due to its ability to form stable dispersions in solution, allowing for simple hydrogel fabrication [42, 50-52]. Furthermore, GO can be functionalised with new chemical compounds [53, 54], functional groups [55, 56], and materials such as nanoparticles [57, 58] through interactions with OCFGs, enabling properties of the resulting GA to be enhanced or customised for specific applications. Drying techniques such as supercritical, vacuum, or freeze drying replace the water in the hydrogel with air, preventing the pores from collapsing and producing aerogels [59, 60].

Compared to other aerogels, such as silica, polymer, and metal-based aerogels, GAs exhibit the lowest density while also demonstrating enhanced electrical conductivity, mechanical strength, and thermal stability (Table 1.1). However, despite these advantages, GAs face significant challenges, particularly regarding scalability and production costs. The synthesis of GO-based hydrogels often require high temperatures or pressures, extreme pH levels, or environmentally harmful reducing agents. Additionally, the drying processes are highly energy-intensive, significantly increasing both their production costs and environmental impact [61]. In contrast, silica aerogels benefit from simpler and more cost-effective ambient pressure drying, making them a more economically viable option for large-scale manufacturing. Additionally, maintaining consistent quality in large-scale GA production remains difficult, as variability in precursor synthesis can lead to batch-to-batch differences, complicating commercialisation. Although GAs offer improved mechanical properties compared to silica aerogels, they are still structurally fragile and prone to collapse under high stress,

Table 1.1 Comparison of different aerogel types

Properties of different aerogels, highlighting their composition, density, surface area, benefits, drawbacks, and key applications

Type of Aerogel	Starting Material	Density (mg/cm^3)	Surface Area (m^2/g)	Advantages	Limitations	Example Applications	Refs.
Silica	TEOS MTMS	3 – 350	600-1000	Low thermal conductivity Low dielectric constant Low refractive index Low cost	Poor mechanical properties Long processing times High hygroscopicity	Thermal insulation Acoustic barriers Supercapacitors Catalysts Absorbents	[62, 63]
Synthetic polymers	PI PDMS PVA PVC PUA	30-480	20–632	High mechanical strength Low dielectric constant	Expensive, toxic precursors Poor biodegradability	Drug delivery Tissue engineering Thermal insulation Antennas	[16, 63-66]
Bio-polymers	Cellulose Chitosan Alginate Gelatin Starch	0.8-920	10-970	High compressive strength Biodegradable Stability in organic solvents	Poor mechanical properties Poor long-term stability Limited operating temperatures	Biosensors Medical devices Absorbents Catalysis	[63, 67]
Carbon	Carbon GO rGO CNTs	0.16-190	360–1000	High thermal and electrical conductivity Chemical and thermal stability Biocompatible	Poor mechanical properties High cost	Electrodes Supercapacitors Absorbents Energy storage Biomedical	[63, 68, 69]
Metal	Transition metals e.g. nickel, copper, titanium Noble metals e.g. gold, silver	5-580	2-170	High chemical stability High electrical conductivity High catalytic activity High ductility	High production complexity Limited compositions Poor structural control Poor mechanical properties	Electrocatalysts Sensing Energy storage and conversion Water remediation	[70]
Metal oxide	Alumina Titania Zirconia	20-1200	1120-1750	High chemical stability Compositional variety	Poor mechanical properties Poor heat resistance	Photocatalysts Thermal insulation Absorbents	[71-73]

limiting their suitability for applications requiring long-term mechanical durability. As a result, despite their superior functional properties, GAs are not yet widely adopted in commercial industries [50, 74]. Overcoming these challenges requires the development of cost-effective precursor materials, improved drying techniques, and scalable production methods to enhance their viability and promote their widespread use in high-performance applications.

1.2.3 Biocomposite Graphene-Based Aerogels

The fabrication of biocomposite graphene-based structures, through interactions with the functional groups on their surface with the OCFGs in GO, offers a promising solution to these challenges. Biomaterials are non-toxic, biodegradable and often offer low cost, high throughput and environmentally friendly production, reducing the expense of precursor materials while significantly enhancing the scalability of the resulting biocomposite graphene-based aerogels (BGAs). However, the weak and reversible interactions between graphene derivatives and the biomaterials can result in low stability in aqueous solvents and poor mechanical properties. Extreme temperatures and pH levels can denature the biomaterials, limiting their applicability in harsh environments. Additionally, the literature lacks comprehensive comparisons between graphene-based biocomposites and other graphene-based structures, as well as systematic follow-ups on optimising their fabrication, processing, and integration into functional graphene-based devices for real-world applications. Addressing these gaps is crucial for advancing the development and commercialisation of BGAs [75].

A rapidly growing area of research involves the synthesis of graphene-based biocomposites by combining GO or rGO with biopolymers [75]. These include polysaccharides such as starch, chitosan, cellulose and alginates; protein-based biopolymers such as gelatin and wheat gluten, and biodegradable polymers such as polylactic acid, polypropylene carbonate and polyamides [76]. Incorporating graphene derivatives into these materials has been shown to enhance their mechanical and electrical properties, generating a biocompatible material with a high surface area [77]. Several recent studies have demonstrated the potential of BGAs fabricated with graphene derivatives and biopolymers for applications in water contaminant removal [78-80]. For instance, Kovtun et al. developed chitosan-gelatin-GO (CCGO) aerogels for the absorption of fluoroquinolone antibiotics and lead. Two distinct formulations were fabricated, with GO either embedded within the structure (CCGO-E) or applied as a coating (CCGO-C). These were then compared to chitosan-gelatin (CG) aerogels, which served as control samples (Figure 1.2). While the CG aerogels exhibited negligible adsorption, both CCGO formulations achieved up to 90% removal of fluoroquinolone antibiotics within 24 hours. Notably, CCGO-C rapidly removed 60% of lead (Pb) before reaching saturation, whereas CCGO-E demonstrated a more gradual uptake. CCGO-E ultimately exhibited a superior sorption capacity, achieving 43% Pb removal within the first hour and reaching complete (100%) removal after 24 hours [78]. However, to fully realise the potential of BGAs in this field, several challenges must be addressed. It remains difficult to develop a fabrication process that is cost-effective, environmentally friendly, and scalable while preserving the desirable characteristics of the biocomposite. Graphene-based materials also have a tendency to aggregate, which can result in a non-uniform distribution of graphene within the

composite and lead to inconsistencies in mechanical and electrical properties. Additionally, the biocompatibility of these materials depends on the fabrication process and must be carefully assessed before they can be implemented into biomedical applications to ensure their non-toxicity [77].

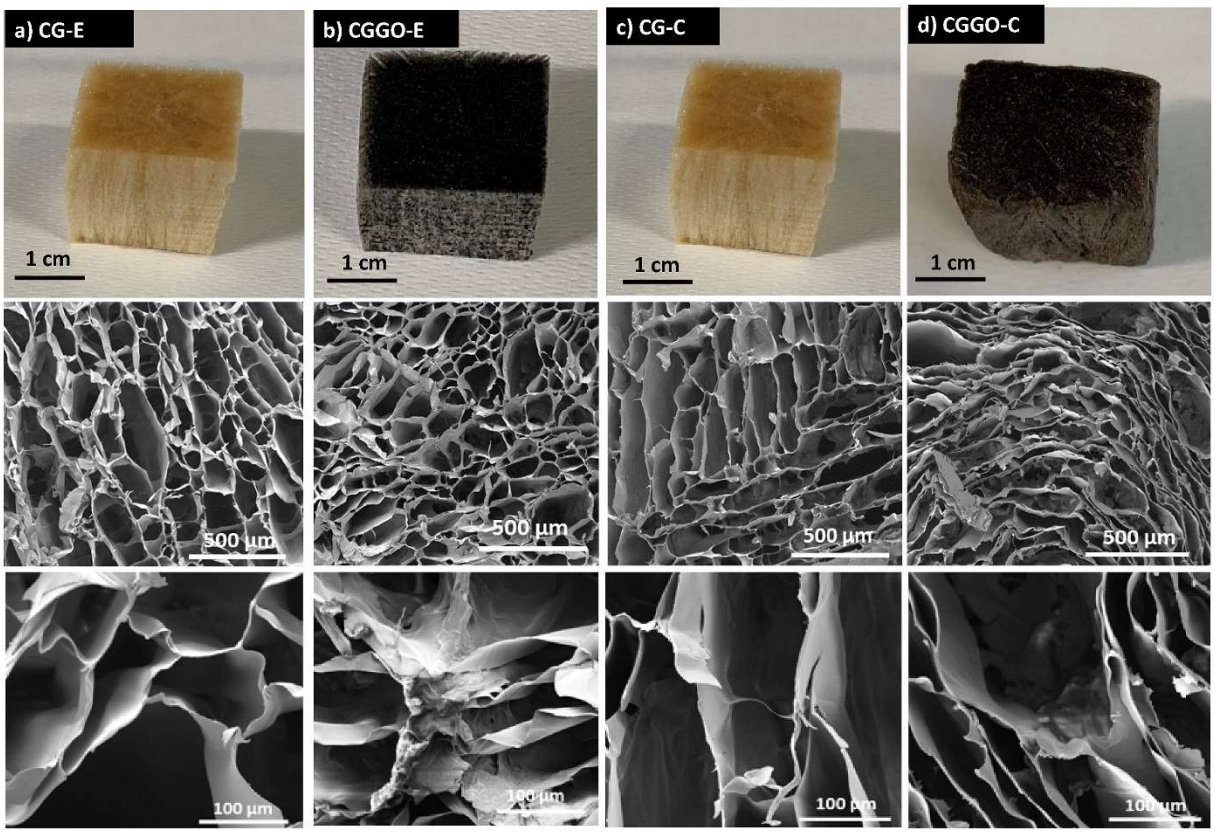

Figure 1.2: Chitosan-gelatin and chitosan-gelatin-GO aerogels

Optical and environmental scanning electron microscopy (ESEM) images of chitosan-gelatin (CG) aerogels and chitosan-gelatin-graphene oxide (CGGO) aerogels with GO either being embedded within the structure (CGGO-E) or coating the aerogel (CGGO-C). Image from [78].

Additionally, BGAs can also be fabricated using DNA. The first reported study, conducted by Xu et al., demonstrated that GO and DNA self-assembled via π-π stacking interactions, forming a hydrogel with high mechanical strength, stability, and adsorption capacity, while remaining resistant to extreme pH levels and organic solvents. Although this material was not converted into an aerogel, future studies could

explore its drying process and the properties of the resulting BGA [81]. More recently, Leng et al. developed a DNA-based rGO aerogel, where rGO functioned as a structural scaffold, improving conductivity and stability. Additionally, DNA swelling upon water immersion created bioadhesive microcompartments, enabling bacterial capture and the formation of a bioanode with high current density [82]. Like proteins, DNA can be modified for specific applications; however, its use is limited by the high cost of its large-scale synthesis, and instability under extreme temperatures, pH levels and aqueous environments [83, 84]. A further limitation of DNA nanostructures is that the resolution of molecular positioning is generally restricted by the minimum spacing between attachment sites on staple strands, approximately 3–5 nm [85].

Proteins such as soy [86], egg white [87, 88] and silk proteins [89] have also been used in the fabrication of BGAs. These have shown potential in sorption applications, with GO serving as the primary adsorbent, while the proteins function as low-cost, non-toxic precursors that facilitate self-assembly [86, 87]. Additionally, one study explored the fabrication of BGAs using GO and the ring-like peroxiredoxin protein *Sm*PrxI. Ardini et al. demonstrated GO and *Sm*PrxI self-assembled through weak intermolecular interactions at a neutral pH while also partially reducing the GO. Additionally, proteins can be engineered to modify their functional groups (further discussed in Section 1.3.2), allowing for the incorporation of additional amino acid residues capable of binding metal ions at the N-terminal. This approach enabled the functionalisation of the rGO–*Sm*PrxI aerogel with gold and palladium nanoparticles, broadening its potential applications [90]. However, proteins are highly susceptible denaturation when exposed to fluctuations in temperature, pressure, or pH. Since the function of the protein is

dependent on its structure, deviations from optimal conditions may disrupt assembly, reduce functionality, and diminish the long-term durability of BGAs [75].

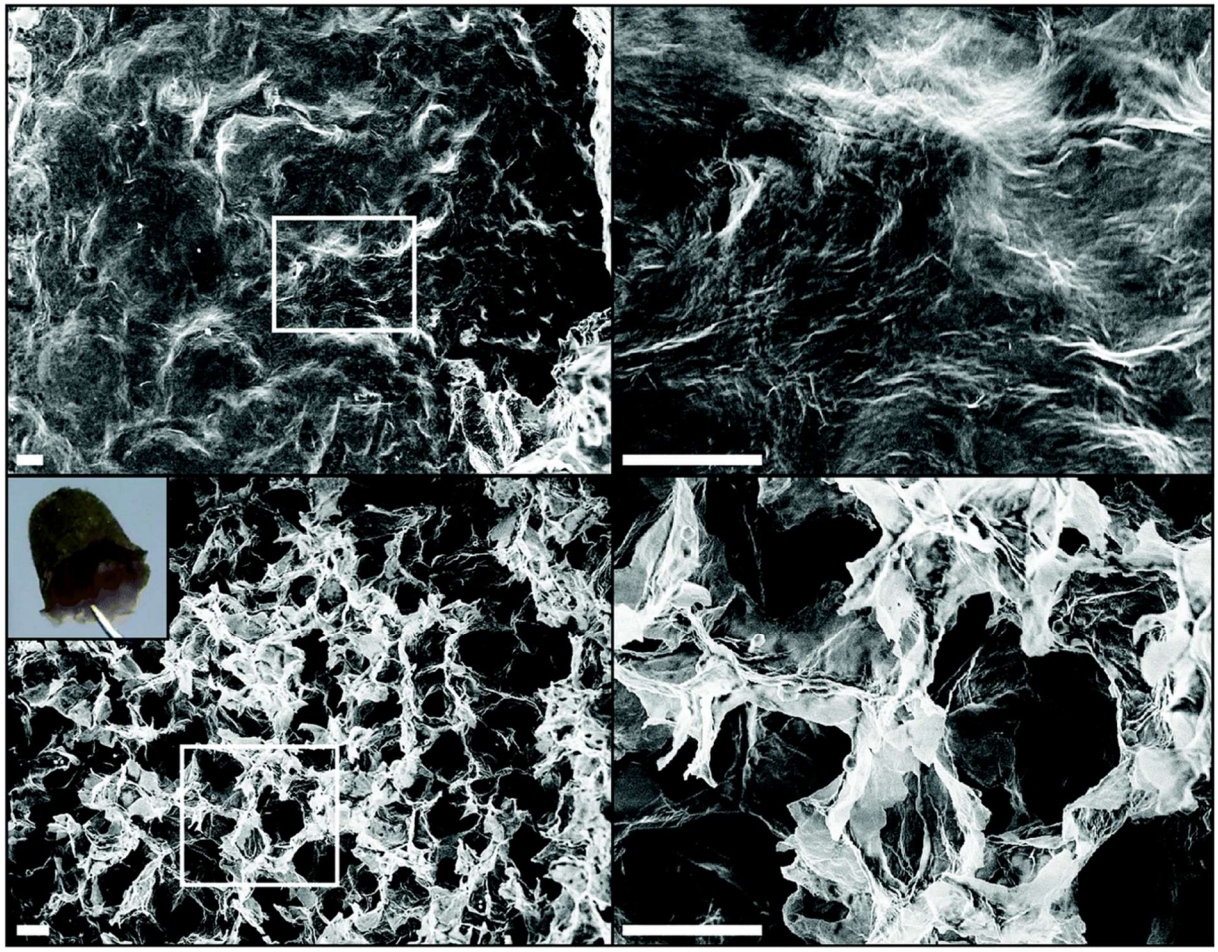

Figure 1.3: SEM images of rGO-*Sm*PrxI composites

Scanning electron microscopy (SEM) images of a composite fabricated with reduced graphene oxide (rGO) and the ring-like protein *Sm*PrxI. Image adapted from [90].

Viruses have also been employed in BGA fabrication due to their unique nanoscale properties. Viruses are naturally occurring biomolecular nanostructures composed of genetic material enclosed in a protein capsid. Their precisely defined nanostructure and dimensions make them highly suitable as scaffolds for bionanostructures. Additionally, viruses can be efficiently mass-produced through propagation within their infected hosts, which is ideal for large-scale applications, and their well-characterised

genetic material allows for precise modifications through genetic engineering, enabling tailored functionality for specific applications [91].

Compared to isolated proteins, viruses exhibit greater resistance to extreme conditions such as temperature and pH fluctuations [92], and are generally less expensive and time-consuming to produce [93]. Their well-defined structure is ideal for the generation of highly ordered bionanomaterials, improving the efficiency, performance and functionality resulting devices [94]. Moreover, viral capsids offer a higher resolution for molecular placement (approximately 0.5–1 nm) compared to DNA nanostructures [85]. However, the use of viruses in the fabrication of graphene-based biocomposites remains relatively unexplored, limiting their potential applications. Expanding research in this area could unlock new possibilities for employing viruses as structural components, enhancing the functionality and versatility of graphene-based biocomposites across various fields. the limited studies conducted thus far have primarily focused on the generation of graphene-virus bionanocomposites with GO and the M13 bacteriophage [20, 95], which will be discussed in greater detail in the following section.

1.3 M13 Bacteriophage

1.3.1 Structure and Replication

M13 bacteriophage is a filamentous virus belonging to the *Inoviridae* family with dimensions of approximately 6.6 nm width and 880 nm length, and a mass of 16.3 MDa (2.7×10^{-8} ng) [96, 97]. It consists of a circular-shaped single-stranded DNA (ssDNA) molecule encapsulated by approximately 2700 copies of the major coat

protein PVIII. Minor coat proteins PIII and PVI are located at its head, while PVII and PIX are found at its tail (Figure 1.4).

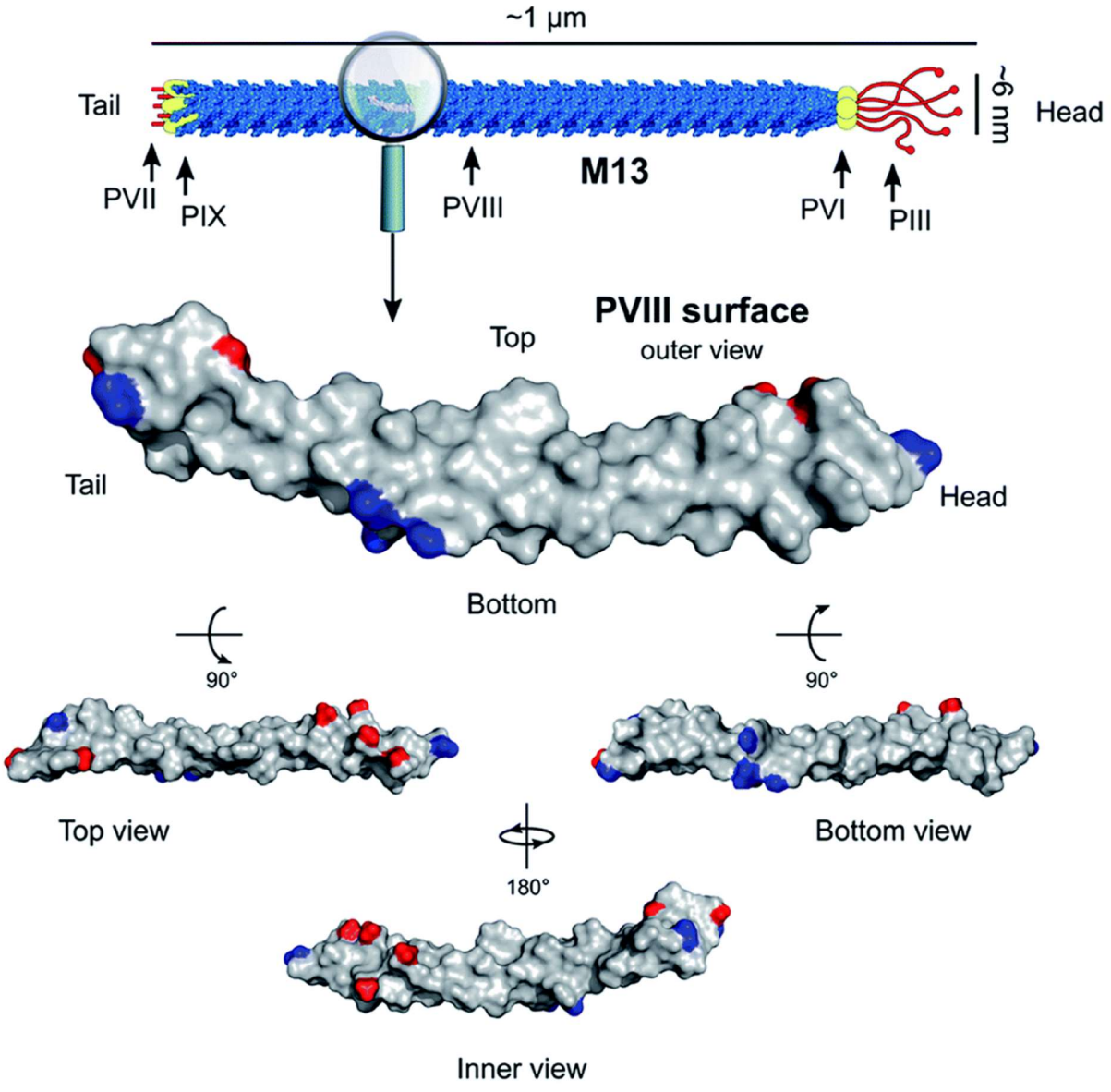

Figure 1.4: Structure of M13 bacteriophage

A schematic representation of M13 bacteriophage, highlighting its structural proteins: the major coat protein PVIII and the minor coat proteins PIII, PVI, PVII and PIX. Below demonstrates a detailed view of an individual PVIII structure. The ionisable residues are indicated in blue and red, representing negative and positive charges, respectively. Image adapted from [98].

Each of these proteins consists of a positively charged region (C-terminus), a neutral region and a negatively charged region (N-terminus). The major coat proteins PVIII exhibit a right-handed helical structure and are orientated at an angle of 20° relative to the longitudinal axis of the phage, forming a pentagonal structure. As a result, M13 phages display five-fold rotational symmetry and two-fold screw symmetry [99].

The surface charge of M13 is determined by the amino acids present on its PVIII proteins, including alanine (A), aspartate (D), glutamate (E), lysine (K), serine (S), and tyrosine (Y). Passaretti et al. identified the primary contributors to M13's surface charge as the positively charged A1 and K8 amino acids and the negatively charged D4, D5, E2, and E20 amino acids, due to their chemical characteristics and their external positioning on M13's surface. As these amino acids protonate and deprotonate at different pH levels, altering the acidity or alkalinity of the suspension solution allows for the manipulation of its surface charge [98].

One advantage of using M13 for the generation of bionanocomposites is its low-cost, high throughput and environmentally friendly production. M13 reproduces by infecting bacteria that possess *F-pili*, such as *Escherichia coli* (*E.coli*). The phage injects its genetic material into *E.coli* cells and utilises its metabolic machinery to replicate.

Newly generated phages then migrate to the bacterial cell membrane and leave the cell through protein pore channels. Importantly, M13 is a lysogenic phage, meaning that this process does not damage the cell membrane or destroy the host cell [100, 101]. The continuing replication of *E.coli* while infected with M13 results in the production and release of additional phages, leading to their mass amplification [102]. The use of a non-pathogenic TOP10 *E.coli* strain (Section 2.1.3) reduces the potential

risks associated with M13 production [103], and the generated phages are non-toxic and not harmful to humans, animals or the environment [104].

1.3.2 Chemical and Genetic Modifications

The properties of unmodified M13, known as wild-type M13, can be customised through chemical and genetic modifications (Figure 1.5). The functional groups exposed on M13's coat proteins, such as the N- and C-terminal residues, carboxylic acids, amines, and amino acids like tyrosine and cysteine, can be chemically modified. This allows various chemical moieties to be attached to wild-type M13, tailoring its characteristics for specific applications [97, 105].

Its genetic properties can be modified through a pioneering technique known as phage display, developed by G. Smith in 1985, which allows selected peptides or proteins to be displayed on the surface of bacteriophages [106, 107]. This process involves the incorporation of foreign amino acid sequences into the genes responsible for the phage's coat proteins, most commonly the minor coat protein PIII and the major coat protein PVIII, resulting in the creation of novel hybrid proteins [108]. If the insertion does not compromise the essential functions of the protein, the peptide or protein is displayed on the phage's surface. This allows for its replication and the generation of a substantial population of phages bearing the same peptide or protein on their surfaces [109]. The process of splicing different gene sequences into the phage's coat proteins yields a diverse array of hybrid proteins and surface peptides [110, 111]. By tailoring M13 to display specific peptides and proteins, phages with unique properties and functionalities can be produced, enabling the creation of custom nanostructures for a wide range of applications [112, 113].

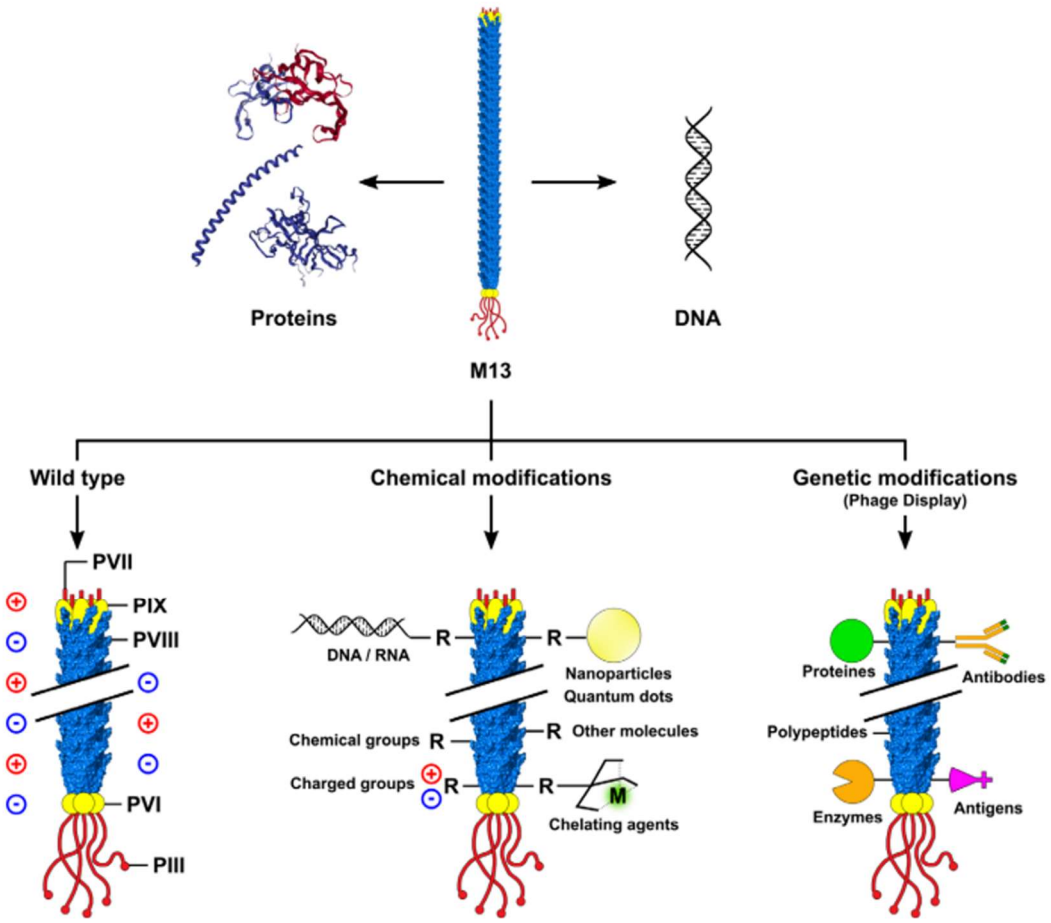

Figure 1.5: M13 components and modifications

A schematic demonstrating the main components of M13, including its single-stranded DNA and proteins (PIII, PVII, PVIII and PIX), and examples of how M13 can be adapted through chemical and genetic modifications. Adapted from [114].

1.3.3 Fabrication of M13-Based Nanostructures

Bacteriophages from the *Inoviridae* family (*fd, f1* and M13) offer several advantages for bionanostructure fabrication due to their well-defined filamentous structure, lysogenic replication, resistance to extreme pH and temperature conditions, and their ability to be chemically and genetically modified. Although these phages share 98% of their DNA, M13 is the most extensively studied for bionanomaterial fabrication [115]. M13 exhibits greater rigidity and symmetry, allowing for the formation of nanostructures

with a stable structure and enhanced mechanical stability [116, 117]. Additionally, M13 is commonly utilised to generate phage display libraries, enabling researchers to replicate modifications to M13 and tune its properties for a given application [118].

1.3.3.1 Liquid Crystals

The helical, nanofibrous structure of M13, combined with its monodispersity and ability to express multiple functional groups, allows it to form a lyotropic crystalline phase, which are generating by dissolving amphiphilic molecules in a solvent. The phase transitions of lyotropic liquid crystals can be precisely controlled by adjusting variables such as the ionic strength, external fields, and M13 concentration [119, 120].

At low concentrations (below 5 mg/mL), M13 exists in the isotropic phase, where the phages are randomly distributed in solution (Figure 1.6). When the concentration increases to the 10-20 mg/mL range, nematic phase liquid crystals are formed (Figure 1.6). Nematic liquid crystals are a type of mesophase in which molecules align parallel to one another along their long molecular axes, but have no long-range positional order [121]. The increase in M13 concentration leads to the distance between phages becoming smaller than the length of M13, generating steric forces that orientationally align the phages. This causes the phages to intertwine along the perpendicular axis of the layers, creating helical phage structures.

At concentrations between 20-80 mg/mL, there remains no long-range positional order, but the layers of M13 develop an increasingly helical structure, forming what is known as the cholesteric phase of liquid crystals (Figure 1.6) [121].

Above 100 mg/mL, smectic phase liquid crystals are formed. Unlike the nematic and cholesteric phases, smectic liquid crystals exhibit both long-range orientational and

positional order. In this phase, the phages are arranged in well-defined layers that can slide over one another, with different smectic phases arising depending on the degree of positional and orientational order (Figure 1.6) [121]. Different smectic phases can form based on the degrees of positional and orientational order. Therefore, by genetically modifying M13, altering the concentration of M13 and incorporating different materials, various crystal structures can be tailored for different applications [94].

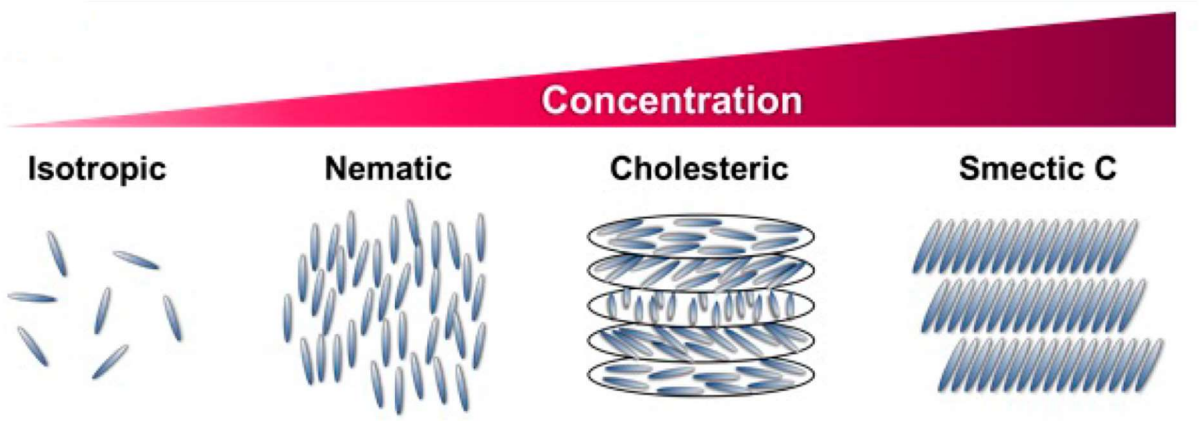

Figure 1.6: Liquid crystal phases of M13 bacteriophage

A schematic showing the change in M13 liquid crystal phase with increasing M13 concentration. Adapted from [96].

For example, M13 films with distinct liquid crystalline phases exhibit optical properties including iridescence and selective reflection or transmission of light, offering potential applications in optical-based sensors [122]. Moreover, combining M13 liquid crystals with other components enables the self-assembly of hybrid structures such as ZnS and CdS nanocrystals [119, 120, 123].

1.3.3.2 Nanoparticle Growth and Templating

Nanoparticles are zero-dimensional materials with nanoscale dimensions and often exhibit unique properties, such as the distinctive plasmon resonance effects of gold

nanoparticles (AuNPs) and silver nanoparticles (AgNPs) [124, 125]. The carboxylic acids present in the amino acid residues on the surface of M13, such as aspartic acid, glutamic acid, tryptophan, tyrosine and cysteine, can coordinate metal ions and become nucleation sites for nanoparticle formation [126, 127].

Wang et al. reported the synthesis of AuNPs on the surface of M13. This process involved depositing phages into a chloroauric acid solution, where the amino acid residues reduce the chloroauric acid, leading to the formation of AuNPs [127]. Further metal nanoparticles such as iron [128], rhodium, palladium and ruthenium nanoparticles [129] and iron-silver [128], cobalt-platinum [130], gold-rhodium, gold-platinum, platinum-rhodium and palladium-rhodium bi-nanoparticles [131] have been generated through mixing filamentous M13 with metals in the presence of sodium borohydride ($NaBH_4$) acting as a reducing agent.

Plank et al. took a similar approach, but instead produced nanoparticles on spheroidal M13 (Figure 1.7). M13 was genetically engineered to display the Au-binding motif on the PVIII major protein and the 9-mer ZnS-binding peptide on the PIII minor coat protein. The phages were then exposed to chloroform, resulting in spheroidal M13. Combining chloroauric acid and spheroidal M13 with $NaBH_4$ produced AuNPs on the PVIII protein. Subsequent mixing with zinc chloride and sodium sulphide generated zinc sulphide nanoparticles on the PIII protein, producing hybrid noncentrosymmetric nanostructures [132].

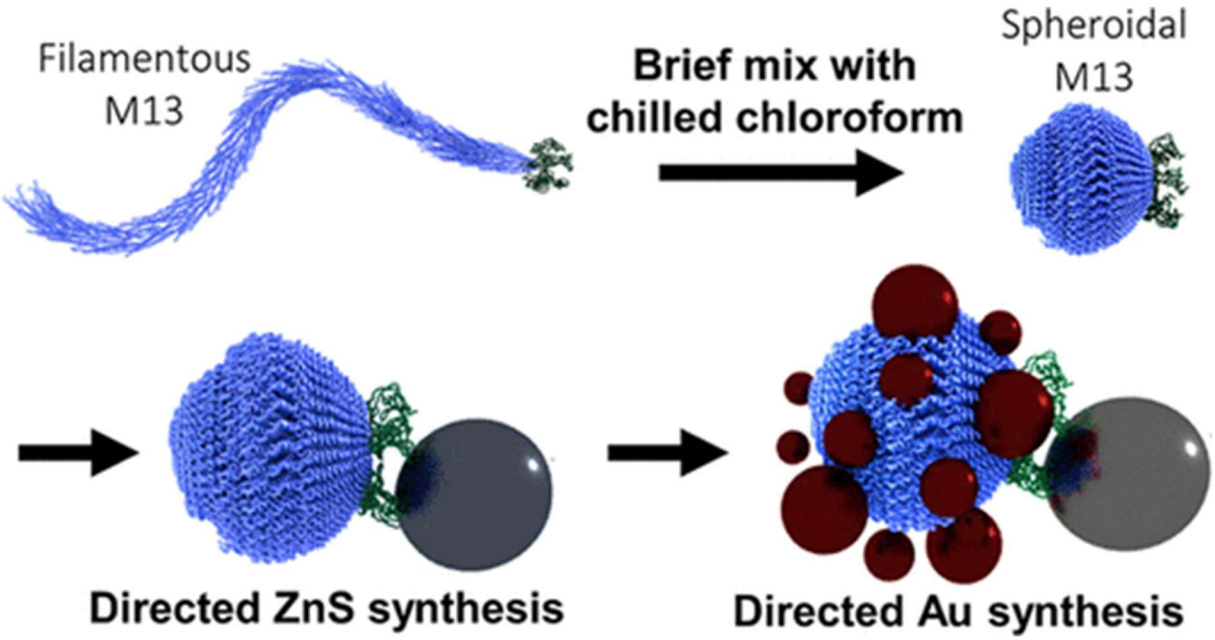

Figure 1.7: Hybrid Au-ZnS-spheriodical M13 bacteriophage nanostructures

A schematic illustrating the synthesis of hybrid Au-ZnS-spheriodical M13-based nanostructures. M13 bacteriophages were genetically engineered to bind gold (Au) and zinc sulfide (ZnS), and was subsequently exposed to chloroform, inducing its transformation into a spheroidal shape. Au and ZnS nanoparticles were then grown on these modified phages, forming hybrid non-centrosymmetric nanostructures. Figure from [132].

1.3.3.3 Nanowires

Nanowires are one-dimensional (1D) crystalline or semicrystalline structures with a diameter less than 100 nm and a high length-to-radius ratio [133, 134]. They possess unique thermal, optical, electrical and mechanical properties, a high surface-to-volume ratio, and can be readily functionalised with biomolecules [135].

Several studies have demonstrated how M13 could be used to assemble gold nanowires (AuNWs) with cadmium selenide (CdSe) nanocrystals. In one approach, M13 was modified to bind to AuNPs serving as seed crystals for the electroless deposition of gold, resulting in the formation of AuNWs that could be subsequently coated with CdSe [136, 137] . Alternatively, Huang et al. genetically modified the PVIII

major coat protein to bind to AuNPs, and the PIII minor coat protein to display streptavidin-binding motifs, enabling interactions with streptavidin-conjugated cadmium selenide (CdSe) quantum dots [138]. More recently, Han et al. produced AuNWs for electrodes in perovskite solar cells. These nanowires were created by growing AuNPs directly onto wild type M13 with the aid of a dimethylamine borane reducing agent. The M13 template facilitated the generation of electrodes with a stretchability of 8%, overcoming the limited mechanical flexibility of other metal NW electrodes (Figure 1.8) [139].

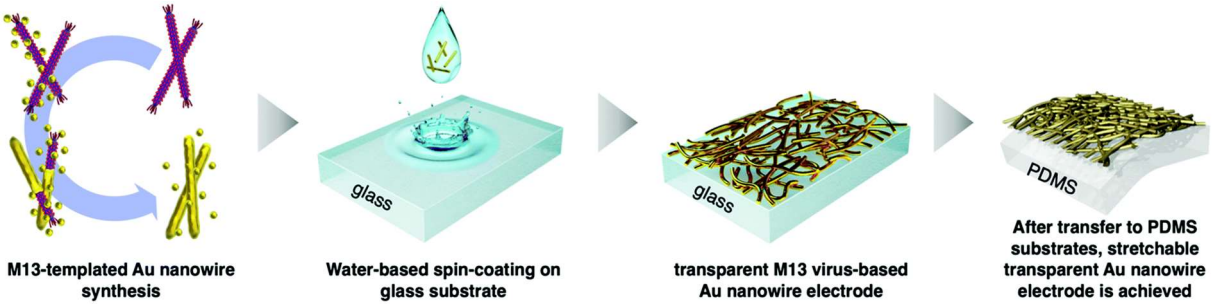

Figure 1.8: M13 bacteriophage-templated gold nanowire electrodes

A schematic demonstrating the fabrication of stretchable electrodes with M13-templated gold nanowires. The nanowires are sin-coated onto a glass substrate to form a film, and then transferred to a PDMS substrate to generate the flexible electrodes. Image from [139].

Furthermore, semiconducting and magnetic nanowires were generated by Mao et al. through genetically engineering the PVIII major coat protein to nucleate and template nanocrystals. Semiconducting nanowires were fabricated by engineering the PVIII protein to nucleate of ZnS and CdS nanocrystals, while the magnetic nanowires were created by nucleating cobalt-platinum and iron-platinum particles [140, 141]. M13 has also been employed in the fabrication of nanowire-like segregating-binary-alloy type phase-change materials. Nanowires were produced through electrostatic interactions

that mediated the nucleation of germanium-tin oxide on the surface of both wild type M13 and M13 modified to exhibit an increased negative surface charge [142].

1.3.3.4 Nanofibers and Fibrous Bundles

Nanofibers are mechanically flexible nanostructures that are typically amorphous and demonstrate a high length-to-radius ratio [134]. As their structure resembles cellular microenvironments, they have attracted considerable attention in the biomedical sector [143]. Nanofibers have also shown promise in applications such as sensors, filtration, and energy storage [144].

M13 nanofibers can be produced through electrospinning, a process in which an M13 suspension is contained in a reservoir connected to a micro nozzle. The application of an electric potential between the nozzle and a substrate generates liquid jets, which are deposited onto the substrate and subsequently dried to form nanofibers [145]. Shin et al. harnessed this technique to create nanofiber matrices with RGD peptide-displaying M13 bacteriophage, suspended in poly(lactic-co-glycolic acid) (PLGA). The resulting nanofibers proved to be suitable for bioactive scaffolds in tissue engineering applications [146]. Sugimoto et al. further developed this method, generating M13 nanofibers using near field electrospinning. This technique involves reducing the distance between the nozzle and the substrate, and allows precise and controlled fibre deposition by adjusting the nozzle's position relative to the substrate (Figure 1.9) [147].

An alternative method for producing M13 nanofibers is wet-spinning, where a M13 suspension is extruded through a capillary tube with glutaraldehyde, facilitating the cross-linking of the phages. The suspension is then air-dried, resulting in M13 nanofibers [145]. Chiang et al. employed this process with M13 genetically engineered

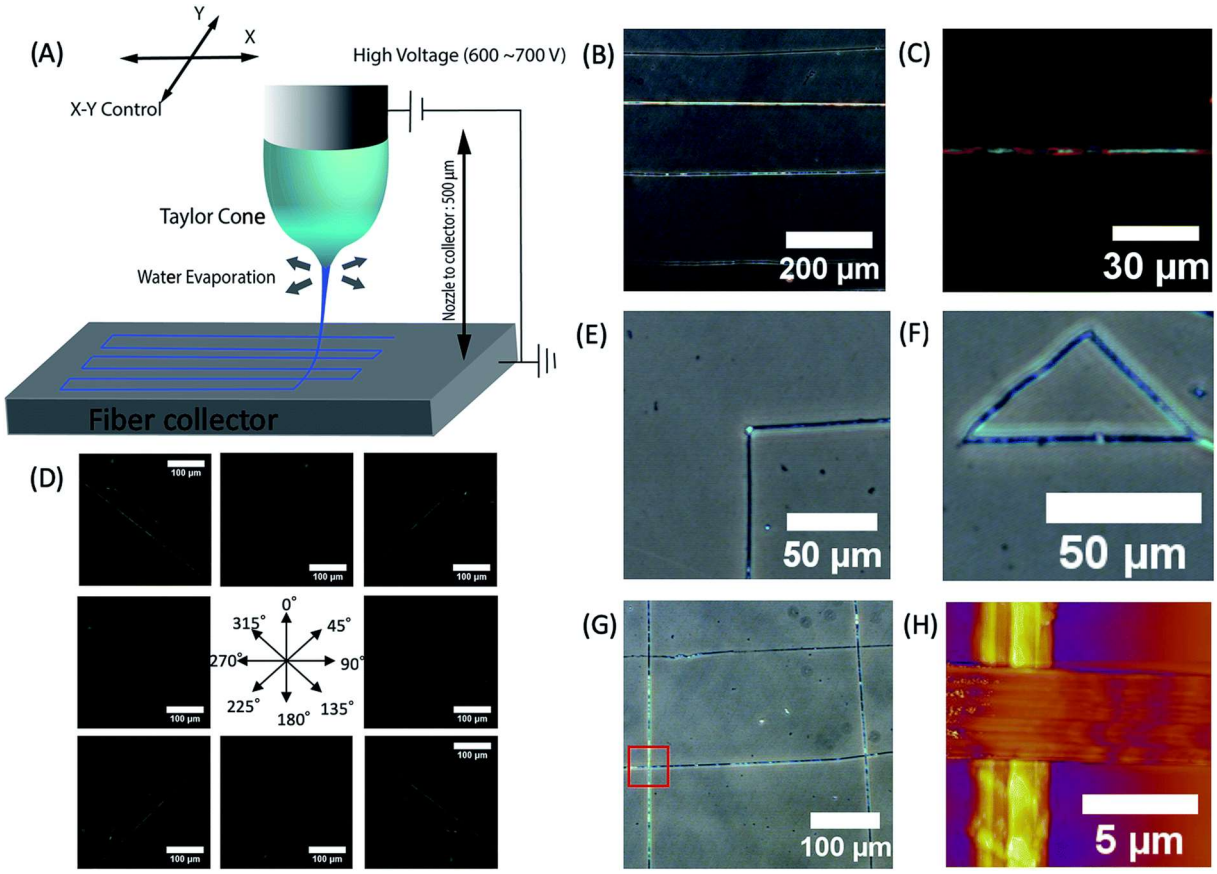

Figure 1.9: M13 phage fibres generated with near-field electrospinning

Deposition and characterisation of M13 phage fibres fabricated with near-field electrospinning. (A) A schematic of M13 phages being deposited onto a gold-coated silicon substrate using a micro nozzle, generated M13 fibres; (B-H) Characterisation of different fibre patterns, including (B-C) optical images of straight line patterns, (D) polarised optical images of aligned phage fibres, (E-G) optical images of varying M13 fibre patterns and (H) AFM images of crossing M13 fibres. Image from [147].

to bind to amine-terminated CdSe quantum dots. The resulting nanofibers exhibited mechanical properties similar to synthetic polymer fibres. The ability to genetically engineer the properties of these nanofibers offering potential applications in electronic devices and medical fields [148]. Incorporating additional materials into the nanofiber structure, such as conductive polymers and nanomaterials, can enhance electrical properties and expand their applications in biomedical engineering, electronics, and sensing [149, 150].

Beyond nanofibers, fibrous bundles can be created with M13. Genetic modification of M13 to display the E8 peptide gave M13 a negative surface charge, and electrostatic interactions between the calcium ions and the anionic phages resulted in the formation of fibrous bundles. Fibrous bundles were also produced with M13 and hydroxyapatite, a non-collagenous protein essential for bone strength and regeneration. These fibrous bundles can further be processed into nonfibrous bio-inorganic hybrid structures, offering potential applications in the development of biomaterials that mimic bone tissue for bone tissue engineering purposes [151, 152].

1.3.3.5 Fims, Monolayers and Patterned Surfaces

Thin films of M13 bacteriophage can be generated through solvent evaporation. The liquid flows radially as it evaporates, leading to the formation of a circular area of phage, with most of the phage accumulating around the outer circumference. This structure is known as the “coffee-ring” and can be controlled by adjusting factors such as the evaporation temperature, substrate, and concentration [153]. More recently, Park et al. also demonstrated the production of M13 films through evaporation by pulling the M13 suspension over a substrate, and subsequently drying to self-assemble chiral M13 films. The morphology of the films could be adjusted by varying the concentration and pulling speed of the shear flow (Figure 1.10) [154].

By genetically modifying M13 to bind to metals, M13 films can be produced on metallic surfaces such as gold and titanium to create biofunctional and multifunctional surfaces [155-158]. Warner et al. produced M13 films on gold substrates, altering the film

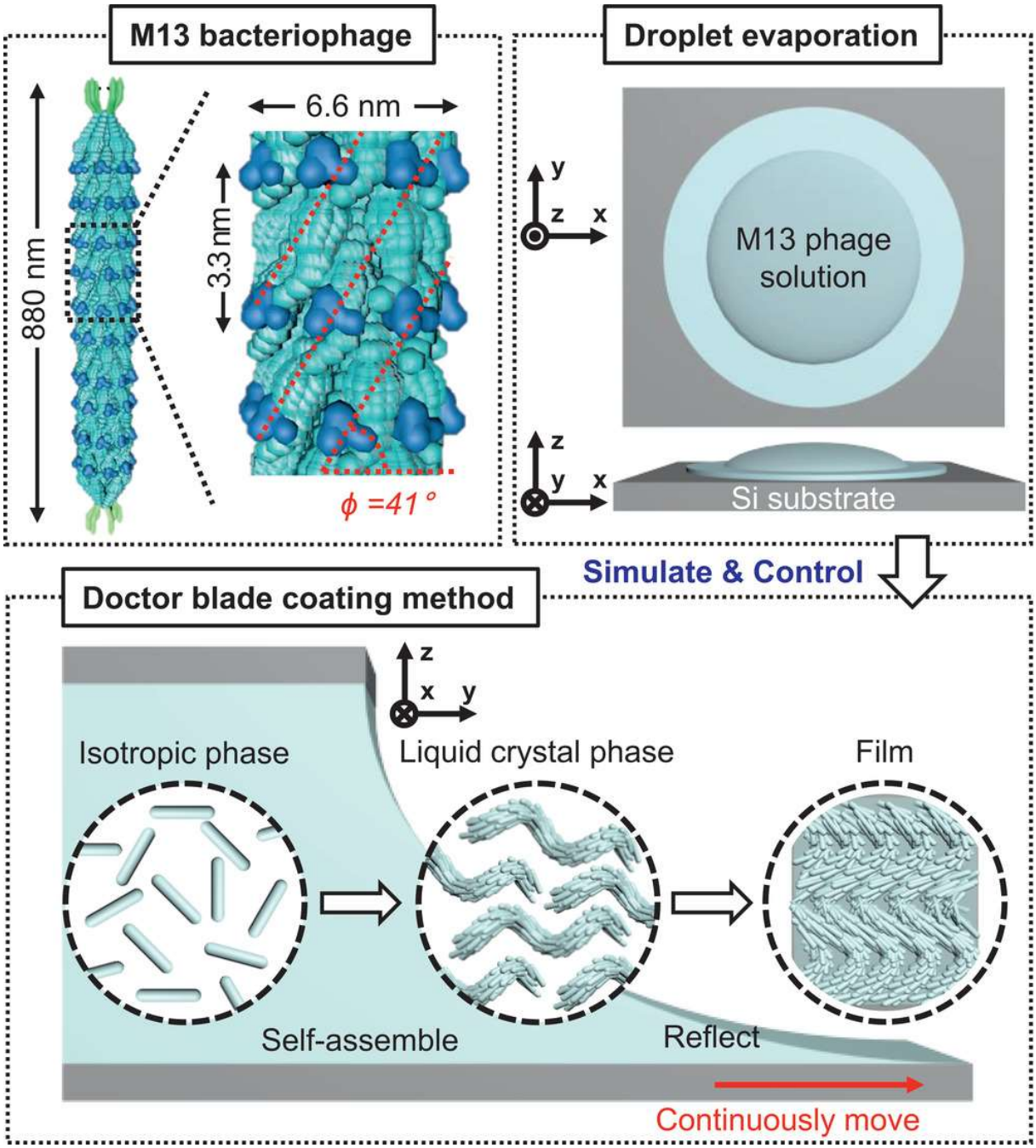

Figure 1.10: Evaporation-induced self-assembly of M13 bacteriophage thin films

The fabrication of M13 bacteriophage thin films through the deposition of M13 phage solution onto a silicon substrate and subsequent pulling across the substrate. Image from [154].

morphology by varying the roughness of the gold surface. Genetically engineering M13 to bind to inorganic components affected the morphology and the mechanical properties of the films [159]. Additionally, M13 can be combined with polymers to create

biocomposite films and, by modifying the concentration of M13, the morphology and electrical properties of these films can be varied [160].

Furthermore, the use of substrates with various topological patterns can lead to a wider range of M13 films. Gold substrates can be patterned using lithographic techniques such as capillary force lithography and microcontact printing. Through the functionalisation of the exposed gold surface and the genetic modification of M13, the phages can bind to the gold surface. These structured surfaces can subsequently be used to immobilise biomolecules and facilitate the growth of gold and ZnS nanostructures [161, 162].

Additionally, multilayer biofilms can be generated by alternating layers of phages and polymers. Yoo et al. developed multilayer and topological patterns with M13 and a positively charged polyelectrolyte multilayer (PEM) consisting of cationic linear-polyethylenimine and anionic polyacrylic acid. Attractive electrostatic forces between the PEM and M13, along with electrostatic repulsion between phages, resulted in the formation of a monolayer of M13. This surface was further functionalised by depositing additional PEMs on top of the M13 monolayer, or by genetically modifying M13 to bind to metal or semiconducting nanoparticles [163]. Another approach involves patterning the PEM using solvent-assisted capillary moulding to selectively deposit the M13 monolayer onto specific areas of the substrate [164]. Moreover, Devaraj et al. developed nanoporous biocomposite films with alternating layers of genetically engineered M13 phage and polydiallyldimethylammonium chloride (PDDA). The substrate was repeatedly submerged and removed from M13 and PDDA solutions, producing nanoporous biocomposite films with pore sizes ranging from 150-500 nm [165].

1.3.3.6 Hydrogels and Aerogels

1.3.3.6.1 Hydrogels

Hydrogels are three-dimensional (3D), cross-linked, porous structures comprised of hydrophilic polymers which are capable of absorbing at least 10% of their dry weight in water or biological fluids. However, modern hydrogels have demonstrated the remarkable ability to absorb water up to thousands of times their dry weight [166]. Hydrogels consisting of natural components like proteins and peptides offer distinct advantages, such as their ability to engage in varying chemical reactions. This allows for their cross-linking and functionalisation, creating a diverse range of hydrogels [167, 168]. Consequently, there has been great interest in developing hydrogels with M13 building blocks [169-171].

For instance, Peivandi et al. fabricated highly ordered hydrogels using M13 in the form of lyotropic liquid crystals and glutaraldehyde as a cross-linker. The resulting hydrogel exhibited bioactivity, self-healing properties and auto-fluorescence. However, these hydrogels require substantial concentrations of M13 to form the lyotropic liquid crystals [172]. This limitation was overcome by introducing low concentrations of bovine serum albumin (BSA), which initiated liquid crystal formation without disrupting the cross-linking between M13 and glutaraldehyde. The resulting M13-BSA hydrogels, while demonstrating a lower compression modulus, exhibited a greater flexibility than M13 hydrogels and a higher swelling ratio than BSA hydrogels. The M13-BSA hydrogels retained the same bioactive, self-healing and autofluorescence properties while requiring M13 concentrations up to 50,000 times lower than previously needed for lyotropic liquid crystal formation [173].

Sawada et al. developed regular, transparent hybrid hydrogels composed of M13 bacteriophage and antibody-immobilised AuNPs, which were modified to interact with each other. The phages assembled into lyotropic liquid crystals, while the AuNPs formed an ordered network. These two phases combined to create regular structures with sub-centimetre domains through time-dependent cross-linking. The mechanical strength of these hydrogels depended on the interactions between the antibodies on the AuNPs and the peptides at the phage termini [174].

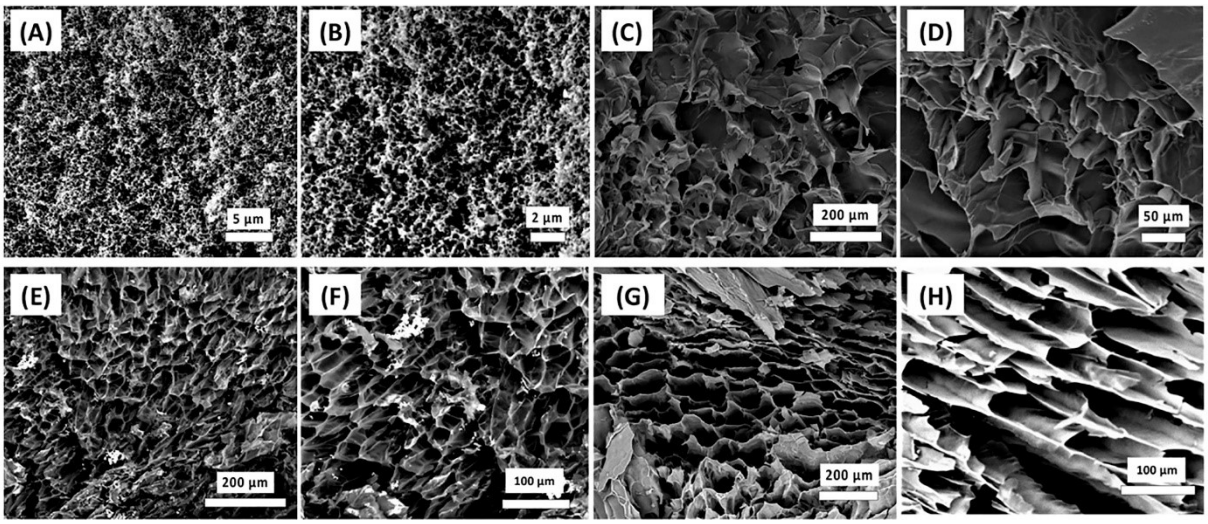

Figure 1.11: SEM images of M13-BSA hydrogels

SEM images of **(A, B)** the hybrid M13 + 1% BSA hydrogel, critical point dried; **(C, D)** the hybrid M13 + 1% BSA hydrogel, freeze-dried; **(E, F)** the hybrid M13 + 3% BSA hydrogel, critical point dried; **(G, H)** the 3% BSA hydrogel, critical point dried. Image from [173].

Further work by Sawada et al. explored hybrid hydrogels consisting of liquid crystalline M13 and gelatin. The cross-linking between gelatin and M13 resulted in decreased hydrogelation time, improved mechanical strength, and reduced susceptibility to degradation by collagenase compared to pure gelatin hydrogels [175]. This was further developed by incorporating both wild type M13, and M13 modified to display the hemagglutinin (HA) peptide (HA-phages), with gelatin containing the anti-HA peptide antibodies. The resulting hybrid hydrogel was utilised as a drug delivery system. The

interactions between the peptide and antibodies slowed the drug release, and the rate and amount of drug released was controlled with the concentration of HA-phages. Moreover, combining FLAG-phages, which are phages displaying the FLAG peptide sequence DYKDDDDK, with the HA-phages within the hydrogel, allowed for the controlled release of many antibodies from a single hydrogel, highlighting the potential of M13-based hydrogels in medical applications [176].

1.3.3.6.2 Aerogels

Drying hydrogels, replacing the liquid with air, can result in the formation of aerogels. Aerogels are characterised by their highly porous structure, low density, and high surface area, which offer numerous advantages across a range of industries [177]. Their extensive surface sites enable efficient functionalisation, prevent the aggregation of sensing materials, enhance electron transfer, and facilitate the adsorption and transport of target analytes. These properties contribute to high sensitivity, selectivity, and rapid response rates, making aerogels highly suitable for applications in biomedicine, energy storage, and sensing technologies [46, 178].

Jung et al. developed M13 aerogels by increasing the M13 concentration in solution through solvent evaporation, enabling the phages to interact via van der Waals interactions. These phages were subsequently subjected to lyophilisation, yielding M13 aerogels. The researchers also demonstrated the feasibility of integrating inorganic materials into the aerogel structure by genetically engineering M13 to bind with ruthenium and cobalt ferrite. This highlighted the potential to incorporate inorganic materials into aerogels to tailor their properties for specific applications [179]. Cha et al. further emphasised the tuneability of M13-based aerogels through phage display and the integration of inorganic materials. The electroless deposition of nickel (Ni) into

the M13 hydrogel, followed by freeze drying, generated M13-Ni aerogels. Subsequent electrodeposition of a manganese oxide (MnO_2) active material resulted in Ni–MnOx cathodes. Precision control over the length of the phages through genetic engineering enabled their porosity and mechanical strength to be altered [180]. Wang et al. also produced M13-based aerogels by freeze-drying a high concentration M13 suspension (Figure 1.12) and demonstrated that the addition of nickel, copper, and aluminium into M13-based aerogels improved their mechanical strength. Investigations into these aerogels demonstrated that their properties, such as their morphology and the local piezoelectric effect, give the aerogels sound absorption properties which can be adjusted by changing the aerogel thickness [181, 182].

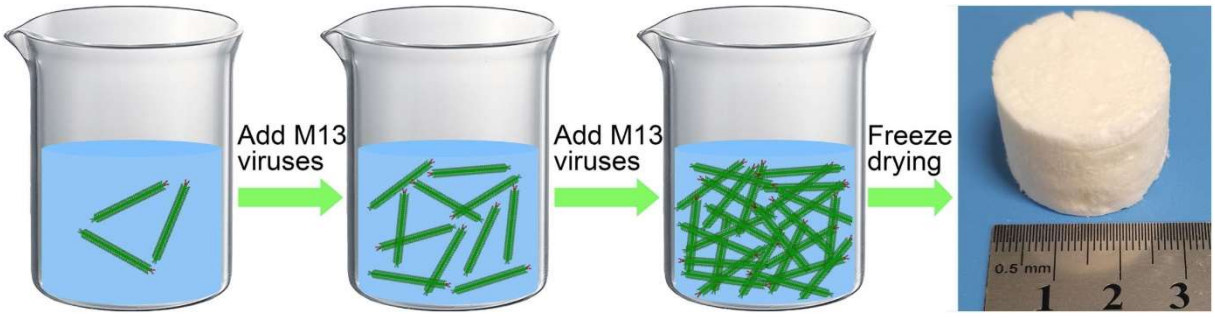

Figure 1.12: Fabrication of M13 aerogels

Fabrication of M13 bacteriophage aerogels by steadily increasing the concentration of M13 in solution and freeze-drying. Image from [182].

1.3.3.7 Energy Storage and Conversion

1.3.3.7.1 Piezoelectric Materials

Piezoelectric materials demonstrate the unique ability to convert energy between mechanical and electrical forms [183]. In 2012, Lee et al. demonstrated the piezoelectric properties of self-assembled M13 bacteriophage films, which arise from the absence of inversion symmetry in the structure of the major coat proteins, PVIII

[184]. To enhance these properties, researchers introduced additional negative charges at their N-termini through genetic modification, creating a stronger dipole moment between the negative N-terminus and the positive C-terminus of each major coat protein. The piezoelectric properties were tuned by controlling the film thickness [184, 185].

The inherent self-assembling nature of M13, which enables the creation of nanostructures such as vertically self-assembled M13 fibres, films, and hierarchical nanostructures, has proven advantageous in the development of tuneable biopiezoelectric materials. Shin et al extruded a suspension of M13 phages through a porous template, causing their spontaneous self-assembly into M13 nanopillars with tuneable piezoelectric properties [186] (Figure 1.13), and Yan et al. demonstrated that nematically aligned M13 films can serve as the piezoelectric component in quadrant-electroded nanogenerators [187].

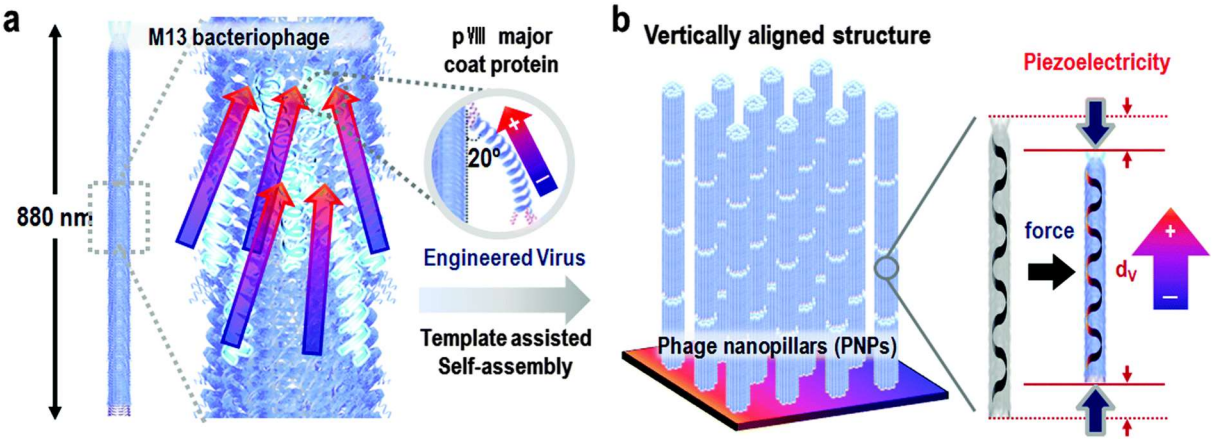

Figure 1.13: Schematic of vertically aligned M13 nanopillars

The dipole moment of each PVIII protein is directed from the tail (blue) to the anchoring domain (red), resulting in a net polarization from the PIX protein (grey) to the PIII protein (cyan), indicated by the rainbow arrow. Phage nanopillars, fabricated via templated-assisted self-assembly, demonstrated piezoelectric properties when deformed in the axial direction. Image from [186].

Alternatively, M13 can act as a biotemplate for the fabrication of piezoelectric nanowires. Cung et al. utilised an M13 phage template to produce lead zirconate titanate nanowires with controllable properties [188], while Kilper et al. leveraged M13 template to generate zinc oxide (ZnO)/M13 nanowires. Genetically modifying the PVIII protein to display an additional two aspartic acid residues at the N-terminus significantly increased its intrinsic dipole moment, resulting in enhanced piezoelectricity compared to ZnO nanowires templated with unmodified, wild-type M13 [189].

1.3.3.7.2 Nanocatalysts

M13 has proven valuable in the formation of nanocatalysts. Nanocatalysts composed of metal and metal oxide nanoparticles offer high reactivity, selectivity, and size-dependent catalytic activity, but are susceptible to aggregation, which diminishes their surface area and, subsequently, their catalytic activity. Genetic engineering of M13 via phage display has addressed this challenge by creating absorption sites on the surface of the phages to immobilise the nanoparticles [190]. For instance, Zhang et al. engineered M13 to enhance its surface charge density, thereby increasing its binding affinity for nickel (Ni) compared to wild-type M13. Immobilising bi-metal nanoparticles composed of Fe and Ni on the M13 surface significantly accelerated the reduction of p-chloronitrobenzene under mild conditions [191]. In a more recent development, Fang et al. utilised M13 phages to create nanocomposites with AuNPs and AgNPs, effectively enhancing the catalytic activity of immunosensors [192].

Several research papers have focused on using M13 to improve catalytic activity in the context of hydrogen evolution reactions. Jeon et al. pioneered the production of highly porous hydrogels through the cross-linking of M13 bacteriophages. These hydrogels

exhibited superaerophobic properties. Coating a platinum (Pt) electrode or catalyst with this hydrogel increased its specific catalytic activity, by preventing gas bubbles from adhering to the surface and obstructing active sites during the reactions [193].

The production of hydrogen gas via hydrogen evolution reactions was the central focus of a study by Records et al. in 2019. The research highlighted platinum nickel hydroxide (Pt-Ni(OH)$_2$) as a promising electrocatalyst for clean hydrogen fuel generation. Genetically engineering M13 to bond to metal cation nanoparticles and using it as a biotemplate offers a cost-effective and sustainable approach to produce Pt-Ni(OH)$_2$ catalysts under ambient conditions (Figure 1.14) [194].

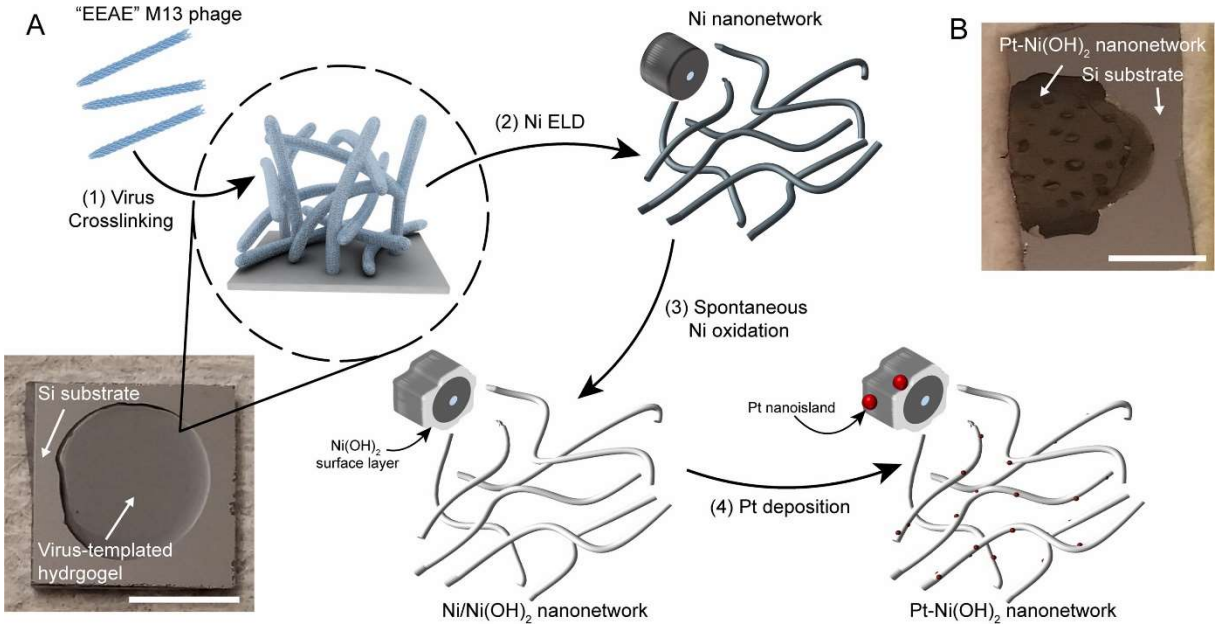

Figure 1.14: Phage-templated synthesis of Pt-Ni(OH)$_2$ nanonetworks

(a) Synthesis of Pt–Ni(OH)$_2$ nanonetworks. The phages are (1) crosslinked and (2) metallised with nickel, which then (3) undergoes spontaneous oxidation to form Ni(OH)$_2$ under aerobic conditions. Finally, (4) platinum is deposited onto the phage-templated scaffold. **(b)** Macroscopic image of the Pt–Ni(OH)$_2$ nanonetwork. Image from [194].

1.3.3.7.3 Photoconversion

As environmental consciousness rises, there is a growing focus on enhancing the production and performance of solar cells. Bio-templated nanoplatforms with viruses like the M13 bacteriophage offer advantages such as ease of mass production, renewability, and the ability to be genetically engineered to bind with specific atoms [195].

Dye-sensitised solar cells are low-cost photovoltaic devices that use light to excite dye molecules, and the excited electrons are channelled into the conduction band of wide band-gap semiconductors. Their photoanodes typically contain nanoparticles like titanium oxide (TiO_2) and controlling the structure of these nanoparticle layers proves vital in enhancing the solar cell efficiency. The substitution of a planar 2D nanoparticle surface with a 3D M13 phage-templated nanostructure optimises surface area, thereby increasing the number of reactive sites and extending the optical path to improve the probability of light absorption [196]. Chen et al. and Dang et al. demonstrated that incorporating compounds such as AuNPs and single-walled CNTs with TiO_2 on an M13 phage template can enhance electron accumulation and consequently improve the power conversion efficiency of the solar cells [197, 198].

Light harvesting antennas have also been produced with M13, by replicating the energy transfer mechanism found in natural light-harvesting materials during photosynthesis. Nam et al. genetically engineered M13 to enable the N-terminus of the major coat protein PVIII to bind to pigments. The sub-nanoscale distance between the pigments and the flexible nature of the N-terminus allowed pigments to interact and transfer energy, enhancing exciton transport and subsequently photosynthesis [199].

Park et al. further developed this by using an M13 template to create a chromophore nanonetwork to improve exciton transfer and the exciton diffusion length [200].

Moreover, there has been research into enhancing perovskite solar cells with M13 bacteriophage, with nanoscale perovskites exhibiting advanced properties compared to their bulk material counterparts. Perovskite crystals grown on an M13 bacteriophage template demonstrate a high-power conversion efficiency without the need for toxic solvents typically required for conventional, non-biodegradable additives to enhance performance [201]. Lin et al. used wild type M13 to bind to perovskites, intensifying long-wavelength light absorption through scattering effects. Denaturing the M13 prior to combining it with the perovskites enhanced both its binding and absorption, resulting in improved photovoltaic properties [202]. More recently, Kumar et al. incorporated genetically engineered M13 into a tin oxide (SnO_2) colloidal spray solution to create an electron transport layer for perovskite solar cells. The generated M13-SnO_2 biohybrid film exhibited enhanced optoelectronic properties, stability, and scalability in comparison to pure SnO_2 films, providing a method to fabricate low-cost, high surface area perovskite solar cells [203].

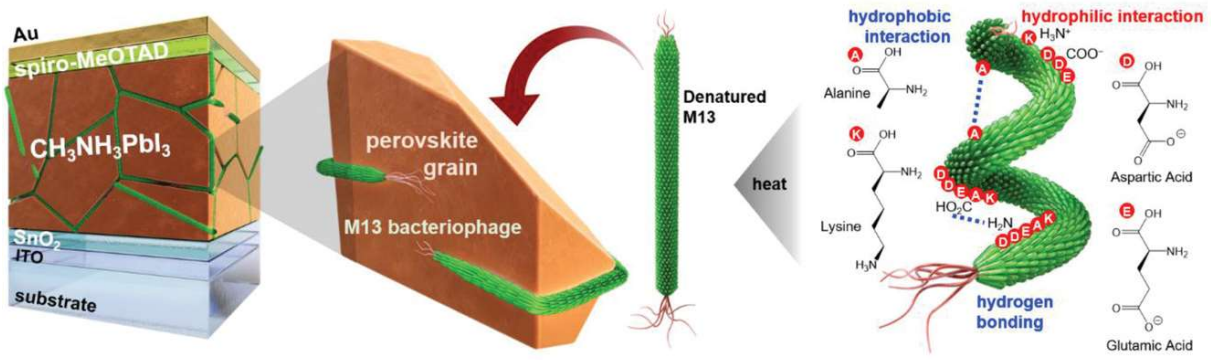

Figure 1.15: Perovskite solar cells based on denatured M13 phages

Schematic of M13 bacteriophage denaturation via heat exposure, serving as a template for perovskite crystal growth in perovskite solar cell fabrication. Image from [202].

1.3.3.7.4 Batteries

The size of batteries must decrease to allow for the continued advancement of portable devices. However, the challenge is producing these batteries while maintaining high performance. One approach to improving lithium-ion batteries is to manufacture them using nanostructures such as M13 bacteriophage [196]. For instance, M13 bio-templated cobalt oxide (Co_3O_4) electrodes, combined with AuNPs, single-walled CNTs, or integrated onto polyelectrolyte micro-islands, have shown improved lithium storage capacity [126, 204, 205]. Alternatively, Lee et al. genetically engineered M13 to bind to single-walled CNTs and display peptides able to nucleate amorphous iron phosphate (a-$FePO_4$) on its major coat proteins, resulting in improved a-FePO4 electrode power [206]. Further research by Lee et al. explored M13 phage-templated AuNWs and AgNWs to amplify the capabilities of lithium-ion battery electrodes [207].

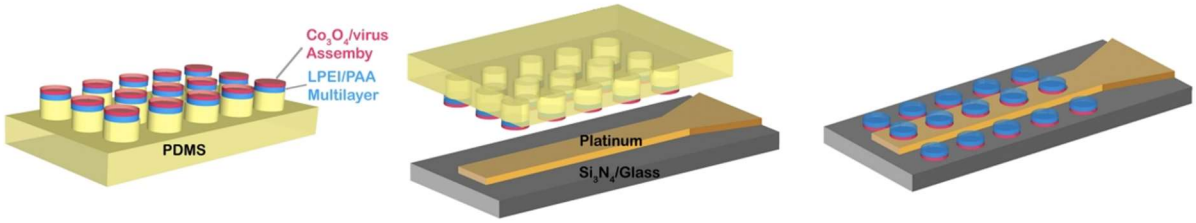

Figure 1.16: M13-based microbattery electrodes

Illustration of the process for creating virus-based microbattery electrodes, where cobalt oxide nanowires templated by viruses are assembled on a polyelectrolyte multilayer and subsequently transferred onto Pt microband current collectors. Image adapted from [126].

Additionally, research has been conducted into the production of non-lithium-ion high power batteries with M13. Both Dong et al. and Zhang et al. genetically modified M13 to bind to sulphur, facilitating the development of lithium-sulphur batteries and zinc sulphide nanofiber anodes for sodium-ion batteries, respectively [208, 209].

Another innovative battery type under investigation is the lithium-oxygen (Li-O_2) battery, featuring manganese oxide (MnO_2) nanowires templated by M13 phage as nano-catalysts. While taking slightly different approaches, with Oh et al. incorporating a small amount of palladium into their nanowires and Pakseresht et al. introducing ruthenium into α-MnO_2 structured nanowires, the absence of carbon in these electrodes reduced the number of side reactions, improving the stability and specific capacity of the electrocatalysts, which is especially valuable in the context of portable batteries [210, 211].

1.3.3.8 Biosensors

Biosensors have emerged as a valuable platform for point-of-care biomarker detection. Biosensors incorporate a biorecognition element, such as aptamers, proteins, or antibodies, that interact with the target analyte, enabling its identification [102, 212].

Bacteriophages offer numerous advantages over traditional biorecognition elements. They are cost-effective, possess an extended shelf life, and exhibit robust stability across various environmental conditions, including temperature, pH, and exposure to solvents [213-215].

Non-lytic phages like M13 can serve as scaffolds to immobilise target molecules through physical and chemical functionalisation. Alternatively, they can be genetically engineered to selectively detect specific analytes, enhancing the capabilities of biosensor technology [216].

1.3.3.8.1 Colorimetric Sensors

Colorimetric sensors offer a straightforward, cost-effective, and rapid means for detecting specific analytes [217]. The ability to genetically engineer M13 to present

peptides with varying binding affinities, alongside the sensitivity and selectivity of these peptides, enables the creation of highly efficient colorimetric sensors capable of detecting a wide array of chemicals [102, 218].

The inspiration for such colorimetric sensors often derives from nature. For instance, M13-based biosensors have been developed by drawing inspiration from collagen bundles found in turkey skin [219]. Thin films of M13 bacteriophage can be produced by submerging a substrate in an aqueous M13 bacteriophage solution and gradually withdrawing it. By manipulating factors like pulling speed, M13 concentration, and surface properties of M13 or the substrate, control over the liquid crystal phase of the M13 film can be achieved [220]. Adjusting the pulling speed results in varying distances between the phage-bundle nanostructures, affecting coherent light scattering and, consequently, the colour appearance of the film [221]. The interaction between M13 and the target analyte causes the bundles to swell or contract, altering the spacing between the nanostructures and leading to a colour change (Figure 1.17) [219]. By engineering M13 films to detect specific target analytes, colorimetric sensors have been developed for applications such as differential cell recognition [222], antibiotic detection [222, 223], origin tracing of agricultural products [224], and the detection of volatile organic compounds (VOCs) [225, 226] including trinitrotoluene (TNT) [225], endocrine disrupting chemicals (EDCs) [224], and polycyclic aromatic hydrocarbons (PAHs) [227].

Furthermore, colorimetric sensors have been developed by using M13 as a biotemplate for nanoparticles and nanowires, with the aim of monitoring contaminant levels that could have adverse effects on human health. For instance, the presence of mercury (Hg) ions in the body, potentially introduced through food and drinking water,

can lead to bodily harm and chronic diseases. Manivannan et al. devised a nanomaterial consisting of silicate sol–gel matrix-stabilised AgNPs and 4E-peptide-engineered M13 bacteriophage. These phages could effectively pre-concentrate Hg(II) ions, facilitating their interaction with AgNPs. This interaction was characterised by quenching associated with a blue shift in the surface plasmon resonance (SPR) absorption band and a resultant colour change due to Ag and Hg amalgamation [228]. Subsequent research expanded on this by genetically engineering M13 to act as a template for binding to AuNPs, thereby producing AuNWs. Partially deposited AgNPs over the AuNWs effectively pre-concentrated the Hg(II) ions, enabling their interactions with the AuNW and permitting the detection of lower concentrations of Hg(II) [229].

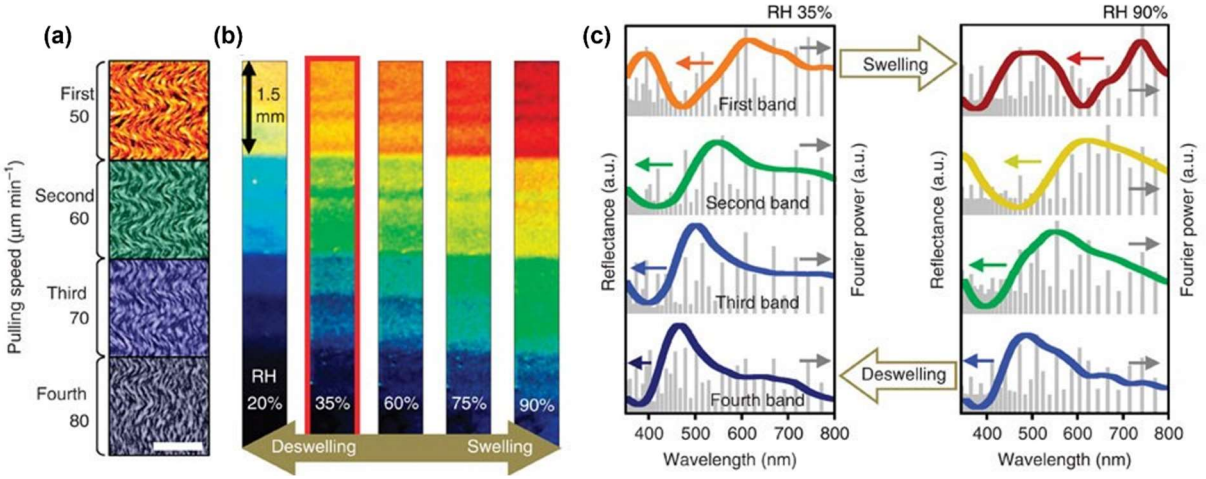

Figure 1.17: M13-based colorimetric sensors

(a) Composite AFM images of different phage matrices (bands) from a phage-based litmus sensor, each consisting of quasi-ordered fibre bundles with varying diameters and spacing. These structural variations give rise to distinct colours. **(b)** Photograph of the fabricated phage litmus showing four colour bands – orange, green, blue, and deep blue (highlighted in red). Variations in relative humidity (RH) induce colour changes due to differential swelling of the phage bundles, which is dependent on the initial bundle architecture. **(c)** Reflectance spectra (coloured lines) and corresponding Fourier power spectra (grey bars) for each matrix at 35% and 90% RH. Peak position and shape correlate with observed hue and chroma, respectively (a.u. = arbitrary units). Adapted from [226].

1.3.3.8.2 Surface Plasmon Resonance (SPR) Sensors

Surface plasmon resonance (SPR) is a phenomenon that occurs when light is incident on a metal surface at the resonance angle, exciting the electrons in the surface layer and causing them to propagate parallel to the surface. This results in the minimum intensity of light being reflected. When an analyte is deposited onto the metal surface, it changes the refractive index, altering the resonance angle and the intensity of the reflected light. Monitoring these changes in reflected light intensity allows for the detection and quantification of analytes. SPR sensors are highly sensitive, enabling real-time measurements including kinetics involving ligands and receptors, DNA hybridisation, and characterisation of polyclonal antibodies [230, 231].

M13-based SPR biosensors have been used to monitor levels of contaminants that can have adverse effects on human health. For example, Wang et al. demonstrated one-step, in situ detection of lead ions (Pb^{2+}) using M13 and SPR. The AuNPs were directly synthesised on the surface of M13. The presence of Pb^{2+} changed the redox environment of the AuNPs, altering their shape and causing a blue shift in the SPR spectrum. With a limit of detection of 45 nmol/L, this technique offers a simple and cost-efficient method for the detection of lead [232]. Another approach taken by Peng et al. involved the development of genetically engineered phages displaying binding proteins to various bacterial species and AuNPs. The combination of these elements led to a visible shift in the SPR spectrum, thereby creating a sensor for gram negative bacterial species with a limit of detection of approximately 100 cells [233].

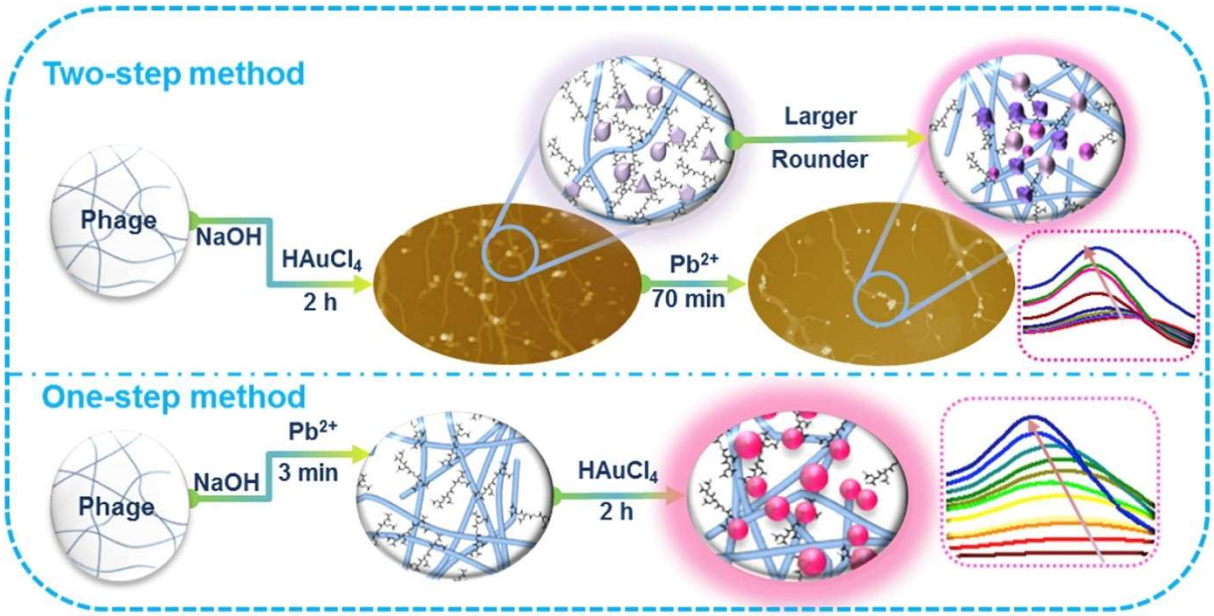

Figure 1.18: M13-based SPR sensor

Schematic for generating phage-AuNP network for the two-step and one-step detection of lead. Image from [232].

In recent research, Hou et al. produced a biosensor to detect the avian influenza virus H9N2, which can negatively impact human health and the food industry. M13 was genetically engineered to display the gold-binding peptide on the PVIII major coat protein, and the H9N2-binding peptide was displayed on the PIII minor coat protein. This enabled the development of a simple and robust biosensor capable of detecting H9N2, and adaptable for the detection of other viruses [234]. Hou et al. also applied M13-based SPR biosensors to the early detection of tumours. The PVIII major coat protein was again modified to bind to AuNPs, while the PIII minor coat protein displayed an anti-CEA single-chain variable region fragment (scFv). The biosensor could detect tumour biomarkers in liquid biopsies, achieving a limit of detection of 0.83 fM, which is 2000 times greater than a conventional SPR sensor and four orders of magnitude more sensitive than enzyme-linked immunosorbent assay (ELISA). This provides a non-

invasive technique for early tumour detection and monitoring, essential for determining the prognosis and selecting the most effective treatment method [235].

1.3.3.8.3 Surface-Enhanced Raman Spectroscopy (SERS) Sensors

Surface-enhanced Raman spectroscopy (SERS) is a technique that can enhance a Raman signal as much as 10^{11} through the adsorption of molecules on rough metal surfaces [236]. One of the primary applications of SERS is the detection of low-abundance biomolecules. Nguyen et al. developed an M13-based SERS sensor for sepsis diagnostics, using AuNPs and Raman dyes incorporated into a mesoporous M13-based biotemplate. This enabled the observation of three distinct peaks corresponding to sepsis-specific biomarkers due to the high capture rate of the substrate [237]. In recent research, M13-based SERS platforms have been employed for the detection and inactivation of bacteria. Wang et al. developed a biosensor to detect *Staphylococcus aureus* (*S. aureus*), a gram-positive bacterium which can cause food poisoning, toxic shock syndrome and septic shock. The biosensor was generated with AuNP-decorated phages. The AuNPs were labelled with the SERS active molecule 5, 5-dithiobis-(2-nitrobenzoic acid) (DTNB), and the M13 phages were modified to display a heptapeptide on the PIII protein, allowing them to bind to *S.aureus* (Figure 1.19). This platform also exhibited antibacterial capabilities, enabling it to be a multifunctional platform for both the detection and inactivation of bacteria [238]. Similarly, Bi et al. developed a M13-based SERS platform for the detection and inactivation of *Escherichia coli* (*E.coli*). The phages were modified by attaching gold-coated silver nanorods (Au@AgNRs) to the PVIII protein with a carboxy-PEG-thiol (CTPEG) linker, and the PIII minor coat protein was modified to detect *E.coli.* The

Au@AgNRs were also able to disrupt the bacterial membrane, giving the platform bactericidal properties [239].

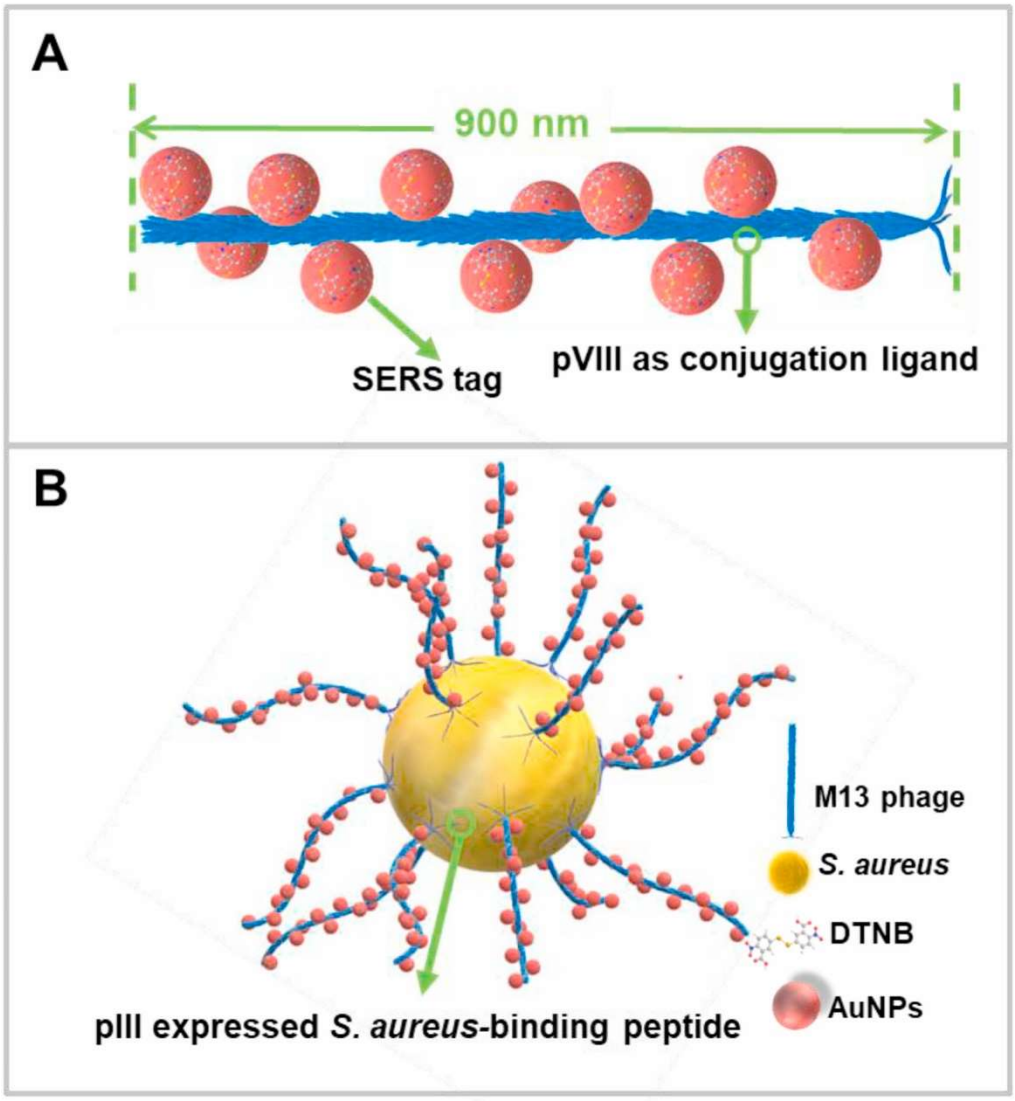

Figure 1.19: M13-SERS probe

(a) Schematic illustration of the M13-based SERS probe. The major coat protein (PVIII) facilitates in situ growth of gold nanoparticles (AuNPs) through surface conjugation.**(b)** The M13-SERS probe capturing *Staphylococcus aureus*, enabled by the genetically modified PIII protein displaying a target-specific peptide sequence. Image from [238].

1.3.3.9 Therapeutic Applications

1.3.3.9.1 Drug Delivery

M13 emerges as a promising drug delivery platform due to its lack of intrinsic tropism for mammalian cells, non-toxicity, biocompatibility, biodegradability, high number of binding sites, morphological uniformity and ease of functionalisation [240-242]. Genetically engineering M13 to target specific tissues allows for precise drug delivery with minimal damage to surrounding healthy tissues, which is particular advantageous in cancer treatment, where the nonspecific cytotoxicity of chemotherapy often causes adverse side effects [243, 244]. In a proof-of-concept study, Bar et al. both chemically and genetically engineered M13 for its use as a drug delivery platform, with chemical modifications enabling the conjugation of cytotoxic drugs to the phage, and genetic modifications allowing the M13 to bind to the targeted cells [245]. Building on this work, Suthiwangcharoen et al. developed a targeted antitumour drug delivery system with folate-conjugated M13 (FA-M13) and assembled core-shell nanoassemblies with the biodegradable copolymer poly(caprolactone-b-2-vinylpyridine) (PCL–P2VP). The FA-M13 interacted with folate receptors on malignant tissues and the PCL–P2VP encapsulated the hydrophobic antitumour drug doxorubicin, which enabled its targeted delivery to tumour cells (Figure 1.20) [246].

Mozar et al. also investigated M13-based doxorubicin delivery platforms. The authors first coated tungsten disulfide (WS2) nanosheets, a promising thermal agent, in polyethylene glycol (PEG) to improve its thermal stability and biocompatibility. Subsequently, M13 with a high affinity for HER2, a protein often overexpressed in breast cancer cells, and doxorubicin, were attached to the PEG surface. The resulting

nanostructures show potential for combined chemotherapy and thermal therapy in treating breast cancer [247].

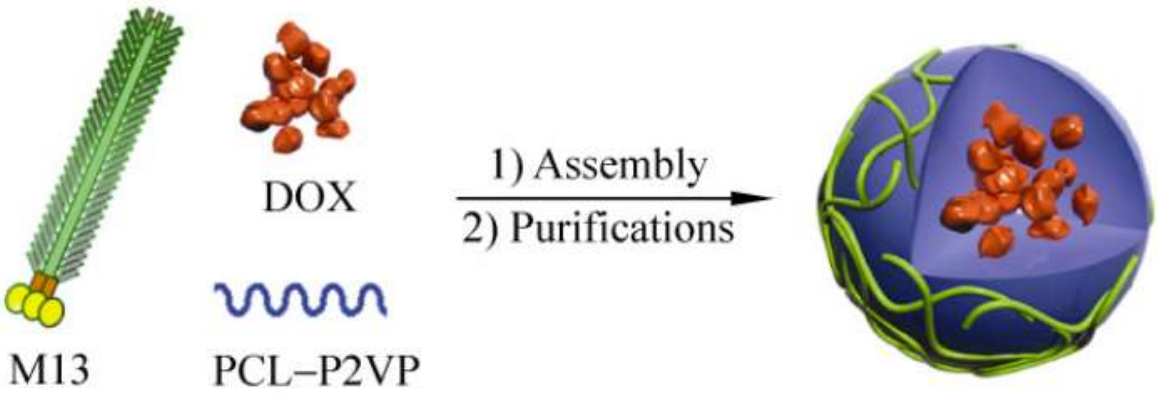

Figure 1.20: M13-based Drug Delivery Platform

Schematic of DOX-loaded M13–PCL–P2VP nanoassembly fabrication for antitumour drug delivery. Image from [246].

Furthermore, M13 can be used to improve current drug delivery vehicles. Liposomes, while effective in targeted drug delivery, face challenges such as instability in biological media and susceptibility to external influences. Ngweniform et al. improved liposome stability by genetically engineering M13 to promote strong electrostatic interactions with cationic liposomes, initiating the self-assembly of phage–liposome complexes and improving liposome stability. This modification enabled targeted drug delivery for breast cancer treatment using photodynamic therapy [248].

1.3.3.9.2 Gene Therapy

M13 can act as a stable carrier to protect DNA and RNA from degradation in bodily fluids, enabling the delivery of nucleic acids to specific locations [244, 249]. Notably, M13 has been utilised for glioblastoma treatment, overcoming the size-exclusionary properties of the blood-brain barrier. Tsedev et al. engineered ultrashort M13 phage particles to display the CTX peptide, enabling the delivery of therapeutic gene

cassettes for glioma treatment and other central nervous system diseases [250]. Chongchai et al. explored the potential to treat chondrosarcoma with M13, by inserting the human tumour necrosis factor alpha (TNFα) therapeutic transgene expression cassette into the phage genome and modifying the phage to bind αvβ3 or αvβ5 integrin receptors, which are overexpressed on tumour cells [251]. Further work by the authors demonstrated that M13 displaying the chondrocyte-affinity peptide on the PIII protein enabled the delivery of transgenes to human articular chondrocytes for the potential treatment of cartilage-related diseases such as osteoarthritis [252].

Although M13 has great potential as a gene delivery vehicle, its applications have been limited by its low transduction efficiency. Research by both Suwan et al. and Staquicini et al. improved the transduction efficiency by combining M13 bacteriophage and the adeno-associated virus (AAV). The AAV component improved the transduction efficiency, while M13 was modified to display target ligands and improve its degradation-resistance. The resulting hybrid AAVP particle has shown potential for gene therapy targeting cancer cells such as glioblastomas (Figure 1.21) [253, 254]. Recent work by Kao et al. found that the up-regulation of PrimPol, down-regulation of DMBT1, and reducing the size of the phage significantly improved the transduction efficiency. Modifying M13 accordingly generated the TransPhage, which showed an efficiency of up to 95% and an enhanced specificity towards selected tropisms, enabling its application in suppressing cancer cells [255].

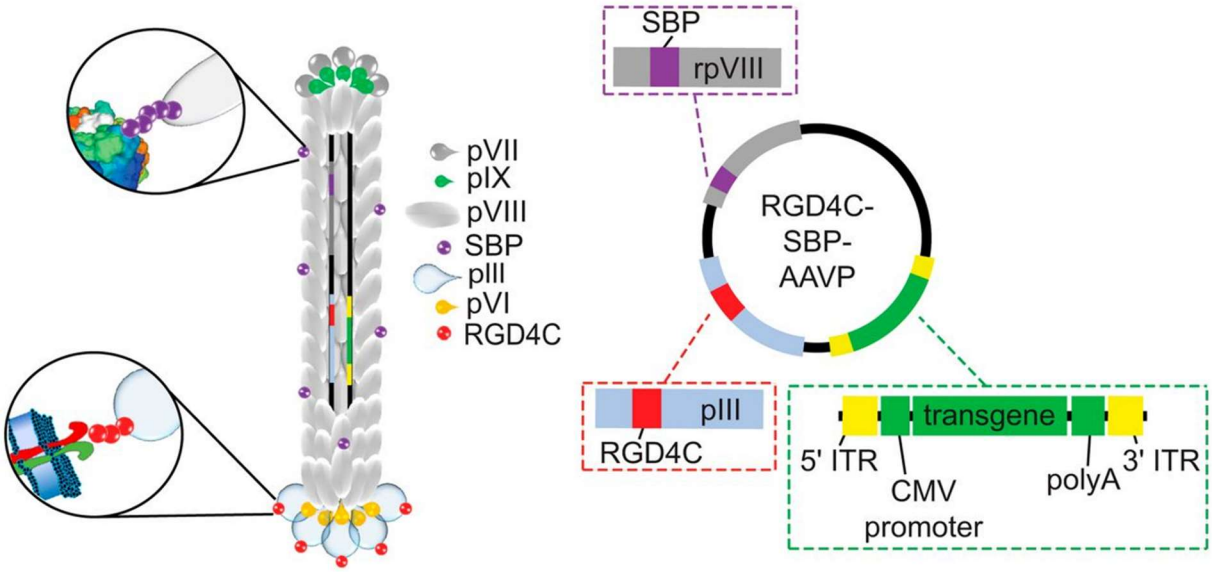

Figure 1.21: M13-AAVP hybrid particles for gene delivery

Schematic of the multifunctional AAVP vector, which displays RGD4C peptide ligands on the PIII minor coat protein at one end of the phage and multiple streptavidin-binding peptide (SBP) motifs on the rPVIII major coat protein along the phage body. A mammalian transgene cassette, driven by a CMV promoter and flanked by AAV inverted terminal repeats (ITRs), is incorporated into the internal single-stranded genome for transgene expression. Image from [254].

1.3.3.9.3 Immunotherapy

M13 has been used for the delivery of exogenous therapeutic proteins and antigens for cancer immunotherapies. Proteins, though effective in identifying and controlling diseased cells, often struggle to penetrate mammalian cell membranes. Genetically modifying M13 to display specific proteins facilitates their intracellular delivery. DePorter et al. successfully demonstrated this by engineering M13 to display a prostate cancer cell-penetrating peptide, allowing the uptake of therapeutic proteins into prostate cancer cells [256]. For the treatment of colorectal cancer, Murgas et al. genetically engineered M13 to target the carcinoembryonic antigen, which is overexpressed on colorectal cancer cells, to reduce tumour growth [257]. Dong et al. instead targeted *Fusobacterium nucleatum* (*Fn*), a bacterium present in the gut

microbiome which increases the level of immunosuppressive cells and therefore lowers the immune response to colorectal cancer. The authors genetically engineered M13 to bind to *Fn* and electrostatically bound AgNPs to its coat proteins. The interaction between AgNPs and *Fn*, mediated by M13, killed the *Fn* cells and reduced the number of immunosuppressive cells, improving the body's immune response to colorectal cancer cells [258].

Moreover, M13 can be employed for stem cell-based therapies. Jang et al. modified M13 to display the RGD peptide on the PIII protein to bind to human cardiac progenitor cells (hCPCs), and the SDKP peptide on the PVIII protein gave the phage angiogenic and fibrotic properties. This enhanced the engraftment of the hCPCs in the ischemic heart region, showing its potential as a stem cell-based therapy for ischemic cardiovascular disease [259].

1.3.3.9.4 Vaccines

Bacteriophages emerge as promising candidates for the development of vaccines owing to their stability, biodegradability, biocompatibility, immunogenicity, non-infectious nature, and ease of functionalisation. There are three main categories of phage-based vaccine: phage display vaccines, phage DNA vaccines, and a hybrid phage vaccines, a combination of phage display and phage DNA vaccines () [260].

In phage display vaccines, the foreign antigens are presented on the phage surface either through direct phage display or indirect phage display methods [241, 261]. Phage display vaccines have been developed with M13 against various diseases such as hepatitis B [262], HIV [263] and porcine diseases [264]. González-Mora et al. devised a low-cost M13-based vaccine against cattle ticks by displaying the Bm86-

derived Sbm7462 antigen on the PIII protein [265]. Wang et al. explored using M13 as a vaccine for breast cancer by displaying the extracellular and transmembrane domains of human HER2 or its Δ16HER2 splice variant on the PIII protein, which induced a significant anti-HER2 antibody response [266]. Similarly, Martínez-Cortés et al. engineered M13 to display G3d mimitopes on the PVIII protein to stimulate T cell proliferation and antitumor immune responses [267], and Salehi et al. demonstrated the promise of phage display vaccines for COVID-19 by displaying a truncated RBD-derived spike protein (P1) on the PVIII coat protein, resulting in the immunisation of mice against COVID-19 [268].

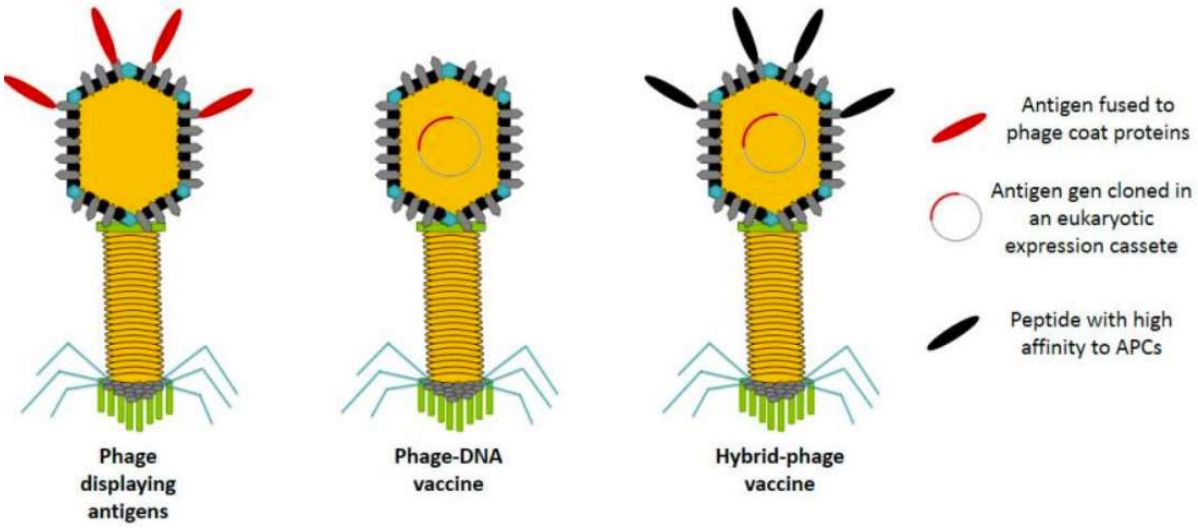

Figure 1.22: Phage-based vaccines

A schematic demonstrating the three categories of phage-based antigen delivery systems – phage display vaccines, phage DNA vaccines, and a hybrid-phage vaccines. Image from [260].

Phage DNA vaccine utilise phages to deliver DNA. M13-based DNA vaccines have been developed for viruses including HSV-1 [269], vaccinia [270], and duck hepatitis B [271]. Furthermore, phage display and phage DNA vaccines can be combined to produce hybrid bacteriophage vaccines, which employ bacteriophages displaying proteins or peptides with a strong affinity for either an antigen or antigen-presenting

cells. Simultaneously, these phages contain in their genome a eukaryotic expression cassette that encodes a specific antigen [260]. Khalili et al. developed a hybrid M13 phage by inserting the AAV expression cassette and displaying the TAT peptide on the PVIII protein to target the Dickkopf-1 (DKK1) glycoprotein, demonstrating the potential of this approach for cancer detection and prevention [272].

Moreover, phage display serves as a valuable technique for identifying immunogenic proteins and peptides, allowing for the rapid and cost-effective development of vaccines [260]. Recent research includes finding antigens for potential vaccines for blood diseases and infections [273], intestinal infections [274], parasitic infections [275], and viruses [276].

1.4 GraPhage13 Aerogels (GPA)

1.4.1 Fabrication

Harnessing the properties of both GAs and M13 presents a promising approach for fabricating BGAs with exceptional properties and tuneable characteristics. In 2019, Passaretti et al. combined GO (Figure 1.23a) and M13 (Figure 1.23b) in a pH 4.9 citrate buffer, leading to their immediate self-assembly into an aggregate. This aggregate was then isolated via centrifugation. By removing 90% of the supernatant and resuspending the aggregate in the remaining solution, the researchers obtained a hydrogel, which they termed GraPhage13 hydrogel (GPH). Further drying of GPH under vacuum conditions yielded GraPhage13 aerogel (GPA) (Figure 1.23c) [20]. Unlike traditional GA fabrication methods, GPA synthesis does not require extreme temperatures, pressures, or pH conditions, nor does it rely on toxic reducing agents, making it a more environmentally friendly approach to GA production [42].

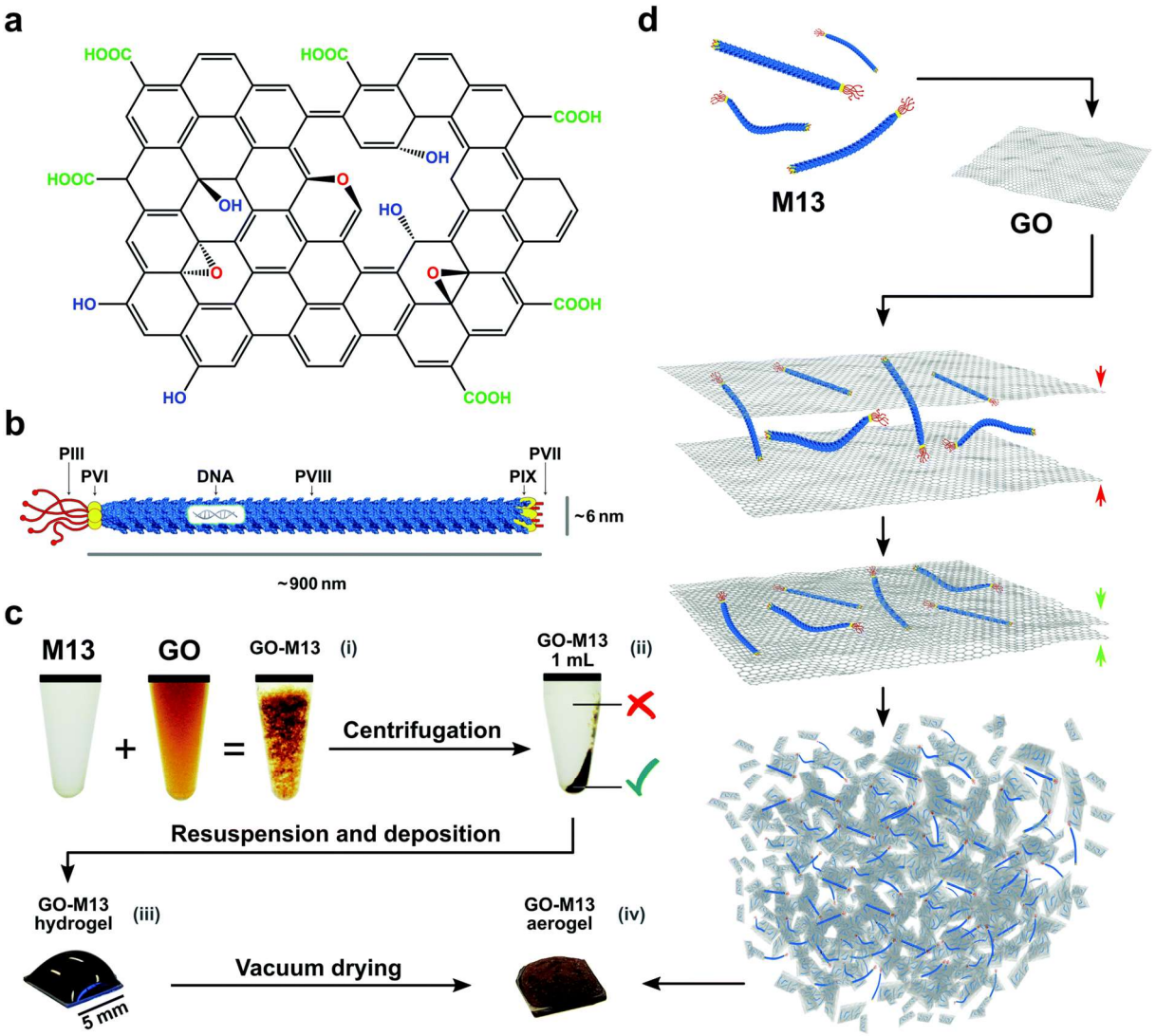

Figure 1.23: Fabrication of GPA

A schematic depicting the process of fabricating GPAs through the self-assembly of **(a)** GO and **(b)** M13 bacteriophage. The fabrication process is shown in **(c)** and involves **(i)** combining GO and M13, which self-assemble to form an aggregate; **(ii)** centrifuging precipitates the GO-M13 from solution; **(iii)** resuspending the GO-M13 in 10% of the supernatant and depositing the resulting hydrogel on the substrate; **(iv)** drying the substrate in a vacuum to form GPA. **(d)** The hypothesised self-assembly mechanism, with the M13 acting as a cross-linker between the GO sheets. Image from [20].

Passaretti et al. hypothesised that M13 functions as a cross-linker between GO sheets (Figure 1.23d). GO is negatively charged, while M13 contains amino acids with varying surface charges. The surface charge of M13 depends on the protonation and

deprotonation of these amino acids, which, in turn, is influenced by the pH of the suspension solution. If M13 carries a negative charge, it repels the negatively charged GO sheets. Therefore, for M13 to effectively act as a cross-linker, it must possess a positive surface charge [20].

The authors thoroughly investigated three specific pH values (3.5, 4.9, and 6.9), identifying pH 4.9 as optimal, as this was where aggregation was observed and the maximum amount of GO and M13 precipitated upon centrifugation. They also explored varying the pH to determine the range at which GO-M13 aggregation occurred, finding aggregation between pH 4.8 and 5.4. However, a systematic analytical investigation to detect interactions between GO and M13 in conditions where aggregation still occurs but is more challenging to observe, as well as an analysis of the resulting aerogels, was not conducted. Future investigations should focus on employing advanced analytical techniques to further characterise these interactions and assess the structural properties of aerogels formed under varying pH conditions [20, 98].

1.4.2 Characterisation and Modifications

The resulting GPAs exhibited a 3D porous structure, with both nano- and microscale pores observed (Figure 1.24), although no quantification of the pore size distribution was conducted [20]. The density and surface area of GPA were measured as 8.82 ± 0.03 mg/cm^3 and 330 ± 30 m^2/g respectively. These values place GPA toward the lower end of the density and surface area ranges observed for other types of aerogels (Table 1.1). Specifically compared to others GAs in the literature (Table 1.2), GPAs falls within in the median range for both density and surface area.

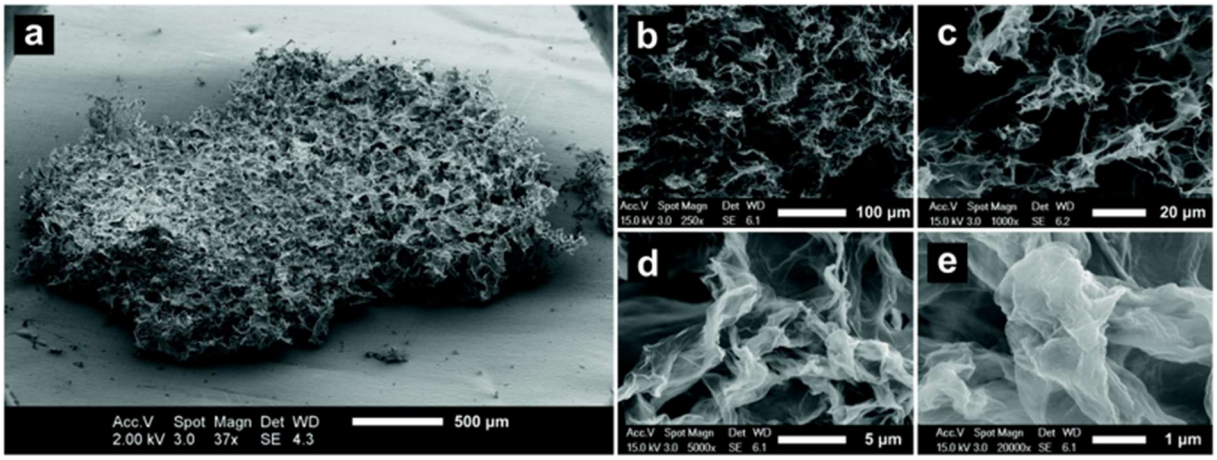

Figure 1.24: SEM images of GPA

Scanning electron microscopy (SEM) images of GraPhage13 aerogels (GPA). Image adapted from [20].

Table 1.2: Comparison of graphene-based aerogels

Comparing the density, surface area and target applications of graphene-based aerogels (GAs) generated with varying precursors

Name	Precursors	Density (mg/cm^3)	Surface Area (m^2/g)	Target Application	Refs.
GPA	GO, M13 bacteriophage	8.8	330		[20]
GA	GO with L-ascorbic acid reduction media	12-96	512	Electrodes	[277]
	Graphene hydrogel, ammonia	16-23	81-350	Lead absorption	[278]
	GO with L-ascorbic acid and/or sodium bisulfite reduction media	8.8	75	Electrochemical applications	[279]
N-doped GA	GO, ammonia	80	830	Supercapacitors and gas adsorbents	[280]
Resorcional-GA	GO, resorcinol	110-190	361-763	Catalysts	[281]
Resol-GA	GO, resol	3.2-8.4	325-1019	Electrodes	[282]
EA-GA	GO, Enteromorpha	5.2-9.8	148-428	Oil-water separation	[283]
MBCNF/GOPA	GO, bacterial cellulose nanofibers, Fe_3O_4 nanoparticles, polyvinyl alcohol	6.8	215	Malachite green removal	[284]
MXene-GA	GO, Mxene	3.9	259	Anodes	[285]
MOF-GA	GO, ammonia, cobalt oxide nanoparticles	12	1359	Energy storage and conversion	[286]
MWCNT-GA	GO, multi-walled carbon nanotubes	41-54	435	Water purification	[287]
Cellulose-GA	GO, cellulose	5.9	47.3	Oil absorption	[288]
PPys-GA	GO, polypyrrole nanospheres	7.8	686	,	[289]
MGGNA	GO, GO nanoribbons, APTES	2.32-4.11	45.1	Organic pollutant absorption	[290]

Sun et al further explored the microstructure of GPA with Raman spectroscopy (for further details on Raman spectroscopy please see Section 2.2.8) [291]. Four peaks were observed. The disorder-induced D-peak was observed at 1390 cm^{-1}, with its profile over the D-mode range influenced by sp^2 and sp^3 peaks. In graphene-based materials, the D-band is often associated with the presence of defects, edges, or other structural disorders, therefore sp^2 hybridised carbon atoms in the graphene lattice can contribute to the D-band, especially if there are defects or irregularities in the hexagonal structure. Additionally, the sp^3 hybridised carbon atoms, which are characteristic of amorphous carbon or carbon with a more disordered structure, can also contribute to the D-band [20, 291, 292]. However, the main component of this peak was not identified.

The G-mode (~1570 cm^{-1}) arises from the stretching of the sp^2 bonds between pairs of carbon atoms, while the D'-mode (~1610 cm^{-1}) was linked to defects introduced by the functionalisation of sp^2 bonds in GO, resulting in a disorder-induced phonon mode. The G^- mode (~1530 cm^{-1}) was associated with the presence of defects from amorphous sp^2 bonded structures, resulting from the softening of carbon-carbon bonds due to the functionalisation of GO (Figure 1.25). This was attributed to the presence of M13 disrupting the graphene plane, or charge transfer between M13 and GO [291].

Sun et al. also examined the conductivity of GPA, revealing its insulating nature with a conductance of 0.2 nS. However, they demonstrated that integrating carbon nanotubes into the GPA structure significantly enhanced its conductance to 6 nS. This ability to modify GPA's properties through nanomaterial incorporation broadens its potential applications [291].

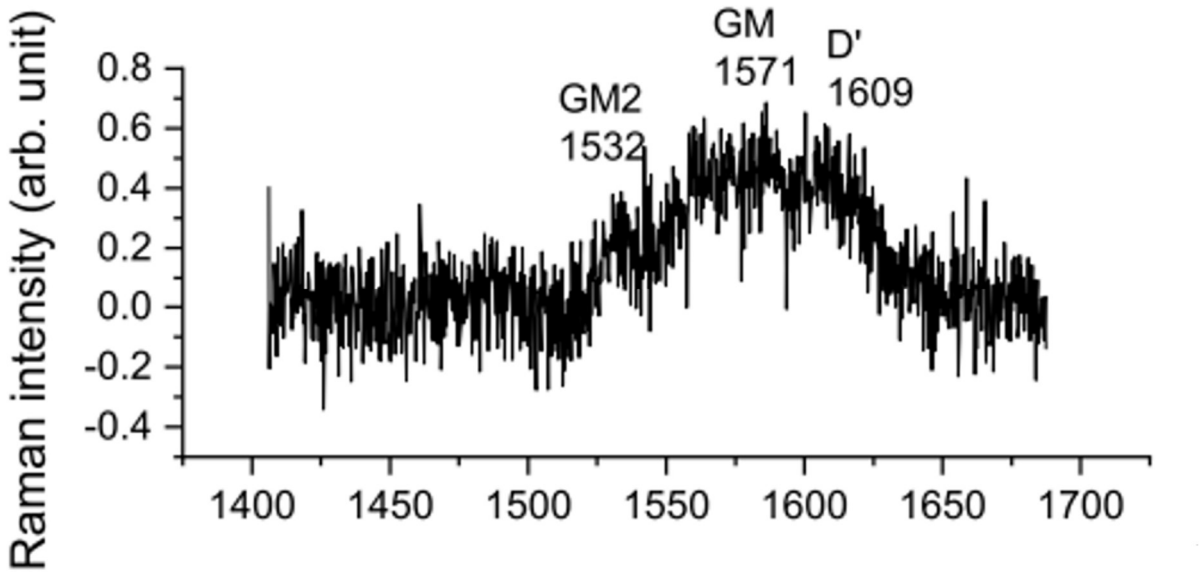

Figure 1.25: Raman spectra of GPA in the G-mode frequency range

Raman spectrum of GPA between 1400-1700 cm^{-1}, showing three peaks: the G^- (GM2) peak at 1532 cm^{-1}, the G (GM) peak at 1571 cm^{-1}, and the D' peak at 1609 cm^{-1}. Image adapted from [291].

1.4.3 Potential Applications

As shown in Table 1.2, GAs have diverse applications, including catalysts, supercapacitors, electrodes, and absorbents. GPA offers additional advantages, such as simple, cost-effective, and environmentally friendly production. Furthermore, through the integration of different nanomaterials, chemical and genetic modification of M13, and functionalisation of both GO and M13, its properties can be tuned for a targeted application.

For instance, GPA offers potential applications in the military and defence sector. For instance, carbon-based aerogels have shown electromagnetic shielding properties [293] and, by integrating noble metals and magnetic materials into their structure, both reflection and absorption-based EMI shielding has been achieved. Further exploration of integrating nanoparticles into GPA could significantly enhance its potential for EMI shielding applications [294]. Furthermore, due to their porous morphology and low

density, aerogels are typically highly adsorbent, and therefore GPA could lend itself to the removal of CWA through adsorption [295]. The integration of metallic-organic frameworks within GPA may enable the bre0akdown of these CWAs via solar-thermal enhanced catalytic and photocatalytic conversion [296]. This offers a promising approach for both the detection and elimination of CWAs. Additionally, studies on the stability of GPA at high temperature ranges, such as the typical range of aircraft oil temperatures, could lead to its use in adsorbing hot oils to mitigate fuel leakages and reduce the risk of aircraft explosions [297].

1.5 Characterising the Properties of GPA

A comprehensive understanding of the self-assembly mechanism and properties of GPA is crucial for assessing its potential applications. This section explores key theoretical frameworks that underpin its analysis in this thesis, including acid-base theory, peak analysis, and kinetic modelling.

1.5.1 Acid – Base Theory

Acids and bases can be described with the Brønsted-Lowry theory, which defines acids as proton (H^+) donors and bases as accept protons. A base that dissolves in water is known as an alkali, forming hydroxide (OH^-) ions in solution.

The acidity or alkalinity of a solution is described by its pH, which is a measure of the concentration of H^+ ions, $[H^+]$, in solution:

$$pH = -\log_{10}[H^+] \tag{1.1}$$

The pH scale classifies a solution as acidic (pH < 7), neutral (pH = 7), or basic (pH > 7). Acids and bases interact through neutralisation reactions, where H^+ ions from the acid combine with OH^- ions from the base to form water, shifting the solution's pH.

The strength of an acid or base depends on its ability to dissociate in solution and release H^+ and OH^- ions, respectively. For instance, when an acid HA dissociates, it forms H^+ and A^- ions:

$$HA_{aq} \rightleftharpoons H^+_{(aq)}\, A^-_{(aq)} \tag{1.2}$$

The extent of the dissociation is quantified by its acid dissociation constant, K_a:

$$K_a = \frac{[H^+][A^-]}{[HA]} \tag{1.3}$$

A larger K_a value indicates a stronger acid that dissociates more readily, whereas a smaller K_a value corresponds to a weaker acid. The strength of acids is more commonly expressed using pK_a, which is the negative logarithm of K_a [298]:

$$pK_a = -\log_{10}[K_a]. \tag{1.4}$$

Both GO and M13 contain a variety of functional groups, which will gain or lose H^+ ions depending on their pK_a values and the pH of the solution [98, 299]. This alters the charge of GO and M13 and consequently affects their electrostatic interactions. As it was previously hypothesised by Passaretti et al that electrostatic interactions between GO and M13 may govern their self-assembly, understanding the concentration of these

groups and their ionisation state at a given pH is essential in understanding and optimising the conditions required for GO-M13 self-assembly [20].

1.5.2 Peak Analysis

Peak fitting enables the extraction of information from experimental results. For instance, the position of peaks in a pK_a distribution enables the identification of specific acidic functional groups (Chapter 3) [299]. Meanwhile, in Raman spectroscopy, the peak type and its position, full width half maximum (FWHM) and intensity can provide insights into the structural composition of the sample, including any stresses, defects and functionalisation (Chapter 4 and Chapter 6) [300].

Two common functions used in peak fitting are the Lorentzian and Gaussian profiles. In Raman spectroscopy, these can describe different spectral features based on material properties and phonon interactions.

Lorentzian peaks are characterised by a sharp, narrow central peak with slowly decaying tails [301]. The Lorentzian function, *L*, is defined as:

$$L = a_0 \left[1 + \left(\frac{x - a_1}{a_2}\right)^2\right]^{-1} \tag{1.5}$$

where a_0, a_1 and a_2 represent the peak position, FWHM and peak height, respectively [302]. Lorentzian functions are often used in Raman spectra to describe crystalline materials or disordered graphite [303].

Gaussian peaks have a smoother, bell-shaped profile, with less narrow central peaks and more rapidly decaying tails compared to Lorentzian peaks [301]. The Gaussian function, *G*, is given by:

$$G = a_0 \exp\left[-\ln 2\left(\frac{x - a_1}{a_2}\right)^2\right] \quad (1.6)$$

with a_0, a_1 and a_2 retain the same definitions as in the Lorentzian function [302]. In Raman spectra, Gaussian functions are often used to describe a random variation of phonon lifetimes within disordered materials [303].

1.5.3 Sorption Kinetics

The sorption behaviour of GPA provides insight into its stability in different environments and potential applications in sorption-based technologies. Identifying the optimal kinetic model for sorption data allows for a deeper understanding of the mechanisms governing adsorption, offering valuable information on how relative humidity and solvent interactions influence material performance.

Several kinetic models can be used to describe sorption behaviour, each capturing different physical adsorption mechanisms. The most common kinetic models are summarised below:

Langmuir model – The Langmuir model describes monolayer adsorption onto a surface with a finite number of identical sites. It assumes that once a site is occupied, no further adsorption can occur at that site. The adsorption kinetics are proportional to the concentration of free adsorbate molecules and the number of available adsorption sites:

$$\frac{d\theta}{dt} = r_a - r_d = k_a C(1 - \theta) - k_d \theta \quad (1.7)$$

where $\frac{d\theta}{dt}$ is the net adsorption rate, θ is ratio of the adsorbed amount per mass of adsorbent compared to its maximum adsorption capacity, *t* is time, r_a and r_d are the rate of adsorption and desorption respectively, k_a and k_d are the adsorption and desorption rate constants respectively, and *C* is the concentration of adsorbate [304].

Pseudo-second-order model – The PSO model is used to describe chemisorption, where adsorption is driven by chemical interactions rather than physical attraction. The rate of occupation of adsorption sites is proportional to the square of the number of unoccupied sites. It is given by:

$$\frac{d\theta}{dt} = k_2^c(\theta_0 - \theta_t) \tag{1.8}$$

where k_2^c is the PSO rate constant, and θ_0 and θ are the amount adsorbed at equilibrium and time *t*, respectively [305].

Avrami model – The Avrami model describes adsorption processes that involve nucleation and growth, typically found in heterogeneous adsorption systems. It accounts for the effect of growth dimensionality on sorption kinetics. It is given by:

$$\frac{d\theta}{dt} = k_a^n t^{n-1}(\theta_0 - \theta_t) \tag{1.9}$$

where k_a is the Avrami kinetic constant and *n* is the Avrami constant, reflecting the dimensionality of growth [306].

Weibull model – The Weibull model is a statistical distribution function that may be used to describe adsorption when there is a distribution of adsorption energies,

accounting for heterogeneous adsorption sites. This is particularly useful for systems with irregular pore structures or variable surface energies. It is given by:

$$\frac{C_t}{C_0} = 1 - \exp\left[-\left(\frac{t}{a}\right)^b\right] \quad (1.10)$$

where C_t is the adsorbate concentration at time t, C_0 is the feed adsorbate concentration of adsorbate, *a* is the rate parameter and *b* is the shape parameter [307].

Intra-particle diffusion model – This describes adsorption as a process controlled by the diffusion of adsorbate molecules into the pores of the adsorbent. It is given by:

$$q_t = kt^{\frac{1}{2}} \quad (1.11)$$

where q_t is the adsorption capacity at time *t* and *k* is the kinetics [308].

1.6 Thesis Scope

GraPhage13 aerogels (GPAs) offer a simple and cost-effective method to produce graphene-based bionanocomposites with unique and tuneable properties. While GPA exhibits significant potential across various applications, further research is required to optimise its production, characterise its properties, and explore its tuneability to fully harness its capabilities.

Prior to industrial implementation, it is imperative to gain a deep understanding of the mechanism behind the self-assembly of GO and M13. Moreover, optimising the chemical conditions is crucial to ensure successful nanostructure synthesis and

consistent, reliable production. These steps are essential to achieving the quality and reproducibility needed for large-scale manufacturing [309].

However, the practical application of aerogels has been limited by their suboptimal nanomechanical properties, including poor stability and deformation recovery. Additionally, previous research has highlighted the temperature-dependent properties of graphene-based composites. Therefore, it is essential to evaluate both the temperature-dependent and nanomechanical properties of GPA to determine its viability and performance in industrial applications [310-312].

Regarding their practical uses, aerogels such as GPA are typically highly adsorbent due to their high porosity and surface area. This leads to a wide range of applications, including water sorption for humidity sensing and the sorption of volatile organic compounds (VOCs) for biomedical sensing and environmental monitoring [61, 313]. Therefore, assessing the sorption characteristics of GPA and its versatility in adsorbing different solvents is essential for its future integration into graphene-based sensors.

Another important consideration in the integration of GPA into graphene-based devices is its inherently insulating nature, which can limit its applications. However, the ability to integrate conductive nanomaterials into GPA offers a promising method to improve its conductivity. Therefore, it is imperative to investigate the incorporation of conductive materials, such as gold nanoparticles (AuNPs), into GPA and to characterise its resulting electronic properties to enable its use in future applications.

This thesis focuses on the optimisation, characterisation, and tuneability of GPA, exploring its unique, tuneable properties and potential applications.

Chapter 1 introduced nanostructures and their unique properties, applicability in industry, and the limitations of current fabrication methods. It discussed the generation of complex nanostructures through self-assembly, and the advantages of utilising biological components. The chapter continued to introduce M13 bacteriophage and an extensive literature review on M13-based nanostructures and their applications. It then explored the properties of graphene and its derivatives, specifically graphene oxide (GO), and its ability to form nanostructures like aerogels. The chapter then highlighted the novel bionanocomposite GraPhage13 aerogels (GPA), generated through the self-assembly of GO and M13, detailing their properties and potential applications. Finally, the required investigations into GPA and the thesis scope was outlined.

Chapter 2 introduces the materials and methods used throughout the thesis.

Chapter 3 assesses the chemical conditions required to initiate the self-assembly of GO and M13, and the mechanism behind their interaction.

Chapter 4 explores the thermonanomechanical properties of GPA, investigating its morphology, nanomechanics, and microstructure, and the effect of temperature on these properties.

Chapter 5 explores the sorption properties of GPA for water, ethanol and acetone, investigating its sorption capacity and kinetics.

Chapter 6 investigates the incorporation of carboxylic acid-functionalised gold nanoparticles (AuNPs) into GPA. The interactions between GPA and Au are examined, and the saturation concentration of AuNPs in GPA is determined. The conductivity of the resulting GPA-Au bionanocomposite is then measured, and the mechanism behind the observed conductivity enhancement explored.

Chapter 7 summarises the work in this thesis and highlights the potential future investigations required to fully realise the integration of GPA in industry.

By optimising the fabrication processes, understanding the self-assembly mechanisms, and investigating the effects of different chemical and physical modifications, this research aims to unlock new possibilities for GraPhage13 aerogels in advanced technological and industrial applications.

1.7 References

[1] D. Datta, K. P. Das, K. S. Deepak, and B. Das, "Candidates of Functionalized Nanomaterial-Based Membranes," in *Membranes with Functionalized Nanomaterials*, S. Dutta and C. M. Hussain Eds.: Elsevier, 2022, ch. 3, pp. 81-127.

[2] N. Joudeh and D. Linke, "Nanoparticle Classification, Physicochemical Properties, Characterization, and Applications: A Comprehensive Review for Biologists," *Journal of Nanobiotechnology,* vol. 20, no. 1, p. 262, 2022, doi: 10.1186/s12951-022-01477-8.

[3] Q. Wu, W.-s. Miao, Y.-d. Zhang, H.-j. Gao, and D. Hui, "Mechanical Properties of Nanomaterials: A Review," *Nanotechnology Reviews,* vol. 9, no. 1, pp. 259-273, 2020, doi: 10.1515/ntrev-2020-0021.

[4] L. Qiu, N. Zhu, Y. Feng, E. E. Michaelides, G. Żyła, D. Jing, X. Zhang, P. M. Norris, C. N. Markides, and O. Mahian, "A Review of Recent Advances in Thermophysical Properties at the Nanoscale: From Solid State to Colloids," *Physics Reports,* vol. 843, pp. 1-81, 2020, doi: 10.1016/j.physrep.2019.12.001.

[5] C.-Y. Hsu, A. M. Rheima, Z. s. Abbas, M. U. Faryad, M. M. Kadhim, U. S. Altimari, A. H. Dawood, A. d. jawad al-bayati, Z. T. Abed, R. S. Radhi, A. S. Jaber, S. K. Hachim, F. K. Ali, Z. H. Mahmoud, G. Behzadi pour, and E. Kianfar, "Nanowires Properties and Applications: A Review Study," *South African Journal of Chemical Engineering,* vol. 46, pp. 286-311, 2023, doi: 10.1016/j.sajce.2023.08.006.

[6] A. R. Urade, I. Lahiri, and K. S. Suresh, "Graphene Properties, Synthesis and Applications: A Review," *JOM,* vol. 75, no. 3, pp. 614-630, 2023, doi: 10.1007/s11837-022-05505-8.

[7] T. D. Burchell, "Graphite: Properties and Characteristics," in *Comprehensive Nuclear Materials*, R. J. M. Konings Ed. Oxford: Elsevier, 2012, ch. 2.10, pp. 285-305.

[8] N. Kumar, P. Chamoli, M. Misra, M. K. Manoj, and A. Sharma, "Advanced Metal and Carbon Nanostructures for Medical, Drug Delivery and Bio-Imaging Applications," *Nanoscale,* 10.1039/D1NR07643D vol. 14, no. 11, pp. 3987-4017, 2022, doi: 10.1039/D1NR07643D.

[9] A. M. Díez-Pascual and A. Rahdar, "Graphene-Based Polymer Composites for Flexible Electronic Applications," *Micromachines,* vol. 13, no. 7, p. 1123, 2022, doi: 10.3390/mi13071123.

[10] N. Abid, A. M. Khan, S. Shujait, K. Chaudhary, M. Ikram, M. Imran, J. Haider, M. Khan, Q. Khan, and M. Maqbool, "Synthesis of Nanomaterials Using Various Top-Down and Bottom-up Approaches, Influencing Factors, Advantages, and Disadvantages: A Review," *Advances in Colloid and Interface Science,* vol. 300, p. 102597, 2022, doi: 10.1016/j.cis.2021.102597.

[11] K. Stokes, K. Clark, D. Odetade, M. Hardy, and P. Goldberg Oppenheimer, "Advances in Lithographic Techniques for Precision Nanostructure Fabrication in Biomedical Applications," *Discover Nano,* vol. 18, no. 1, p. 153, 2023, doi: 10.1186/s11671-023-03938-x.

[12] M. Mastrangeli and M. Perego, "Bottom-up Assembly of Micro/Nanostructures," *Advanced Materials Interfaces,* vol. 7, no. 5, p. 2000182, 2020, doi: 10.1002/admi.202000182.

[13] I. Insua, J. Bergueiro, A. Méndez-Ardoy, I. Lostalé-Seijo, and J. Montenegro, "Bottom-up Supramolecular Assembly in Two Dimensions," *Chemical Science,* 10.1039/D1SC05667K vol. 13, no. 11, pp. 3057-3068, 2022, doi: 10.1039/D1SC05667K.

[14] D. Lombardo, P. Calandra, L. Pasqua, and S. Magazù, "Self-Assembly of Organic Nanomaterials and Biomaterials: The Bottom-up Approach for Functional Nanostructures Formation and Advanced Applications," *Materials (Basel),* vol. 13, no. 5, 2020, doi: 10.3390/ma13051048.

[15] C. Gong, S. Sun, Y. Zhang, L. Sun, Z. Su, A. Wu, and G. Wei, "Hierarchical Nanomaterials Via Biomolecular Self-Assembly and Bioinspiration for Energy and Environmental Applications," *Nanoscale,* 10.1039/C9NR00218A vol. 11, no. 10, pp. 4147-4182, 2019, doi: 10.1039/C9NR00218A.

[16] F. M. Husain, A. Khan, R. A. Khan, J. A. Siddique, M. Oves, A. A. P. Khan, M. O. Ansari, and H. D. Cancar, "Bio-Based Aerogels and Their Environment Applications: An Overview," in *Advances in Aerogel Composites for Environmental Remediation*, A. A. P. Khan, M. O. Ansari, A. Khan, and A. M. Asiri Eds.: Elsevier, 2021, ch. 18, pp. 347-356.

[17] M. Fijalkowski, R. Coufal, A. Ali, K. Adach, S. Petrik, H. Bu, and C. W. Karl, "Flexible Hybrid and Single-Component Aerogels: Synthesis, Characterization, and Applications," *Langmuir,* vol. 39, no. 47, pp. 16760-16775, 2023, doi: 10.1021/acs.langmuir.3c01811.

[18] K. S. Novoselov, A. K. Geim, S. V. Morozov, D. Jiang, Y. Zhang, S. V. Dubonos, I. V. Grigorieva, and A. A. Firsov, "Electric Field Effect in Atomically Thin Carbon Films," *Science,* vol. 306, no. 5696, pp. 666-669, 2004, doi: 10.1126/science.1102896.

[19] A. K. Samantara, S. Ratha, and S. Raj, "Functionalized Graphene Nanocomposites in Air Filtration Applications," in *Functionalized Graphene Nanocomposites and Their Derivatives*, M. Jawaid, R. Bouhfid, and A. e. Kacem Qaiss Eds.: Elsevier, 2019, ch. 4, pp. 65-89.

[20] P. Passaretti, Y. Sun, I. Khan, K. Chan, R. Sabo, H. White, T. R. Dafforn, and P. G. Oppenheimer, "Multifunctional Graphene Oxide-Bacteriophage Based Porous Three-Dimensional Micro-Nanocomposites," *Nanoscale,*

10.1039/C9NR03670A vol. 11, no. 28, pp. 13318-13329, 2019, doi: 10.1039/C9NR03670A.

[21] J. H. Gosling, O. Makarovsky, F. Wang, N. D. Cottam, M. T. Greenaway, A. Patanè, R. D. Wildman, C. J. Tuck, L. Turyanska, and T. M. Fromhold, "Universal Mobility Characteristics of Graphene Originating from Charge Scattering by Ionised Impurities," *Communications Physics,* vol. 4, no. 1, p. 30, 2021, doi: 10.1038/s42005-021-00518-2.

[22] M. Sang, J. Shin, K. Kim, and K. J. Yu, "Electronic and Thermal Properties of Graphene and Recent Advances in Graphene Based Electronics Applications," *Nanomaterials (Basel),* vol. 9, no. 3, 2019, doi: 10.3390/nano9030374.

[23] Y. W. Sun, D. G. Papageorgiou, C. J. Humphreys, D. J. Dunstan, P. Puech, J. E. Proctor, C. Bousige, D. Machon, and A. San-Miguel, "Mechanical Properties of Graphene," *Applied Physics Reviews,* vol. 8, no. 2, 2021, doi: 10.1063/5.0040578.

[24] P. Kamedulski, M. Skorupska, P. Binkowski, W. Arendarska, A. Ilnicka, and J. P. Lukaszewicz, "High Surface Area Micro-Mesoporous Graphene for Electrochemical Applications," *Scientific Reports,* vol. 11, no. 1, p. 22054, 2021, doi: 10.1038/s41598-021-01154-0.

[25] E. D. Obraztsova, M. G. Rybin, and P. A. Obraztsov, "Optical Properties of Graphene," in *Graphene (Second Edition)*, V. Skakalova and A. B. Kaiser Eds.: Woodhead Publishing, 2021, ch. 7, pp. 133-142.

[26] E. W. Hill, A. Vijayaragahvan, and K. Novoselov, "Graphene Sensors," *IEEE Sensors Journal,* vol. 11, no. 12, pp. 3161-3170, 2011, doi: 10.1109/JSEN.2011.2167608.

[27] Y. Liu, X. Dong, and P. Chen, "Biological and Chemical Sensors Based on Graphene Materials," *Chemical Society Reviews,* 10.1039/C1CS15270J vol. 41, no. 6, pp. 2283-2307, 2012, doi: 10.1039/C1CS15270J.

[28] T.-H. Han, H. Kim, S.-J. Kwon, and T.-W. Lee, "Graphene-Based Flexible Electronic Devices," *Materials Science and Engineering: R: Reports,* vol. 118, pp. 1-43, 2017, doi: 10.1016/j.mser.2017.05.001.

[29] T. Das, B. K. Sharma, A. K. Katiyar, and J.-H. Ahn, "Graphene-Based Flexible and Wearable Electronics," *Journal of Semiconductors,* vol. 39, no. 1, p. 011007, 2018, doi: 10.1088/1674-4926/39/1/011007.

[30] R. Raccichini, A. Varzi, S. Passerini, and B. Scrosati, "The Role of Graphene for Electrochemical Energy Storage," *Nature Materials,* vol. 14, no. 3, pp. 271-279, 2015, doi: 10.1038/nmat4170.

[31] A. G. Olabi, M. A. Abdelkareem, T. Wilberforce, and E. T. Sayed, "Application of Graphene in Energy Storage Device – a Review," *Renewable and Sustainable Energy Reviews,* vol. 135, p. 110026, 2021, doi: 10.1016/j.rser.2020.110026.

[32] Y. Ma and L. Zhi, "Graphene-Based Transparent Conductive Films: Material Systems, Preparation and Applications," *Small Methods,* vol. 3, no. 1, p. 1800199, 2019, doi: 10.1002/smtd.201800199.

[33] A. B. Suriani, Muqoyyanah, A. Mohamed, S. Alfarisa, M. H. Mamat, M. K. Ahmad, M. D. Birowosuto, and T. Soga, "Synthesis, Transfer and Application of Graphene as a Transparent Conductive Film: A Review," *Bulletin of Materials Science,* vol. 43, no. 1, p. 310, 2020, doi: 10.1007/s12034-020-02270-9.

[34] H. Chen, W. Ma, Z. Huang, Y. Zhang, Y. Huang, and Y. Chen, "Graphene-Based Materials toward Microwave and Terahertz Absorbing Stealth Technologies," *Advanced Optical Materials,* vol. 7, no. 8, p. 1801318, 2019, doi: 10.1002/adom.201801318.

[35] R. Pandey, N. Singhal, P. Kumar, K. Choudhary, and S. Kumar, "Graphene and Its Immense Contribution in Defense and Security: A Review," *Analytical Chemistry Letters,* vol. 12, no. 1, pp. 1-12, 2022, doi: 10.1080/22297928.2021.1980099.

[36] G. Ulian and G. Valdrè, "Facile Band Gap Tuning in Graphene–Brucite Heterojunctions," *Scientific Reports,* vol. 13, no. 1, p. 23090, 2023, doi: 10.1038/s41598-023-50037-z.

[37] L. Yan, Y. Zheng, F. Zhao, S. Li, X. Gao, B. Xu, P. Weiss, and Y. Zhao, "Chemistry and Physics of a Single Atomic Layer: Strategies and Challenges for Functionalization of Graphene and Graphene-Based Materials," *Chemical Society reviews,* vol. 41, pp. 97-114, 2011, doi: 10.1039/c1cs15193b.

[38] O. C. Compton and S. T. Nguyen, "Graphene Oxide, Highly Reduced Graphene Oxide, and Graphene: Versatile Building Blocks for Carbon-Based Materials," *Small,* vol. 6, no. 6, pp. 711-723, 2010, doi: 10.1002/smll.200901934.

[39] S. C. Ray, "Application and Uses of Graphene Oxide and Reduced Graphene Oxide," in *Applications of Graphene and Graphene-Oxide Based Nanomaterials*, S. C. Ray Ed. Oxford: William Andrew Publishing, 2015, pp. 39-55.

[40] K. Tadyszak, J. Wychowaniec, and J. Litowczenko, "Biomedical Applications of Graphene-Based Structures," *Nanomaterials,* vol. 8, p. 944, 2018, doi: 10.3390/nano8110944.

[41] J. Pang, J. Li, J. Guo, M. Jia, and J. Zhang, "Tuning the Aggregation Structure and Surface Composition of Reduced Graphene Oxide Microspheres for High-Rate Supercapacitors," *Diamond and Related Materials,* vol. 136, p. 109920, 2023, doi: 10.1016/j.diamond.2023.109920.

[42] G. Nassar, E. Daou, R. Najjar, M. Bassil, and R. Habchi, "A Review on the Current Research on Graphene-Based Aerogels and Their Applications," *Carbon Trends,* vol. 4, p. 100065, 2021, doi: 10.1016/j.cartre.2021.100065.

[43] S. Long, H. Wang, K. He, C. Zhou, G. Zeng, Y. Lu, M. Cheng, B. Song, Y. Yang, Z. Wang, X. Luo, and Q. Xie, "3d Graphene Aerogel Based Photocatalysts: Synthesized, Properties, and Applications," *Colloids and Surfaces A: Physicochemical and Engineering Aspects,* vol. 594, p. 124666, 2020, doi: 10.1016/j.colsurfa.2020.124666.

[44] E. Garcia-Bordejé, A. M. Benito, and W. K. Maser, "Graphene Aerogels Via Hydrothermal Gelation of Graphene Oxide Colloids: Fine-Tuning of Its Porous and Chemical Properties and Catalytic Applications," *Advances in Colloid and Interface Science,* vol. 292, p. 102420, 2021, doi: 10.1016/j.cis.2021.102420.

[45] R. Mao, W. Yao, A. Qadir, W. Chen, W. Gao, Y. Xu, and H. Hu, "3-D Graphene Aerogel Sphere-Based Flexible Sensors for Healthcare Applications," *Sensors and Actuators A: Physical,* vol. 312, p. 112144, 2020, doi: 10.1016/j.sna.2020.112144.

[46] M. Mahmoudpour, J. E.-N. Dolatabadi, M. Hasanzadeh, and J. Soleymani, "Carbon-Based Aerogels for Biomedical Sensing: Advances toward Designing

the Ideal Sensor," *Advances in Colloid and Interface Science,* vol. 298, p. 102550, 2021, doi: 10.1016/j.cis.2021.102550.
[47] S. Korkmaz and İ. A. Kariper, "Graphene and Graphene Oxide Based Aerogels: Synthesis, Characteristics and Supercapacitor Applications," *Journal of Energy Storage,* vol. 27, p. 101038, 2020, doi: 10.1016/j.est.2019.101038.
[48] Y. B. Pottathara, H. R. Tiyyagura, Z. Ahmad, and K. K. Sadasivuni, "Graphene Based Aerogels: Fundamentals and Applications as Supercapacitors," *Journal of Energy Storage,* vol. 30, p. 101549, 2020, doi: 10.1016/j.est.2020.101549.
[49] S. S. Ashok Sharma, S. Bashir, R. Kasi, and R. T. Subramaniam, "The Significance of Graphene Based Composite Hydrogels as Smart Materials: A Review on the Fabrication, Properties, and Its Applications," *FlatChem,* vol. 33, p. 100352, 2022, doi: 10.1016/j.flatc.2022.100352.
[50] G. Gorgolis and C. Galiotis, "Graphene Aerogels: A Review," *2D Materials,* vol. 4, no. 3, p. 032001, 2017, doi: 10.1088/2053-1583/aa7883.
[51] G. Liao, J. Hu, Z. Chen, R. Zhang, G. Wang, and T. Kuang, "Preparation, Properties, and Applications of Graphene-Based Hydrogels," (in

), *Front Chem,* vol. 6, p. 450, 2018, doi: 10.3389/fchem.2018.00450.
[52] H. Lu, S. Zhang, L. Guo, and W. Li, "Applications of Graphene-Based Composite Hydrogels: A Review," *RSC Advances,* 10.1039/C7RA09634H vol. 7, no. 80, pp. 51008-51020, 2017, doi: 10.1039/C7RA09634H.
[53] A. Ehsani, M. Esfahaniha, P. Khodaei kahriz, R. Safari, and H. Parsimehr, "Functionalized Graphene Oxide Aerogel as a High Efficient Material for Electrochemical Sensing of Organic Pollutant," *Surfaces and Interfaces,* vol. 22, p. 100817, 2021, doi: 10.1016/j.surfin.2020.100817.
[54] X. Liu, K. Jing, S. Peng, Q. Shi, and H. Liu, "Mild Preparation of Amino-Functionalized Graphene Oxide-Based Recyclable Aerogel to Efficiently Adsorb Methyl Orange," *Journal of Materials Science,* vol. 58, no. 39, pp. 15336-15351, 2023, doi: 10.1007/s10853-023-08982-7.
[55] J. Park, J. Sharma, C. J. Jafta, L. He, H. M. Meyer, J. Li, J. K. Keum, N. A. Nguyen, and G. Polizos, "Reduced Graphene Oxide Aerogels with Functionalization-Mediated Disordered Stacking for Sodium-Ion Batteries," *Batteries,* vol. 8, no. 2, p. 12, 2022, doi: 10.3390/batteries8020012.
[56] A. Islam and S. Fatima, "Zirconium-2-Imidazolidinethione Functionalized Reduced Graphene Oxide Aerogel for Efficient Removal of Fluoride Ions and Anionic Dyes from Aqueous Solutions: Multivariate Process Optimization," *CLEAN – Soil, Air, Water,* vol. 51, no. 5, p. 2200193, 2023, doi: 10.1002/clen.202200193.
[57] S. Zhang, J. Sun, D. Hu, C. Xiao, Q. Zhuo, J. Wang, C. Qin, and L. Dai, "Large-Sized Graphene Oxide/Modified Tourmaline Nanoparticle Aerogel with Stable Honeycomb-Like Structure for High-Efficiency Pm2.5 Capture," *Journal of Materials Chemistry A,* 10.1039/C8TA05506H vol. 6, no. 33, pp. 16139-16148, 2018, doi: 10.1039/C8TA05506H.
[58] C. Ferrag, M. Noroozifar, and K. Kerman, "Ultralight 3d Graphene Oxide Aerogel Decorated with Pd–Fe Nanoparticles for the Simultaneous Detection of Eight Biomolecules," *ACS Applied Materials & Interfaces,* vol. 15, no. 23, pp. 27502-27514, 2023, doi: 10.1021/acsami.3c01600.
[59] J. Xie, L. Niu, Y. Qiao, Y. Lei, G. Li, X. Zhang, and P. Chen, "The Influence of the Drying Method on the Microstructure and the Compression Behavior of

Graphene Aerogel," *Diamond and Related Materials,* vol. 121, p. 108772, 2022, doi: 10.1016/j.diamond.2021.108772.
[60] Ö. Kavak, B. Can, and E. Bat, "Water-Based Route for Dopamine and Reduced Graphene Oxide Aerogel Production," *ACS Omega,* vol. 8, no. 49, pp. 46728-46737, 2023, doi: 10.1021/acsomega.3c05955.
[61] F. Pinelli, C. Piras, and F. Rossi, "A Perspective on Graphene Based Aerogels and Their Environmental Applications," *FlatChem,* vol. 36, p. 100449, 2022, doi: 10.1016/j.flatc.2022.100449.
[62] A. Soleimani Dorcheh and M. H. Abbasi, "Silica Aerogel; Synthesis, Properties and Characterization," *Journal of Materials Processing Technology,* vol. 199, no. 1, pp. 10-26, 2008, doi: 10.1016/j.jmatprotec.2007.10.060.
[63] N. M. Bakhori, Z. Ismail, M. Z. Hassan, and R. Dolah, "Emerging Trends in Nanotechnology: Aerogel-Based Materials for Biomedical Applications," *Nanomaterials,* vol. 13, no. 6, p. 1063, 2023, doi: 10.3390/nano13061063.
[64] L. Zuo, Y. Zhang, L. Zhang, Y. E. Miao, W. Fan, and T. Liu, "Polymer/Carbon-Based Hybrid Aerogels: Preparation, Properties and Applications," *Materials (Basel),* vol. 8, no. 10, pp. 6806-6848, 2015, doi: 10.3390/ma8105343.
[65] R. Coufal, M. Fijalkowski, K. Adach, H. Bu, C. W. Karl, E. Mikysková, and S. Petrík, "Preparation and Investigation of High Surface Area Aerogels from Crosslinked Polypropylenes," *Polymers,* vol. 16, no. 10, p. 1382, 2024, doi: 10.3390/polym16101382.
[66] P. Paraskevopoulou, D. Chriti, G. Raptopoulos, and G. C. Anyfantis, "Synthetic Polymer Aerogels in Particulate Form," *Materials,* vol. 12, no. 9, p. 1543, 2019, doi: 10.3390/ma12091543.
[67] S. Zhao, W. J. Malfait, N. Guerrero-Alburquerque, M. M. Koebel, and G. Nyström, "Biopolymer Aerogels and Foams: Chemistry, Properties, and Applications," *Angewandte Chemie International Edition,* vol. 57, no. 26, pp. 7580-7608, 2018, doi: 10.1002/anie.201709014.
[68] S. Araby, A. Qiu, R. Wang, Z. Zhao, C.-H. Wang, and J. Ma, "Aerogels Based on Carbon Nanomaterials," *Journal of Materials Science,* vol. 51, no. 20, pp. 9157-9189, 2016, doi: 10.1007/s10853-016-0141-z.
[69] L. Hu, R. He, H. Lei, and D. Fang, "Carbon Aerogel for Insulation Applications: A Review," *International Journal of Thermophysics,* vol. 40, no. 4, p. 39, 2019, doi: 10.1007/s10765-019-2505-5.
[70] X. Jiang, R. Du, R. Hübner, Y. Hu, and A. Eychmüller, "A Roadmap for 3d Metal Aerogels: Materials Design and Application Attempts," *Matter,* vol. 4, no. 1, pp. 54-94, 2021, doi: 10.1016/j.matt.2020.10.001.
[71] G. Shao, X. Huang, X. Shen, C. Li, and A. Thomas, "Metal–Organic Framework and Covalent–Organic Framework-Based Aerogels: Synthesis, Functionality, and Applications," *Advanced Science,* vol. 11, no. 48, p. 2409290, 2024, doi: 10.1002/advs.202409290.
[72] M. Zhi, H. Tang, M. Wu, C. Ouyang, Z. Hong, and N. Wu, "Synthesis and Photocatalysis of Metal Oxide Aerogels: A Review," *Energy & Fuels,* vol. 36, no. 19, pp. 11359-11379, 2022, doi: 10.1021/acs.energyfuels.2c01049.
[73] Y. Wu, X. Wang, and J. Shen, "Metal Oxide Aerogels for High-Temperature Applications," *Journal of Sol-Gel Science and Technology,* vol. 106, no. 2, pp. 360-380, 2023, doi: 10.1007/s10971-021-05720-w.

[74] X. Zhang, J. Zhou, Y. Zheng, H. Wei, and Z. Su, "Graphene-Based Hybrid Aerogels for Energy and Environmental Applications," *Chemical Engineering Journal,* vol. 420, p. 129700, 2021, doi: 10.1016/j.cej.2021.129700.

[75] P. Passaretti, "Graphene Oxide and Biomolecules for the Production of Functional 3d Graphene-Based Materials," *Frontiers in Molecular Biosciences,* Review vol. 9, 2022, doi: 10.3389/fmolb.2022.774097.

[76] M. Azizi-Lalabadi and S. M. Jafari, "Bio-Nanocomposites of Graphene with Biopolymers; Fabrication, Properties, and Applications," *Advances in Colloid and Interface Science,* vol. 292, p. 102416, 2021, doi: 10.1016/j.cis.2021.102416.

[77] A. H. M. Firdaus, S. M. Sapuan, A. M. Afdzaluddin, and F. M. AL-Oqla, "A Review of Graphene Biopolymer Composite in Piezoelectric Sensor Applications," *Physical Sciences Reviews,* vol. 9, no. 12, pp. 3639-3665, 2024, doi: 10.1515/psr-2024-0080.

[78] A. Kovtun, E. Campodoni, L. Favaretto, M. Zambianchi, A. Salatino, S. Amalfitano, M. L. Navacchia, B. Casentini, V. Palermo, M. Sandri, and M. Melucci, "Multifunctional Graphene Oxide/Biopolymer Composite Aerogels for Microcontaminants Removal from Drinking Water," *Chemosphere,* vol. 259, p. 127501, 2020, doi: 10.1016/j.chemosphere.2020.127501.

[79] J. M. Bloor, R. D. Handy, S. A. Awan, and D. F. L. Jenkins, "Graphene Oxide Biopolymer Aerogels for the Removal of Lead from Drinking Water Using a Novel Nano-Enhanced Ion Exchange Cascade," *Ecotoxicology and Environmental Safety,* vol. 208, p. 111422, 2021, doi: 10.1016/j.ecoenv.2020.111422.

[80] A. Masud, C. Zhou, and N. Aich, "Emerging Investigator Series: 3d Printed Graphene-Biopolymer Aerogels for Water Contaminant Removal: A Proof of Concept," *Environmental Science: Nano,* 10.1039/D0EN00953A vol. 8, no. 2, pp. 399-414, 2021, doi: 10.1039/D0EN00953A.

[81] Y. Xu, Q. Wu, Y. Sun, H. Bai, and G. Shi, "Three-Dimensional Self-Assembly of Graphene Oxide and DNA into Multifunctional Hydrogels," *ACS Nano,* vol. 4, no. 12, pp. 7358-7362, 2010, doi: 10.1021/nn1027104.

[82] X. Leng, S. Chen, S. R. McCuskey, Y. Zhang, S. J. W. Chan, G. Quek, M. C. F. Costa, P. Zhang, J. Wu, K. G. Nikolaev, G. C. Bazan, K. S. Novoselov, and D. V. Andreeva, "DNA-Rgo Aerogel Bioanodes with Microcompartmentalization for High-Performance Bioelectrochemical Systems," *Advanced Electronic Materials,* vol. 10, no. 10, p. 2400137, 2024, doi: 10.1002/aelm.202400137.

[83] M. Sun, R. Song, Y. Fang, J. Xu, Z. Yang, and H. Zhang, "DNA-Based Complexes and Composites: A Review of Fabrication Methods, Properties, and Applications," *ACS Applied Materials & Interfaces,* vol. 16, no. 39, pp. 51899-51915, 2024, doi: 10.1021/acsami.4c13357.

[84] Y. K. Sunkari, T. L. Nguyen, V. K. Siripuram, and M. Flajolet, "Impact of Organic Chemistry Conditions on DNA Durability in the Context of DNA-Encoded Library Technology," *iScience,* vol. 26, no. 9, p. 107573, 2023, doi: 10.1016/j.isci.2023.107573.

[85] N. Stephanopoulos, "Hybrid Nanostructures from the Self-Assembly of Proteins and DNA," *Chem,* vol. 6, no. 2, pp. 364-405, 2020, doi: 10.1016/j.chempr.2020.01.012.

[86] Y. Zhuang, F. Yu, J. Ma, and J. Chen, "Facile Synthesis of Three-Dimensional Graphene–Soy Protein Aerogel Composites for Tetracycline Adsorption," *Desalination and Water Treatment,* vol. 57, no. 20, pp. 9510-9519, 2016, doi: 10.1080/19443994.2015.1029530.

[87] Y. Jin, Q. Du, Y. Li, Y. Zhang, B. Chen, M. Wang, K. Chen, Y. Sun, S. Zhao, and Z. Jing, "Removal of Methylene Blue by Crosslinked Egg White Protein/Graphene Oxide Bionanocomposite Aerogels," *Nanomaterials,* vol. 12, no. 15, p. 2659, 2022, doi: 10.3390/nano12152659.

[88] S. Ozden, S. Monti, V. Tozzini, N. S. Dutta, S. Gili, N. Caggiano, A. J. Link, N. M. Pugno, J. Higgins, R. D. Priestley, and C. B. Arnold, "Egg Protein Derived Ultralightweight Hybrid Monolithic Aerogel for Water Purification," *Materials Today,* vol. 59, pp. 46-55, 2022, doi: 10.1016/j.mattod.2022.08.001.

[89] Y.-S. Xiong, M.-X. Li, M. Li, H.-Q. Lu, Y. Liu, W. Wei, Y.-H. Wei, W. Li, and K. Li, "Amine-Functionalized Soy Protein/Graphene Oxide Aerogel for Efficient Removal of Multiple Sugar-Derived Contaminants (Sdcs): Full Life Cycle Exploration and Interaction Simulation," *Chemical Engineering Journal,* vol. 499, p. 156479, 2024, doi: 10.1016/j.cej.2024.156479.

[90] M. Ardini, G. Golia, P. Passaretti, A. Cimini, G. Pitari, F. Giansanti, L. D. Leandro, L. Ottaviano, F. Perrozzi, S. Santucci, V. Morandi, L. Ortolani, M. Christian, E. Treossi, V. Palermo, F. Angelucci, and R. Ippoliti, "Supramolecular Self-Assembly of Graphene Oxide and Metal Nanoparticles into Stacked Multilayers by Means of a Multitasking Protein Ring," *Nanoscale,* 10.1039/C5NR08632A vol. 8, no. 12, pp. 6739-6753, 2016, doi: 10.1039/C5NR08632A.

[91] S.-Y. Lee, J.-S. Lim, and M. T. Harris, "Synthesis and Application of Virus-Based Hybrid Nanomaterials," *Biotechnology and Bioengineering,* vol. 109, no. 1, pp. 16-30, 2012, doi: 10.1002/bit.23328.

[92] E. Jończyk, M. Kłak, R. Międzybrodzki, and A. Górski, "The Influence of External Factors on Bacteriophages--Review," *Folia Microbiol (Praha),* vol. 56, no. 3, pp. 191-200, 2011, doi: 10.1007/s12223-011-0039-8.

[93] M. Fischlechner and E. Donath, "Viruses as Building Blocks for Materials and Devices," *Angew Chem Int Ed Engl,* Review vol. 46, no. 18, pp. 3184-93, 2007, doi: 10.1002/anie.200603445.

[94] S. H. Yang, W. J. Chung, S. McFarland, and S. W. Lee, "Assembly of Bacteriophage into Functional Materials," *Chem Rec,* Review vol. 13, no. 1, pp. 43-59, 2013, doi: 10.1002/tcr.201200012.

[95] Y. M. Lee, B. Jung, Y. H. Kim, A. R. Park, S. Han, W. S. Choe, and P. J. Yoo, "Nanomesh-Structured Ultrathin Membranes Harnessing the Unidirectional Alignment of Viruses on a Graphene-Oxide Film," *Adv Mater,* vol. 26, no. 23, pp. 3899-904, 2014, doi: 10.1002/adma.201305862.

[96] I. W. Park, K. W. Kim, Y. Hong, H. J. Yoon, Y. Lee, D. Gwak, and K. Heo, "Recent Developments and Prospects of M13- Bacteriophage Based Piezoelectric Energy Harvesting Devices," *Nanomaterials (Basel),* vol. 10, no. 1, 2020, doi: 10.3390/nano10010093.

[97] W. J. Chung, D. Y. Lee, and S. Y. Yoo, "Chemical Modulation of M13 Bacteriophage and Its Functional Opportunities for Nanomedicine," *Int J Nanomedicine,* Review vol. 9, pp. 5825-36, 2014, doi: 10.2147/IJN.S73883.

[98] P. Passaretti, Y. Sun, T. R. Dafforn, and P. G. Oppenheimer, "Determination and Characterisation of the Surface Charge Properties of the Bacteriophage M13 to Assist Bio-Nanoengineering," *RSC Advances,* vol. 10, no. 42, pp. 25385-25392, 2020, doi: 10.1039/d0ra04086j.

[99] W. J. Chung, M. Sena, A. Merzlyak, and S. W. Lee, "Phages as Tools for Functional Nanomaterials Development," in *Comprehensive Biomaterials*, P. Ducheyne Ed. Oxford: Elsevier, 2011, ch. 2.206, pp. 95-111.

[100] Z. Wan and N. L. Goddard, "Competition between Conjugation and M13 Phage Infection in Escherichia Coli in the Absence of Selection Pressure: A Kinetic Study," *G3 (Bethesda),* vol. 2, no. 10, pp. 1137-44, 2012, doi: 10.1534/g3.112.003418.

[101] H. S. Lin, J. M. Lee, J. Han, C. Lee, S. Seo, S. Tan, H. M. Lee, E. J. Choi, M. S. Strano, Y. Yang, S. Maruyama, I. Jeon, Y. Matsuo, and J. W. Oh, "Denatured M13 Bacteriophage-Templated Perovskite Solar Cells Exhibiting High Efficiency," *Advanced Science,* 2020, doi: 10.1002/advs.202000782.

[102] J. S. Moon, E. J. Choi, N. N. Jeong, J. R. Sohn, D. W. Han, and J. W. Oh, "Research Progress of M13 Bacteriophage-Based Biosensors," *Nanomaterials (Basel),* vol. 9, no. 10, 2019, doi: 10.3390/nano9101448.

[103] C. Potts, "Statement of Nonpathogenicity," Thermo Fisher Scientific 2016. [Online]. Available: https://assets.fishersci.com/TFS-Assets/LSG/manuals/PG1572-PJT1331-COL12226-Statement-NonPathogenicity-FHR.PDF

[104] S. A. Ranveer, V. Dasriya, M. F. Ahmad, H. S. Dhillon, M. Samtiya, E. Shama, T. Anand, T. Dhewa, V. Chaudhary, P. Chaudhary, P. Behare, C. Ram, D. V. Puniya, G. D. Khedkar, A. Raposo, H. Han, and A. K. Puniya, "Positive and Negative Aspects of Bacteriophages and Their Immense Role in the Food Chain," *npj Science of Food,* vol. 8, no. 1, p. 1, 2024, doi: 10.1038/s41538-023-00245-8.

[105] Z. M. Carrico, M. E. Farkas, Y. Zhou, S. C. Hsiao, J. D. Marks, H. Chokhawala, D. S. Clark, and M. B. Francis, "N-Terminal Labeling of Filamentous Phage to Create Cancer Marker Imaging Agents," *ACS Nano,* vol. 6, no. 8, pp. 6675-6680, 2012, doi: 10.1021/nn301134z.

[106] G. P. Smith and V. A. Petrenko, "Phage Display," *Chem Rev,* Review vol. 97, no. 2, pp. 391-410, 1997, doi: 10.1021/cr960065d.

[107] D. J. Rodi and L. Makowski, "Phage-Display Technology--Finding a Needle in a Vast Molecular Haystack," *Curr Opin Biotechnol,* Review vol. 10, no. 1, pp. 87-93, 1999, doi: 10.1016/s0958-1669(99)80016-0.

[108] L. Ledsgaard, M. Kilstrup, A. Karatt-Vellatt, J. McCafferty, and A. H. Laustsen, "Basics of Antibody Phage Display Technology," *Toxins (Basel),* Review vol. 10, no. 6, 2018, doi: 10.3390/toxins10060236.

[109] L. Makowski, "Phage Display: Structure, Assembly and Engineering of Filamentous Bacteriophage M13," *Current Opinion in Structural Biology,* vol. 4, no. 2, pp. 225-230, 1994, doi: 10.1016/s0959-440x(94)90312-3.

[110] J. Rakonjac, N. J. Bennett, J. Spagnuolo, D. Gagic, and M. Russel, "Filamentous Bacteriophage: Biology, Phage Display and Nanotechnology Applications," *Curr Issues Mol Biol,* Review vol. 13, no. 2, pp. 51-76, 2011, doi: 10.21775/cimb.013.051.

[111] S. S. Sidhu, "Engineering M13 for Phage Display," *Biomol Eng,* Review vol. 18, no. 2, pp. 57-63, 2001, doi: 10.1016/s1389-0344(01)00087-9.
[112] H. M. E. Azzazy and W. E. Highsmith, "Phage Display Technology: Clinical Applications and Recent Innovations," *Clinical Biochemistry,* vol. 35, no. 6, pp. 425-445, 2002, doi: 10.1016/S0009-9120(02)00343-0.
[113] D. P. Pires, S. Cleto, S. Sillankorva, J. Azeredo, and T. K. Lu, "Genetically Engineered Phages: A Review of Advances over the Last Decade," *Microbiol Mol Biol Rev,* Review vol. 80, no. 3, pp. 523-43, 2016, doi: 10.1128/MMBR.00069-15.
[114] P. Passaretti, "M13 Bacteriophage: A Nanotool for the Fabrication of Novel Self-Assembled Nanostructures " PhD Thesis in Nanotechnology, Chemical Engineering, University of Birmingham, 2019.
[115] J. Rakonjac, "Filamentous Bacteriophages: Biology and Applications," in *Els*, pp. 1-15.
[116] O. Morag, G. Abramov, and A. Goldbourt, "Similarities and Differences within Members of the Ff Family of Filamentous Bacteriophage Viruses," *J Phys Chem B,* vol. 115, no. 51, pp. 15370-9, 2011, doi: 10.1021/jp2079742.
[117] S. M. Han, Y. J. Lee, M. H. Lee, C. W. Park, S. M. Lee, J. O. Soh, and J. H. Lee, "M13 Bacteriophage-Based Bio-Nano Systems for Bioapplication," *BioChip Journal,* vol. 16, no. 3, pp. 227-245, 2022, doi: 10.1007/s13206-022-00069-w.
[118] R. Wang, H. D. Li, Y. Cao, Z. Y. Wang, T. Yang, and J. H. Wang, "M13 Phage: A Versatile Building Block for a Highly Specific Analysis Platform," *Anal Bioanal Chem,* vol. 415, no. 18, pp. 3927-3944, 2023, doi: 10.1007/s00216-023-04606-w.
[119] C. E. Flynn, S.-W. Lee, B. R. Peelle, and A. M. Belcher, "Viruses as Vehicles for Growth, Organization and Assembly of Materials," *Acta Materialia,* Review vol. 51, no. 19, pp. 5867-5880, 2003, doi: 10.1016/j.actamat.2003.08.031.
[120] J. Ni, S.-W. Lee, J. M. White, and A. M. Belcher, "Molecular Orientation of a Zns-Nanocrystal-Modified M13 Virus on a Silicon Substrate," *Journal of Polymer Science Part B: Polymer Physics,* vol. 42, no. 4, pp. 629-635, 2004, doi: 10.1002/polb.10754.
[121] D. Andrienko, "Introduction to Liquid Crystals," *Journal of Molecular Liquids,* vol. 267, pp. 520-541, 2018, doi: 10.1016/j.molliq.2018.01.175.
[122] I. Kim, J. S. Moon, and J. W. Oh, "Recent Advances in M13 Bacteriophage-Based Optical Sensing Applications," *Nano Converg,* Review vol. 3, no. 1, p. 27, 2016, doi: 10.1186/s40580-016-0087-5.
[123] S. W. Lee, C. Mao, C. E. Flynn, and A. M. Belcher, "Ordering of Quantum Dots Using Genetically Engineered Viruses," *Science,* vol. 296, no. 5569, pp. 892-5, 2002, doi: 10.1126/science.1068054.
[124] S. K. Murthy, "Nanoparticles in Modern Medicine: State of the Art and Future Challenges," *Int J Nanomedicine,* vol. 2, no. 2, pp. 129-41, 2007.
[125] K. Paramasivam, Y. Shen, J. Yuan, I. Waheed, C. Mao, and X. Zhou, "Advances in the Development of Phage-Based Probes for Detection of Bio-Species," *Biosensors,* vol. 12, no. 1, p. 30, 2022, doi: 10.3390/bios12010030.
[126] K. T. Nam, R. Wartena, P. J. Yoo, F. W. Liau, Y. J. Lee, Y. M. Chiang, P. T. Hammond, and A. M. Belcher, "Stamped Microbattery Electrodes Based on

Self-Assembled M13 Viruses," *Proc Natl Acad Sci U S A,* vol. 105, no. 45, pp. 17227-31, 2008, doi: 10.1073/pnas.0711620105.

[127] X. Wang, T. Yang, X. Zhang, M. Chen, and J. Wang, "In Situ Growth of Gold Nanoparticles on Hg(2+)-Binding M13 Phages for Mercury Sensing," *Nanoscale,* vol. 9, no. 43, pp. 16728-16734, 2017, doi: 10.1039/c7nr06292c.

[128] S. Zhang, K. Nakano, S.-l. Zhang, and H.-m. Yu, "Synthesis of Dispersive Iron or Iron–Silver Nanoparticles on Engineered Capsid Pviii of M13 Virus with Electronegative Terminal Peptides," *Journal of Nanoparticle Research,* vol. 17, no. 10, 2015, doi: 10.1007/s11051-015-3221-0.

[129] K. N. Avery, J. E. Schaak, and R. E. Schaak, "M13 Bacteriophage as a Biological Scaffold for Magnetically-Recoverable Metal Nanowire Catalysts: Combining Specific and Nonspecific Interactions to Design Multifunctional Nanocomposites," *Chemistry of Materials,* vol. 21, no. 11, pp. 2176-2178, 2009, doi: 10.1021/cm900869u.

[130] S. K. Lee, D. S. Yun, and A. M. Belcher, "Cobalt Ion Mediated Self-Assembly of Genetically Engineered Bacteriophage for Biomimetic Co-Pt Hybrid Material," *Biomacromolecules,* vol. 7, no. 1, pp. 14-7, 2006, doi: 10.1021/bm050691x.

[131] E. R. Essinger-Hileman, D. DeCicco, J. F. Bondi, and R. E. Schaak, "Aqueous Room-Temperature Synthesis of Au–Rh, Au–Pt, Pt–Rh, and Pd–Rh Alloy Nanoparticles: Fully Tunable Compositions within the Miscibility Gaps," *Journal of Materials Chemistry,* 10.1039/C0JM03913F vol. 21, no. 31, pp. 11599-11604, 2011, doi: 10.1039/C0JM03913F.

[132] J. M. Plank, Z. Alibay, T.-T. Ngo-Duc, M. Lai, E. A. S. Mayes, and E. D. Haberer, "Bifunctional M13 Bacteriophage Nanospheroids for the Synthesis of Hybrid Noncentrosymmetric Nanoparticles," *ACS Applied Nano Materials,* vol. 3, no. 11, pp. 10668-10677, 2020, doi: 10.1021/acsanm.0c01876.

[133] R. Choubey, N. Sonker, J. Bajpai, P. Jain, and A. Singh, "Synthesis of Polymer Nanomaterials, Mechanisms, and Their Structural Control," in *Advances in Polymeric Nanomaterials for Biomedical Applications*, A. K. Bajpai and R. K. Saini Eds.: Elsevier, 2021, ch. 2, pp. 41-63.

[134] D. Pisignano, L. Persano, and A. Camposeo, "Perspectives: Nanofibers and Nanowires for Disordered Photonics," *APL Materials,* vol. 5, no. 3, 2017, doi: 10.1063/1.4974481.

[135] O. Inal, U. Badilli, A. S. Ozkan, and F. Mollarasouli, "Bioactive Hybrid Nanowires for Drug Delivery," in *Hybrid Nanomaterials for Drug Delivery*, P. Kesharwani and N. K. Jain Eds.: Woodhead Publishing, 2022, ch. 11, pp. 269-301.

[136] E. D. Haberer, J. H. Joo, J. F. Hodelin, and E. L. Hu, "Enhanced Photogenerated Carrier Collection in Hybrid Films of Bio-Templated Gold Nanowires and Nanocrystalline Cdse," *Nanotechnology,* vol. 20, no. 41, p. 415206, 2009, doi: 10.1088/0957-4484/20/41/415206.

[137] J. H. Joo, J. F. Hodelin, E. L. Hu, and E. D. Haberer, "Viral-Assisted Assembly and Photoelectric Response of Individual Au/Cdse Core–Shell Nanowires," *Materials Letters,* vol. 89, pp. 347-350, 2012, doi: 10.1016/j.matlet.2012.09.001.

[138] Y. Huang, C. Y. Chiang, S. K. Lee, Y. Gao, E. L. Hu, J. De Yoreo, and A. M. Belcher, "Programmable Assembly of Nanoarchitectures Using Genetically Engineered Viruses," *Nano Lett,* vol. 5, no. 7, pp. 1429-34, 2005, doi: 10.1021/nl050795d.

[139] J. Han, J.-S. Nam, K. Kim, E. J. Choi, J.-M. Lee, S. Maruyama, I. Jeon, and J.-W. Oh, "M13 Bacteriophage-Templated Gold Nanowires as Stretchable Electrodes in Perovskite Solar Cells," *Materials Advances,* 10.1039/D0MA00935K vol. 2, no. 1, pp. 488-496, 2021, doi: 10.1039/D0MA00935K.

[140] C. Mao, C. E. Flynn, A. Hayhurst, R. Sweeney, J. Qi, G. Georgiou, B. Iverson, and A. M. Belcher, "Viral Assembly of Oriented Quantum Dot Nanowires," *Proc Natl Acad Sci U S A,* vol. 100, no. 12, pp. 6946-51, 2003, doi: 10.1073/pnas.0832310100.

[141] C. Mao, D. J. Solis, B. D. Reiss, S. T. Kottmann, R. Y. Sweeney, A. Hayhurst, G. Georgiou, B. Iverson, and A. M. Belcher, "Virus-Based Toolkit for the Directed Synthesis of Magnetic and Semiconducting Nanowires," *Science,* vol. 303, no. 5655, pp. 213-7, 2004, doi: 10.1126/science.1092740.

[142] D. K. Loke, G. J. Clausen, J. F. Ohmura, T.-C. Chong, and A. M. Belcher, "Biological-Templating of a Segregating Binary Alloy for Nanowire-Like Phase-Change Materials and Memory," *ACS Applied Nano Materials,* vol. 1, no. 12, pp. 6556-6562, 2018, doi: 10.1021/acsanm.8b01508.

[143] M. Ramalingam and S. Ramakrishna, "Introduction to Nanofiber Composites," in *Nanofiber Composites for Biomedical Applications*, M. Ramalingam and S. Ramakrishna Eds.: Woodhead Publishing, 2017, ch. 1, pp. 3-29.

[144] Y. Cai, Q. Wei, and F. Huang, "Processing of Composite Functional Nanofibers," in *Functional Nanofibers and Their Applications*, Q. Wei Ed.: Woodhead Publishing, 2012, ch. 3, pp. 38-54.

[145] S.-W. Lee and A. M. Belcher, "Virus-Based Fabrication of Micro- and Nanofibers Using Electrospinning," *Nano Letters,* vol. 4, no. 3, pp. 387-390, 2004, doi: 10.1021/nl034911t.

[146] Y. C. Shin, J. H. Lee, L. Jin, M. J. Kim, J. W. Oh, T. W. Kim, and D. W. Han, "Cell-Adhesive Rgd Peptide-Displaying M13 Bacteriophage/Plga Nanofiber Matrices for Growth of Fibroblasts," *Biomater Res,* vol. 18, p. 14, 2014, doi: 10.1186/2055-7124-18-14.

[147] R. Sugimoto, J. H. Lee, J.-H. Lee, H.-E. Jin, S. Y. Yoo, and S.-W. Lee, "Bacteriophage Nanofiber Fabrication Using near Field Electrospinning," *RSC Advances,* 10.1039/C9RA07510K vol. 9, no. 67, pp. 39111-39118, 2019, doi: 10.1039/C9RA07510K.

[148] C. Y. Chiang, C. M. Mello, J. Gu, E. C. C. M. Silva, K. J. Van Vliet, and A. M. Belcher, "Weaving Genetically Engineered Functionality into Mechanically Robust Virus Fibers," *Advanced Materials,* vol. 19, no. 6, pp. 826-832, 2007, doi: 10.1002/adma.200602262.

[149] Z. Niu, M. A. Bruckman, B. Harp, C. M. Mello, and Q. Wang, "Bacteriophage M13 as a Scaffold for Preparing Conductive Polymeric Composite Fibers," *Nano Research,* vol. 1, no. 3, pp. 235-241, 2008, doi: 10.1007/s12274-008-8027-2.

[150] T. Yu, Y. Li, T. Yang, Y. Gong, H. G. Sudibya, P. Chen, K. Q. Luo, and K. Liao, "Fabrication of All-in-One Multifunctional Phage Liquid Crystalline Fibers," *RSC Advances,* vol. 3, no. 43, 2013, doi: 10.1039/c3ra43034k.

[151] T. He, G. Abbineni, B. Cao, and C. Mao, "Nanofibrous Bio-Inorganic Hybrid Structures Formed through Self-Assembly and Oriented Mineralization of Genetically Engineered Phage Nanofibers," *Small,* vol. 6, no. 20, pp. 2230-2235, 2010, doi: 10.1002/smll.201001108.

[152] F. Wang, B. Cao, and C. Mao, "Bacteriophage Bundles with Prealigned Ca2+ Initiate the Oriented Nucleation and Growth of Hydroxylapatite," *Chemistry of Materials,* vol. 22, no. 12, pp. 3630-3636, 2010, doi: 10.1021/cm902727s.
[153] E. Alberts, C. Warner, E. Barnes, K. Pilkiewicz, E. Perkins, and A. Poda, "Genetically Tunable M13 Phage Films Utilizing Evaporating Droplets," *Colloids Surf B Biointerfaces,* vol. 161, pp. 210-218, 2018, doi: 10.1016/j.colsurfb.2017.10.039.
[154] S. M. Park, W.-G. Kim, J. Kim, E.-J. Choi, H. Kim, J.-W. Oh, and D. K. Yoon, "Fabrication of Chiral M13 Bacteriophage Film by Evaporation-Induced Self-Assembly," *Small,* vol. 17, no. 26, p. 2008097, 2021, doi: 10.1002/smll.202008097.
[155] F. Causa, R. Della Moglie, E. Iaccino, S. Mimmi, D. Marasco, P. L. Scognamiglio, E. Battista, C. Palmieri, C. Cosenza, L. Sanguigno, I. Quinto, G. Scala, and P. A. Netti, "Evolutionary Screening and Adsorption Behavior of Engineered M13 Bacteriophage and Derived Dodecapeptide for Selective Decoration of Gold Interfaces," *J Colloid Interface Sci,* vol. 389, no. 1, pp. 220-9, 2013, doi: 10.1016/j.jcis.2012.08.046.
[156] Y. Sun, Y. Li, B. Wu, J. Wang, X. Lu, S. Qu, J. Weng, and B. Feng, "Biological Responses to M13 Bacteriophage Modified Titanium Surfaces in Vitro," *Acta Biomater,* vol. 58, pp. 527-538, 2017, doi: 10.1016/j.actbio.2017.06.019.
[157] Y. Sun, J. Tan, B. Wu, J. Wang, S. Qu, J. Weng, and B. Feng, "Identification and Binding Mechanism of Phage Displayed Peptides with Specific Affinity to Acid-Alkali Treated Titanium," *Colloids Surf B Biointerfaces,* vol. 146, pp. 307-17, 2016, doi: 10.1016/j.colsurfb.2016.06.032.
[158] Y. Sun, C. Yang, B. Wu, J. Wang, S. Qu, J. Weng, and B. Feng, "Fabrication of Nanostructured M13 Bacteriophage Films on Titanium Surfaces," *Materials Letters,* vol. 182, pp. 39-42, 2016, doi: 10.1016/j.matlet.2016.06.078.
[159] C. Warner, A. Ghoshal, M. Cuddy, A. Poda, N. Barker, D. Morse, S.-W. Lee, and E. Perkins, "M13 Bacteriophage Biolaminates for Nanomaterials with Improved Stiffness," *MRS Proceedings,* vol. 1722, 2015, doi: 10.1557/opl.2015.603.
[160] K. C. Donavan, J. A. Arter, G. A. Weiss, and R. M. Penner, "Virus-Poly(3,4-Ethylenedioxythiophene) Biocomposite Films," *Langmuir,* vol. 28, no. 34, pp. 12581-7, 2012, doi: 10.1021/la302473j.
[161] P. J. Yoo, W.-S. Choe, Y. H. Kim, and Y. M. Lee, "Physically and Chemically Confined Nano-Patterns of Proteins and Bacteriophages," *Materials Express,* vol. 1, no. 1, pp. 51-58, 2011, doi: 10.1166/mex.2011.1007.
[162] S. Chung, W. J. Chung, D. Wang, S. W. Lee, and J. J. De Yoreo, "Growth of Au and Zns Nanostructures Via Engineered Peptide and M13 Bacteriophage Templates," *Soft Matter,* vol. 14, no. 16, pp. 2996-3002, 2018, doi: 10.1039/c8sm00090e.
[163] P. J. Yoo, K. T. Nam, J. Qi, S. K. Lee, J. Park, A. M. Belcher, and P. T. Hammond, "Spontaneous Assembly of Viruses on Multilayered Polymer Surfaces," *Nat Mater,* vol. 5, no. 3, pp. 234-40, 2006, doi: 10.1038/nmat1596.
[164] P. J. Yoo, K. T. Nam, A. M. Belcher, and P. T. Hammond, "Solvent-Assisted Patterning of Polyelectrolyte Multilayers and Selective Deposition of Virus Assemblies," *Nano Lett,* vol. 8, no. 4, pp. 1081-9, 2008, doi: 10.1021/nl073079f.

[165] V. Devaraj, J. Han, C. Kim, Y. C. Kang, and J. W. Oh, "Self-Assembled Nanoporous Biofilms from Functionalized Nanofibrous M13 Bacteriophage," *Viruses,* vol. 10, no. 6, 2018, doi: 10.3390/v10060322.
[166] A. S. Hoffman, "Hydrogels for Biomedical Applications," *Advanced Drug Delivery Reviews,* vol. 64, pp. 18-23, 2012, doi: 10.1016/j.addr.2012.09.010.
[167] K. Jackson, A. Peivandi, M. Fogal, L. Tian, and Z. Hosseinidoust, "Filamentous Phages as Building Blocks for Bioactive Hydrogels," *ACS Applied Bio Materials,* vol. 4, no. 3, pp. 2262-2273, 2021, doi: 10.1021/acsabm.0c01557.
[168] R. Foudazi, R. Zowada, I. Manas-Zloczower, and D. L. Feke, "Porous Hydrogels: Present Challenges and Future Opportunities," *Langmuir,* vol. 39, no. 6, pp. 2092-2111, 2023, doi: 10.1021/acs.langmuir.2c02253.
[169] P. Y. Chen, M. N. Hyder, D. Mackanic, N. M. Courchesne, J. Qi, M. T. Klug, A. M. Belcher, and P. T. Hammond, "Assembly of Viral Hydrogels for Three-Dimensional Conducting Nanocomposites," *Adv Mater,* vol. 26, no. 30, pp. 5101-7, 2014, doi: 10.1002/adma.201400828.
[170] W. Qi and H. Yu, "Virus-Templated Magnetic Composite Hydrogels for Surface Immobilization of Mimic-Free-Lipase," *Nanoscale,* 10.1039/D1NR03571A vol. 13, no. 42, pp. 17871-17880, 2021, doi: 10.1039/D1NR03571A.
[171] Y. Wang, X. Zheng, W. Zhong, Z. Ye, X. Wang, Z. Dong, and Z. Zhang, "Multicomponent Chiral Hydrogel Fibers with Block Configurations Based on the Chiral Liquid Crystals of Cellulose Nanocrystals and M13 Bacteriophages," *Polymer Chemistry,* 10.1039/D2PY00965J vol. 13, no. 36, pp. 5200-5211, 2022, doi: 10.1039/D2PY00965J.
[172] A. Peivandi, L. Tian, R. Mahabir, and Z. Hosseinidoust, "Hierarchically Structured, Self-Healing, Fluorescent, Bioactive Hydrogels with Self-Organizing Bundles of Phage Nanofilaments," *Chemistry of Materials,* vol. 31, no. 15, pp. 5442-5449, 2019, doi: 10.1021/acs.chemmater.9b00720.
[173] A. Peivandi, K. Jackson, L. Tian, L. He, A. Mahmood, C. Fradin, and Z. Hosseinidoust, "Inducing Microscale Structural Order in Phage Nanofilament Hydrogels with Globular Proteins," *ACS Biomaterials Science & Engineering,* vol. 8, no. 1, pp. 340-347, 2022, doi: 10.1021/acsbiomaterials.1c01112.
[174] T. Sawada, S. Kang, J. Watanabe, H. Mihara, and T. Serizawa, "Hybrid Hydrogels Composed of Regularly Assembled Filamentous Viruses and Gold Nanoparticles," *ACS Macro Letters,* vol. 3, no. 4, pp. 341-345, 2014, doi: 10.1021/mz500073t.
[175] T. Sawada, H. Otsuka, H. Yui, and T. Serizawa, "Preparation and Characterization of Hybrid Hydrogels Composed of Physically Cross-Linked Gelatin and Liquid-Crystalline Filamentous Viruses," *Polymer Bulletin,* vol. 72, no. 6, pp. 1487-1496, 2015, doi: 10.1007/s00289-015-1350-3.
[176] T. Sawada, M. Yanagimachi, and T. Serizawa, "Controlled Release of Antibody Proteins from Liquid Crystalline Hydrogels Composed of Genetically Engineered Filamentous Viruses," *Materials Chemistry Frontiers,* 10.1039/C6QM00140H vol. 1, no. 1, pp. 146-151, 2017, doi: 10.1039/C6QM00140H.
[177] C. Erkey and M. Türk, "Support Materials," in *Supercritical Fluid Science and Technology*, vol. 8, C. Erkey and M. Türk Eds.: Elsevier, 2021, ch. 3, pp. 19-30.

[178] M. T. Noman, N. Amor, A. Ali, S. Petrik, R. Coufal, K. Adach, and M. Fijalkowski, "Aerogels for Biomedical, Energy and Sensing Applications," *Gels,* vol. 7, no. 4, 2021, doi: 10.3390/gels7040264.
[179] S. M. Jung, J. Qi, D. Oh, A. Belcher, and J. Kong, "M13 Virus Aerogels as a Scaffold for Functional Inorganic Materials," *Advanced Functional Materials,* vol. 27, no. 4, 2017, doi: 10.1002/adfm.201603203.
[180] T.-G. Cha, U. Tsedev, A. Ransil, A. Embree, D. B. Gordon, A. M. Belcher, and C. A. Voigt, "Genetic Control of Aerogel and Nanofoam Properties, Applied to Ni–Mnox Cathode Design," *Advanced Functional Materials,* vol. 31, no. 35, p. 2010867, 2021, doi: 10.1002/adfm.202010867.
[181] G. Wang, P. Yuan, B. Ma, W. Yuan, and J. Luo, "Hierarchically Structured M13 Phage Aerogel for Enhanced Sound-Absorption," *Macromolecular Materials and Engineering,* vol. 305, no. 11, p. 2000452, 2020, doi: 10.1002/mame.202000452.
[182] G. Wang, B. Ma, W. Yuan, and J. Luo, "Microperforated Metasurface Panel Backed by Aerogel-Filled Cavities for Broadband Low Frequency Sound Absorption," *Applied Acoustics,* vol. 208, p. 109377, 2023, doi: 10.1016/j.apacoust.2023.109377.
[183] S. S. Panda, H. E. Katz, and J. D. Tovar, "Solid-State Electrical Applications of Protein and Peptide Based Nanomaterials," *Chem Soc Rev,* Review vol. 47, no. 10, pp. 3640-3658, 2018, doi: 10.1039/c7cs00817a.
[184] B. Y. Lee, J. Zhang, C. Zueger, W. J. Chung, S. Y. Yoo, E. Wang, J. Meyer, R. Ramesh, and S. W. Lee, "Virus-Based Piezoelectric Energy Generation," *Nat Nanotechnol,* vol. 7, no. 6, pp. 351-6, 2012, doi: 10.1038/nnano.2012.69.
[185] J. Li, Y. Long, F. Yang, and X. Wang, "Degradable Piezoelectric Biomaterials for Wearable and Implantable Bioelectronics," *Curr Opin Solid State Mater Sci,* Review vol. 24, no. 1, 2020, doi: 10.1016/j.cossms.2020.100806.
[186] D.-M. Shin, H. J. Han, W.-G. Kim, E. Kim, C. Kim, S. W. Hong, H. K. Kim, J.-W. Oh, and Y.-H. Hwang, "Bioinspired Piezoelectric Nanogenerators Based on Vertically Aligned Phage Nanopillars," *Energy & Environmental Science,* vol. 8, no. 11, pp. 3198-3203, 2015, doi: 10.1039/c5ee02611c.
[187] Y. Yan, X. Ma, T. M. Nguyen, S.-H. Ha, H. Ahn, D. Aben, K. Kim, J.-M. Kim, J.-W. Oh, D.-M. Shin, and Y.-H. Hwang, "Quadrant-Electroded Nanogenerators for Decoupling Piezoelectricity and Flexoelectricity in the Electromechanical Outputs in Flexible Devices," *Nano Energy,* vol. 104, p. 107909, 2022, doi: 10.1016/j.nanoen.2022.107909.
[188] K. Cung, B. J. Han, T. D. Nguyen, S. Mao, Y.-W. Yeh, S. Xu, R. R. Naik, G. Poirier, N. Yao, P. K. Purohit, and M. C. McAlpine, "Biotemplated Synthesis of Pzt Nanowires," *Nano Letters,* vol. 13, no. 12, pp. 6197-6202, 2013, doi: 10.1021/nl4035708.
[189] S. Kilper, T. Jahnke, M. Aulich, Z. Burghard, D. Rothenstein, and J. Bill, "Genetically Induced in Situ-Poling for Piezo-Active Biohybrid Nanowires," *Adv Mater,* vol. 31, no. 6, p. e1805597, 2019, doi: 10.1002/adma.201805597.
[190] M. Liu, T. Yu, R. Huang, W. Qi, Z. He, and R. Su, "Fabrication of Nanohybrids Assisted by Protein-Based Materials for Catalytic Applications," *Catalysis Science & Technology,* vol. 10, no. 11, pp. 3515-3531, 2020, doi: 10.1039/c9cy02466b.

[191] S. Zhang, H. Yu, J. Yang, and Z. Shen, "Design of the Nanoarray Pattern Fe–Ni Bi-Metal Nanoparticles@M13 Virus for the Enhanced Reduction of P-Chloronitrobenzene through the Micro-Electrolysis Effect," *Environmental Science: Nano,* vol. 4, no. 4, pp. 876-885, 2017, doi: 10.1039/c7en00120g.
[192] H. Fang, S. Zhan, L. Feng, X. Chen, Q. Guo, Y. Guo, Q. He, and Y. Xiong, "Chemical Modification of M13 Bacteriophage as Nanozyme Container for Dramatically Enhanced Sensitivity of Colorimetric Immunosensor," *Sensors and Actuators B: Chemical,* vol. 346, 2021, doi: 10.1016/j.snb.2021.130368.
[193] D. Jeon, J. Park, C. Shin, H. Kim, J.-W. Jang, D. W. Lee, and J. Ryu, "Superaerophobic Hydrogels for Enhanced Electrochemical and Photoelectrochemical Hydrogen Production," *Science Advances,* vol. 6, no. 15, p. eaaz3944, 2020, doi: 10.1126/sciadv.aaz3944.
[194] W. C. Records, Y. Yoon, J. F. Ohmura, N. Chanut, and A. M. Belcher, "Virus-Templated Pt–Ni(Oh)2 Nanonetworks for Enhanced Electrocatalytic Reduction of Water," *Nano Energy,* vol. 58, pp. 167-174, 2019, doi: 10.1016/j.nanoen.2018.12.083.
[195] D. Vilona, R. Di Lorenzo, M. Carraro, G. Licini, L. Trainotti, and M. Bonchio, "Viral Nano-Hybrids for Innovative Energy Conversion and Storage Schemes," *J Mater Chem B,* Review vol. 3, no. 33, pp. 6718-6730, 2015, doi: 10.1039/c5tb00924c.
[196] W. Jo, U. K. Cheang, and M. J. Kim, "Development of Flagella Bio-Templated Nanomaterials for Electronics," *Nano Converg,* Review vol. 1, no. 1, p. 10, 2014, doi: 10.1186/s40580-014-0010-x.
[197] P.-Y. Chen, R. Ladewski, R. Miller, X. Dang, J. Qi, F. Liau, A. M. Belcher, and P. T. Hammond, "Layer-by-Layer Assembled Porous Photoanodes for Efficient Electron Collection in Dye-Sensitized Solar Cells," *J. Mater. Chem. A,* vol. 1, no. 6, pp. 2217-2224, 2013, doi: 10.1039/c2ta00771a.
[198] X. Dang, H. Yi, M. H. Ham, J. Qi, D. S. Yun, R. Ladewski, M. S. Strano, P. T. Hammond, and A. M. Belcher, "Virus-Templated Self-Assembled Single-Walled Carbon Nanotubes for Highly Efficient Electron Collection in Photovoltaic Devices," *Nat Nanotechnol,* vol. 6, no. 6, pp. 377-84, 2011, doi: 10.1038/nnano.2011.50.
[199] Y. S. Nam, T. Shin, H. Park, A. P. Magyar, K. Choi, G. Fantner, K. A. Nelson, and A. M. Belcher, "Virus-Templated Assembly of Porphyrins into Light-Harvesting Nanoantennae," *Journal of the American Chemical Society,* vol. 132, no. 5, pp. 1462-+, 2010, doi: 10.1021/ja908812b.
[200] H. Park, N. Heldman, P. Rebentrost, L. Abbondanza, A. Iagatti, A. Alessi, B. Patrizi, M. Salvalaggio, L. Bussotti, M. Mohseni, F. Caruso, H. C. Johnsen, R. Fusco, P. Foggi, P. F. Scudo, S. Lloyd, and A. M. Belcher, "Enhanced Energy Transport in Genetically Engineered Excitonic Networks," *Nat Mater,* vol. 15, no. 2, pp. 211-6, 2016, doi: 10.1038/nmat4448.
[201] N. Nuraje, X. Dang, J. Qi, M. A. Allen, Y. Lei, and A. M. Belcher, "Biotemplated Synthesis of Perovskite Nanomaterials for Solar Energy Conversion," *Adv Mater,* vol. 24, no. 21, pp. 2885-9, 2012, doi: 10.1002/adma.201200114.
[202] H.-S. Lin, J.-M. Lee, J. Han, C. Lee, S. Seo, S. Tan, H. M. Lee, E. J. Choi, M. S. Strano, Y. Yang, S. Maruyama, I. Jeon, Y. Matsuo, and J.-W. Oh, "Denatured M13 Bacteriophage-Templated Perovskite Solar Cells Exhibiting High

Efficiency," *Advanced Science,* vol. 7, no. 20, p. 2000782, 2020, doi: 10.1002/advs.202000782.

[203] N. Kumar, H. B. Lee, B. Tyagi, M. M. Ovhal, S. Cho, J.-S. Lee, J.-W. Oh, and J.-W. Kang, "Spray-Deposited, Virus-Templated Sno2 Mesoporous Electron Transport Layer for High-Efficiency, Sequential-Deposited Perovskite Solar Cells," *Solar RRL,* vol. 7, no. 13, p. 2300065, 2023, doi: 10.1002/solr.202300065.

[204] K. T. Nam, D. W. Kim, P. J. Yoo, C. Y. Chiang, N. Meethong, P. T. Hammond, Y. M. Chiang, and A. M. Belcher, "Virus-Enabled Synthesis and Assembly of Nanowires for Lithium Ion Battery Electrodes," *Science,* vol. 312, no. 5775, pp. 885-8, 2006, doi: 10.1126/science.1122716.

[205] S. Kim, Y. Lim, T.-H. Kang, J. Moon, I.-S. Choi, Y. J. Lee, and H. Yi, "Biotemplated Nanocomposites of Transition-Metal Oxides/Carbon Nanotubes with Highly Stable and Efficient Electrochemical Interfaces for High-Power Lithium-Ion Batteries," *ACS Applied Energy Materials,* vol. 3, no. 8, pp. 7804-7812, 2020, doi: 10.1021/acsaem.0c01208.

[206] Y. J. Lee, H. Yi, W. J. Kim, K. Kang, D. S. Yun, M. S. Strano, G. Ceder, and A. M. Belcher, "Fabricating Genetically Engineered High-Power Lithium-Ion Batteries Using Multiple Virus Genes," *Science,* vol. 324, no. 5930, pp. 1051-5, 2009, doi: 10.1126/science.1171541.

[207] Y. J. Lee, Y. Lee, D. Oh, T. Chen, G. Ceder, and A. M. Belcher, "Biologically Activated Noble Metal Alloys at the Nanoscale: For Lithium Ion Battery Anodes," *Nano Lett,* vol. 10, no. 7, pp. 2433-40, 2010, doi: 10.1021/nl1005993.

[208] D. Dong, Y. Zhang, S. Sutaria, A. Konarov, and P. Chen, "Binding Mechanism and Electrochemical Properties of M13 Phage-Sulfur Composite," *PLoS One,* vol. 8, no. 11, p. e82332, 2013, doi: 10.1371/journal.pone.0082332.

[209] G. Zhang, S. Wei, and A. M. Belcher, "Biotemplated Zinc Sulfide Nanofibers as Anode Materials for Sodium-Ion Batteries," *ACS Applied Nano Materials,* vol. 1, no. 10, pp. 5631-5639, 2018, doi: 10.1021/acsanm.8b01254.

[210] D. Oh, J. Qi, Y. C. Lu, Y. Zhang, Y. Shao-Horn, and A. M. Belcher, "Biologically Enhanced Cathode Design for Improved Capacity and Cycle Life for Lithium-Oxygen Batteries," *Nat Commun,* vol. 4, p. 2756, 2013, doi: 10.1038/ncomms3756.

[211] S. Pakseresht, A. W. M. Al-Ogaili, T. Cetinkaya, M. Celik, and H. Akbulut, "Prevention of Side Reactions with a Unique Carbon-Free Catalyst Biosynthesized by a Virus Template for Non-Aqueous and Quasi-Solid-State Li–O2 Batteries," *Journal of Power Sources,* vol. 509, 2021, doi: 10.1016/j.jpowsour.2021.230374.

[212] K. B. Shivaram, P. Bhatt, M. S. Verma, K. Clase, and H. Simsek, "Bacteriophage-Based Biosensors for Detection of Pathogenic Microbes in Wastewater," *Science of The Total Environment,* vol. 901, p. 165859, 2023, doi: 10.1016/j.scitotenv.2023.165859.

[213] S. J. Machera, J. Niedziółka-Jönsson, and K. Szot-Karpińska, "Phage-Based Sensors in Medicine: A Review," *Chemosensors,* Review vol. 8, no. 3, 2020, doi: 10.3390/chemosensors8030061.

[214] J. Xu, Y. Chau, and Y. K. Lee, "Phage-Based Electrochemical Sensors: A Review," *Micromachines (Basel),* vol. 10, no. 12, 2019, doi: 10.3390/mi10120855.

[215] R. R. Al-Hindi, A. D. Teklemariam, M. G. Alharbi, I. Alotibi, S. A. Azhari, I. Qadri, T. Alamri, S. Harakeh, B. M. Applegate, and A. K. Bhunia, "Bacteriophage-Based Biosensors: A Platform for Detection of Foodborne Bacterial Pathogens from Food and Environment," *Biosensors (Basel),* vol. 12, no. 10, 2022, doi: 10.3390/bios12100905.

[216] R. Peltomaa, I. Lopez-Perolio, E. Benito-Pena, R. Barderas, and M. C. Moreno-Bondi, "Application of Bacteriophages in Sensor Development," *Anal Bioanal Chem,* Review vol. 408, no. 7, pp. 1805-28, 2016, doi: 10.1007/s00216-015-9087-2.

[217] M. Kochetkova, I. Timofeeva, D. Frolova, and A. Bulatov, "Low-Cost Digital Colorimetric Sensor for Rapid on-Site Determination of Ascorbic Acid in Vegetable- and Fruit-Based Purees and Juices," *Journal of Food Composition and Analysis,* vol. 137, p. 106920, 2025, doi: 10.1016/j.jfca.2024.106920.

[218] J. S. Moon, W. G. Kim, C. Kim, G. T. Park, J. Heo, S. Y. Yoo, and J. W. Oh, "M13 Bacteriophage-Based Self-Assembly Structures and Their Functional Capabilities," *Mini Rev Org Chem,* vol. 12, no. 3, pp. 271-281, 2015, doi: 10.2174/1570193x1203150429105418.

[219] L. Wang, Y. Sun, Z. Li, A. Wu, and G. Wei, "Bottom-up Synthesis and Sensor Applications of Biomimetic Nanostructures," *Materials (Basel),* Review vol. 9, no. 1, 2016, doi: 10.3390/ma9010053.

[220] W. J. Chung, J. W. Oh, K. Kwak, B. Y. Lee, J. Meyer, E. Wang, A. Hexemer, and S. W. Lee, "Biomimetic Self-Templating Supramolecular Structures," *Nature,* vol. 478, no. 7369, pp. 364-8, 2011, doi: 10.1038/nature10513.

[221] S.-J. Kim, Y. Lee, E. J. Choi, J.-M. Lee, K. H. Kim, and J.-W. Oh, "The Development Progress of Multi-Array Colourimetric Sensors Based on the M13 Bacteriophage," *Nano Convergence,* vol. 10, no. 1, p. 1, 2023, doi: 10.1186/s40580-022-00351-5.

[222] J. S. Moon, W. G. Kim, D. M. Shin, S. Y. Lee, C. Kim, Y. Lee, J. Han, K. Kim, S. Y. Yoo, and J. W. Oh, "Bioinspired M-13 Bacteriophage-Based Photonic Nose for Differential Cell Recognition," *Chem Sci,* vol. 8, no. 2, pp. 921-927, 2017, doi: 10.1039/c6sc02021f.

[223] K. H. Kim, T. M. Nguyen, S. H. Ha, E. J. Choi, Y. Kim, W. G. Kim, J. W. Oh, and J. M. Kim, "M13 Bacteriophage-Assisted Morphological Engineering of Crack-Based Sensors for Highly Sensitive and Wide Linear Range Strain Sensing," *ACS Appl Mater Interfaces,* 2020, doi: 10.1021/acsami.0c13307.

[224] D. Seol, D. Jang, J. W. Oh, K. Cha, and H. Chung, "Discrimination of Phthalate Species Using a Simple Phage-Based Colorimetric Sensor in Conjunction with Hierarchical Support Vector Machine," *Environ Res,* vol. 170, pp. 238-242, 2019, doi: 10.1016/j.envres.2018.12.030.

[225] J.-S. Moon, J. Choi, Y.-H. Hwang, and J.-W. Oh, "Liquid Sensing of a M-13 Bacteriophage-Based Colorimetric Sensor," *Macromolecular Research,* vol. 26, no. 9, pp. 775-779, 2018, doi: 10.1007/s13233-018-6079-z.

[226] J. W. Oh, W. J. Chung, K. Heo, H. E. Jin, B. Y. Lee, E. Wang, C. Zueger, W. Wong, J. Meyer, C. Kim, S. Y. Lee, W. G. Kim, M. Zemla, M. Auer, A. Hexemer, and S. W. Lee, "Biomimetic Virus-Based Colourimetric Sensors," *Nat Commun,* vol. 5, p. 3043, 2014, doi: 10.1038/ncomms4043.

[227] J.-M. Lee, V. Devaraj, N.-N. Jeong, Y. Lee, Y.-J. Kim, T. Kim, S. H. Yi, W.-G. Kim, E. J. Choi, H.-M. Kim, C. L. Chang, C. Mao, and J.-W. Oh, "Neural

Mechanism Mimetic Selective Electronic Nose Based on Programmed M13 Bacteriophage," *Biosensors and Bioelectronics,* vol. 196, p. 113693, 2022, doi: 10.1016/j.bios.2021.113693.

[228] S. Manivannan, Y. Seo, D.-K. Kang, and K. Kim, "Colorimetric and Optical Hg(Ii) Ion Sensor Developed with Conjugates of M13-Bacteriophage and Silver Nanoparticles," *New Journal of Chemistry,* vol. 42, no. 24, pp. 20007-20014, 2018, doi: 10.1039/c8nj04496a.

[229] S. Manivannan, S. Park, J. Jeong, and K. Kim, "Aggregation-Free Optical and Colorimetric Detection of Hg(Ii) with M13 Bacteriophage-Templated Au Nanowires," *Biosens Bioelectron,* vol. 161, p. 112237, 2020, doi: 10.1016/j.bios.2020.112237.

[230] B. Liedberg, I. Lundström, and E. Stenberg, "Principles of Biosensing with an Extended Coupling Matrix and Surface Plasmon Resonance," *Sensors and Actuators B: Chemical,* vol. 11, no. 1-3, pp. 63-72, 1993, doi: 10.1016/0925-4005(93)85239-7.

[231] H. H. Nguyen, J. Park, S. Kang, and M. Kim, "Surface Plasmon Resonance: A Versatile Technique for Biosensor Applications," *Sensors (Basel),* vol. 15, no. 5, pp. 10481-510, 2015, doi: 10.3390/s150510481.

[232] X. Y. Wang, T. Yang, S. Y. Wang, K. D. Du, M. L. Chen, and J. H. Wang, "M13 Phage as Network Frame for the Quantification of Pb(2+) Based on the Pb(2+)-Induced in-Situ Growth of Gold Nanoparticles," *Anal Chim Acta,* vol. 1073, pp. 72-78, 2019, doi: 10.1016/j.aca.2019.04.065.

[233] H. Peng and I. A. Chen, "Rapid Colorimetric Detection of Bacterial Species through the Capture of Gold Nanoparticles by Chimeric Phages," *ACS Nano,* vol. 13, no. 2, pp. 1244-1252, 2019, doi: 10.1021/acsnano.8b06395.

[234] J. Hou, X. Qian, Y. Xu, Z. Guo, B. Thierry, C.-T. Yang, X. Zhou, and C. Mao, "Rapid and Reliable Ultrasensitive Detection of Pathogenic H9n2 Viruses through Virus-Binding Phage Nanofibers Decorated with Gold Nanoparticles," *Biosensors and Bioelectronics,* vol. 237, p. 115423, 2023, doi: 10.1016/j.bios.2023.115423.

[235] J. Hou, Y. Xu, S. Sun, X. Zhong, C.-T. Yang, and X. Zhou, "Gold Nanoparticles-Decorated M13 Phage Spr Probe for Dual Detection of Antigen Biomarkers in Serum," *Sensors and Actuators B: Chemical,* vol. 374, p. 132811, 2023, doi: 10.1016/j.snb.2022.132811.

[236] M. Moskovits, "Surface-Enhanced Raman Spectroscopy: A Brief Retrospective," *Journal of Raman Spectroscopy,* vol. 36, no. 6-7, pp. 485-496, 2005, doi: 10.1002/jrs.1362.

[237] A. H. Nguyen, Y. Shin, and S. J. Sim, "Development of Sers Substrate Using Phage-Based Magnetic Template for Triplex Assay in Sepsis Diagnosis," *Biosens Bioelectron,* vol. 85, pp. 522-528, 2016, doi: 10.1016/j.bios.2016.05.043.

[238] X.-Y. Wang, J.-Y. Yang, Y.-T. Wang, H.-C. Zhang, M.-L. Chen, T. Yang, and J.-H. Wang, "M13 Phage-Based Nanoprobe for Sers Detection and Inactivation of Staphylococcus Aureus," *Talanta,* vol. 221, p. 121668, 2021, doi: 10.1016/j.talanta.2020.121668.

[239] L. Bi, H. Zhang, W. Hu, J. Chen, Y. Wu, H. Chen, B. Li, Z. Zhang, J. Choo, and L. Chen, "Self-Assembly of Au@Agnr Along M13 Framework: A Sers

Nanocarrier for Bacterial Detection and Killing," *Biosensors and Bioelectronics,* vol. 237, p. 115519, 2023, doi: 10.1016/j.bios.2023.115519.
[240] Y. Ma, R. J. Nolte, and J. J. Cornelissen, "Virus-Based Nanocarriers for Drug Delivery," *Adv Drug Deliv Rev,* Review vol. 64, no. 9, pp. 811-25, 2012, doi: 10.1016/j.addr.2012.01.005.
[241] A. E. Czapar and N. F. Steinmetz, "Plant Viruses and Bacteriophages for Drug Delivery in Medicine and Biotechnology," *Curr Opin Chem Biol,* Review vol. 38, pp. 108-116, 2017, doi: 10.1016/j.cbpa.2017.03.013.
[242] Z. Ju and W. Sun, "Drug Delivery Vectors Based on Filamentous Bacteriophages and Phage-Mimetic Nanoparticles," *Drug Deliv,* vol. 24, no. 1, pp. 1898-1908, 2017, doi: 10.1080/10717544.2017.1410259.
[243] O. A. Fagbouhn, "Bacteriophage Fusion Peptides Based Targeted Delivery of Therapeutics to Cancer Cells," *Afr. J. Biomed. Res.,* Review vol. 21, pp. 93-99, 2018.
[244] R. Farr, D. S. Choi, and S. W. Lee, "Phage-Based Nanomaterials for Biomedical Applications," *Acta Biomater,* Review vol. 10, no. 4, pp. 1741-50, 2014, doi: 10.1016/j.actbio.2013.06.037.
[245] H. Bar, I. Yacoby, and I. Benhar, "Killing Cancer Cells by Targeted Drug-Carrying Phage Nanomedicines," *BMC Biotechnology,* vol. 8, no. 1, p. 37, 2008, doi: 10.1186/1472-6750-8-37.
[246] N. Suthiwangcharoen, T. Li, K. Li, P. Thompson, S. You, and Q. Wang, "M13 Bacteriophage-Polymer Nanoassemblies as Drug Delivery Vehicles," *Nano Research,* vol. 4, no. 5, pp. 483-493, 2011, doi: 10.1007/s12274-011-0104-2.
[247] F. S. Mozar, M. P. Meivita, S.-X. Go, L. Li, N. Bajalovic, and D. K. Loke, "Ultra-Efficient Mcf-7 Cell Ablation and Chemotherapy-Integrated Electrothermal Therapy with Dox–Ws2–Peg–M13 Nanostructures," *Discover Materials,* vol. 4, no. 1, p. 5, 2024, doi: 10.1007/s43939-024-00076-8.
[248] P. Ngweniform, G. Abbineni, B. Cao, and C. Mao, "Self-Assembly of Drug-Loaded Liposomes on Genetically Engineered Target-Recognizing M13 Phage: A Novel Nanocarrier for Targeted Drug Delivery," *Small,* vol. 5, no. 17, pp. 1963-9, 2009, doi: 10.1002/smll.200801902.
[249] M. Karimi, H. Mirshekari, S. M. Moosavi Basri, S. Bahrami, M. Moghoofei, and M. R. Hamblin, "Bacteriophages and Phage-Inspired Nanocarriers for Targeted Delivery of Therapeutic Cargos," *Adv Drug Deliv Rev,* vol. 106, no. Pt A, pp. 45-62, 2016, doi: 10.1016/j.addr.2016.03.003.
[250] U. Tsedev, C.-W. Lin, G. T. Hess, J. N. Sarkaria, F. C. Lam, and A. M. Belcher, "Phage Particles of Controlled Length and Genome for in Vivo Targeted Glioblastoma Imaging and Therapeutic Delivery," *ACS Nano,* vol. 16, no. 8, pp. 11676-11691, 2022, doi: 10.1021/acsnano.1c08720.
[251] A. Chongchai, S. Waramit, K. Suwan, M. Al-Bahrani, S. Udomruk, T. Phitak, P. Kongtawelert, P. Pothacharoen, and A. Hajitou, "Bacteriophage-Mediated Therapy of Chondrosarcoma by Selective Delivery of the Tumor Necrosis Factor Alpha (Tnfα) Gene," *The FASEB Journal,* vol. 35, no. 5, p. e21487, 2021, doi: 10.1096/fj.202002539R.
[252] A. Chongchai, S. Waramit, T. Wongwichai, J. Kampangtip, T. Phitak, P. Kongtawelert, A. Hajitou, K. Suwan, and P. Pothacharoen, "Targeting Human Osteoarthritic Chondrocytes with Ligand Directed Bacteriophage-Based Particles," *Viruses,* vol. 13, no. 12, p. 2343, 2021, doi: 10.3390/v13122343.

[253] F. I. Staquicini, T. L. Smith, F. H. F. Tang, J. G. Gelovani, R. J. Giordano, S. K. Libutti, R. L. Sidman, W. K. Cavenee, W. Arap, and R. Pasqualini, "Targeted Aavp-Based Therapy in a Mouse Model of Human Glioblastoma: A Comparison of Cytotoxic Versus Suicide Gene Delivery Strategies," *Cancer Gene Therapy,* vol. 27, no. 5, pp. 301-310, 2020, doi: 10.1038/s41417-019-0101-2.

[254] K. Suwan, T. Yata, S. Waramit, J. Przystal, C. Stoneham, K. Bentayebi, P. Asavarut, A. Chongchai, P. Pothacharoen, K.-Y. Lee, S. Topanurak, T. Smith, J. Gelovani, R. Sidman, R. Pasqualini, W. Arap, and A. Hajitou, "Next-Generation of Targeted Aavp Vectors for Systemic Transgene Delivery against Cancer," *Proceedings of the National Academy of Sciences,* vol. 116, p. 201906653, 2019, doi: 10.1073/pnas.1906653116.

[255] C.-Y. Kao, Y.-C. Pan, Y.-H. Hsiao, S.-K. Lim, T.-W. Cheng, S.-W. Huang, S. M.-Y. Wu, C.-P. Sun, M.-H. Tao, and K. Y. Mou, "Improvement of Gene Delivery by Minimal Bacteriophage Particles," *ACS Nano,* vol. 17, no. 15, pp. 14532-14544, 2023, doi: 10.1021/acsnano.3c01295.

[256] S. M. DePorter and B. R. McNaughton, "Engineered M13 Bacteriophage Nanocarriers for Intracellular Delivery of Exogenous Proteins to Human Prostate Cancer Cells," *Bioconjug Chem,* vol. 25, no. 9, pp. 1620-5, 2014, doi: 10.1021/bc500339k.

[257] P. Murgas, N. Bustamante, N. Araya, S. Cruz-Gomez, E. Duran, D. Gaete, C. Oyarce, E. Lopez, A. A. Herrada, N. Ferreira, H. Pieringer, and A. Lladser, "A Filamentous Bacteriophage Targeted to Carcinoembryonic Antigen Induces Tumor Regression in Mouse Models of Colorectal Cancer," *Cancer Immunol Immunother,* vol. 67, no. 2, pp. 183-193, 2018, doi: 10.1007/s00262-017-2076-x.

[258] X. Dong, P. Pan, D. W. Zheng, P. Bao, X. Zeng, and X. Z. Zhang, "Bioinorganic Hybrid Bacteriophage for Modulation of Intestinal Microbiota to Remodel Tumor-Immune Microenvironment against Colorectal Cancer," *Sci Adv,* vol. 6, no. 20, p. eaba1590, 2020, doi: 10.1126/sciadv.aba1590.

[259] W. B. Jang, S. T. Ji, J. H. Park, Y. J. Kim, S. Kang, D. Y. Kim, N. K. Lee, J. S. Kim, H. J. Lim, J. Choi, T. H. V. Le, T. T. G. Ly, V. K. Rethineswaran, D. H. Kim, J. S. Ha, J. Yun, S. H. Baek, and S. M. Kwon, "Engineered M13 Peptide Carrier Promotes Angiogenic Potential of Patient-Derived Human Cardiac Progenitor Cells and in Vivo Engraftment," *Tissue Eng Regen Med,* vol. 17, no. 3, pp. 323-333, 2020, doi: 10.1007/s13770-020-00244-w.

[260] A. Gonzalez-Mora, J. Hernandez-Perez, H. M. N. Iqbal, M. Rito-Palomares, and J. Benavides, "Bacteriophage-Based Vaccines: A Potent Approach for Antigen Delivery," *Vaccines (Basel),* Review vol. 8, no. 3, 2020, doi: 10.3390/vaccines8030504.

[261] Q. Bao, X. Li, G. Han, Y. Zhu, C. Mao, and M. Yang, "Phage-Based Vaccines," *Advanced Drug Delivery Reviews,* vol. 145, pp. 40-56, 2019, doi: 10.1016/j.addr.2018.12.013.

[262] Y. Wang, G. Zhang, L. Zhong, M. Qian, M. Wang, and R. Cui, "Filamentous Bacteriophages, Natural Nanoparticles, for Viral Vaccine Strategies," *Nanoscale,* 10.1039/D1NR08064D vol. 14, no. 16, pp. 5942-5959, 2022, doi: 10.1039/D1NR08064D.

[263] J. Morales, J. J. Martinez, K. Manoutcharian, M. Hernandez, A. Fleury, G. Gevorkian, G. Acero, A. Blancas, A. Toledo, J. Cervantes, V. Maza, F. Quet, H.

Bonnabau, A. S. de Aluja, G. Fragoso, C. Larralde, and E. Sciutto, "Inexpensive Anti-Cysticercosis Vaccine: S3pvac Expressed in Heat Inactivated M13 Filamentous Phage Proves Effective against Naturally Acquired Taenia Solium Porcine Cysticercosis," *Vaccine,* vol. 26, no. 23, pp. 2899-905, 2008, doi: 10.1016/j.vaccine.2008.03.042.

[264] M. R. Santos, V. S. Assao, F. A. A. Santos, R. L. Salgado, A. P. Carneiro, J. L. R. Fietto, G. C. Bressan, M. R. de Almeida, Z. I. P. Lobato, C. Ueira-Veira, L. R. Goulart, and A. Silva-Junior, "Utilization of Phage Display to Identify Antigenic Regions in the Pcv2 Capsid Protein for the Evaluation of Serological Responses in Mice and Pigs," *Arch Virol,* vol. 163, no. 7, pp. 1877-1887, 2018, doi: 10.1007/s00705-018-3816-8.

[265] A. González-Mora, K. M. Calvillo-Rodríguez, J. Hernández-Pérez, M. Rito-Palomares, A. C. Martínez-Torres, and J. Benavides, "Evaluation of the Immune Response of a Candidate Phage-Based Vaccine against Rhipicephalus Microplus (Cattle Tick)," *Pharmaceutics,* vol. 13, no. 12, p. 2018, 2021, doi: 10.3390/pharmaceutics13122018.

[266] J. Wang, A. Lamolinara, L. Conti, M. Giangrossi, L. Cui, M. B. Morelli, C. Amantini, M. Falconi, C. Bartolacci, C. Andreani, F. Orlando, M. Provinciali, F. D. Del Pizzo, F. Russo, B. Belletti, F. Riccardo, E. Bolli, E. Quaglino, F. Cavallo, A. Amici, M. Iezzi, and C. Marchini, "Her2-Displaying M13 Bacteriophages Induce Therapeutic Immunity against Breast Cancer," *Cancers,* vol. 14, no. 16, p. 4054, 2022, doi: 10.3390/cancers14164054.

[267] F. Martínez-Cortés, A. N. Domínguez-Romero, E. G. Pérez-Hernández, D. L. Orozco-Delgado, S. Avila, J. Odales, J. Guzman Valle, G. Gevorkian, and K. Manoutcharian, "Tumor Antigen-Unbiased Variable Epitope Library Contains Mimotopes with Antitumor Effect in a Mouse Model of Breast Cancer," *Molecular Immunology,* vol. 157, pp. 91-100, 2023, doi: 10.1016/j.molimm.2023.03.019.

[268] Z. Salehi and M. J. Rasaee, "A Recombinant Rbd-Based Phage Vaccine Report: A Solution to the Prevention of New Diseases?," *Vaccines,* vol. 11, no. 4, p. 833, 2023, doi: 10.3390/vaccines11040833.

[269] H. Hashemi, T. Bamdad, A. Jamali, S. Pouyanfard, and M. G. Mohammadi, "Evaluation of Humoral and Cellular Immune Responses against Hsv-1 Using Genetic Immunization by Filamentous Phage Particles: A Comparative Approach to Conventional DNA Vaccine," *Journal of Virological Methods,* vol. 163, no. 2, pp. 440-444, 2010, doi: 10.1016/j.jviromet.2009.11.008.

[270] K. Mori, T. Kubo, Y. Kibayashi, T. Ohkuma, and A. Kaji, "Anti-Vaccinia Virus Effect of M13 Bacteriophage DNA," *Antiviral Res,* vol. 31, no. 1-2, pp. 79-86, 1996, doi: 10.1016/0166-3542(96)00951-5.

[271] A. Iizuka, T. Watanabe, T. Kubo, M. Yamamoto, K. Ogawa, T. Ohkuma, and A. Kaji, "M13 Bacteriophage DNA Inhibits Duck Hepatitis B Virus During Acute Infection," *Hepatology,* vol. 19, no. 5, pp. 1079-87, 1994.

[272] S. Khalili, M. J. Rasaee, T. Bamdad, M. Mard-Soltani, M. Asadi Ghalehni, A. Jahangiri, M. H. Pouriayevali, M. R. Aghasadeghi, and F. Malaei, "A Novel Molecular Design for a Hybrid Phage-DNA Construct against Dkk1," *Mol Biotechnol,* vol. 60, no. 11, pp. 833-842, 2018, doi: 10.1007/s12033-018-0115-2.

[273] H. Xin, P. Glee, A. Adams, F. Mohiuddin, and K. Eberle, "Design of a Mimotope-Peptide Based Double Epitope Vaccine against Disseminated Candidiasis,"

Vaccine, vol. 37, no. 18, pp. 2430-2438, 2019, doi: 10.1016/j.vaccine.2019.03.061.

[274] A. Navarro, D. Licona-Moreno, A. Monsalvo-Reyes, U. Hernandez-Chinas, and C. A. Eslava-Campos, "Phage Display Detection of Mimotopes That Are Shared Epitopes of Clinically and Epidemiologically Relevant Enterobacteria," *Microorganisms,* vol. 8, no. 5, 2020, doi: 10.3390/microorganisms8050780.

[275] M. A. Juárez-Estrada, G. Tellez-Isaias, D. M. Graham, L. Laverty, A. Gayosso-Vázquez, and R. A. Alonso-Morales, "Identification of Eimeria Tenella Sporozoite Immunodominant Mimotopes by Random Phage-Display Peptide Libraries-a Proof of Concept Study," *Front Vet Sci,* vol. 10, p. 1223436, 2023, doi: 10.3389/fvets.2023.1223436.

[276] E. Cuevas-Juárez, A. Liñan-Torres, C. Hernández, M. Kopylov, C. S. Potter, B. Carragher, O. T. Ramírez, and L. A. Palomares, "Mimotope Discovery as a Tool to Design a Vaccine against Zika and Dengue Viruses," *Biotechnology and Bioengineering,* vol. 120, no. 9, pp. 2658-2671, 2023, doi: 10.1002/bit.28392.

[277] X. Zhang, Z. Sui, B. Xu, S. Yue, Y. Luo, W. Zhan, and B. Liu, "Mechanically Strong and Highly Conductive Graphene Aerogel and Its Use as Electrodes for Electrochemical Power Sources," *Journal of Materials Chemistry,* 10.1039/C1JM10239G vol. 21, no. 18, pp. 6494-6497, 2011, doi: 10.1039/C1JM10239G.

[278] Z. Han, Z. Tang, S. Shen, B. Zhao, G. Zheng, and J. Yang, "Strengthening of Graphene Aerogels with Tunable Density and High Adsorption Capacity Towards Pb2+," *Scientific Reports,* vol. 4, no. 1, p. 5025, 2014, doi: 10.1038/srep05025.

[279] R. Shadkam, M. Naderi, A. Ghazitabar, A. Asghari-Alamdari, and S. Shateri, "Enhanced Electrochemical Performance of Graphene Aerogels by Using Combined Reducing Agents Based on Mild Chemical Reduction Method," *Ceramics International,* vol. 46, no. 14, pp. 22197-22207, 2020, doi: 10.1016/j.ceramint.2020.05.297.

[280] Z.-Y. Sui, Y.-N. Meng, P.-W. Xiao, Z.-Q. Zhao, Z.-X. Wei, and B.-H. Han, "Nitrogen-Doped Graphene Aerogels as Efficient Supercapacitor Electrodes and Gas Adsorbents," *ACS Applied Materials & Interfaces,* vol. 7, no. 3, pp. 1431-1438, 2015, doi: 10.1021/am5042065.

[281] F. Meng, X. Zhang, B. Xu, S. Yue, H. Guo, and Y. Luo, "Alkali-Treated Graphene Oxide as a Solid Base Catalyst: Synthesis and Electrochemical Capacitance of Graphene/Carbon Composite Aerogels," *Journal of Materials Chemistry,* 10.1039/C1JM13960F vol. 21, no. 46, pp. 18537-18539, 2011, doi: 10.1039/C1JM13960F.

[282] Y. Qian, I. M. Ismail, and A. Stein, "Ultralight, High-Surface-Area, Multifunctional Graphene-Based Aerogels from Self-Assembly of Graphene Oxide and Resol," *Carbon,* vol. 68, pp. 221-231, 2014, doi: 10.1016/j.carbon.2013.10.082.

[283] K. Ji, Y. Gao, L. Zhang, S. Wang, Q. Yue, X. Xu, W. Kong, B. Gao, Z. Cai, and Y. Chen, "A Tunable Amphiphilic Enteromorpha-Modified Graphene Aerogel for Oil/Water Separation," *Science of The Total Environment,* vol. 763, p. 142958, 2021, doi: 10.1016/j.scitotenv.2020.142958.

[284] P. Arabkhani and A. Asfaram, "Development of a Novel Three-Dimensional Magnetic Polymer Aerogel as an Efficient Adsorbent for Malachite Green

Removal," *Journal of Hazardous Materials,* vol. 384, p. 121394, 2020, doi: 10.1016/j.jhazmat.2019.121394.

[285] H. Shi, C. J. Zhang, P. Lu, Y. Dong, P. Wen, and Z.-S. Wu, "Conducting and Lithiophilic Mxene/Graphene Framework for High-Capacity, Dendrite-Free Lithium–Metal Anodes," *ACS Nano,* vol. 13, no. 12, pp. 14308-14318, 2019, doi: 10.1021/acsnano.9b07710.

[286] W. Xia, C. Qu, Z. Liang, B. Zhao, S. Dai, B. Qiu, Y. Jiao, Q. Zhang, X. Huang, W. Guo, D. Dang, R. Zou, D. Xia, Q. Xu, and M. Liu, "High-Performance Energy Storage and Conversion Materials Derived from a Single Metal–Organic Framework/Graphene Aerogel Composite," *Nano Letters,* vol. 17, no. 5, pp. 2788-2795, 2017, doi: 10.1021/acs.nanolett.6b05004.

[287] Z. Sui, Q. Meng, X. Zhang, R. Ma, and B. Cao, "Green Synthesis of Carbon Nanotube–Graphene Hybrid Aerogels and Their Use as Versatile Agents for Water Purification," *Journal of Materials Chemistry,* 10.1039/C2JM00055E vol. 22, no. 18, pp. 8767-8771, 2012, doi: 10.1039/C2JM00055E.

[288] H.-Y. Mi, X. Jing, A. L. Politowicz, E. Chen, H.-X. Huang, and L.-S. Turng, "Highly Compressible Ultra-Light Anisotropic Cellulose/Graphene Aerogel Fabricated by Bidirectional Freeze Drying for Selective Oil Absorption," *Carbon,* vol. 132, pp. 199-209, 2018, doi: 10.1016/j.carbon.2018.02.033.

[289] E. Zhang, W. Liu, Q. Liang, X. Liu, Z. Zhao, and Y. Yang, "Polypyrrole Nanospheres@Graphene Aerogel with High Specific Surface Area, Compressibility, and Proper Water Wettability Prepared in Dimethylformamide-Dependent Environment," *Polymer,* vol. 185, p. 121974, 2019, doi: 10.1016/j.polymer.2019.121974.

[290] S. Hou, X. Wu, Y. Lv, W. Jia, J. Guo, L. Wang, F. Tong, and D. Jia, "Ultralight, Highly Elastic and Bioinspired Capillary-Driven Graphene Aerogels for Highly Efficient Organic Pollutants Absorption," *Applied Surface Science,* vol. 509, p. 144818, 2020, doi: 10.1016/j.apsusc.2019.144818.

[291] Y. Sun, P. Passaretti, I. Hernandez, J. Gonzalez, W. Liu, F. Rodriguez, D. J. Dunstan, P. Goldberg Oppenheimer, and C. J. Humphreys, "Nanomechanics of Graphene Oxide-Bacteriophage Based Self-Assembled Porous Composites," *Scientific Reports,* vol. 10, no. 1, p. 15618, 2020, doi: 10.1038/s41598-020-72372-1.

[292] V. Georgakilas, M. Otyepka, A. B. Bourlinos, V. Chandra, N. Kim, K. C. Kemp, P. Hobza, R. Zboril, and K. S. Kim, "Functionalization of Graphene: Covalent and Non-Covalent Approaches, Derivatives and Applications," *Chemical Reviews,* vol. 112, no. 11, pp. 6156-6214, 2012, doi: 10.1021/cr3000412.

[293] N. Hebalkar, K. S. Kollipara, Y. Ananthan, and M. K. Sudha, "Nanoporous Aerogels for Defense and Aerospace Applications," in *Handbook of Advanced Ceramics and Composites: Defense, Security, Aerospace and Energy Applications*, Y. R. Mahajan and R. Johnson Eds. Cham: Springer International Publishing, 2020, pp. 121-163.

[294] S. Gupta, S. K. Sharma, D. Pradhan, and N.-H. Tai, "Ultra-Light 3d Reduced Graphene Oxide Aerogels Decorated with Cobalt Ferrite and Zinc Oxide Perform Excellent Electromagnetic Interference Shielding Effectiveness," *Composites Part A: Applied Science and Manufacturing,* vol. 123, pp. 232-241, 2019, doi: 10.1016/j.compositesa.2019.05.025.

[295] Q. Han, L. Yang, Q. Liang, and M. Ding, "Three-Dimensional Hierarchical Porous Graphene Aerogel for Efficient Adsorption and Preconcentration of Chemical Warfare Agents," *Carbon,* vol. 122, pp. 556-563, 2017, doi: 10.1016/j.carbon.2017.05.031.
[296] Q. Hu, X. Wang, Y. Zheng, T. Zhao, J. Qu, Z.-Z. Yu, and D. Yang, "Solar-Thermally Enhanced Catalytic Hydrolysis of Chemical Warfare Agent Simulant with Uio-66-Ncs Decorated Reduced Graphene Oxide Aerogels," *Chemical Engineering Journal,* vol. 476, p. 146606, 2023, doi: 10.1016/j.cej.2023.146606.
[297] S. Zhang, L. Tian, X. Chen, Y. Wang, and Q. Zhang, "Ultralight Graphene/Carbon Nanofibers/Carbon Nanotubes Aerogels with Thermal Insulating and Hot-Oil Adsorption Performance," *Journal of Materials Science,* vol. 56, no. 12, pp. 7409-7419, 2021, doi: 10.1007/s10853-021-05772-x.
[298] J. Feher, "Acid–Base Physiology I: The Bicarbonate Buffer System and Respiratory Compensation," in *Quantitative Human Physiology (Second Edition)*, J. Feher Ed. Boston: Academic Press, 2017, ch. 6.5, pp. 665-671.
[299] B. Konkena and S. Vasudevan, "Understanding Aqueous Dispersibility of Graphene Oxide and Reduced Graphene Oxide through Pka Measurements," *The Journal of Physical Chemistry Letters,* vol. 3, no. 7, pp. 867-872, 2012, doi: 10.1021/jz300236w.
[300] Z. Li, L. Deng, I. A. Kinloch, and R. J. Young, "Raman Spectroscopy of Carbon Materials and Their Composites: Graphene, Nanotubes and Fibres," *Progress in Materials Science,* vol. 135, p. 101089, 2023, doi: 10.1016/j.pmatsci.2023.101089.
[301] L. Petrakis, "Spectral Line Shapes: Gaussian and Lorentzian Functions in Magnetic Resonance," *Journal of Chemical Education,* vol. 44, no. 8, p. 432, 1967, doi: 10.1021/ed044p432.
[302] X. Yuan and R. A. Mayanovic, "An Empirical Study on Raman Peak Fitting and Its Application to Raman Quantitative Research," *Appl. Spectrosc.,* vol. 71, no. 10, pp. 2325-2338, 2017, doi: 10.1177/0003702817721527.
[303] A. C. Ferrari and J. Robertson, "Interpretation of Raman Spectra of Disordered and Amorphous Carbon," *Physical Review B,* vol. 61, no. 20, pp. 14095-14107, 2000, doi: 10.1103/PhysRevB.61.14095.
[304] S. Salvestrini, "Analysis of the Langmuir Rate Equation in Its Differential and Integrated Form for Adsorption Processes and a Comparison with the Pseudo First and Pseudo Second Order Models," *Reaction Kinetics, Mechanisms and Catalysis,* vol. 123, no. 2, pp. 455-472, 2018, doi: 10.1007/s11144-017-1295-7.
[305] H. Wang, L. Zhao, and W. Hou, "Pseudo-Second-Order Kinetic Equation for Describing the Effect of Sorbent and Sorbate Concentrations," *Langmuir,* vol. 40, no. 7, pp. 3559-3568, 2024, doi: 10.1021/acs.langmuir.3c03235.
[306] Y. Liu and X. Yu, "Carbon Dioxide Adsorption Properties and Adsorption/Desorption Kinetics of Amine-Functionalized Kit-6," *Applied Energy,* vol. 211, pp. 1080-1088, 2018, doi: 10.1016/j.apenergy.2017.12.016.
[307] K. H. Chu, "Fixed Bed Adsorption of Chromium and the Weibull Function," *Journal of Hazardous Materials Letters,* vol. 2, p. 100022, 2021, doi: 10.1016/j.hazl.2021.100022.
[308] J. Wang and X. Guo, "Rethinking of the Intraparticle Diffusion Adsorption Kinetics Model: Interpretation, Solving Methods and Applications,"

Chemosphere, vol. 309, p. 136732, 2022, doi: 10.1016/j.chemosphere.2022.136732.

[309] W. W. Gerberich, J. M. Jungk, and W. M. Mook, "The Bottom-up Approach to the Materials by Design," in *Nano and Microstructural Design of Advanced Materials*, M. A. Meyers, R. O. Ritchie, and M. Sarikaya Eds. Oxford: Elsevier Science Ltd, 2003, pp. 211-220.

[310] Y. Hanzawa, H. Hatori, N. Yoshizawa, and Y. Yamada, "Structural Changes in Carbon Aerogels with High Temperature Treatment," *Carbon,* vol. 40, no. 4, pp. 575-581, 2002, doi: 10.1016/S0008-6223(01)00150-6.

[311] M. M. Atta, E. O. Taha, and A. M. Abdelreheem, "Nitrogen Plasma Effect on the Structural, Thermal, and Dynamic Mechanical Properties of Pva/Starch/Graphene Oxide Nanocomposite," *Applied Physics A,* vol. 127, no. 7, p. 532, 2021, doi: 10.1007/s00339-021-04671-x.

[312] P. Qi, H. Zhu, F. Borodich, and Q. Peng, "A Review of the Mechanical Properties of Graphene Aerogel Materials: Experimental Measurements and Computer Simulations," *Materials (Basel),* vol. 16, no. 5, 2023, doi: 10.3390/ma16051800.

[313] B. Gao, X. Feng, Y. Zhang, Z. Zhou, J. Wei, R. Qiao, F. Bi, N. Liu, and X. Zhang, "Graphene-Based Aerogels in Water and Air Treatment: A Review," *Chemical Engineering Journal,* vol. 484, p. 149604, 2024, doi: 10.1016/j.cej.2024.149604.

CHAPTER 2

MATERIALS AND METHODS

The methods presented in this chapter includes extracts from the following papers, which are the basis of the subsequent chapters:

K. Stokes, Y. Sun, P. Passaretti, H. White, and P. G. Oppenheimer, "Optimisation of Graphage13 Macro-Dispersibility via Understanding the pH-Dependent Ionisation During Self-Assembly: Towards the Manufacture of Graphene-Based Nanodevices," *Nanoscale* vol. 15, pp. 13304 - 13312, 2023, doi: 10.1039/d3nr00778b.

K. Stokes, Y. Sun, H. Zhang, P. Passaretti, H. White, and P. Goldberg Oppeneheimer, "Thermonanomechanics of Graphene Oxide-M13 Bacteriophage Nanocomposites -Towards Graphene-Based Nanodevices," *Carbon Trends,* vol. 15, p. 100343, 2024/06/01/ 2024, doi: 10.1016/j.cartre.2024.100343

K. Stokes, Y. Sun, H. Zhang, P. Passaretti, H. White, and P. Goldberg Oppeneheimer, " Unveiling the Sorption Properties of Graphene Oxide-M13 Bacteriophage Aerogels for Advanced Sensing and Environmental Applications," *ACS Applied Materials and Interfaces,* 2024, doi: 10.1021/acsami.4c16202

K. Stokes, Y. Sun, J. L. Thomas, P. Passaretti, H. White, and P. Goldberg Oppeneheimer, “Conductivity Optimisation of Graphene Oxide-M13 Bacteriophage Nanocomposites: Towards Graphene-Based Gas Micronano-sensors”, *Discover Nano,* vol. 19, p. 152, 2024, doi: 10.1186/s11671-024-04101-w

2.1 Materials

The following section outlines the materials used to generate GPA and conduct subsequent investigations. Unless otherwise specified, all materials were used as received.

2.1.1 Graphene Oxide (GO)

A solution of highly concentrated graphene oxide (GO) was obtained from Graphene supermarket (SKU-HCGO-W-175ML, 5 g/L). The GO was in the form of an aqueous dispersion of GO flakes suspended in water (Figure 2.1a). These GO flakes are composed of 79% carbon and 20% oxygen, with flake sizes ranging from 0.5 to 5 μm, and at least 60% exhibiting a thickness of one atomic layer (Figure 2.1b) [1]. The combination of GO and M13 enabled the fabrication of GPA.

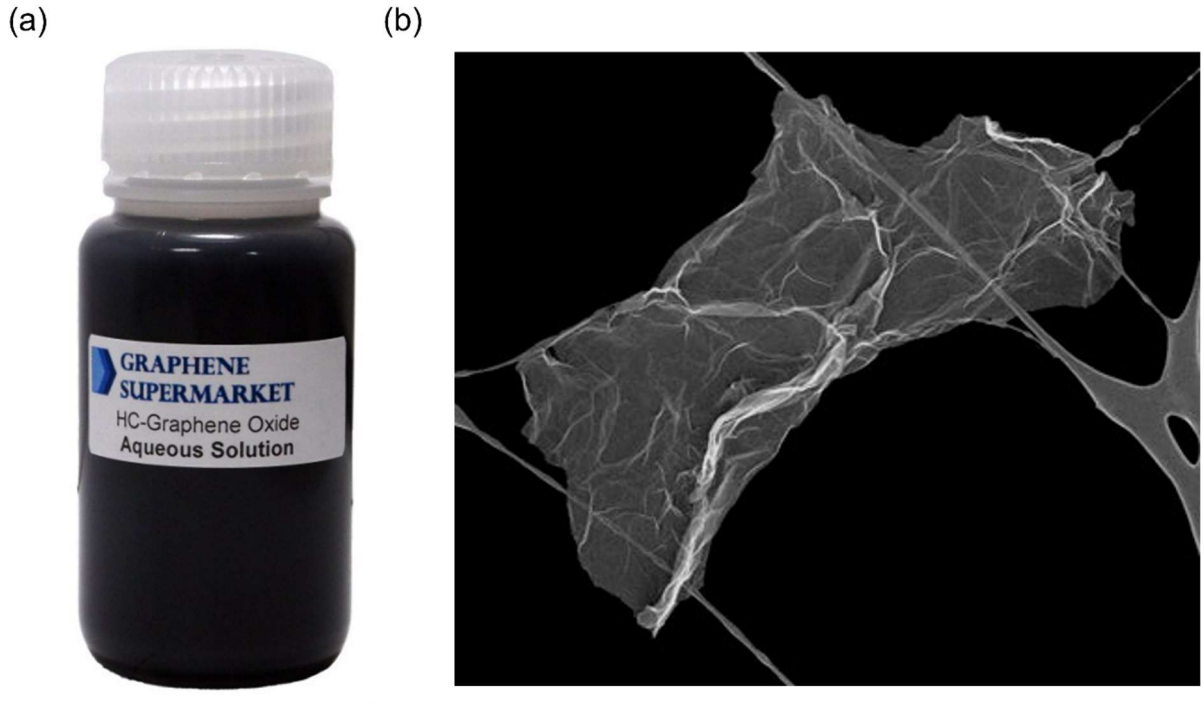

Figure 2.1: Image of GO solution and flakes

(a) Image of graphene oxide (GO) stock purchased from Graphene Supermarket and **(b)** SEM image of a single GO flake. Images sourced from [2].

2.1.2 M13 Bacteriophage

M13 bacteriophage (M13KE) was originally purchased from New England Biolabs in the form of double-stranded DNA (dsDNA). This was transferred to the *E.coli* via heat shock and propagated to generate an initial stock of M13 [3]. Further propagation from this stock (detailed in Section 2.2.1), provided the M13 phages (Figure 2.2) required for the self-assembly of GraPhage13 aerogels (GPA).

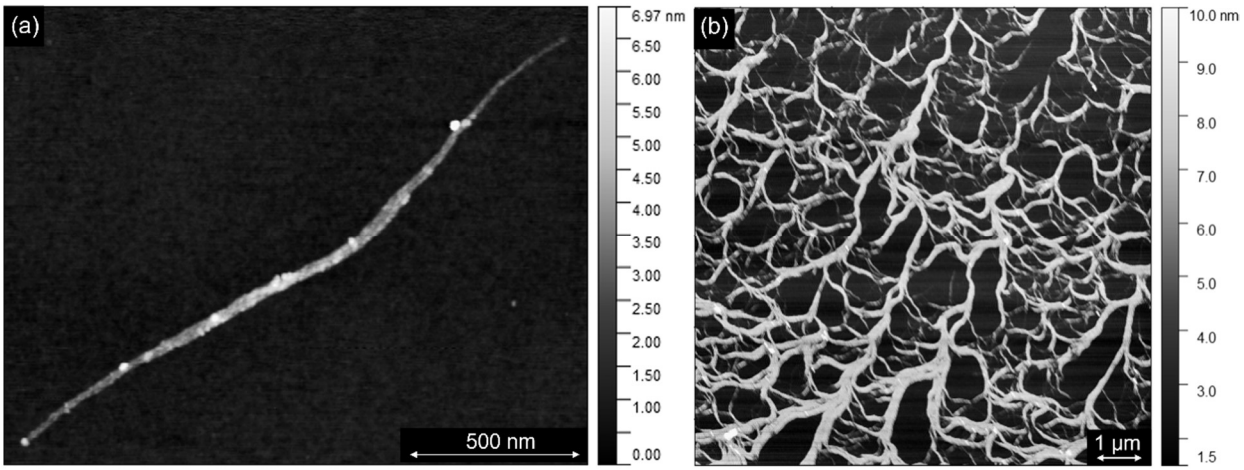

Figure 2.2: AFM images of M13 bacteriophage

Atomic force microscopy images of **(a)** a single M13 bacteriophage and **(b)** a network of M13 bacteriophages.

2.1.3 E.coli

One Shot TOP10F´ Chemically Competent *Escherichia coli* (*E.coli*) was purchased from Thermo Fisher Scientific and utilised for the large-scale propagation of M13 bacteriophage. TOP10 *E.coli* are non-pathogenic and show stable replication, high transformation efficiency and are resilient to stress induced by acidic conditions and osmotic shock, making them ideal for high-yield and reliable phage amplification. The addition of the *F'* episome provides the *E.coli* with resistance to the antibiotic

tetracycline, which can be incorporated into the M13 propagation process to eliminate any unwanted *E.coli* strains [4, 5].

2.1.4 Gold Nanoparticles

Chapter 6 investigates the integration of carboxylic acid functionalised gold nanoparticles (AuNPs) into integrated GPA to modify its conductivity. The AuNPs were in the form of a dispersion in water, with an optical density of 50 and coated in polyethylene glycol (PEG) to improve their stability. The 5 nm diameter AuNPs (765430-1ML) had a core diameter ranging from 3-7 nm [6], and the 20 nm diameter AuNPs (765511-1ML) exhibited a core diameter from 18–22 nm (Sigma-Aldrich) [7].

2.1.5 Chemicals and Reagents

In addition to the specific materials discussed above, the following chemicals and reagents were used in various experimental procedures throughout this study:

Tetracycline (TCN) – an antibiotic employed to control bacterial growth and isolate target bacterial cultures (VWR).

Nutrient broth (NB) – A liquid medium used to provide nutrients for the growth and proliferation of *E.coli* cells (Merck Life Sciences).

Nutrient agar – a solid nutrient medium for the cultivation of *E.coli* cells (VWR).

Polyethylene glycol (PEG) – a polyether which, when combined with NaCl and DIW, generates a buffer utilised for the precipitation of M13 from solution (Scientific Laboratory Supplies).

Sodium chloride (NaCl) – An ionic compound which, when combined with NaCl and DIW, generates a buffer utilised for the precipitation of M13 from solution (VWR).

Citric acid – A weak acid used to generate a citrate buffer for GPA production (VWR).

Sodium citrate dihydrate – A weak acid used to generate a citrate buffer for GPA production (Sigma-Aldrich).

Hydrochloric acid (HCl) – A strong, highly corrosive acid used for adjusting the pH of solution in titration and zeta potential experiments (Chapter 3) (Sigma-Aldrich).

Sodium hydroxide (NaOH) – A strong, highly corrosive base used for adjusting the pH of solution in titration and zeta potential experiments (Chapter 3) (Sigma-Aldrich).

Conductive silver paint – A conductive adhesive used to create electrical connections between GPAs and the electrometer (Chapter 6) (RS Pro).

Ethanol – A simple, volatile, flammable alcohol used as a solvent for TCN and for a solvent in sorption experiments (Chapter 5) (Sigma-Aldrich).

Acetone – A simple, volatile, flammable ketone used as a solvent in sorption experiments (Chapter 5) (Sigma-Aldrich).

Deionised water (DIW) – Highly purified water used as a solvent to prepare solutions.

2.2 Experimental Methods

2.2.1 Propagation and Purification of M13 Bacteriophage

The protocol for the propagation and purification of M13 bacteriophage is given by Passaretti et al. [3] and shown by Figure 2.3.

Nutrient agar, NB and mixture of 25% PEG 6000 and 2.5M NaCl, and 5 mg/mL TCN dissolved in ethanol were first prepared. Ensuring the environment remained sterile, TCN was added to the nutrient agar to a final concentration of 5 μg/mL, poured into

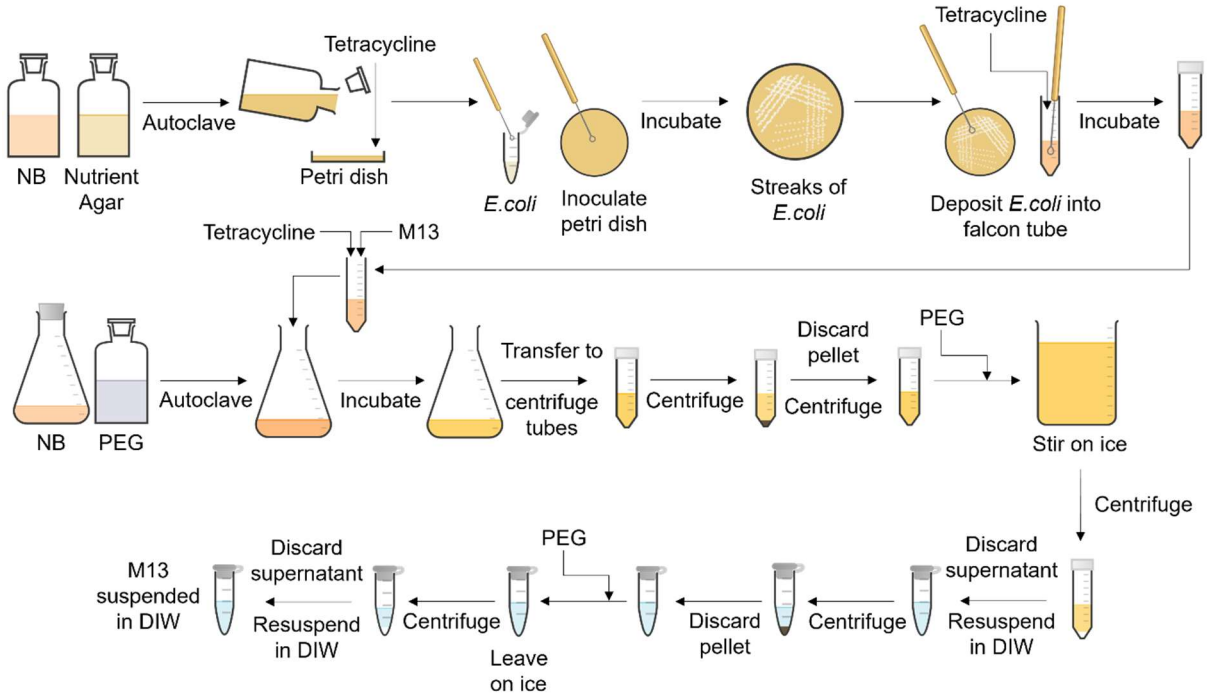

Figure 2.3: Propagation and purification of M13 bacteriophage

Petri dishes containing nutrient agar and tetracycline are innoculated with E.coli TOP10F'. Following incubation, the E.coli is deposited into a nutrient broth (NB) and tetracycline solution, incubated overnight and then deposited into conical flasks containing NB, tetracycline and M13. The solution is incubated overnight and centrifuged twice to remove the E.coli cells. A mixture of polyethylene glycol (PEG) 6000 and 2.5M NaCl is mixed with the supernatant whilst on ice, precipitating the M13, which is separated through centrifugation. The supernatant is discarded and the white pellet containing M13 is then resuspended in deionised water (DIW). To purify the M13, the solution is centrifuged and any remaining contamination is discarded. The supernatant is combined on PEG, left on ice and then centrifuged, producing a pellet of M13. The supernatant is discarded and the pellet resuspended to produce the final solution of M13 in deionised water. Created with Chemix (https://chemix.org).

petri dishes, and left to cool. Once solidified, the petri dishes were inoculated with *E.coli* and incubated overnight at 37°C. Following this, 40 mL of NB and 40 µL of 5 mg/mL TCN were deposited into falcon tubes, and the *E.coli* was transferred from the petri

dishes to 50 mL falcon tubes *via* inoculating loops. The falcon tubes were placed in a shaker incubator overnight at 37°C, 150 rpm.

Subsequently, 2.16 L of NB was prepared and divided between six 2L conical flasks and autoclaved. The contents of one falcon tube, 360 µL TCN and 0.05 mg M13 was added to each conical flask using aseptic technique and incubated for 16 hours in an orbital shaker at 37°C, 180 rpm, allowing the M13 to propagate.

Following incubation, the solution was separated into six 400 mL centrifuge tubes, and centrifuged (Beckman Coulter, JLA 10.5) at 8,500 rpm for 15 minutes at 4°C, forming a pellet of *E.coli* which was subsequently discarded. The supernatant was then centrifuged under the same conditions for 30 minutes to sediment any excess *E.coli*, and the upper 80% (300 mL) of the supernatant from each centrifuge tube was collected. The PEG solution was added to the supernatant in a 1:5 ratio and stirred with a magnetic stirrer for 90 minutes at 4°C, precipitating the M13. The solution was centrifuged at 10,000 rpm for 25 minutes, generating a white pellet at the bottom of the centrifuge tubes. The supernatant was discarded, and white pellet is resuspended in deionised water (DIW) and deposited in 1.5 mL microcentrifuge tubes.

To ensure the *E.coli* had been removed, the solution was centrifuged in a microcentrifuge (SciSpin Micro) at 15,000 rpm for 5 minutes and the supernatant transferred to new centrifuge tubes. If a the brown pellet was observed, containing any remaining *E.coli*, this was discarded. If a white pellet of M13 bacteriophage was instead observed, the supernatant was transferred to new centrifuge tubes, and the white pellet was resuspended in DIW and recentrifuged. This process was repeated until no white pellet remained. PEG solution was then added to each tube in a 1:5 ratio of PEG

solution to supernatant, and left on ice for 60 minutes. The solution was centrifuged at 15,000 rpm for 15 minutes, producing pellets of M13. The supernatant was discarded, the pellets resuspended in DIW, and the solution collected in a falcon tube.

2.2.2 Fabrication of GraPhage13 Aerogels (GPA)

The fabrication of GraPhage13 Aerogels (GPAs) (Figure 2.4), as outlined by Passaretti et al. [8], involves the self-assembly of M13 with Graphene Oxide (GO).

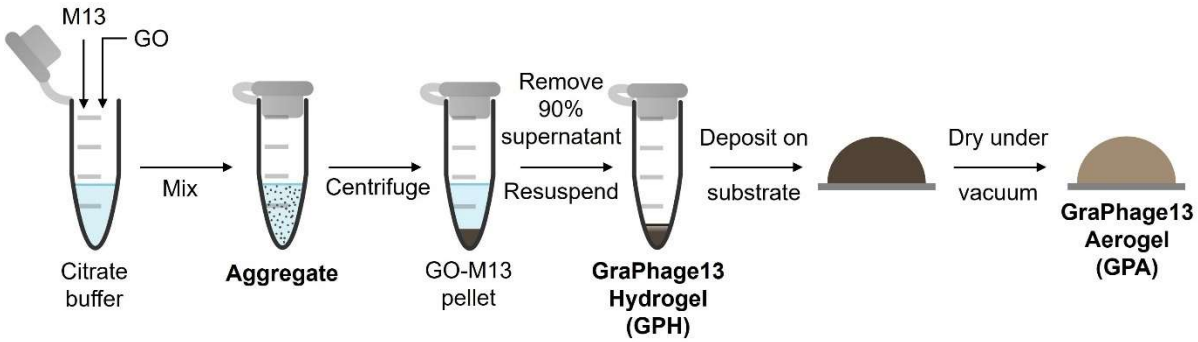

Figure 2.4: Fabrication of GraPhage13 aerogels (GPA)

A schematic showing the fabrication of GraPhage13 aerogels (GPA). M13 bacteriophage and graphene oxide (GO) are combined in a citrate buffer, where they self-assemble into an aggregate. Centrifuging produces a GO-M13 pellet, which is resuspended in 10% of the supernant to generate the GraPhage13 hydrogel (GPH). The GPH is then deposited onto a substrate and dried under a vacuum, creating the GPA. Created with Chemix (*https://chemix.org*).

A 10 mM pH citrate buffer was generated by combining 0.72 g of citric acid and 1.84 g of sodium citrate dihydrate in 1 L of DIW. The pH was measured with a pH meter (Mettler Toledo FiveEasy) and adjusted with additional citric acid or sodium citrate dihydrate as required until a pH of 4.9 is achieved. In Chapter 3, when fabricating GPAs at varying pH, the pH of this solution is adjusted by adding additional citric acid or sodium citrate dihydrate to solution.

After autoclaving the citrate buffer, 910 µL was deposited into an Eppendorf tube, followed by 30 µL of M13 in DIW, and 60 µL of GO. The concentration of GO is given as 5 mg/mL by the supplier (Section 2.1.1) and the concentration of M13 in DIW was calculated with UV-Vis Spectroscopy (described in Section 2.2.3) and diluted to 10 mg/mL This generated a 1 mL solution, with a final concentration of 0.3 mg/mL GO and 0.3 mg/mL M13 in solution.

Inverting the Eppendorf tube immediately initiated the self-assembly of GO and M13, forming an aggregate. The solution was mixed with an orbital shaker for 15 minutes at 250 rpm, and then centrifuged at 15,000 rpm for 1 minute. This produced a GO-M13 pellet at the bottom of the Eppendorf tube. Following this, 900 µL of the supernatant was removed, and the GO-M13 pellet was resuspended in the remaining solution, producing the GraPhage13 hydrogel (GPH). Finally, GPH was deposited onto a silicon or glass substrate, and dried in a vacuum chamber to a final pressure of ~0.05 mbar. This caused the transition of GPH into GPA.

In Chapter 6, AuNPs are incorporated into GPA to form GPA-Au. To achieve this, the volume of citrate buffer was reduced proportionally as the volume of the AuNP solution increased, ensuring a consistent final solution volume of 1 mL. For instance, when adding 10 µL of AuNPs, 900 µL of citrate buffer was first introduced into an Eppendorf tube, followed by 10 µL of AuNPs, resulting in a total volume of 910 µL. The subsequent process for synthesising GPA-Au followed the same procedure as for standard GPA formation: GO and M13 introduced into the citrate buffer-AuNP solution, inverted to initiate interactions between the components, centrifuged to form the hydrogel, and dried under vacuum to generate GPA-Au.

2.2.3 Ultraviolet – Visible (UV-Vis) Spectroscopy

Ultraviolet-visible (UV-Vis) spectroscopy enables the presence, concentration and purity of a sample to be determined, by measuring the absorbance of visible and ultraviolet light through a solution [9]. A single wavelength of light, λ, is selected per measurement using a monochromator, and is directed through the sample with a sequence of mirrors [10]. A detector then measures the intensity of the transmitted light I in comparison to the intensity of incident light I_0 [11]. Repeating this process across a range of wavelengths 0generates absorbance spectra as a function of wavelength [12]. The absorbance at a given wavelength, A_λ, is determined by the Beer-Lambert Law:

$$A_\lambda = \log_{10}\left(\frac{I}{I_0}\right) = \epsilon_\lambda LC \tag{2.1}$$

where ϵ_λ is the extinction coefficient at wavelength λ, C is the concentration of the sample in solution and L is the length of the light path through the sample [13].

The limitation of the Beer-Lambert law is the breakdown of the linear relationship between A and C when $A > 1$. To overcome this, the samples can be diluted by a known factor to reduce its concentration and therefore its absorbance. The concentration of the diluted sample can then be determined with the Beer-Lambert law and extrapolated to calculate the original concentration [14].

The concentration of M13 in DIW, generated as described in Section 2.2.1, was determined using a UV-Vis spectrophotometer (Agilent Cary 60 UV-Vis), using a quartz cuvette with a 1 cm light path quartz cuvette and volume of 700 µL. Prior to sample analysis, a spectrum of DIW was first taken as a baseline. The end product from Section 2.2.1, a solution of M13 in DIW in the falcon tube, was first placed in an orbital

shaker to ensure the uniformity of M13 in solution. Between 10-100 µL of this suspension was removed with a pipette, placed into a 1.5 mL Eppendorf tube, and additional DIW was added to a final volume of 700 µL. Following mixing in the orbital shaker for a further minute, the diluted M13 solution was placed in the quartz cuvette and a UV-Vis spectrum was taken from a wavelength of 800 nm to 200 nm in 0.2 nm intervals. The concentration of the initial M13 solution can then be calculated by multiplying the concentration of the diluted solution by the dilution factor, which is the ratio of the volume of the diluted solution to the volume of concentrated M13 solution deposited in the Eppendorf tube.

UV-Vis spectroscopy was also utilised in Chapter 6 to analyse the supernatants of GO, M13, AuNPs and combinations of these materials. In this case, the conditions required to generate GPA were replicated. Citrate buffer was used as the baseline and the same concentrations of each analyte were used as when generating GPA and GPA-Au, as previously described in Section 2.2.2. For example, when analysing the combination of AuNPs and GO, 10 µL AuNPs and 60 µL GO were added to an Eppendorf tube with 930 µL citrate buffer, generating a final volume of 1 mL. This was inverted, placed on the orbital shaker at 250 rpm for 15 minutes, and then centrifuged for 1 minute at 15,000 rpm. Then, instead of discarding 900 µL supernatant, 700 µL of supernatant was placed in the quartz cuvette and analysed. Observing the spectra of the supernatants of the pure components (GO, M13 and AuNPs), compared to the spectra of combinations of the components (GO+M13, GO+AuNPs, M13+AuNPs, GO+M13+AuNPs) enabled the observation of whether the components remained in solution, or interacted and precipitated from solution, enabling their integration into GPH and subsequently GPA.

2.2.4 Scanning Electron Microscopy (SEM) and Energy Dispersive X-Ray Spectroscopy (EDX)

Scanning electron microscopy (SEM), in conjunction with energy dispersive x-ray (EDX) spectroscopy (Figure 2.5), enabled GPA characterisation through the acquisition of high-resolution images to observe their morphology, and analysis of their elemental composition [15].

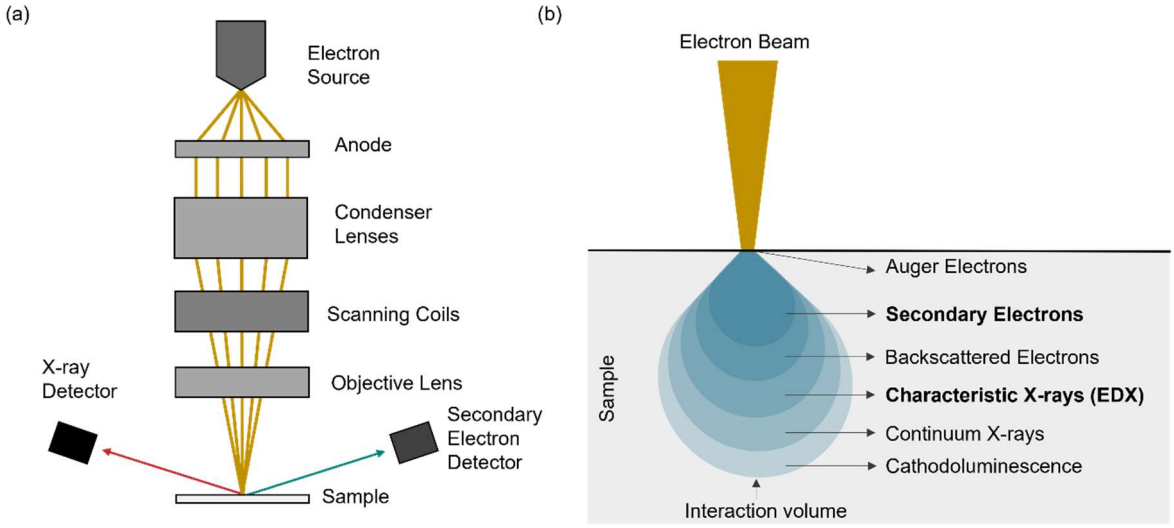

Figure 2.5: Scanning electron microscopy

(a) A schematic of a scanning electron microscope (SEM); **(b)** the products of the interaction between the electron beam and the sample. Images based on [16, 17].

In SEM, an electron gun emits a beam of electrons, which are directed through a vacuum, and focused onto the sample using electromagnetic lenses and apertures. The electron beam scans over and interacts with the surface of the sample, generating varying electrons and photons. Generally, to observe the morphology of a sample, the secondary electrons are detected and recorded, with the resulting image showing contrast based on the surface topology [18, 19].

The interaction between the electron beam and the sample surface can ionise an atom by ejecting a core electron from its inner shell. Subsequently, an outer shell electron may fall into the inner shell to fill the vacancy, emitting a photon with energy equal to the difference between the two orbitals, specific to the element involved. Integrating an x-ray detector into the SEM therefore enables the detection of these characteristic x-rays, creating a spectrum that plots energy against counts, revealing distinct peaks corresponding to each element [20].

The morphology of the fabricated GPAs was analysed with a Hitachi SU5000 scanning electron microscope. Due to the insulating nature of GPAs, SEM images were acquired at voltages between 0.5 - 5 kV to minimise charging effects. The elemental composition was further analysed via energy-dispersive X-ray spectroscopy (EDX). The EDX spectra were obtained at 15 kV using a Hitachi TM3030 microscope equipped with Swift ID.

2.2.5 Zeta Potential

The zeta potential (ζ) is a measure of the surface charge of colloids. It originates from the formation of an electric double layer, consisting of a stern layer of bound counterions and a diffuse layer of free ions. The zeta potential is then defined as the electrical potential at the slipping plane, the outer boundary of the double later (Figure 2.6) [21]. If $|\zeta| > 30$ mV, the electrostatic repulsion between particles is sufficiently strong to ensure their stability and dispersibility in solution. Conversely, when $|\zeta| < 30$

mV, the electrostatic repulsion cannot overcome the van der Waals attraction between colloids, leading to their aggregation [22].

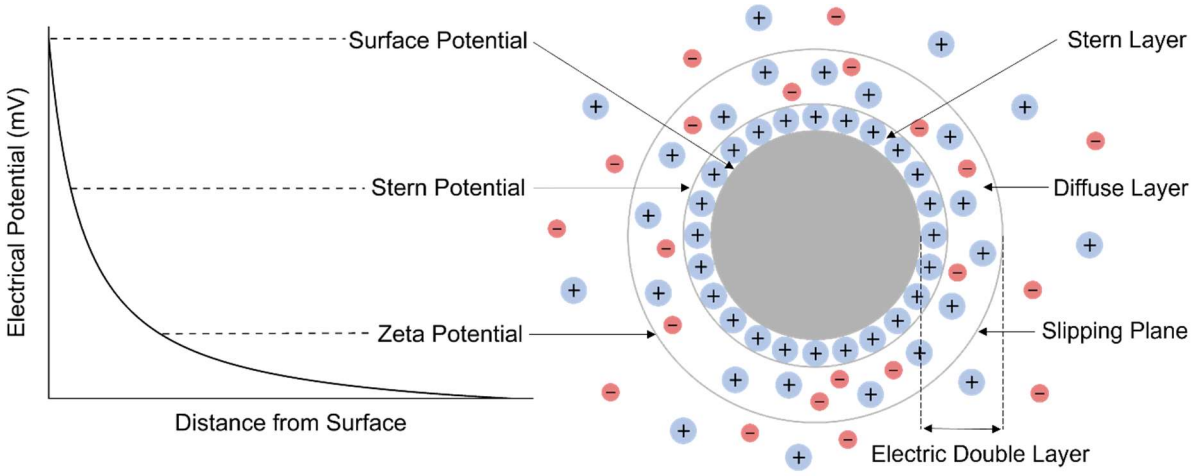

Figure 2.6: Electric double layer formation

A diagram of the electrical double layer formed when a colloid is dispersed in aqueous media and representation of the electrical potential generated. Image based on [23].

Measurements were taken using a Malvern Zetasizer Ultra, which analyses the zeta potential using the electrophoretic light scattering (ELS) with Mixed Mode Measurement – Phase Analysis Light Scattering (M3-PALS). This technique involves placing a colloidal dispersion in a folded capillary zeta cell and applying an electric field across the electrodes of the cell, causing the charged particles to migrate towards the oppositely charged electrode. Directing a laser beam at the solution and analysing the phase shift of scattered light gives a measure of the zeta potential [24].

To measure the zeta potential, and hence the stability, of GO, M13 and GO-M13 across various pH levels, solutions between pH 2–11 were produced with NaOH and HCl, and GO and/or M13 were added to a final concentration of 1 mg/mL. The pH of the resulting solution was measured with a pH meter (Mettler Toledo FiveEasy). The solutions were deposited in DTS1070 folded capillary zeta cells (Malvern Panalytical) and placed in

the Zetasizer for analysis. The temperature was set to at 25°C, and an equilibration time of 120 seconds was allowed to ensure the sample was thermally stable once this temperature was achieved. Three repeat measurements were taken for each solution ensure repeatability.

2.2.6 Acid – Base Titrations

Acid-base titrations offer a simple and cost-effective method to determine an analyte's concentration of ionised groups and their pK_a values. The investigations in Chapter 3 involve incrementally adding an acid (the titrant) to a titrand, a solution containing a base and the analyte (GO, M13 or GPH) (Figure 2.7a). The resulting change in pH was monitored to generate titration curves (Figure 2.7b) [25]. Analysing these curves (Section 2.3.4) can provide insights into the concentration of ionised groups present in GO, M13 and GPH at a specific pH, and the pK_a values of these groups [26].

Initially, 1M solution of HCl and NaOH were prepared by diluting concentrated HCl and dissolving NaOH pellets respectively in DIW. Subsequently, 50 mL of each solution was measured with a volumetric flask and mixed with 950 mL of DIW to produce 1 L of 50 mM HCl and 1L of 50 mM NaCl. To confirm the concentrations the pH of these solutions was measured; assuming the HCl and NaOH were the only source of H^+ ions, 50 mM HCl and 50 mM NaOH corresponding to pH 1.3 and pH 12.7, respectively.

The titrations were carried out within a 50 mL beaker with a stirrer bar placed on a magnetic stirring plate. During the titrations the stirrer bar was continually rotated to ensure the pH was uniform throughout the solution. The sensor at the end of the pH probe was held above the stirrer bar within the solution (Figure 2.7a). As pH is temperature-dependent, all pH readings were taken in a temperature-controlled

environment to reduce error. The target temperature of the titrand was 25 °C; this was continuously monitored with the pH meter and the room temperature adjusted if required to account for heating induced through stirring or neutralisation reactions [27].

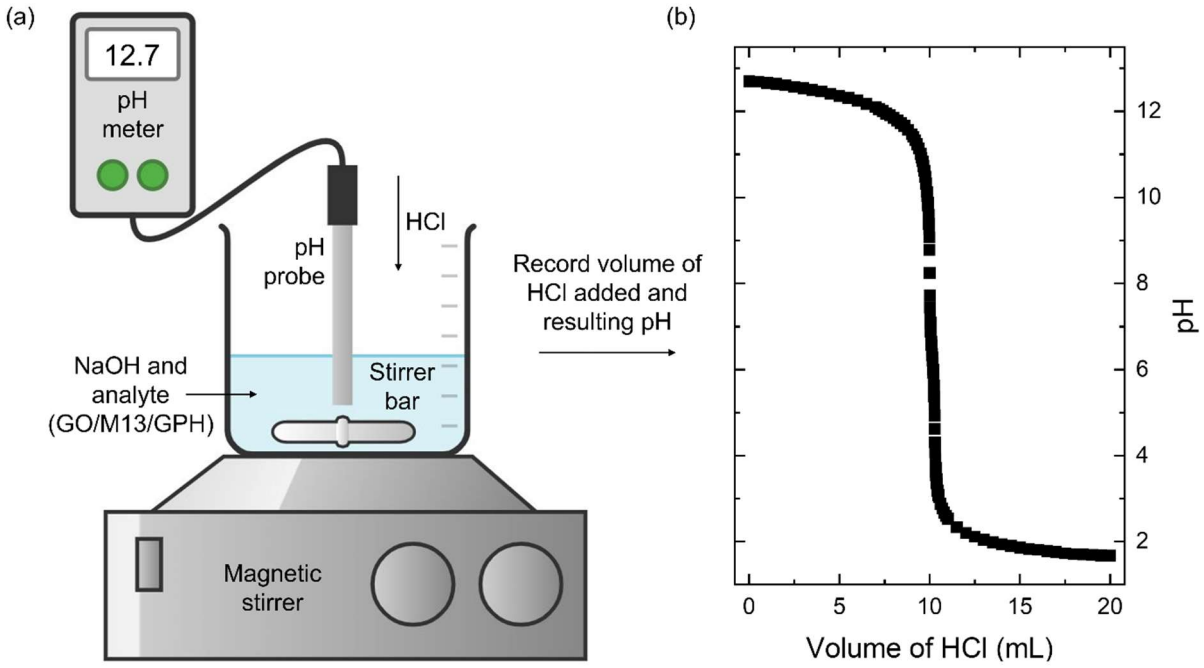

Figure 2.7: Titrations experimental set-up

(a) The experimental set-up for acid-base titrations and **(b)** an example of the results obtained by recording the volume of hydrochloric acid (HCl) to a solution of soidum hydroxide (NaOH) and measirong the pH. Created with Chemix **(**https://chemix.org**).**

Blank titrations were first taken as a baseline, with 20 mL of HCl being added incrementally to 10 mL of NaOH with a pipette. According to the stoichiometry, HCl and NaOH neutralises to pH 7 when equal concentrations and volumes are combined. Therefore, the addition of 20 mL of HCl to 10 mL of NaOH allowed pH changes in both the acid and alkali ranges to be observed. 10 mL of NaOH was deposited into the beaker. Varying volumes of HCl were then added to the NaOH with a pipette and the total volume of HCl and the pH was recorded. The volume of HCl added was dependent on the required pH. At the extrema of the pH scale, the addition of 1000 µL

produced a change in pH of between 0.01–0.1 whereas between pH 4–5 and pH 8–9, 10 µL of HCl altered the pH by up to 0.54. Therefore, the increments in which HCl was added to NaOH varied depending on the measured pH. For the GO and M13 titrations, 8 mL of NaOH was combined with 2 mL (10 mg) of GO and 2 mL (10 mg) M13 respectively, prior to the addition of HCl. Similarly, the GPH titrations involved combining 6 mL of NaOH with 2 mL of GO and 2 mL of M13. Each titration (blank, GO, M13 and GPH) was carried out three times to demonstrate repeatability.

The analysis of the titration data to determine the concentration of ionised groups and pK_a are given in Section 2.3.4.

2.2.7 Atomic Force Microscopy

Atomic force microscopy (AFM) uses an AFM probe, consisting of sharp tip attached to a cantilever, for high-resolution imaging. The tip raster scans across the sample surface and causes the cantilever to bend. The cantilever bending is detected with a laser beam, which reflects off the cantilever to a position-sensitive detector, translating it into cantilever movement (Figure 2.8a). This enables an image of the three-dimensional surface topography to be generated [28].

There are in two primary imaging modes for AFM: contact mode and tapping mode. In contact mode, the tip maintains constant contact with the sample, adjusting its height to ensure a constant applied force. However, lateral forces caused by the tip moving across soft samples can lead to damage. Tapping mode offers a viable alternative, where the cantilever oscillates close to its resonant frequency in a sinusoidal motion while scanning the sample. The tip only contacts the sample at the wave trough of the

oscillation, minimising lateral force. Proximity-induced changes in cantilever amplitude and resonance frequency serve as feedback parameters for mapping the sample morphology [29].

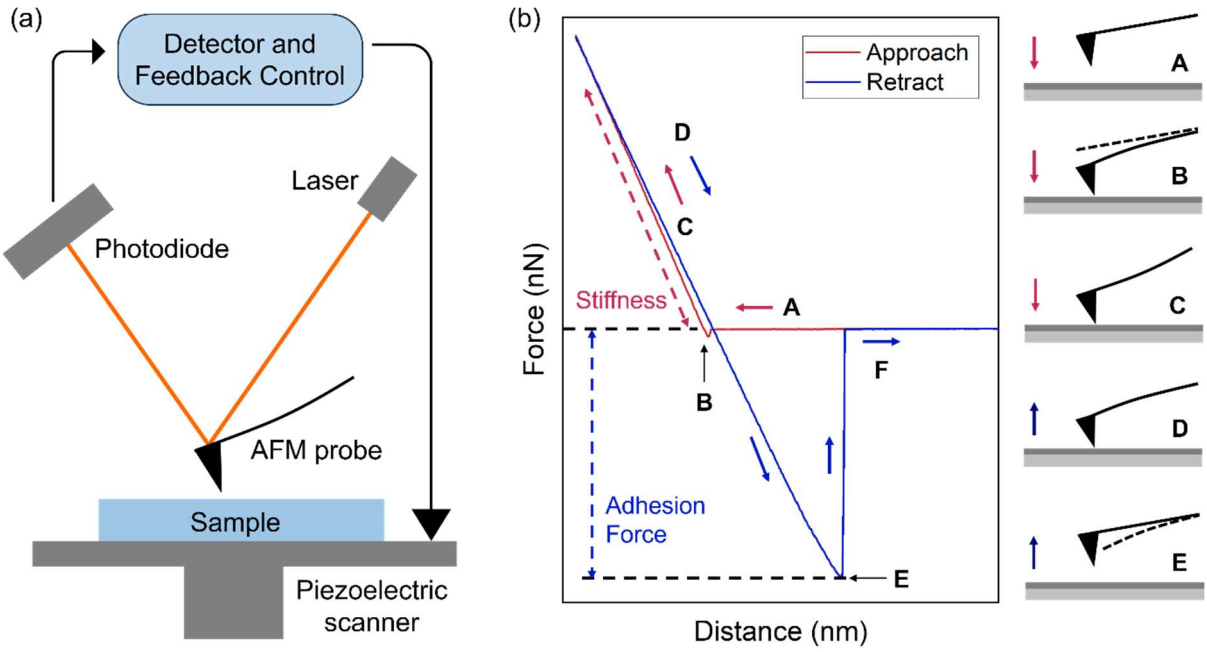

Figure 2.8: Atomic force microscopy

(a) A schematic of an atomic force microscope (AFM); **(b)** an example of a force-displace curve and a representation of the cantilever bending. Images based on [30, 31].

Additionally, AFM offers insights into the nanomechanical properties of a sample through force spectroscopy. The tip approaches and retracts from the sample from the sample, and the deflection of the cantilever is measured to generate deflection-distance curves. The deflection can be converted into force by determining the spring constant and sensitivity of the cantilever. Analysing the resulting force-distance curves (Figure 2.8b) enables the extraction of properties such as the stiffness of the sample and the adhesion force between the tip and the sample [32].

Force-distance curves were acquired using a Bruker Innova atomic force microscope equipped with Bruker DNP-10 probes. These probes consist of silicon nitride cantilevers with 20 nm silicon nitride tips, with a resonance frequency of 65 KHz and spring constant of 0.35 N/m.

2.2.8 Raman Spectroscopy

Raman spectroscopy is a rapid, non-destructive analytical technique which uses inelastic scattering to give insights into the chemical and structural composition of a sample [33]. During the scattering process, a molecule absorbs a photon and is excited from its initial state to a virtual energy state. As these states can only exist temporarily, the molecule instantaneously decays to a real energy state and a photon is emitted, with an energy corresponding to the energy difference between the real and virtual states [34]. If the initial state is identical to the final state, the photon has undergone elastic scattering, otherwise known as Rayleigh scattering, and the wavelength of the photon remains the same. On the other hand, inelastic scattering occurs if the initial state is not the same as the final state, causing a change in the photon's wavelength [35, 36]. If the scattered photon has a longer wavelength than the incident photon, it is referred to as Stokes Raman scattering. Conversely, if the scattered photon has a shorter wavelength, it is known as anti-Stokes Raman scattering (Figure 2.9a). In conventional Raman spectroscopy, typically only the Stokes Raman scattering is recorded and analysed as it produces a much higher intensity than anti-Stokes scattering [37]. The change in wavelength, known as the Raman shift, can be expressed in terms of the wavenumber and plotted against intensity to generate a Raman spectrum. This spectrum is characteristic of the sample's molecular environment, allowing detailed insights into its chemical composition, structure, lattice

vibrations and defects within a sample by analysing the positions, widths and intensities of the observed peaks [23, 38, 39].

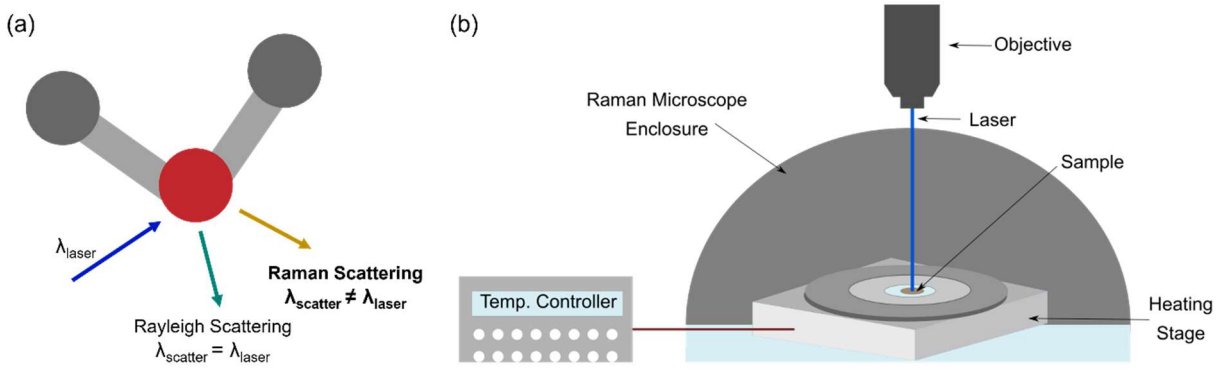

Figure 2.9: Raman spectroscopy

(a) A diagram depicting a laser incident on a molecule and the resulting scattered light. Image based on [16]. **(b)** Experimental set-up for Raman spectroscopy with an insitu heating stage.

In Chapter 4, Raman spectroscopy with an insitu heating stage was used to analyse changes to the structure of GPA with temperature (Figure 2.9b). The Raman microscope (Renishaw inVia Reflex Spectrometer System) was calibrated using Silicon with peak at 520 cm^{-1} [40]. The sample was then placed in the heating chamber, inserted into the chamber of Raman microscope, and connected to a temperature controller (Linkam Scientific Instruments Ltd TMS 94). Through initial investigations, it was found that the optimal laser wavelength to reduce damage to GPA was 442 nm at 0.5% laser power, with an exposure time of 120 s to reduce the fluorescent background. The temperature varied between 25°C and 300°C at a heating rate of 10°C/min and spectra were acquired at various increments. Three spectra were taken at the same position for each temperature to observe repeatability and ensure that the interaction between the laser and the sample was not inducing any structural changes. The spectra were processed using Origin Pro-through subtracting the baseline and fitting Lorentzian peaks to each spectrum (see Section 1.5.2).

In Chapter 6, Raman spectroscopy was utilised to observe changes to the structure of GPA through the integration of AuNPs. The Raman spectrometer (Renishaw inVia Qontor) was calibrated with Silicon, characterised by a Raman peak at 520 cm^{-1} [41]. GPA and GPA with 5 nm and 20 nm diameter AuNPs were then placed into the chamber and Raman spectra were obtained at both 514 nm and 633 nm wavelengths. The 633 nm spectra were recorded with x50 objective, 5% laser power (719 μW), 10 seconds acquisition time and 10 accumulations and the 514 nm spectra were recorded with a x20 objective, 5% laser power (1.03 mW), 60 seconds acquisition time and 3 accumulations. The spectra were processed with Python, subtracting the baseline and optimising the peak fitting.

2.2.9 Dynamic Vapor Sorption (DVS)

Dynamic vapor sorption (DVS) is a gravimetric technique used to characterise the interactions between solids and vapours. A sample is placed in a chamber on an ultrabalance within a temperature-controlled chamber, allowing for highly accurate mass measurements. A humidity control system regulates the relative humidity (RH), or partial pressure (PP), of the solvent vapour within the chamber through the mixing of dry and saturated air (Figure 2.10). As the PP within the chamber is varied in a stepwise manner, the mass change of the sample is continuously monitored, establishing the relationship between the sample mass and PP over time. By allowing the mass to reach equilibrium at each PP stage, whereby the sample mass does not change by more than 0.002% over a period of 10 minutes, an isotherm of the equilibrium mass at each measured PP can be determined [42]. By analysing the mass variation over time as the PP is varied, and the resulting isotherm, insights into the sample characteristics can be ascertained, such as its sorption capacity, pore

structure, stability, sorption kinetics, and interactions between the sample and the vapour [43, 44].

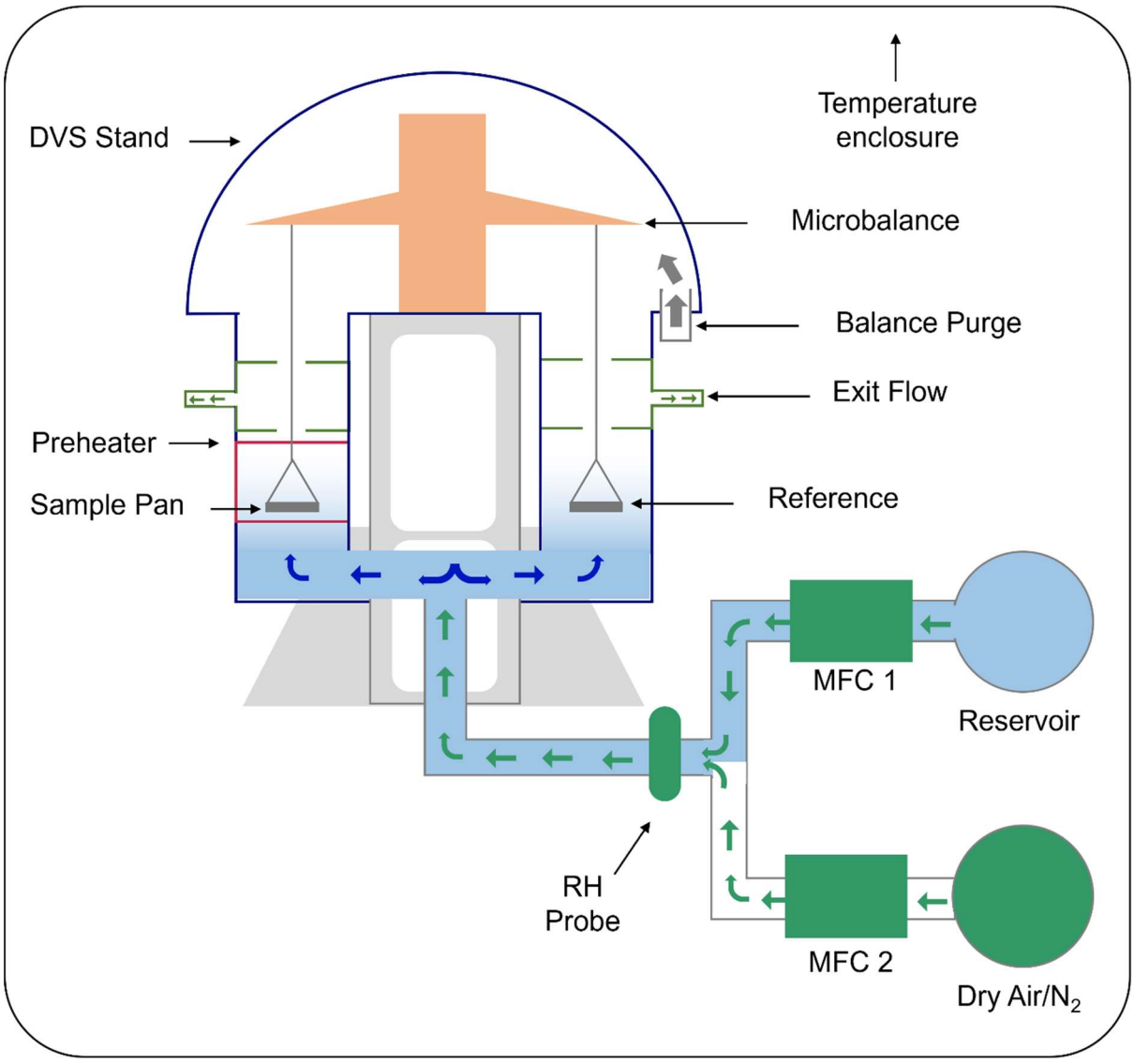

Figure 2.10: Dynamic vapor sorption

A schematic illustration of the dynamic vapor sorption (DVS) instrument. The system mixes dry and saturated air in precise proportions using mass flow controllers (MFCs). The sample, positioned on a microbalance, is subjected to a continuous airflow with a controlled and constant relative humidity. Image based on [45].

Sorption measurements were performed with a DVS Resolution, at a constant temperature of 25 °C and flow rate of 200 mL/min. The partial pressure (PP) of water,

ethanol and acetone were varied from 0% to 90% to 0% in increments of 10%. The stop criterion for each stage was defined as a mass change of less than 0.002% per minute, stable over a period of 10 min, for a minimum duration of 30 min and a maximum of 12 h. This process was repeated with at least three GPA samples to ensure reproducibility of the sorption measurements.

2.2.10 Electrical Conductivity

Electrical conductivity, σ, refers to material's capacity to conduct an electrical current, which depends on the carrier concentration and carrier mobility.

The electrical conductivity of a material is determined by attaching electrodes to the material to form a circuit, allowing the application of a variable voltage (*V*) across the sample. By systematically varying the applied voltage and measuring the resulting current (*I*) through the material, an I-V characteristic curve is generated. The slope of the I-V curve, which corresponds to the ratio of current to voltage, is directly related to the material's resistance *R* and the conductivity σ:

$$\sigma = \frac{1}{R}\frac{L}{A} = \frac{V}{I}\frac{L}{A} \tag{2.2}$$

where *L* and *A* correspond to the sample length and cross sectional area respectively [46].

The conductivity of the GPAs, GPAs with 5 nm AuNPs (GPA-Au_{5nm}) and GPAs with 20 nm AuNPs (GPA-Au_{20nm}) were measured with a Keithley 617 Electrometer. 100 µL of GPH were dried on 10 x 10 mm glass substrates with conductive copper tape (RS Pro) spanning 25 mm at each end, allowing the current to pass through 5 mm of the

resulting GPA. An electrical connection between the GPA and conductive tape was ensured with silver conductive lacquer. To minimise current leakage, triaxial cables were used and the set-up was placed within a grounded outer electromagnetic interference shielding enclosure (Figure 2.11). The conductivity of three different GPA, GPA-Au_{5nm} and GPA-Au_{20nm} were measured and averaged to ensure reproducibility and measurement accuracy.

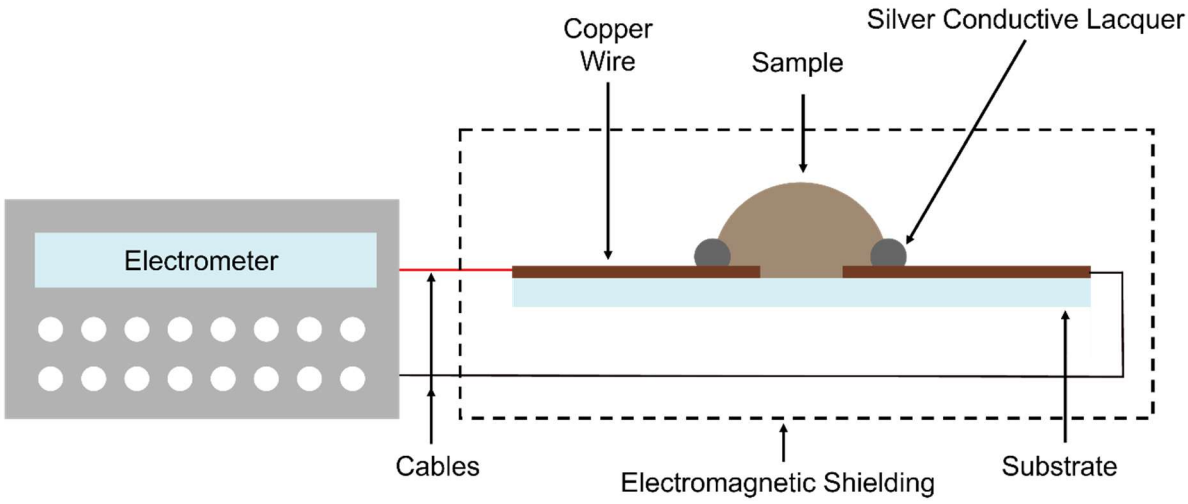

Figure 2.11: Experimental setup for conductivity measurements

A schematic illustrating the experimental setup for measuring the conductivity of GPAs. The GPAs were connected to copper wires using conductive silver lacquer, which were then linked to an electrometer for applying voltage and measuring current. Electromagnetic shielding was employed to ensure accurate measurement of nanoamp-scale currents.

2.3 Data Analysis

2.3.1 Error Propagation

Error propagation describes how measurement uncertainties are processed through calculations performed using those measurements. One error propagation method is the functional approach, which essentially maps the changes in a variable and a function (Figure 2.12). It offers several advantages, such as its suitability for

spreadsheet analysis, ability to generate asymmetric error bars, and ease of application for both single-variable and multi-variable functions [47].

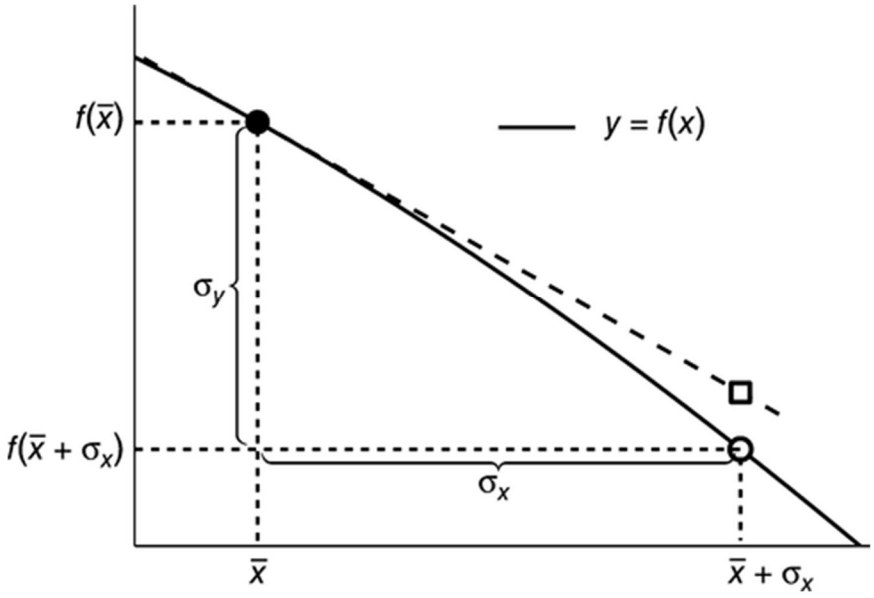

Figure 2.12: Error propagation using the functional approach

A schematic of the functional approach illustrating how this error propagation method maps the uncertainty in a variable x, σ_x, through a function $y = f(\bar{x})$ to determine the error of the function, σ_y. The value of the ordinate of the white square is given by $f(\bar{x}) + \sigma_x \frac{df}{dx}$. Figure from [48].

For a variable $\bar{x}$ with an error of σ_x, inputted into a function $y = f(\bar{x})$, the functional approach gives its error σ_y, as:

$$\sigma_y = |f(\bar{x} + \sigma_x) - f(\bar{x})|. \tag{2.3}$$

For multivariable functions, the method of error propagation varies depending on the specific function, with detailed calculations outlined in [49].

In this thesis, the primary application of the functional approach involved propagating errors when calculating the mean of multiple values, each with its own error. For n number of variables x_i with errors σ_{x_i}, the mean Z and its error σ_Z are given by:

$$Z = \frac{\sum_{i=1}^{n} x_i}{n} \tag{2.4}$$

$$\sigma_Z = \frac{\sqrt{\sum_{i=1}^{n} \left[\left(x_i + \sigma_{x_i} \right) - x_i \right]^2}}{n} \tag{2.5}$$

2.3.2 Bayesian Information Criterion (BIC)

The Bayesian Information Criterion (BIC) is a numerical metric used as a criterion for model selection in statistical analysis. It provides a balance between the goodness of fit and model complexity by penalising the addition of parameters, which is not included in the traditional least squares fitting. It is given by:

$$BIC = -2 \log L + K \log N \tag{2.6}$$

where *L* is the likelihood, *K* is the number of parameters and *N* is the number of data points [50].

When evaluating the goodness of fit for different models applied to the same dataset, a lower BIC value indicates a better fit. However, the difference in BIC values between models ΔBIC should also be considered. For two models, M_1 and M_2, where M_2 has a higher BIC value than M_1:

- ΔBIC < 2: Indicates weak evidence favouring M_2, and additional factors such as the physical relevance of the fitted parameters should guide model selection.
- 2 < Δ BIC < 6: Provides positive evidence to favour M_2 over M_1.

- $6 < \Delta BIC < 10$: Suggests strong evidence supporting M_2 as the better model.
- $\Delta BIC > 10$: Indicates very strong evidence in favour of M_2.

These thresholds are widely accepted in statistical literature and provide a framework for model selection [51].

An important characteristic of BIC is its asymptotic properties, which describe how the criterion behaves as *N* becomes very large. The term *K log N* grows with *N*, increasingly penalising models with more parameters. This ensures that additional complexity is only accepted if it leads to a substantial improvement in the likelihood function, log *L* [52].

Compared to other model selection criteria, BIC is particularly suited for balancing goodness of fit and minimalism in modelling. For example, the Akaike Information Criterion (AIC) emphasises goodness of fit more heavily than BIC and may favour more complex models, and methods such as cross-validation or adjusted R^2 focus on goodness of fit but may not directly penalise complexity to the same extent. In this analysis, BIC was chosen because it provides an objective and rigorous method for comparing models while minimising the risk of overfitting [53].

The determination of the BIC values enabled the optimal fitting for peak identification in the Raman spectra presented in Chapter 4 and Chapter 6, as well as for the selection of the optimal kinetic sorption models discussed in Chapter 5.

2.3.3 Peak Fitting

The optimal number of peaks and peak fit were determined with Origin Pro (Chapter 3, Chapter 4) or Python (Chapter 6). To identify the best fit, initial guesses were

provided for the peak type (see Section 1.5.2 for further information of Gaussian and Lorentzian peaks) the number of peaks, as well as their positions and widths. Each model was evaluated, and the optimal fit was selected based on the lowest Bayesian Information Criterion (BIC) value (Section 2.3.2). In cases where a mixed Gaussian–Lorentzian line shape provided a better representation of the experimental data, such as in Chapter 6, this was implemented by fitting both a Gaussian and Lorentzian peak at the same position.

2.3.4 Concentration of Ionised Groups and pK_a

An optimised data analysis method was utilised to accurately yield the concentration of ionised groups and pK_a distribution from the titration experiments (obtained as described in Section 2.2.6). Firstly, the measured pH was set as the abscissa and the input amount of acid as the ordinate (i.e., difference in acid added between the sample and the reference) to reach the pH of interest. Subsequently, the difference in volume of HCl added at each pH between the blank titration and the titrations involving each analyte must be calculated. However, as the measured pH values vary between titrations, these cannot be directly subtracted.

Although there are multiple established methods to enable, they have distinct disadvantages. For example, a polynomial fit or spline interpolation can be applied to the pH curve to estimate new data points, enabling the curves to be subtracted from one another at each pH. However, this can often lead to errors due to over-smoothing of the data, and, near extreme pH values, this can produce very large or “infinite” slopes due to the logarithmic nature of pH [54, 55]. Another method is by using a Gran

plot, which uses linear approximations between pH and volume, however these can be less accurate for multiproteic systems over wide pH ranges [56].

An alternative method is the time-series approach. Each measurement point is recorded as a triplet (t_i, pH_i, V_i) where t_i is the time, pH_i is the measured pH, and V_i is the volume of acid added. Time is treated as an independent variable, and then interpolating in time generates the continuous functions pH(t) and V(t). Then, for each given pH, the point at which pH = pH(t) is found for both the sample (t_{sample}) and the reference (t_{ref}). These times are then used to find V(t_{sample}) and V(t_{ref}) and compute their difference for the specific pH. This difference, normalised by the amount of analyte, is the corrected volume of acid needed to shift from one pH to another, which can then differentiate to obtain the pK_a distribution. This approach circumvents the numerical difficulties that arise from polynomial fitting directly in pH–volume space, especially near extreme pH regions.

Using this method, the difference between the time series of the sample and the reference was obtained and the abscissa of times was converted back to pH, enabling plotting the difference as discrete points, representing the concentration of analysed groups for each analyte. To compare the concentration of ionised groups for each analyte, the volume of HCl was converted into moles and divided by the quantity of NaOH within the titrand and subsequently divided by the weight of analyte in the titrand. Finally, the first derivative of the difference as a time series was calculated to obtain the pK_a distribution. The abscissa of times was converted back to pKa after the differentiation. The optimised data analysis method was performed using built-in functions via Wolfram Mathematica.

2.3.5 Pore Size Analysis

Understanding the pore sizes present in GPAs is critical for evaluating their structural and functional properties, as pore size plays a pivotal role in determining properties such as mechanical stability and compressive strength [57]. However, measuring pore size accurately poses significant challenges, particularly considering the structural characteristics of GPAs.

Conventional methods like gas sorption, such as the Brunauer–Emmett–Teller (BET) method, are widely used for detecting pore sizes in the range of 2–50 nm [58]. While effective for mesoporous materials, BET is unsuitable for GPAs, which predominantly exhibit macropores with sizes exceeding this range. Furthermore, the mass requirements for BET measurements, combined with the inherently low density of GPAs, complicate the generation of sufficient sample quantities for analysis [59, 60]. Another widely used technique, mercury porosimetry, relies on the infiltration of pores with high-pressure mercury to measure pore size distribution. However, this method often deforms the pore structure or destroys the aerogel [61].

Considering these challenges, SEM imaging emerges as an alternative for assessing the pore size distribution in GPAs, following a methodology described by Hojat et al. [57], depicted in Figure 2.13. The process involved using ImageJ software to analyse SEM images systematically. First, the pixel size was converted to μm using the image scale bar for accurate pore size analysis. A Gaussian Blur filter was then applied to reduce noise and artefacts, ensuring that small imperfections in the images were not misinterpreted as pores. Subsequently, the contrast was enhanced to improve pore visibility, and a threshold was applied to generate a binary image. The separation of

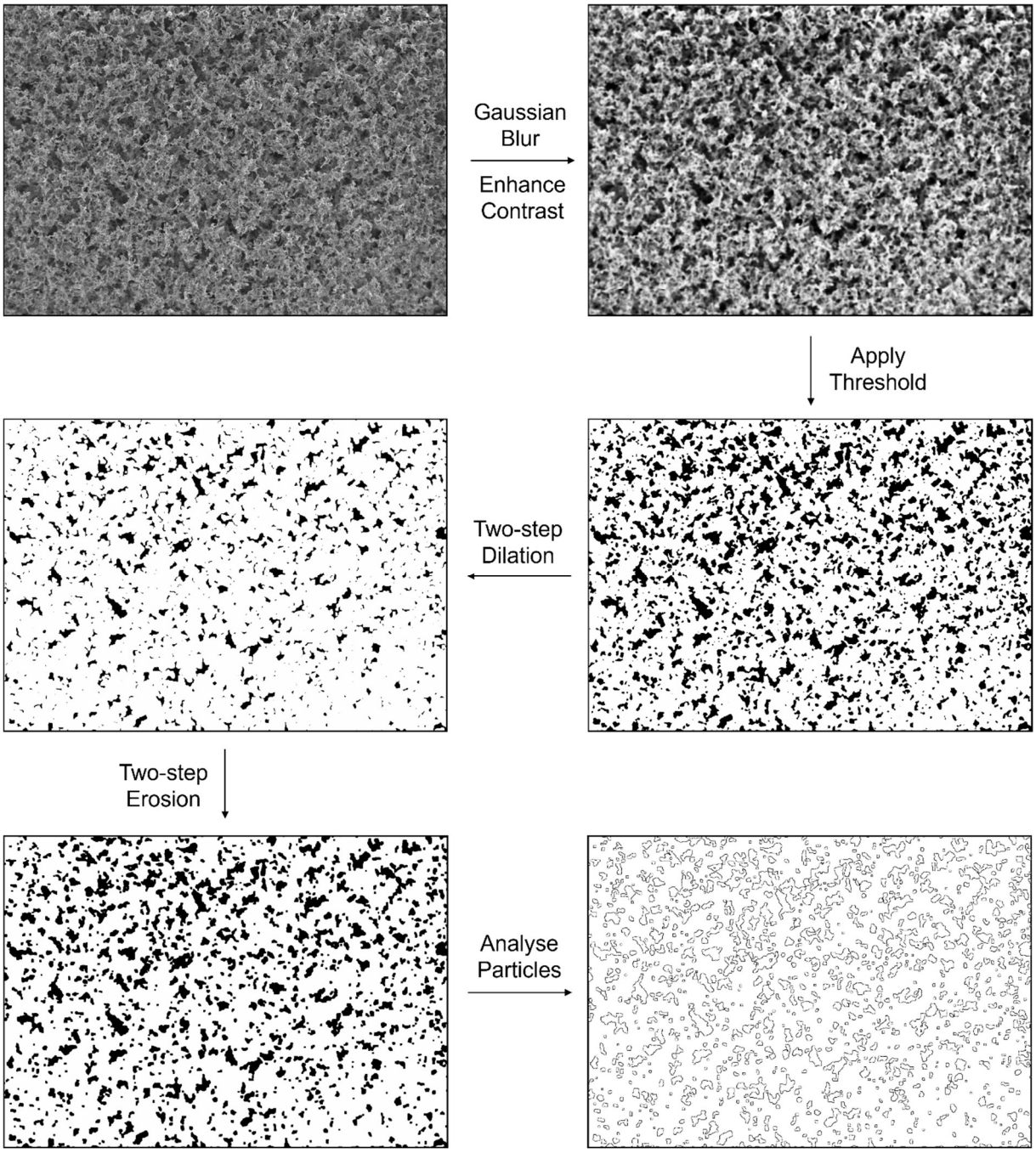

Figure 2.13: Pore size analysis

The workflow for determining the pore size distribution of GPA from SEM images, based on the method developed by Hojat et al [57]. Using ImageJ, a Gaussian blur is applied to the images, and the contrast is enhanced. To identify and isolate the pores, the image is threshold and is subsequently subjected a two-step dilation followed by a two-step erosion. Finally, the “Analyse Particles” function in ImageJ is applied to provide the areas of the identified pores.

individual pores was achieved through a two-step dilation followed by a two-step erosion process. This allowed for pore area determination, enabling the calculation of pore diameters and obtaining the pore size distribution.

The high-resolution images of the pore morphology and spatial distribution offers detailed insights into the pore size distribution [57]. However, this technique has inherent limitations, as SEM provides only a 2D representation of the pore distribution near the GPA surface. While this limitation could be partially addressed by slicing the GPA to analyse cross-sections, its fragile nature made this impractical, as any attempt to obtain a cross-section compressed the aerogel, altering its pore structure.

Furthermore, thresholding could not be automated due to image variability, introducing an element of subjectivity and potential human error in the measurements. To mitigate this, multiple measurements were taken. Specifically, three aerogels of each type were analysed, with three images captured per aerogel, resulting in a total of nine images.

From these images, the pore size distribution was determined, and the mean pore size along with the standard error was calculated, mitigating potential thresholding inconsistencies.

2.4 References

[1] Graphene Supermarket. "Graphene Oxide." Graphene Supermarket. https://cdn.shopify.com/s/files/1/0572/0188/5393/files/Graphene_Oxide-Data-Sheet-Graphene-Supermarket.pdf?v=1626799704 (accessed 26/06, 2023).

[2] S. Nahar, "Phase-Separation Characteristics of Bitumen and Their Relation to Damage-Healing," PhD, Structural Engineering, Delft University of Technology 2016.

[3] P. Passaretti, I. Khan, T. R. Dafforn, and P. Goldberg Oppenheimer, "Improvements in the Production of Purified M13 Bacteriophage Bio-Nanoparticle," *Scientific Reports,* vol. 10, no. 1, p. 18538, 2020, doi: 10.1038/s41598-020-75205-3.

[4] C. Potts, "Statement of Nonpathogenicity," Thermo Fisher Scientific 2016. [Online]. Available: https://assets.fishersci.com/TFS-Assets/LSG/manuals/PG1572-PJT1331-COL12226-Statement-NonPathogenicity-FHR.PDF

[5] Fisher Scientific. "Invitrogen One Shot™ Top10f' Chemically Competent E. Coli." Fisher Scientific. https://www.thermofisher.com/order/catalog/product/C303003 (accessed 24/12, 2024).

[6] Sigma-Aldrich. "765430 Gold Nanoparticles." Sigma-Aldrich,. https://www.sigmaaldrich.com/GB/en/product/aldrich/765430#product-documentation (accessed 24/12, 2024).

[7] Sigma-Aldrich. "765511 Gold Nanoparticles." Sigma-Aldrich. https://www.sigmaaldrich.com/GB/en/product/aldrich/765511 (accessed 24/12, 2024).

[8] P. Passaretti, "M13 Bacteriophage: A Nanotool for the Fabrication of Novel Self-Assembled Nanostructures " PhD Thesis in Nanotechnology, Chemical Engineering, University of Birmingham, 2019.

[9] S. Pentassuglia, V. Agostino, and T. Tommasi, "Eab—Electroactive Biofilm: A Biotechnological Resource," in *Encyclopedia of Interfacial Chemistry*, K. Wandelt Ed. Oxford: Elsevier, 2018, pp. 110-123.

[10] S. M. Nilapwar, M. Nardelli, H. V. Westerhoff, and M. Verma, "Absorption Spectroscopy," in *Methods in Enzymology*, vol. 500, D. Jameson, M. Verma, and H. V. Westerhoff Eds.: Academic Press, 2011, ch. 4, pp. 59-75.

[11] C. Jose Chirayil, J. Abraham, R. Kumar Mishra, S. C. George, and S. Thomas, " Instrumental Techniques for the Characterization of Nanoparticles," in *Thermal and Rheological Measurement Techniques for Nanomaterials Characterization*, S. Thomas, R. Thomas, A. K. Zachariah, and R. K. Mishra Eds.: Elsevier, 2017, ch. 1, pp. 1-36.

[12] Z. P. Tshabalala, D. N. Oosthuizen, H. C. Swart, and D. E. Motaung, "Tools and Techniques for Characterization and Evaluation of Nanosensors," in *Nanosensors for Smart Cities*, B. Han, V. K. Tomer, T. A. Nguyen, A. Farmani, and P. Kumar Singh Eds.: Elsevier, 2020, ch. 5, pp. 85-110.

[13] H. Wang and P. K. Chu, "Surface Characterization of Biomaterials," in *Characterization of Biomaterials*, A. Bandyopadhyay and S. Bose Eds. Oxford: Academic Press, 2013, ch. 4, pp. 105-174.

[14] T. G. Mayerhöfer, S. Pahlow, and J. Popp, "The Bouguer-Beer-Lambert Law: Shining Light on the Obscure," *ChemPhysChem,* vol. 21, no. 18, pp. 2029-2046, 2020, doi: 10.1002/cphc.202000464.

[15] M. Abd Mutalib, M. A. Rahman, M. H. D. Othman, A. F. Ismail, and J. Jaafar, "Scanning Electron Microscopy (Sem) and Energy-Dispersive X-Ray (Edx) Spectroscopy," in *Membrane Characterization*, N. Hilal, A. F. Ismail, T. Matsuura, and D. Oatley-Radcliffe Eds.: Elsevier, 2017, ch. 9, pp. 161-179.

[16] C.-Y. Hsu, A. M. Rheima, Z. s. Abbas, M. U. Faryad, M. M. Kadhim, U. S. Altimari, A. H. Dawood, A. d. jawad al-bayati, Z. T. Abed, R. S. Radhi, A. S. Jaber, S. K. Hachim, F. K. Ali, Z. H. Mahmoud, G. Behzadi pour, and E. Kianfar, "Nanowires Properties and Applications: A Review Study," *South African Journal of Chemical Engineering,* vol. 46, pp. 286-311, 2023, doi: 10.1016/j.sajce.2023.08.006.

[17] C. Zeng, C. Vitale-Sullivan, and X. Ma, "In Situ Atomic Force Microscopy Studies on Nucleation and Self-Assembly of Biogenic and Bio-Inspired Materials," *Minerals,* vol. 7, p. 158, 2017, doi: 10.3390/min7090158.

[18] P. P. Pednekar, S. C. Godiyal, K. R. Jadhav, and V. J. Kadam, "Mesoporous Silica Nanoparticles: A Promising Multifunctional Drug Delivery System," in *Nanostructures for Cancer Therapy*, A. Ficai and A. M. Grumezescu Eds.: Elsevier, 2017, pp. 593-621.

[19] M. Omidi, A. Fatehinya, M. Farahani, Z. Akbari, S. Shahmoradi, F. Yazdian, M. Tahriri, K. Moharamzadeh, L. Tayebi, and D. Vashaee, "Characterization of Biomaterials," in *Biomaterials for Oral and Dental Tissue Engineering*, L. Tayebi and K. Moharamzadeh Eds.: Woodhead Publishing, 2017, ch. 7, pp. 97-115.

[20] A. F. Ismail, K. C. Khulbe, and T. Matsuura, "Ro Membrane Characterization," in *Reverse Osmosis*, A. F. Ismail, K. C. Khulbe, and T. Matsuura Eds.: Elsevier, 2019, ch. 3, pp. 57-90.

[21] S.-J. Park and M.-K. Seo, "Intermolecular Force," in *Interface Science and Technology*, vol. 18, S.-J. Park and M.-K. Seo Eds.: Elsevier, 2011, ch. 1, pp. 1-57.

[22] E. Joseph and G. Singhvi, "Multifunctional Nanocrystals for Cancer Therapy: A Potential Nanocarrier," in *Nanomaterials for Drug Delivery and Therapy*, A. M. Grumezescu Ed.: William Andrew Publishing, 2019, ch. 4, pp. 91-116.

[23] K. Liu, Q. Zhao, B. Li, and X. Zhao, "Raman Spectroscopy: A Novel Technology for Gastric Cancer Diagnosis," *Frontiers in Bioengineering and Biotechnology,* Review vol. 10, 2022, doi: 10.3389/fbioe.2022.856591.

[24] F. Varenne, J. Botton, C. Merlet, J.-J. Vachon, S. Geiger, I. C. Infante, M. Chehimi, and C. Vauthier, "Toward a Standardization of Physico-Chemical Protocols for Nanomedicine Characterization: Ii. Zeta Potential Measurements," presented at the International Congress of Metrology, Paris, France, 2015. [Online]. Available: 10.1051/metrology/20150014003.

[25] M. Korn, "Titrimetry: Photometric," in *Reference Module in Chemistry, Molecular Sciences and Chemical Engineering*: Elsevier, 2019.

[26] G. Lefèvre, M. Duc, and M. Fédoroff, "Accuracy in the Determination of Acid-Base Properties of Metal Oxides Surfaces," in *Interface Science and Technology*, vol. 11, J. Lützenkirchen Ed.: Elsevier, 2006, ch. 2, pp. 35-66.

[27] V. S. Kulkarni and C. Shaw, "Miscellaneous Physical, Chemical, and Microbiological Test Methods," in *Essential Chemistry for Formulators of Semisolid and Liquid Dosages*, V. S. Kulkarni and C. Shaw Eds. Boston: Academic Press, 2016, ch. 11, pp. 193-221.

[28] P. Eaton, P. West, P. Eaton, and P. West, "Afm Instrumentation," in *Atomic Force Microscopy*: Oxford University Press, 2010, ch. 2, sec. Oxford Academic, p. 0.

[29] Y. F. Dufrêne, T. Ando, R. Garcia, D. Alsteens, D. Martinez-Martin, A. Engel, C. Gerber, and D. J. Müller, "Imaging Modes of Atomic Force Microscopy for Application in Molecular and Cell Biology," *Nature Nanotechnology,* vol. 12, no. 4, pp. 295-307, 2017, doi: 10.1038/nnano.2017.45.

[30] M. Shawky, E.-S. El-Shereafy, I. Ahmed, and A. Shenouda, "A Study on Synthesis and Characterization of Some (I -Iv -Vi) Groups Compounds for Solar Cells Energy Application," 2016.

[31] Y. Sun, P. Passaretti, I. Hernandez, J. Gonzalez, W. Liu, F. Rodriguez, D. J. Dunstan, P. Goldberg Oppenheimer, and C. J. Humphreys, "Nanomechanics of Graphene Oxide-Bacteriophage Based Self-Assembled Porous Composites," *Scientific Reports,* vol. 10, no. 1, p. 15618, 2020, doi: 10.1038/s41598-020-72372-1.

[32] P. Eaton, P. West, P. Eaton, and P. West, "Afm Modes," in *Atomic Force Microscopy*: Oxford University Press, 2010, ch. 3, sec. Oxford Academic, p. 0.

[33] L. Mandrile, S. Rotunno, L. Miozzi, A. M. Vaira, A. M. Giovannozzi, A. M. Rossi, and E. Noris, "Nondestructive Raman Spectroscopy as a Tool for Early Detection and Discrimination of the Infection of Tomato Plants by Two Economically Important Viruses," *Analytical Chemistry,* vol. 91, no. 14, pp. 9025-9031, 2019, doi: 10.1021/acs.analchem.9b01323.

[34] A. Orlando, F. Franceschini, C. Muscas, S. Pidkova, M. Bartoli, M. Rovere, and A. Tagliaferro, "A Comprehensive Review on Raman Spectroscopy Applications," *Chemosensors,* vol. 9, no. 9, p. 262, 2021, doi: 10.3390/chemosensors9090262.

[35] D. Cialla-May, M. Schmitt, and J. Popp, "Theoretical Principles of Raman Spectroscopy," *Physical Sciences Reviews,* vol. 4, no. 6, 2019, doi: doi:10.1515/psr-2017-0040.

[36] L. Nasdala, D. Smith, R. Kaindl, and M. Ziemann, "Raman Spectroscopy: Analytical Perspectives in Mineralogical Research," in *Spectroscopic Methods in Mineralogy*, vol. 12, A. Beran and E. Libowitzky Eds.: Mineralogical Society of Great Britain and Ireland, 2004, pp. 281-343.

[37] T. H. Kauffmann, N. Kokanyan, and M. Fontana, D., "Use of Stokes and Anti-Stokes Raman Scattering for New Applications," *Journal of Raman Spectroscopy,* vol. 50, no. 3, pp. 418-424, 2019, doi: 10.1002/jrs.5523.

[38] X. Zhang, Q.-H. Tan, J.-B. Wu, W. Shi, and P.-H. Tan, "Review on the Raman Spectroscopy of Different Types of Layered Materials," *Nanoscale,* 10.1039/C5NR07205K vol. 8, no. 12, pp. 6435-6450, 2016, doi: 10.1039/C5NR07205K.

[39] E. del Corro, L. Kavan, M. Kalbac, and O. Frank, "Strain Assessment in Graphene through the Raman 2d′ Mode," *The Journal of Physical Chemistry C,* vol. 119, no. 45, pp. 25651-25656, 2015, doi: 10.1021/acs.jpcc.5b09643.

[40] K. Uchinokura, T. Sekine, and E. Matsuura, "Raman Scattering by Silicon," *Solid State Communications,* vol. 11, no. 1, pp. 47-49, 1972, doi: 10.1016/0038-1098(72)91127-1.

[41] W. Liu and G. Speranza, "Tuning the Oxygen Content of Reduced Graphene Oxide and Effects on Its Properties," *ACS Omega,* vol. 6, no. 9, pp. 6195-6205, 2021, doi: 10.1021/acsomega.0c05578.

[42] S. Glass, C. Boardman, and S. Zelinka, "Short Hold Times in Dynamic Vapor Sorption Measurements Mischaracterize the Equilibrium Moisture Content of Wood," *Wood Science and Technology,* vol. 51, pp. 243-260, 2017, doi: 10.1007/s00226-016-0883-4.

[43] S. Sheokand, S. R. Modi, and A. K. Bansal, "Dynamic Vapor Sorption as a Tool for Characterization and Quantification of Amorphous Content in Predominantly Crystalline Materials," *Journal of Pharmaceutical Sciences,* vol. 103, no. 11, pp. 3364-3376, 2014, doi: 10.1002/jps.24160.

[44] K. S. W. Sing, "Reporting Physisorption Data for Gas/Solid Systems with Special Reference to the Determination of Surface Area and Porosity (Provisional)," *Pure and Applied Chemistry,* vol. 54, no. 11, pp. 2201-2218, 1982, doi: 10.1351/pac198254112201.

[45] L. Qiu, N. Zhu, Y. Feng, E. E. Michaelides, G. Żyła, D. Jing, X. Zhang, P. M. Norris, C. N. Markides, and O. Mahian, "A Review of Recent Advances in Thermophysical Properties at the Nanoscale: From Solid State to Colloids," *Physics Reports,* vol. 843, pp. 1-81, 2020, doi: 10.1016/j.physrep.2019.12.001.

[46] Q. Jiang, "Thermoelectric Pedot Measurement Techniques," in *Advanced Pedot Thermoelectric Materials*, F. Jiang, C. Liu, and J. Xu Eds.: Woodhead Publishing, 2022, ch. 8, pp. 199-217.

[47] I. G. Hughes and T. P. A. Hase, "Error Propagation: A Functional Approach," *Journal of Chemical Education,* vol. 89, no. 6, pp. 821-822, 2012, doi: 10.1021/ed2004627.

[48] S. Claramunt, A. Varea, D. López-Díaz, M. M. Velázquez, A. Cornet, and A. Cirera, "The Importance of Interbands on the Interpretation of the Raman Spectrum of Graphene Oxide," *The Journal of Physical Chemistry C,* vol. 119, no. 18, pp. 10123-10129, 2015, doi: 10.1021/acs.jpcc.5b01590.

[49] I. G. Hughes and T. P. A. Hase, *Measurements and Their Uncertainties: A Practical Guide to Modern Error Analysis*. New York: Oxford University Press Inc., 2010.

[50] W. D. Penny, J. Mattout, and N. Trujillo-Barreto, "Bayesian Model Selection and Averaging," in *Statistical Parametric Mapping*, K. Friston, J. Ashburner, S. Kiebel, T. Nichols, and W. Penny Eds. London: Academic Press, 2007, ch. 35, pp. 454-467.

[51] J. Lorah and A. Womack, "Value of Sample Size for Computation of the Bayesian Information Criterion (Bic) in Multilevel Modeling," *Behavior Research Methods,* vol. 51, no. 1, pp. 440-450, 2019, doi: 10.3758/s13428-018-1188-3.

[52] Z. Bai, K. P. Choi, and Y. Fujikoshi, "Consistency of Aic and Bic in Estimating the Number of Significant Components in High-Dimensional Principal Component Analysis," *The Annals of Statistics,* vol. 46, pp. 1050-1076, 2018, doi: 10.1214/17-AOS1577.

[53] J. Kuha, "Aic and Bic: Comparisons of Assumptions and Performance," *Sociological Methods & Research - SOCIOL METHOD RES,* vol. 33, pp. 188-229, 2004, doi: 10.1177/0049124103262065.

[54] T. J. Bandosz, J. Jagiello, C. Contescu, and J. A. Schwarz, "Characterization of the Surfaces of Activated Carbons in Terms of Their Acidity Constant Distributions," *Carbon,* vol. 31, no. 7, pp. 1193-1202, 1993, doi: 10.1016/0008-6223(93)90072-I.

[55] B. Konkena and S. Vasudevan, "Understanding Aqueous Dispersibility of Graphene Oxide and Reduced Graphene Oxide through Pka Measurements," *The Journal of Physical Chemistry Letters,* vol. 3, no. 7, pp. 867-872, 2012, doi: 10.1021/jz300236w.

[56] W. C. Keene and J. N. Galloway, "Gran's Titrations: Inherent Errors in Measuring the Acidity of Precipitation," *Atmospheric Environment (1967),* vol. 19, no. 1, pp. 199-202, 1985, doi: 10.1016/0004-6981(85)90152-0.

[57] N. Hojat, P. Gentile, A. M. Ferreira, and L. Šiller, "Automatic Pore Size Measurements from Scanning Electron Microscopy Images of Porous

Scaffolds," *Journal of Porous Materials,* vol. 30, no. 1, pp. 93-101, 2023, doi: 10.1007/s10934-022-01309-y.

[58] P. S. Liu and G. F. Chen, "Characterization Methods: Basic Factors," in *Porous Materials*, P. S. Liu and G. F. Chen Eds. Boston: Butterworth-Heinemann, 2014, ch. 9, pp. 411-492.

[59] P. Passaretti, Y. Sun, I. Khan, K. Chan, R. Sabo, H. White, T. R. Dafforn, and P. G. Oppenheimer, "Multifunctional Graphene Oxide-Bacteriophage Based Porous Three-Dimensional Micro-Nanocomposites," *Nanoscale,* 10.1039/C9NR03670A vol. 11, no. 28, pp. 13318-13329, 2019, doi: 10.1039/C9NR03670A.

[60] E. Karg, G. A. Ferron, G. Schumann, and O. Schmid, "Specific Bet Surface Area Measurement of Low-Mass-Samples " in *ETH Nanoparticles Conference*, Zurich, Switzerland, 2008. [Online]. Available: https://www.nanoparticles.ch/archive/2008_Karg_PR.pdf. [Online]. Available: https://www.nanoparticles.ch/archive/2008_Karg_PR.pdf

[61] G. Horvat, M. Pantić, Ž. Knez, and Z. Novak, "A Brief Evaluation of Pore Structure Determination for Bioaerogels," *Gels,* vol. 8, no. 7, 2022, doi: 10.3390/gels8070438.

CHAPTER 3

DISPERSBILITY AND SELF-ASSEMBLY OF GO-M13

This chapter is based on the previously published paper:

K. Stokes, Y. Sun, P. Passaretti, H. White, and P. G. Oppenheimer, "Optimisation of Graphage13 Macro-Dispersibility via Understanding the pH-Dependent Ionisation During Self-Assembly: Towards the Manufacture of Graphene-Based Nanodevices," *Nanoscale* vol. 15, pp. 13304 - 13312, 2023, doi: 10.1039/d3nr00778b.

Author contributions – **P. Passaretti** and **Y. Sun** conceptualised the study. **K. Stokes** and **Y. Sun** carried out the experimental acquisition and analyses and validated the results. **P. Goldberg Oppenheimer** and **H. White** were responsible for funding acquisition and resources provision. **P. Goldberg Oppenheimer** supervised and administered the study, curated the data and overviewed the developed methodology. **K. Stokes**, **Y. Sun** and **P. Goldberg Oppenheimer** wrote the original draft and reviewed and edited the final draft.

3.1 Abstract

GraPhage13 aerogels (GPAs) are micro-porous structures generated through the self-assembly of graphene oxide (GO) and M13 bacteriophage. As GPA fabrication involves the aggregation of GO and M13 in aqueous solution, we aim to understand its dispersibility across a wide pH range. Herein, a novel technique has been developed to relate the ionisation of functional groups to the surface charge, offering insights into the conditions required for GPA fabrication and the mechanism behind its self-assembly. The aggregation of GO and M13 was observed between pH 2–6 and exhibited dependence on the surface charge of the resulting aggregate with the M13 bacteriophage identified as the primary factor contributing to this, whilst originating from the ionisation of its functional groups. In contrast, GO exhibited a lesser impact on the surface charge due to the deprotonation of its carboxylic, enolic and phenolic functional groups at pH 6 and above, which falls outside the required pH range for aggregation. These findings provide deeper insights into the pH conditions necessary to initiate the self-assembly of GPA and the underlying mechanisms driving this process, laying the foundation towards its broad range of applications and the subsequent manufacture of graphene-based nanodevices.

3.2 Introduction

Graphene and related nanomaterials have been attracting an exceptionally high research interest for almost two decades within the scientific community, due to their outstanding structural, optical, electrical, thermal and mechanical properties [1, 2]. To realise their full potential of impacting daily life, it is imperative to establish robust, straightforward, and scalable manufacturing methods for graphene-based

nanomaterials, enabling the development of advanced, high-throughput, miniaturised devices. The recent advancements in manufacturing graphene-based hybrid composites have demonstrated the promising capabilities of these materials in creating switchable devices [3-5], sensors [6-8] and high performance devices [9, 10]. Fabrication of graphene-based micronano structures through the incorporation of biomolecules has shown significant promise due to the complex morphologies with unique functionalities controlled by the inherent components.

In particular, graphene oxide (GO) has been emerging as a highly attractive candidate for the development of graphene-based nanodevices [11]. GO is comprised of graphene, an atomic layer of sp2-hybridised carbon atoms, functionalised with oxygen-containing functional groups (OCFGs) such as carboxyl, carbonyl, epoxide and hydroxyl groups [12]. Non-covalent interactions between these OCFGs and biomolecules enable the self-assembly of micro-nanostructures and the interactions between the OCFGs and water molecules render GO hydrophilic, enabling the mass production of these through chemical methods in aqueous media [13, 14]. Graphene-based aerogels have demonstrated unique properties including, high strength, low density and three-dimensional (3D) interconnected structures with macroscale dimensions [15], which have been exploited for various applications e.g., wearable sensors [13, 14], electrodes [16, 17] and adsorbents [18, 19]. Recently a robust method of fabricating graphene-based aerogels has been demonstrated through the self-assembly of graphene oxide (GO) and M13 bacteriophage, a filamentous virus with a diameter of 6.6 nm and length of 880 nm [20]. M13 replicates by infecting *Escherichia coli* (*E. coli*), without destroying the host cell (lysogenic cycle) and consists of circular-shaped single-stranded DNA encapsulated by 2700 copies of the PVIII

major coat protein, with its terminal areas comprised of minor coat proteins PIII and PVI at its head and PVII and PIX at its tail [21].

The novel micro-nano GraPhage13 has been fabricated via integrating GO and M13 at pH 4.9, yielding an aggregate, where M13 viral strands act as a cross-linker between the GO sheets, enabling its self-assembly. Subsequently, a GraPhage13 hydrogel (GPH) was fabricated, which upon deposition on a supporting substrate in a vacuum, yielded a stable GraPhage13 aerogel (GPA) [20]. The nanofabricated GPA exhibits ultra-high-surface-area (325 $m^2 g^{-1}$) and low-density (8.8 mg cm^{-3}) due to its micro-porous structure, and its production is low-cost, scalable and environmentally-friendly, rending itself suitable for the incorporation with a broad range of further nanomaterials including nanoparticles [22], fluorophores [23] and polymers [24]. For instance, Sun et al. accomplished the incorporation of carbon nanotubes into the GPA structures, resulting in the production of GPA–CNT. This hybrid material exhibited an electrical conductivity enhancement of up to 30 times when compared to pure GPA [25]. Furthermore, harnessing the capacity to manipulate the genetic and chemical properties of M13 holds significant potential for altering the characteristics of GPA, such as enhancing its electrical [26-28] and binding properties [22, 29, 30]. These features make GraPhage13 a promising candidate for applications in functional scaffolds, gas filters, energy storage and biological and chemical sensors [11, 15, 31, 32].

It is therefore important to establish the pH range in which GO and M13 can form a dispersion that enables their aggregation for GPA self-assembly. This will facilitate the evaluation of its processability and, on a broader scale, the exploration of potential significant applications in aqueous environments characterised by varying pH levels.

Acid-base titrations are a simple and cost-effective method for monitoring changes in an analyte across a range of pH values [33]. Previous studies have employed titrations with GO to analyse its ionised functional groups [33-36]. The OCFGs present in GO exhibit varying acidities and are neutralised by bases of differing strengths, enabling titrations to effectively quantify their concentration [35]. By differentiating the concentration of ionised groups with respect to pH, the pK_a values of these groups can be determined, providing a measure of their acidity [36]. Information on the concentration of ionised groups and their pK_a values of nanomaterials offer valuable insights into the mechanisms governing their self-assembly into varying nanostructures [37].

Herein, a systematic examination was conducted to determine the concentration of ionised groups, pK_a distribution of the acid groups and the zeta potential of GO, M13 and GPH. The utilisation of an advanced data analysis technique facilitated the comparison of two distinct experiments, thereby elucidating the relationship between the ionisation of functional groups and surface charge and enabled the investigation of this variation with pH and the determination of its origin. These findings significantly advanced the understanding of the fundamental self-assembly mechanism underlying the GPA fabrication and the specific pH range conducive to GPH assembly. Such insights hold a great significance for further studies of incorporating various nanomaterials into the GPA and exploitation of the GraPhage13 for a wide range of potential applications. This approach could also be for instance, utilised to characterise the interaction of GO with other biomolecules, such as double stranded DNA fragments, proteins and enzymes, to mass produce hydrogels for the manufacture of

graphene-based nanodevices for catalysis, dye adsorption and environmental applications [11, 38-40].

3.3 Results and Discussion

3.3.1 Concentration of Ionised Groups and pK_a

Titration curves were obtained with acid-base titration experiments (for further information, please refer Section 2.2.6). Hydrochloric acid (HCl) was utilised as the titrant, while the titrand was a solution containing sodium hydroxide (NaOH) and the analyte under investigation (GO, M13, or GPH).

To accurately compare the analytes (GO, M13, and GPH) within the titration experiments, it is essential to first determine the concentration of each analyte and ensure that an equal amount is introduced into the titrand. The concentration of GO suspended in deionised water (DIW) is provided by the manufacturer (Graphene Supermarket) as 5 mg/mL (Section 2.1.1). By adding 2 mL of this solution is added to 8 mL of the titrand, a final concentration of 1 mg/mL of GO is obtained. In contrast, the concentration of M13, generated as described in Section 2.2.1, is unknown. This can be determined with UV-Vis spectroscopy and the Beer-Lambert Law, given the known extinction coefficient of $\epsilon = 3.84 \pm 0.06$ cm^2/mg at 269 nm. The Beer-Lambert law is only valid when $A > 1$, and therefore the phage suspension was typically diluted to enable the quantification of its concentration (for further details on UV-Vis spectroscopy and the Beer-Lambert law, please refer to Section 2.2.3) [41].

A UV-Vis spectrum of M13 is presented in Figure 3.1a, illustrating its absorbance (*A*) over the 200 – 800 nm range. over the 200-800 nm wavelength range. The high absorbance observed below 230 nm is due to the $\pi \rightarrow \pi^*$ transitions in peptide bonds,

and a peak at approximately 269 nm is due to a combination of viral DNA and the major coat protein PVIII [20]. To examine the quality of the phages, there are three features which must be present: a local minimum at 245 nm, the peak at 269 nm and a baseline at 350 nm. If $A_{269} / A_{245} \approx 1.37$ and $A_{350} / A_{269} \approx 0.02$, the phages are pure and viable [42].

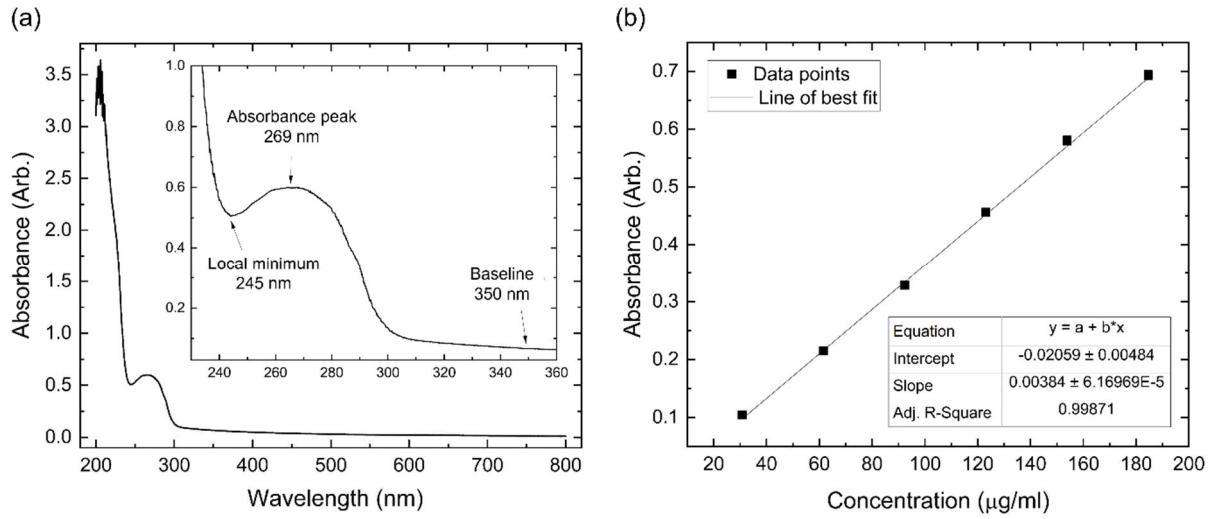

Figure 3.1: UV-Vis spectroscopy of M13 bacteriophage

(a) A typical Ultraviolet-Visible (UV-Vis) spectrum for M13 bacteriophage between 200-800 nm. The inset magnifies the 230-360 nm region to show the key features of the spectrum, which have been labelled accordingly – the local minimum at 245 nm, peak at 269 nm and baseline at 350 nm; **(b)** a calibration curve showing the absorbance at 269 nm for varying concentrations of M13 bacteriophage. The gradient of the line of best fit is (3.84 ± 0.06) x 10^{-3} μg/mL, correspodning to a light path length of 1 cm multiplied by the extinction coefficient of M13, 3.84 ± 0.06 cm^3/mg.

In Figure 3.1a, the measured ratios are $A_{269}/A_{245} \approx 1.17$ and $A_{350}/A_{269} \approx 0.11$, which deviate from these expected values. This discrepancy suggests potential impurities in the phage solution. To further assess the viability of M13, a calibration curve is generated by plotting the concentration of diluted M13 samples against absorbance at 269 nm (Figure 3.1b). According to the Beer-Lambert Law, the slope of this curve

should correspond to the extinction coefficient (ϵ = 3.84 ± 0.06 cm^2/mg at 269 nm) multiplied by the light path length L (L = 1 cm) [43]. As seen in Figure 3.1b, the calibration curve confirms this relationship, indicating that the phages remain viable despite the variation in absorbance ratios.

The observed deviation likely results from residual polyethylene glycol (PEG) in the solution. During the M13 purification process (Section 2.2.1), PEG is employed to precipitate M13 from solution, ensuring complete removal of *E. coli* without compromising the integrity of the phages. However, trace amounts of PEG may persist in solution. While PEG itself has an absorption peak between 180–230 nm, its signal is much weaker than that of M13 and is therefore obscured in the UV-Vis spectrum. The discrepancy in absorbance ratios compared to the expected values is likely attributable to this residual PEG contamination [44].

A 70-fold dilution was used to obtain the spectrum in Figure 3.1a. From this data, the concentration of the diluted M13 solution was calculated as 0.16 mg/mL, leading to a stock concentration of 10.8 mg/mL. To match the 5 mg/mL concentration of GO, the stock solution was diluted by a factor of 10.8/5 = 2.16, ensuring a standardised comparison of ionised group concentrations in subsequent titration experiments

The titration curves (Figure 3.2) represent the relationship between the volume of HCl added and the corresponding pH changes in the solution. At extreme pH values a large volume of HCl is required to change the pH, for example the final 5 mL of HCl added to the titrand adjusted the pH by 0.12–0.25. On the other hand, a plateau is observed between pH 3.5–10.5, with 0.7 mL–2.55 mL of HCl required to generate a significant change. The concentration of ionised groups has been obtained by subtracting the

blank titration data from those involving each of the analytes and is given by the difference in the volume of HCl at a particular pH (for further details see Section 2.3.4). The overall relationship between the concentration of ionised groups and pH for GO, M13, GPH and the average of the GO plus the M13 measurements, GO+M13, is shown in Figure 3.3.

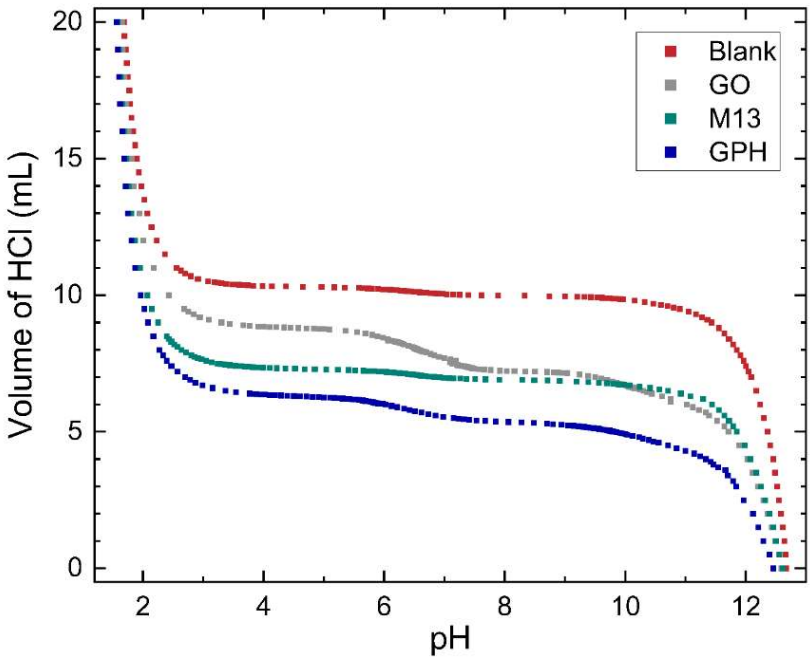

Figure 3.2: Titration curves for GO, M13, and GPH

The relationship between pH and volume of 20 mL 50 mM HCl added to 10 mL of titrand 50 mM NaOH. For titrations involving graphene oxide (GO), M13 bacteriophage and GraPhage13 hydrogel (GPH), 10 mg of analyte was added.

GO shows the greatest variation in the concentration of ionised groups, ranging from 0.75 mmol L^{-1} mg^{-1} at pH 2.2 to 2.15 mmol L^{-1} mg^{-1} at pH 11, with a significant increase between pH 5.5–7.5. This can be explained via the reactions leading to its negative surface charge [45] including firstly the deprotonation of carboxylic groups: C–COOH + H_2O → $C–COO^-$ + H_3O^+ and secondly, the deprotonation of enolic and phenolic groups: C=C–OH + H_2O ↔ $C=CO^-$ + H_3O^+. As the pH increases the deprotonation

equilibrium is shifted to the right-hand side of the reaction, producing a higher concentration of negatively charged carboxylic, enolic and phenolic groups, whilst the increasing concentration of OH^- ions neutralises the disassociated protons, leading to the increase in the concentration of ionised groups with pH [45], while the concentration of ionised groups for M13 remains relatively constant, 1.89 ± 0.03 mmol L^{-1} mg^{-1} over the entire pH range. Therefore, the variation in concentration observed for GPH and GO + M13 can be attributed to the GO component. The difference between the concentration of ionised groups in GPH and GO + M13 decreases as the pH increases, however between pH of 3.1–5.7 and 7.6–9.2 the concentration remains constant at 0.34 mmol L^{-1} mg^{-1} and 0.19 mmol L^{-1} mg^{-1} respectively.

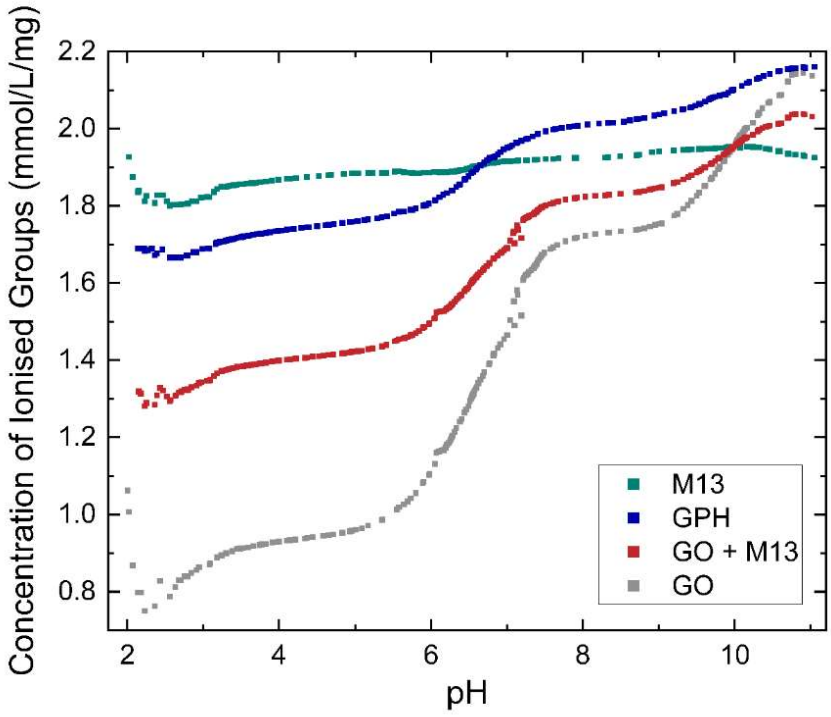

Figure 3.3: Concentration of ionised groups for GO, M13, GPH and GO+M13

The concentration of ionised groups of graphene oxide (GO), M13 bacteriophage, GraPhage13 hydrogel (GPH) and GO + M13 across a range of pH values.

The probability of GO–M13 aggregation at different pH can be determined by the concentration of ionised groups employing Deryaguin–Landau–Verwey–Overbeek (DLVO) theory, which describes how electrostatic force governs colloidal stability. It assumes that electrostatic repulsion and attractive van der Waals are the only electrostatic forces acting on colloids, leading to their dispersion or aggregation within a solution. The electrostatic repulsion originates from the electric double layer, where the particles dispersed in aqueous media gain a negative charge from negative ions adsorbing to its surface, which then attract positive charges and produce the double layer. The magnitude of the electrostatic repulsion depends on the concentration of ions, produced by the dissociation of ionised groups within the solution, whereas the influence of concentration on van der Waals forces is negligible [46, 47]. Consequently, increasing the concentration of ionised groups increases the magnitude of electrostatic repulsion, thus reducing the likelihood of flocculation. Since the concentration of ionised groups for GPH increases with pH, with a particularly rapid increase commencing at pH 6, it is plausible that the van der Waals forces overcome the electrostatic repulsion (between the negatively charged amino acids on the surface of M13 and the deprotonated carboxylic groups on GO) between pH 2–6, enabling flocculation of GO and M13. It is hypothesised that the electrostatic interactions occur between the carboxylic groups on the GO with positively charged groups of the N-terminus and K_8 residues of the M13, following the protonation of the carboxyl groups of E_2, D_4, D_5, E_{20} residues [43].

The inflection points observed in Figure 3.3 indicate the presence of acid groups with varying pK_a. The concentration of groups is subsequently differentiated with respect to pH and Gaussian peaks are fitted to the data to obtain the pK_a distributions (Figure

3.4). Here, f(pK$_a$) represents the derivative of the concentration of ionised groups differentiated with respect to pH (for further details please see Section 2.3.4). This was normalised by dividing the distribution by the maximum value of the derivative i.e. the y-value of the highest peak.

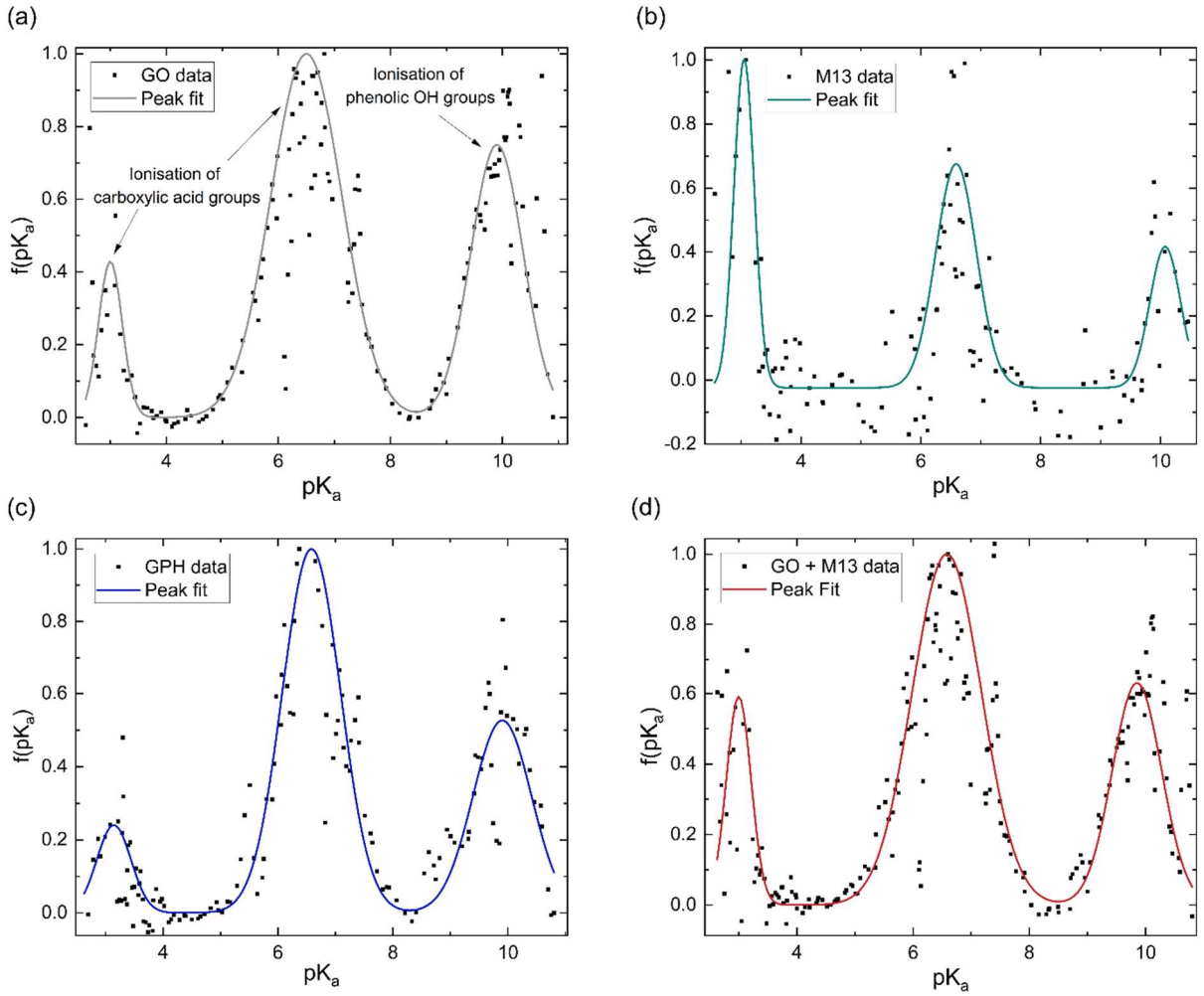

Figure 3.4: pKa distribution of GO, M13, GPH and GO+M13

Normalised pK$_a$ distribution of **(a)** graphene oxide (GO), **(b)** M13 bacteriophage, **(c)** GraPhage13 hydrogel (GPH) and **(d)** GO + M13. The peaks in **(a–d)** at pK$_a$ values of 3.1 and 6.6 are due to the ionisation of carboxylic acid groups and the peak at 9.9 is due to the ionisation of phenolic OH groups.

Three peaks emerge at nearly the same pK$_a$ for each analyte, with average positions of 3.1 ± 0.1, 6.6 ± 0.1 and 9.9 ± 0.1. The overall fitted peak positions, widths and intensities are summarised in Table 3.1.

Table 3.1: pK_a distribution parameters for GO, M13, GPH and GO+M13

pK_a values, full width half maximum and area for pK_a distribution of graphene oxide (GO), M13 bacteriophage, GraPhage13 hydrogel (GPH) and GO + M13.

	Peak 1			Peak 2			Peak 3		
	pK_{a1}	Width	Area	pK_{a2}	Width	Area	pK_{a3}	Width	Area
GO	3.0 ± 0.3	0.5 ± 0.8	0.2 ± 0.3	6.5 ± 0.2	1.5 ± 0.5	1.5 ± 0.5	9.9 ± 0.3	1.1 ± 0.7	0.8 ± 0.5
M13	3.05 ± 0.04	0.40 ± 0.09	0.45 ± 0.09	6.59 ± 0.07	0.8 ± 0.2	0.6 ± 0.1	10.1 ± 0.1	0.6 ± 0.3	0.3 ± 0.1
GPH	3.1 ± 0.1	0.7 ± 0.3	0.19 ± 0.06	6.58 ± 0.03	1.2 ± 0.1	1.31 ± 0.08	9.9 ± 0.1	1.2 ± 0.2	0.7 ± 0.1
GO + M13	3.0 ± 0.2	0.5 ± 0.4	0.3 ± 0.2	6.6 ± 0.1	1.4 ± 0.4	1.4 ± 0.3	9.9 ± 0.2	1.0 ± 0.6	0.7 ± 0.3

It has been previously noted that three peaks are observed in the pK_a distribution of GO, with values of 4.3 and 6.6, originating from the ionisation of carboxylic acid groups and the peak at 9.9 corresponding to the ionisation of a phenolic OH group [36].

The presence of these functional groups therefore, account for the peaks observed for GO, GPH and GO + M13 in Figure 3.4. The difference between the pK_a of the first peak (3.1 ± 0.1) in comparison to the value reported in ref. [36] for GO is likely due to the over-data-smoothing at extreme pH values. Table 3.1 demonstrates that not only are the pK_a values of GPH and GO + M13 the same but also that their widths and intensities match within error of the peak fit. This indicates that there are no new ionised functional groups generated from the GPH interaction, and therefore GPH exhibits dispersibility over a similar pH range as GO.

The known pK_a values for the M13 bacteriophage are given by Passaretti et al [43]. While the M13 has the same pK_a values as GO, GPH and GO + M13, a higher signal-

to-noise ratio hinders the accuracy of the peak fitting and indicates that there may be peaks which are not detected (Figure 3.4b). A second peak fit, the results of which are shown in Table 3.2, demonstrates the inaccuracy of fitting peaks according to the known pK_a values of M13.

Table 3.2: Known pKa values for PVIII amino acids

pK_a values of PVIII amino acids contributing towards the surface charge of M13 bacteriophage, obtained through peak fitting to the known pK_a values of M13 [43]. The K8 residue is not included as its pK_a is beyond the measured values.

PVIII Amino Acid	Known pK_a	Measured pK_a	Peak Width	Peak Area
A1	8.62	8.9 ± 0.3	0.7 ± 0.8	0.2 ± 0.2
E2	3.45	3.4 ± 0.9	0 ± 2	0 ± 1
D4	3.11	3.0 ± 0.3	0.4 ± 0.4	0.4 ± 0.9
D5	4.02	3.9 ± 0.5	0 ± 1	0.1 ± 0.3
E20	5.21	5.7 ± 0.2	0.5 ± 0.2	0.3 ± 0.2

This could be due to these peaks having low intensity or overlap with further peaks demonstrating similar pK_a values or the effect of interactions due to the presence of the electric double layer, HCl and NaOH [35, 45, 48]. Furthermore, for pK_a values of less than 2.7–3.8 and more than 10–11, the values are unlikely to be correct due to the inaccuracy of the pH measurements. The Nernst equation, which relates the electrical potential across the electrode to the pH, breaks down at extreme pH values and therefore, a peak due to the presence of the K_8 residue, which has a pK_a of 11.56, cannot be detected [43, 49]. These limitations, therefore, do not enable the pK_a of specific M13 residues to be identified. This may also impact the comparison of pK_a values of GPH and GO + M13, as there may be variations in the functional groups as a result of the interaction between GO and M13 that have not been observed.

3.3.2 Zeta Potential

The zeta potential (ζ) measurements for GO, M13 and GPH between pH 2–11 are shown in Figure 3.5a (for further details please see Section 2.2.5).The zeta potential of GO is found to exhibit the least variation over this pH range, measuring −32 ± 1 mV at pH 1.9 and −46 ± 1 mV at pH 11.0. M13 shows a larger variation, decreasing from 39.2 ± 0.7 mV at pH 2.1 to −24.6 ± 0.8 mV at pH 5.0, before plateauing at −32.0 ± 0.4 mV between pH 6.1–11.0. GPH demonstrates the widest range, spanning from 31.9 ± 0.1 mV at pH 2.1 to −48.6 ± 0.4 mV at pH 11.1.

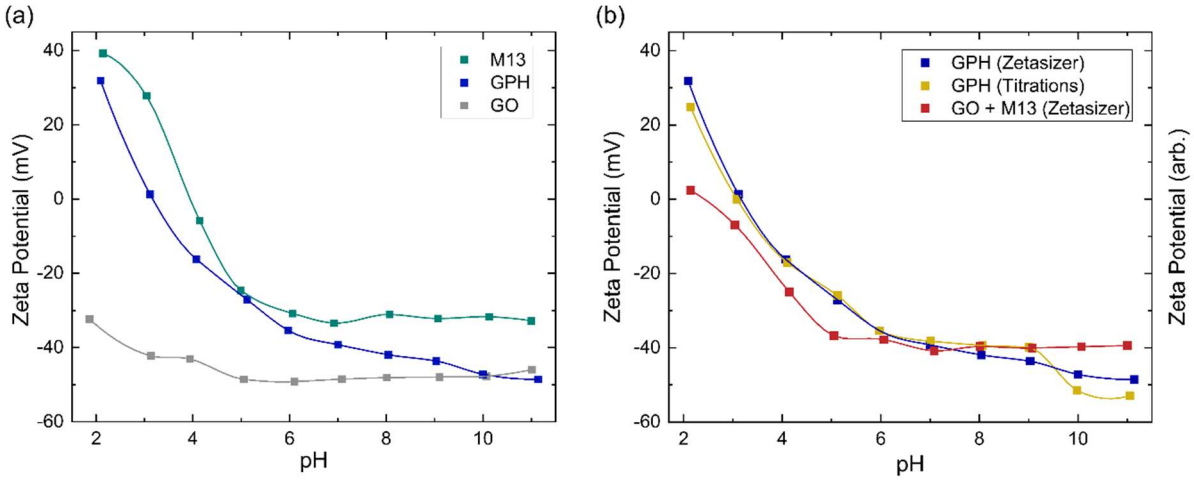

Figure 3.5: Zeta potential for GO, M13, GPH and GO+M13

(a) Zeta potential of GO, M13 bacteriophage and GPH. **(b)** Comparison of zeta potential measurements of GPH to the addition of the individual GO and M13 (GO + M13) along with the zeta potential trend of GPH. The trend lines are generated *via* interpolation.

Figure 3.5a shows that the zeta potential of GO remains below −30 mV. The zeta potential is the electrical potential at the slipping plane, which provides the magnitude of the electrostatic repulsion between adjacent colloids [50]. Colloidal dispersions are generally found to be stable when |ζ| > 30 mV, due to strong electrostatic repulsion between like charges. For the colloids to flocculate the electrostatic repulsion must be

overcome by the attractive van der Waals forces [51], that is to achieve $|\zeta| < 30$ mV [52], which would result in GO forming a stable colloid which does not aggregate between pH 2–11. As the pH of 1 mg mL^{-1} GO was measured to be 2.4, NaOH was added to GO to increase the pH to 3–11. The NaOH acted as a hydrogenating agent and reduced GO to activated graphene, decreasing its sheet size to form a more stable dispersion. This leads to an improved colloidal stability and therefore, decreases the probability of flocculation [53]. HCl was added to measure GO at pH 2, however only a low concentration was required to adjust the pH such that very few protons are disassociated from their acidic functional groups, and therefore the zeta potential remains in the stable colloid range. As the pH increases the zeta potential turns more negative due to the increased concentration of negatively charged ionised groups [45]. A small increase in the zeta potential is observed at high pH, due the high concentration of OH^- ions causing double layer compression [36].

Zeta potential measurements for M13 show that the bacteriophage is a stable colloid at pH < 3 and pH > 6 ($|\zeta| > 30$ mV), and flocculates occurs between pH 3–6 ($|\zeta| < 30$ mV) [52]. The surface charge of M13 is a result of a protonation and deprotonation of the A_1, E_2, D_4, D_5, K_8 and E_{20} residues and the amino group at the N-terminus. Since these residues have differing pK_a values, their charge and therefore the surface charge of M13 are dependent on the pH of the chemical environment [43, 54]. The zeta potential of both M13 and GPH decreases as the pH increases until pH 6, whereafter the zeta potential of M13 plateaus while GPH continues to decrease as the pH increases, eventually overlapping with GO at pH > 10. This suggests that below pH 6 the main contributor towards surface charge of GPH is the M13. Above pH 6, where the chemical environment becomes more basic, there is a higher probability of GO

deprotonation, producing ionised groups, which contribute towards the GPH's surface charge. Having established from the concentration of ionised groups that the aggregation of GO and M13 is only possible between pH 2–6, it can be concluded that M13 is the primary contributor to the surface charge of GPH.

A comparison between the zeta potential of GPH and the addition of the GO and M13 zeta potential measurements (GO + M13) is shown in Figure 3.5b. Zeta potential of GO + M13 is, on average, 34 ± 3 mV lower than GPH for all pH values. The difference between these trends confirms that the interaction between GO and M13 produces an aggregate with a lower surface charge than the sum of the surface charges of GO and M13, which is beneficial to the fabrication of the micronano sponge Figure 3.5b. illustrates the difference between GPH zeta potential measurements and the trend of the zeta potential from the titration data. Zeta potential can be determined by multiplying the concentration of ionised groups with the charge on that group. However, since the electrochemical active surface area is unknown only the trends of the zeta potentials can be compared. As the surface charge is proportional to the zeta potential, the concentration of ionised groups was multiplied by the measured GPH zeta potential and scaled such that the trends could be compared. The significant overlap between titration and Zetasizer measurements imply that the ionised groups almost completely determine the variation of surface charge of GPH with pH.

Figure 3.5a-b further demonstrate that aggregation between GO and M13 occurs between 2.1 ± 0.4 > pH > 5.4 ± 0.9, in agreement with the previously determined range of pH 2–6. To assess the implications of this on the processability of GPA, both the forces involved in aggregation and the likelihood of flocculation need to be examined. The probability of aggregation can be analysed via the sticking probability P_{ij}, which is

the probability of cluster *i* and cluster *j* adhering to each other to form a new, larger particle.

$$P_{ij} = P_1 10^{-|pH-PZC|} \quad (3.1)$$

Here, P_1 is the sticking probability of an individual particle and PZC is the point of zero charge. The PZC corresponds to the pH at which a particle has zero surface charge such that the electrostatic repulsion is minimised. The optimal pH for aggregation is slightly above the PZC. As the pH deviates further from the PZC the electrostatic repulsion increases, reducing the probability of flocculation [55]. Since the GPH aggregation is possible at 2.1 ± 0.4 > pH > 5.4 ± 0.9, it can be estimated that the PZC for GPH is roughly an average pH value of this range, 3.8 ± 0.5, with the error on this average calculated with the functional approach (Section 2.3.1). Previously, Passaretti et al determined that the optimal pH for GPH aggregation is 4.9 , which is in agreement with the discussion establishing that the optimal pH should be slightly above the PZC [20]. This pH was then used in our subsequent experiments when fabricating GPA.

However, upon reviewing the methodology employed by Passaretti et al., it was found that their identification of pH 4.9 being optimal for GPA fabrication was based on titrations experiments, where the authors observed that GO and M13 aggregate within between pH 4.8–5.4, with more pronounced aggregation occurring at the lower end of this range [20]. This differs from our findings from analysing the concentration of ionised groups, zeta potential and observation of the aggregates formed (Figure 3.6), which indicates that GO and M13 can interact between pH 2-6. The discrepancy may arise from our more analytical approach, which enables the detection of interactions between GO and M13 even at stages where aggregation is still visible but more

challenging to observe, such as at pH 2, 3 and 6 (Figure 3.6). Aggregation is clearly visible at pH 4 and pH 5, which also differs from pH range given by Passaretti et al. [20]. This could be attributed to differences in methodologies, however the methodology utilised by Passaretti et al. is not given and therefore a direct comparison between findings is challenging.

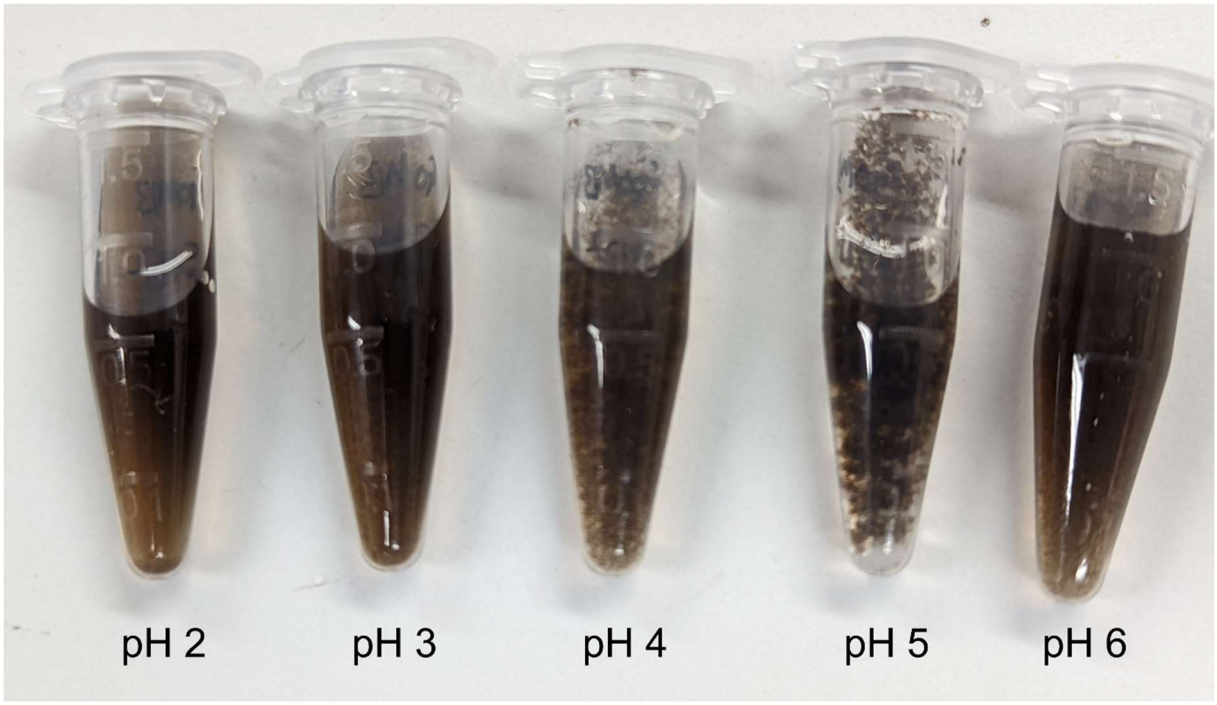

Figure 3.6: GPH generated at pH 2-6

An image of GO-M13 solutions when combining GO and M13 (both to a final concentration of 0.3 mg/mL) in citrate buffers with pHs ranging from 2-6.

3.3.3 Fabrication of GPAs at Varying pH

The composition and morphology of GPAs generated at pH 4.9 were characterised with optical imaging, energy-dispersive x-ray (EDX) spectroscopy, and scanning electron microscopy (SEM) (Section 2.2.4). Compositional analysis with EDX spectroscopy (Figure 3.7a) showed that GPA is composed of carbon and oxygen, originating from the GO and M13, and sodium (Na), phosphorous (P), sulphur (S) and

chlorine (Cl) from the presence of traces of salts introduced in the M13 propagation and purification process (Section 2.2.1), DNA and amino acids. The silicon (Si) peak arises from the silicon substrate the GPH is deposited on to enable GPA fabrication. The porosity of GPA is visible from the optical images (Figure 3.7e), while SEM analysis provides higher magnification images which clearly demonstrate its macroporous structure (Figure 3.7b-d).

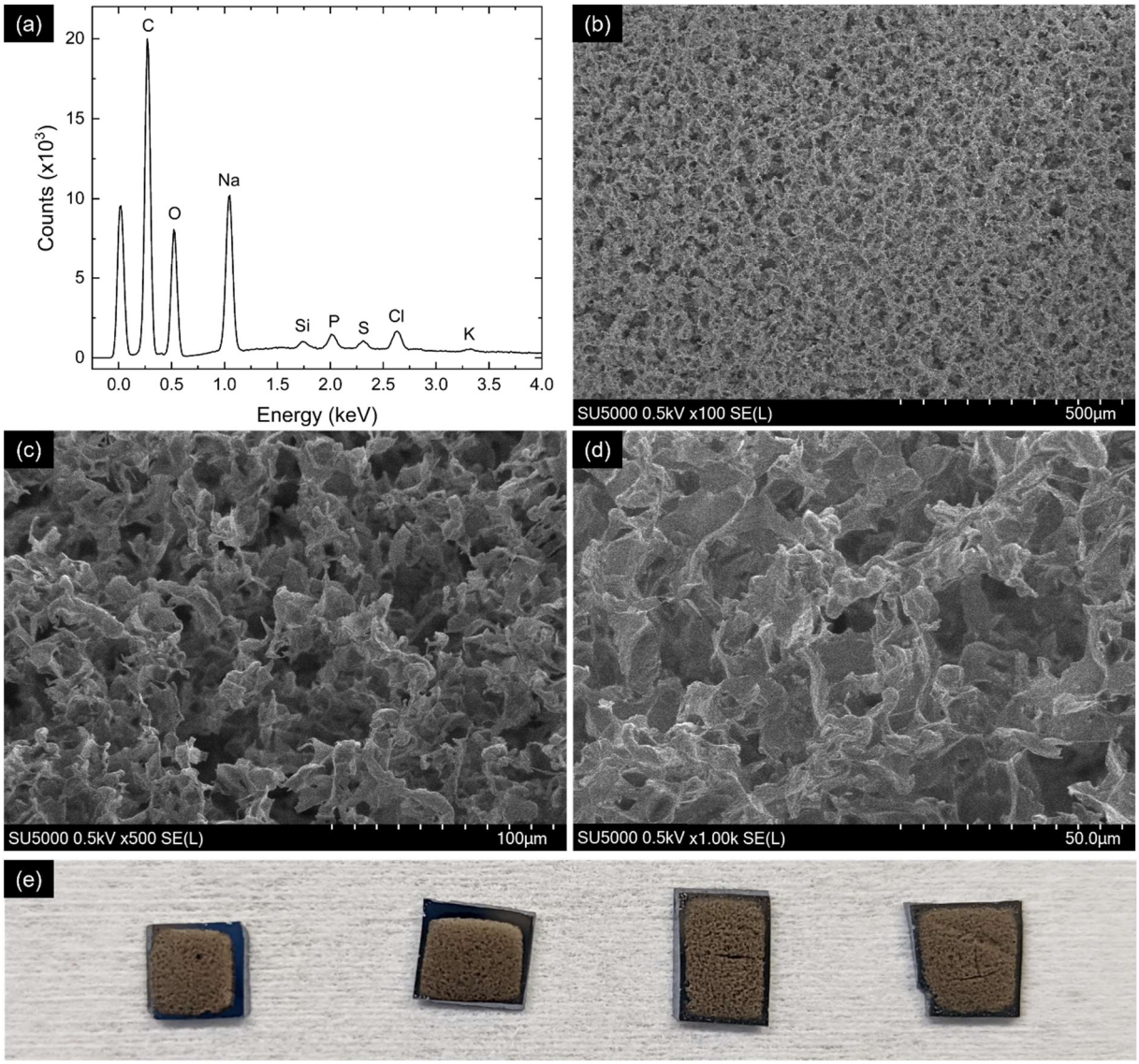

Figure 3.7: Characterisation of GPA

(a) EDX spectrum of GPA, providing its elemental composition; **(b-d)** SEM images and **(e)** optical images of GPAs fabricated at pH 4.9

With pH 2-6 being identified as the range in which GO and M13 can interact, we aimed to investigate the feasibility of fabricating GPA within this pH range. Citrate buffers at pH 2-6 were generated by adjusting the quantity of citric acid or sodium citrate dihydrate in solution. Subsequently, GO and M13 were added to these buffers to a final concentration of 0.3 mg/mL, inverted to form an aggregate and centrifuged to produce a GO-M13 pellet. Removing 90% of the supernatant and resuspending the GO-M13 pellet in the remaining supernatant to generated GPH, which was deposited on a substrate and dried in a vacuum produced GPAs (for further details, please see Section 2.2.2). The resulting morphology of GPA generated at pH 2, 3, 4, and 6, termed GPA_{pH2}, GPA_{pH3}, GPA_{pH4} and GPA_{pH6} respectively, was observed with SEM determine how these pH variations influence the nanocomposite structure (Figure 3.8).

The variation in morphology observed at pH 4 and below (Figure 3.8a-c) can be attributed to the behaviour of M13 in highly acidic conditions. Passaretti et al. established that the isoelectric point (pI) of M13, the pH at which M13 possesses no net electrical charge, is 4.05 ± 0.07. Below the pI, M13 precipitates from solution, reducing the possible interactions between GO and M13, thereby affecting GPA formation and generating the observed amorphous morphologies [43, 56]. The significant morphological variation observed for GPA_{pH2} originates from alterations to the phage structure and damage to the coat proteins (Figure 3.8a). Below pH 3, the M13 phages fold into a looser structure, significantly compromising their structural integrity and increasing their susceptibility to destruction. The increased destruction of phage particles further reduces the bonding between GO and M13, resulting in the

observed low porosity [44, 57]. The observed non-porous regions originate from the aggregation of M13, which forms dense deposits on the surface [54].

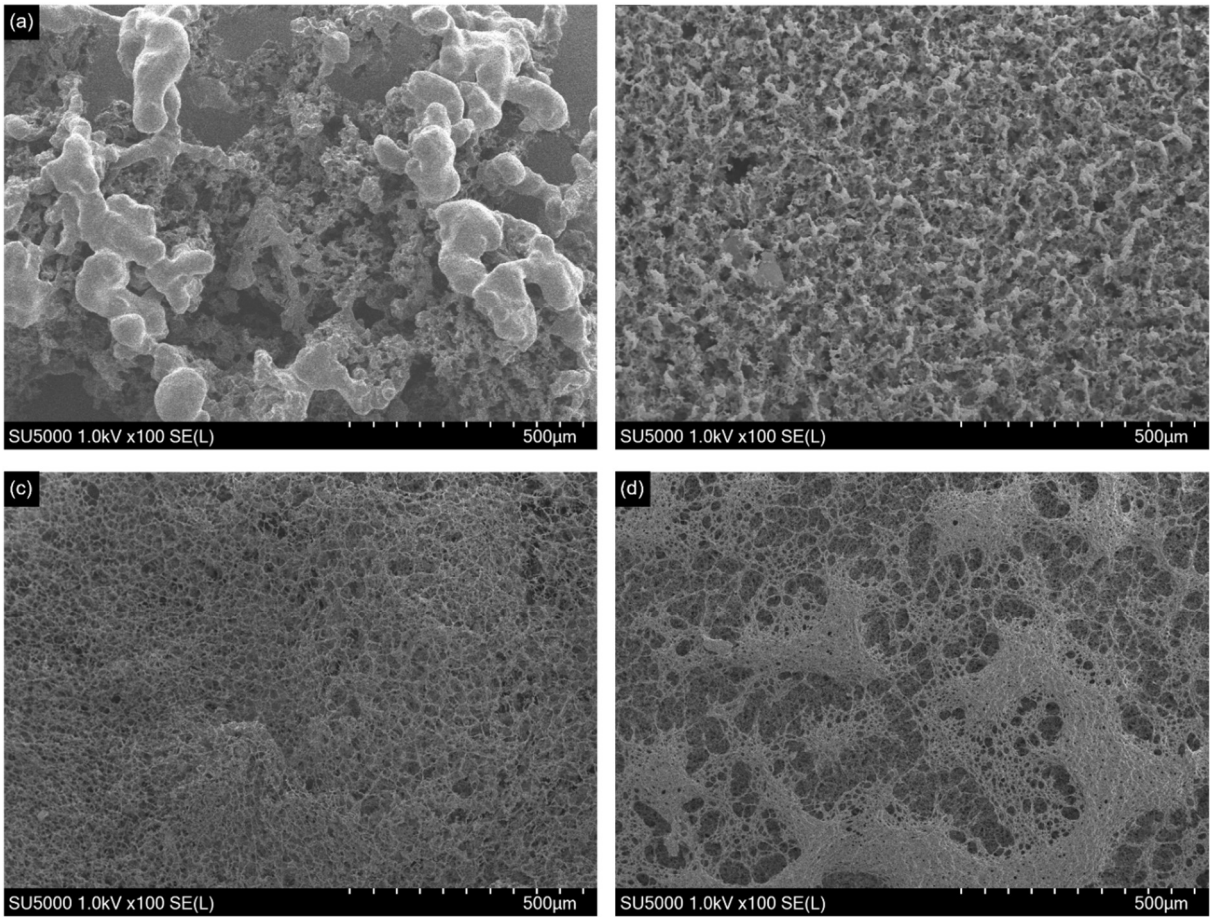

Figure 3.8: SEM images of GPAs generated at pH 2, 3, 4 and 6

Scanning electron microscopy (SEM) images of GraPhage13 aerogels (GPAs) generated by combining GO and M13 in citrate buffers with a measured pH of **(a)** 2 **(b)** 3 **(c)** 4 and **(d)** 6.

On the other hand, pH 6 is above the pI for M13 and therefore M13 will not precipitate from solution. Instead, the reduced porosity observed for GPA_{pH6} (Figure 3.8d) arises from the increased electrostatic repulsion between GO and M13. The concentration of deprotonated functional group on GO increases with pH, enhancing its negative charge. This results in an increased electrostatic repulsion between the deprotonated functional groups on GO and the negatively charged amino acids on M13, reducing

the bonding between GO and M13. Therefore, while GO and M13 can interact between pH 2-6, pH 4.9 is optimal to fabricate consistent porous morphologies.

3.4 Conclusions

The relationship between pH and the aggregation of graphene oxide–M13 bacteriophage, which in turn enables the self-assembly of GraPhage13 aerogels, has been investigated through pH titrations and zeta potential measurements. The concentration of ionised groups for M13 bacteriophage remains constant, whereas for GO it is dependent on the direction of the deprotonation, which is heavily influenced by its chemical environment. Furthermore, it has been shown that the concentration of ionised groups to be higher for GPH than the addition of GO and M13. Using DLVO theory, it has been determined that the GO–M13 aggregation occurs between 2 < pH < 6. The pK_a values for GO were found to be 3.1, 6.6 and 9.9, corresponding to the ionisation of carboxylic and phenolic OH groups, and no new functional groups were found to be formed as a result of the interaction between GO and M13. Zeta potential measurements demonstrate that GO remains stable across a wide pH range of 2–11, whilst M13 forms unstable dispersions and flocculates between pH 3–6. Similar to the concentration of ionised groups, aggregation of GO and M13 occurs at 2.1 ± 0.4 > pH 5.4 ± 0.9. Employing DLVO theory and sticking probabilities the optimal pH was established to be slightly above the estimated value for the point of zero charge at 3.8 ± 0.5, in agreement with previous research showing the optimal pH for aggregation of pH 4.9.

Observing the dispersibility of GPH over a wide range of pH values enabled determining the origin of the GPH surface charge and the pH range in GPA fabrication,

providing an important insight into the underpinning mechanism behind the self-assembly of GraPhage13 aerogels. By employing an innovative technique, a comparative analysis was conducted between the zeta potential trends through titrations and zeta potential measurements. The similarity in zeta potential trends provides evidence that the surface charge of GPH arises from presence of ionised groups and electrostatic interactions between them. More specifically, it can be attributed to interactions between the carboxylic groups of GO with positively charged N-terminus and the K_8 residue of M13 following the protonation of the E_{20} residue. These interactions play an essential role in facilitating the self-assembly of GPAs. Furthermore, within the pH range in which the aggregation occurs, the main contributor to the surface charge was determined to be the M13 bacteriophage. The self-assembly of GraPhage13 depends on reducing the electrostatic repulsion between the negatively charged amino acids of M13 and the deprotonated carboxylic groups of GO, which can be achieved by lowering the concentration of ionised groups. Combining GO and M13 in a chemical environment of pH 2–6 reduces the likelihood of the deprotonation of the carboxylic groups in GO, enabling the generation of GPH and the subsequent fabrication of GPA. However, pH 4.9 remains the optimal condition for GPA fabrication, as it achieves a balance between mitigating the damaging effects of highly acidic environments on M13 phages and minimising electrostatic repulsion between GO and M13.

This novel investigation, utilising analytical techniques to compare the concentration of ionised groups and surface charge across different pH levels, has yielded insights into the dispersibility of GraPhage13 and the origin of the ionised groups responsible for its surface charge and self-assembly. This enhances our understanding of its

processability, thereby providing guidance for the future integration of various nanomaterials including nanoparticles, polymers and fluorophores into the aerogel structure. This opens up possibilities for the development of graphene-based nanodevices for a broad range of applications including micronano filters, functional scaffolds and miniaturised sensors.

3.5 Materials and Methods

Further information on graphene oxide and M13 bacteriophage used in these experiments can found in Sections 2.1.1 and 2.1.2, respectively.

For detailed descriptions of the methods used in this chapter, please refer to Chapter 2, specifically the following sections:

- 2.2.1 Propagation and Purification of M13 Bacteriophage
- 2.2.2 Fabrication of GraPhage13 Aerogels (GPA)
- 2.2.3 Ultraviolet – Visible (UV-Vis) Spectroscopy
- 2.2.4 Scanning Electron Microscopy (SEM) and Energy Dispersive X-Ray Spectroscopy (EDX)
- 2.2.5 Zeta Potential
- 2.2.6 Acid – Base Titrations
- 2.3.3 Peak Fitting
- 2.3.4 Concentration of Ionised Groups and pK_a

3.6 References

[1] D. Maiti, X. Tong, X. Mou, and K. Yang, "Carbon-Based Nanomaterials for Biomedical Applications: A Recent Study," *Frontiers in Pharmacology,* Review vol. 9, 2019, doi: 10.3389/fphar.2018.01401.

[2] R. Rauti, M. Musto, S. Bosi, M. Prato, and L. Ballerini, "Properties and Behavior of Carbon Nanomaterials When Interfacing Neuronal Cells: How Far Have We Come?," *Carbon,* vol. 143, pp. 430-446, 2019, doi: 10.1016/j.carbon.2018.11.026.

[3] K. Pal, M. L. N. M Mohan, M. Foley, and W. Ahmed, "Emerging Assembly of Zno-Nanowires/Graphene Dispersed Liquid Crystal for Switchable Device Modulation," *Organic Electronics,* vol. 56, pp. 291-304, 2018, doi: 10.1016/j.orgel.2017.12.044.

[4] K. Pal, A. Si, G. S. El-Sayyad, M. A. Elkodous, R. Kumar, A. I. El-Batal, S. Kralj, and S. Thomas, "Cutting Edge Development on Graphene Derivatives Modified by Liquid Crystal and Cds/Tio2 Hybrid Matrix: Optoelectronics and Biotechnological Aspects," *Critical Reviews in Solid State and Materials Sciences,* vol. 46, no. 5, pp. 385-449, 2021, doi: 10.1080/10408436.2020.1805295.

[5] A. Si, G. Z. Kyzas, K. Pal, and F. G. de Souza Jr, "Graphene Functionalized Hybrid Nanomaterials for Industrial-Scale Applications: A Systematic Review," *Journal of Molecular Structure,* vol. 1239, p. 130518, 2021, doi: 10.1016/j.molstruc.2021.130518.

[6] T. Arfin, "Functional Graphene-Based Nanodevices: Emerging Diagnostic Tool," in *Nanomaterials in Diagnostic Tools and Devices*, S. Kanchi and D. Sharma Eds.: Elsevier, 2020, ch. 3, pp. 85-112.

[7] A. Cordaro, G. Neri, M. T. Sciortino, A. Scala, and A. Piperno, "Graphene-Based Strategies in Liquid Biopsy and in Viral Diseases Diagnosis," *Nanomaterials,* vol. 10, no. 6, p. 1014, 2020, doi: 10.3390/nano10061014.

[8] S. Soren, S. Chakroborty, and K. Pal, "Enhanced in Tunning of Photochemical and Electrochemical Responses of Inorganic Metal Oxide Nanoparticles Via Rgo Frameworks (Mo/Rgo): A Comprehensive Review," *Materials Science and Engineering: B,* vol. 278, p. 115632, 2022, doi: 10.1016/j.mseb.2022.115632.

[9] K. D. Pham, C. Q. Nguyen, C. V. Nguyen, P. V. Cuong, and N. V. Hieu, "Two-Dimensional Van Der Waals Graphene/Transition Metal Nitride Heterostructures as Promising High-Performance Nanodevices," *New Journal of Chemistry,* 10.1039/D1NJ00374G vol. 45, no. 12, pp. 5509-5516, 2021, doi: 10.1039/D1NJ00374G.

[10] J. P. Fried, J. L. Swett, X. Bian, and J. A. Mol, "Challenges in Fabricating Graphene Nanodevices for Electronic DNA Sequencing," *MRS Communications,* vol. 8, no. 3, pp. 703-711, 2018, doi: 10.1557/mrc.2018.187.

[11] P. Passaretti, "Graphene Oxide and Biomolecules for the Production of Functional 3d Graphene-Based Materials," *Frontiers in Molecular Biosciences,* Review vol. 9, 2022, doi: 10.3389/fmolb.2022.774097.

[12] S. Park and R. S. Ruoff, "Chemical Methods for the Production of Graphenes," *Nature Nanotechnology,* vol. 4, no. 4, pp. 217-224, 2009, doi: 10.1038/nnano.2009.58.

[13] F. Zhang, K. Yang, Z. Pei, Y. Wu, S. Sang, Q. Zhang, and H. Jiao, "A Highly Accurate Flexible Sensor System for Human Blood Pressure and Heart Rate Monitoring Based on Graphene/Sponge," *RSC Advances,* 10.1039/D1RA08608A vol. 12, no. 4, pp. 2391-2398, 2022, doi: 10.1039/D1RA08608A.

[14] D. Zhang, Y. Mao, P. Bai, Q. Li, W. He, H. Cui, F. Ye, C. Li, R. Ma, and Y. Chen, "Multifunctional Superelastic Graphene-Based Thermoelectric Sponges for Wearable and Thermal Management Devices," *Nano Letters,* vol. 22, no. 8, pp. 3417-3424, 2022, doi: 10.1021/acs.nanolett.2c00696.

[15] V. Chabot, D. Higgins, A. Yu, X. Xiao, Z. Chen, and J. Zhang, "A Review of Graphene and Graphene Oxide Sponge: Material Synthesis and Applications to Energy and the Environment," *Energy & Environmental Science,* 10.1039/C3EE43385D vol. 7, no. 5, pp. 1564-1596, 2014, doi: 10.1039/C3EE43385D.

[16] N. Duinslaeger and J. Radjenovic, "Electrochemical Degradation of Per- and Polyfluoroalkyl Substances (Pfas) Using Low-Cost Graphene Sponge Electrodes," *Water Research,* vol. 213, p. 118148, 2022, doi: 10.1016/j.watres.2022.118148.

[17] N. Ormeno-Cano and J. Radjenovic, "Electrochemical Degradation of Antibiotics Using Flow-through Graphene Sponge Electrodes," *Journal of Hazardous Materials,* vol. 431, p. 128462, 2022, doi: 10.1016/j.jhazmat.2022.128462.

[18] P. Xu, F. Rahmani, and Y. C. Chiew, "Adsorption and Diffusion of Methane and Light Gases in 3d Nano-Porous Graphene Sponge," *Molecular Simulation,* vol. 48, no. 10, pp. 882-890, 2022, doi: 10.1080/08927022.2021.2018133.

[19] T. Maimaiti, R. Hu, H. Yuan, C. Liang, F. Liu, Q. Li, S. Lan, B. Yu, and S.-T. Yang, "Magnetic Fe3o4/Tio2/Graphene Sponge for the Adsorption of Methylene Blue in Aqueous Solution," *Diamond and Related Materials,* vol. 123, p. 108811, 2022, doi: 10.1016/j.diamond.2021.108811.

[20] P. Passaretti, Y. Sun, I. Khan, K. Chan, R. Sabo, H. White, T. R. Dafforn, and P. G. Oppenheimer, "Multifunctional Graphene Oxide-Bacteriophage Based Porous Three-Dimensional Micro-Nanocomposites," *Nanoscale,* 10.1039/C9NR03670A vol. 11, no. 28, pp. 13318-13329, 2019, doi: 10.1039/C9NR03670A.

[21] S. M. Han, Y. J. Lee, M. H. Lee, C. W. Park, S. M. Lee, J. O. Soh, and J. H. Lee, "M13 Bacteriophage-Based Bio-Nano Systems for Bioapplication," *BioChip Journal,* vol. 16, no. 3, pp. 227-245, 2022, doi: 10.1007/s13206-022-00069-w.

[22] J. Hou, Y. Xu, S. Sun, X. Zhong, C.-T. Yang, and X. Zhou, "Gold Nanoparticles-Decorated M13 Phage Spr Probe for Dual Detection of Antigen Biomarkers in Serum," *Sensors and Actuators B: Chemical,* vol. 374, p. 132811, 2023, doi: 10.1016/j.snb.2022.132811.

[23] S. Huang, J. Qi, D. W. deQuilettes, M. Huang, C.-W. Lin, N. M. Bardhan, X. Dang, V. Bulović, and A. M. Belcher, "M13 Virus-Based Framework for High Fluorescence Enhancement," *Small,* vol. 15, no. 28, p. 1901233, 2019, doi: 10.1002/smll.201901233.

[24] X. Dong, P. Pan, J.-J. Ye, Q.-L. Zhang, and X.-Z. Zhang, "Hybrid M13 Bacteriophage-Based Vaccine Platform for Personalized Cancer Immunotherapy," *Biomaterials,* vol. 289, p. 121763, 2022, doi: 10.1016/j.biomaterials.2022.121763.

[25] Y. Sun, P. Passaretti, I. Hernandez, J. Gonzalez, W. Liu, F. Rodriguez, D. J. Dunstan, P. Goldberg Oppenheimer, and C. J. Humphreys, "Nanomechanics of Graphene Oxide-Bacteriophage Based Self-Assembled Porous Composites,"

Scientific Reports, vol. 10, no. 1, p. 15618, 2020, doi: 10.1038/s41598-020-72372-1.

[26] H. Kim, J.-H. Lee, J. H. Lee, B. Y. Lee, B. D. Lee, K. Okada, S. Ji, J. Yoon, J. H. Lee, and S.-W. Lee, "M13 Virus Triboelectricity and Energy Harvesting," *Nano Letters,* vol. 21, no. 16, pp. 6851-6858, 2021, doi: 10.1021/acs.nanolett.1c01881.

[27] I. W. Park, K. W. Kim, Y. Hong, H. J. Yoon, Y. Lee, D. Gwak, and K. Heo, "Recent Developments and Prospects of M13- Bacteriophage Based Piezoelectric Energy Harvesting Devices," *Nanomaterials (Basel),* vol. 10, no. 1, 2020, doi: 10.3390/nano10010093.

[28] J. Han, K. Kim, J.-S. Nam, S. J. Hong, E. J. Choi, D. Kim, I. Chung, H.-S. Lin, T.-D. Kim, M. S. Strano, B. Han, J.-W. Oh, H. D. Kim, and I. Jeon, "Genetic Manipulation of M13 Bacteriophage for Enhancing the Efficiency of Virus-Inoculated Perovskite Solar Cells with a Certified Efficiency of 22.3%," *Advanced Energy Materials,* vol. 11, no. 38, p. 2101221, 2021, doi: 10.1002/aenm.202101221.

[29] B. Bortot, M. Apollonio, G. Baj, L. Andolfi, L. Zupin, S. Crovella, M. di Giosia, A. Cantelli, R. Saporetti, L. Ulfo, A. Petrosino, G. Di Lorenzo, F. Romano, G. Ricci, M. Mongiat, A. Danielli, M. Calvaresi, and S. Biffi, "Advanced Photodynamic Therapy with an Engineered M13 Phage Targeting Egfr: Mitochondrial Localization and Autophagy Induction in Ovarian Cancer Cell Lines," *Free Radical Biology and Medicine,* vol. 179, pp. 242-251, 2022, doi: 10.1016/j.freeradbiomed.2021.11.019.

[30] R. Wang, H. D. Li, Y. Cao, Z. Y. Wang, T. Yang, and J. H. Wang, "M13 Phage: A Versatile Building Block for a Highly Specific Analysis Platform," *Anal Bioanal Chem,* vol. 415, no. 18, pp. 3927-3944, 2023, doi: 10.1007/s00216-023-04606-w.

[31] T. T. Tung, M. J. Nine, M. Krebsz, T. Pasinszki, C. J. Coghlan, D. N. H. Tran, and D. Losic, "Recent Advances in Sensing Applications of Graphene Assemblies and Their Composites," *Advanced Functional Materials,* vol. 27, no. 46, p. 1702891, 2017, doi: 10.1002/adfm.201702891.

[32] A. Thakur, "Graphene Aerogel Based Energy Storage Materials – a Review," *Materials Today: Proceedings,* vol. 65, pp. 3369-3376, 2022, doi: 10.1016/j.matpr.2022.05.477.

[33] J. Ederer, P. Janoš, P. Ecorchard, V. Štengl, Z. Bělčická, M. Šťastný, O. Pop-Georgievski, and V. Dohnal, "Quantitative Determination of Acidic Groups in Functionalized Graphene by Direct Titration," *Reactive and Functional Polymers,* vol. 103, pp. 44-53, 2016, doi: 10.1016/j.reactfunctpolym.2016.03.021.

[34] W. Tao, Y. Lan, J. Zhang, L. Zhu, Q. Liu, Y. Yang, S. Yang, G. Tian, and S. Zhang, "Revealing the Chemical Nature of Functional Groups on Graphene Oxide by Integrating Potentiometric Titration and Ab Initio Calculations," *ACS Omega,* vol. 8, no. 27, pp. 24332-24340, 2023, doi: 10.1021/acsomega.3c01596.

[35] A. M. Dimiev, L. B. Alemany, and J. M. Tour, "Graphene Oxide. Origin of Acidity, Its Instability in Water, and a New Dynamic Structural Model," *ACS Nano,* vol. 7, no. 1, pp. 576-588, 2013, doi: 10.1021/nn3047378.

[36] B. Konkena and S. Vasudevan, "Understanding Aqueous Dispersibility of Graphene Oxide and Reduced Graphene Oxide through Pka Measurements," *The Journal of Physical Chemistry Letters,* vol. 3, no. 7, pp. 867-872, 2012, doi: 10.1021/jz300236w.

[37] Y. Li, T. Zhao, C. Wang, Z. Lin, G. Huang, B. D. Sumer, and J. Gao, "Molecular Basis of Cooperativity in Ph-Triggered Supramolecular Self-Assembly," *Nature Communications,* vol. 7, no. 1, p. 13214, 2016, doi: 10.1038/ncomms13214.

[38] W. Xu, Z. Fu, G. Chen, Z. Wang, Y. Jian, Y. Zhang, G. Jiang, D. Lu, J. Wu, and Z. Liu, "Graphene Oxide Enabled Long-Term Enzymatic Transesterification in an Anhydrous Gas Flux," *Nature Communications,* vol. 10, no. 1, p. 2684, 2019, doi: 10.1038/s41467-019-10686-z.

[39] Y. Xu, Q. Wu, Y. Sun, H. Bai, and G. Shi, "Three-Dimensional Self-Assembly of Graphene Oxide and DNA into Multifunctional Hydrogels," *ACS Nano,* vol. 4, no. 12, pp. 7358-7362, 2010, doi: 10.1021/nn1027104.

[40] M. Ardini, G. Golia, P. Passaretti, A. Cimini, G. Pitari, F. Giansanti, L. D. Leandro, L. Ottaviano, F. Perrozzi, S. Santucci, V. Morandi, L. Ortolani, M. Christian, E. Treossi, V. Palermo, F. Angelucci, and R. Ippoliti, "Supramolecular Self-Assembly of Graphene Oxide and Metal Nanoparticles into Stacked Multilayers by Means of a Multitasking Protein Ring," *Nanoscale,* 10.1039/C5NR08632A vol. 8, no. 12, pp. 6739-6753, 2016, doi: 10.1039/C5NR08632A.

[41] T. G. Mayerhöfer, S. Pahlow, and J. Popp, "The Bouguer-Beer-Lambert Law: Shining Light on the Obscure," *ChemPhysChem,* vol. 21, no. 18, pp. 2029-2046, 2020, doi: 10.1002/cphc.202000464.

[42] O. Morag, N. G. Sgourakis, G. Abramov, and A. Goldbourt, "Filamentous Bacteriophage Viruses: Preparation, Magic-Angle Spinning Solid-State Nmr Experiments, and Structure Determination," *Methods Mol Biol,* vol. 1688, pp. 67-97, 2018, doi: 10.1007/978-1-4939-7386-6_4.

[43] P. Passaretti, Y. Sun, T. R. Dafforn, and P. G. Oppenheimer, "Determination and Characterisation of the Surface Charge Properties of the Bacteriophage M13 to Assist Bio-Nanoengineering," *RSC Advances,* vol. 10, no. 42, pp. 25385-25392, 2020, doi: 10.1039/d0ra04086j.

[44] P. Passaretti, I. Khan, T. R. Dafforn, and P. Goldberg Oppenheimer, "Improvements in the Production of Purified M13 Bacteriophage Bio-Nanoparticle," *Scientific Reports,* vol. 10, no. 1, p. 18538, 2020, doi: 10.1038/s41598-020-75205-3.

[45] T. Szabó, E. Tombácz, E. Illés, and I. Dékány, "Enhanced Acidity and Ph-Dependent Surface Charge Characterization of Successively Oxidized Graphite Oxides," *Carbon,* vol. 44, no. 3, pp. 537-545, 2006, doi: 10.1016/j.carbon.2005.08.005.

[46] S.-J. Park and M.-K. Seo, "Intermolecular Force," in *Interface Science and Technology*, vol. 18, S.-J. Park and M.-K. Seo Eds.: Elsevier, 2011, ch. 1, pp. 1-57.

[47] J. E. Hallett, D. A. J. Gillespie, R. M. Richardson, and P. Bartlett, "Charge Regulation of Nonpolar Colloids," *Soft Matter,* 10.1039/C7SM01825H vol. 14, no. 3, pp. 331-343, 2018, doi: 10.1039/C7SM01825H.

[48] E. S. Orth, J. G. L. Ferreira, J. E. S. Fonsaca, S. F. Blaskievicz, S. H. Domingues, A. Dasgupta, M. Terrones, and A. J. G. Zarbin, "Pka Determination

of Graphene-Like Materials: Validating Chemical Functionalization," *Journal of Colloid and Interface Science,* vol. 467, pp. 239-244, 2016, doi: 10.1016/j.jcis.2016.01.013.

[49] P. Gameiro, S. Reis, J. L. F. C. Lima, and B. de Castro, "Calibration of Ph Glass Electrodes by Direct Strong Acid/Strong Base Titrations under Dilute Conditions," *Analytica Chimica Acta,* vol. 405, no. 1, pp. 167-172, 2000, doi: 10.1016/S0003-2670(99)00641-8.

[50] J. H. Adair, E. Suvacı, and J. Sindel, "Surface and Colloid Chemistry," in *Encyclopedia of Materials: Science and Technology*, K. H. J. Buschow, R. W. Cahn, M. C. Flemings, B. Ilschner, E. J. Kramer, S. Mahajan, and P. Veyssière Eds. Oxford Elsevier, 2001, pp. 1-10.

[51] M. V. Lozano, M. J. Santander-Ortega, and M. J. Alonso, "In Vitro Relevant Information for the Assessment of Nanoparticles for Oral Drug Administration," in *Nanotechnology for Oral Drug Delivery*, J. P. Martins and H. A. Santos Eds.: Academic Press, 2020, ch. 14, pp. 419-458.

[52] E. Joseph and G. Singhvi, "Multifunctional Nanocrystals for Cancer Therapy: A Potential Nanocarrier," in *Nanomaterials for Drug Delivery and Therapy*, A. M. Grumezescu Ed.: William Andrew Publishing, 2019, ch. 4, pp. 91-116.

[53] S. Kashyap, S. Mishra, and S. K. Behera, "Aqueous Colloidal Stability of Graphene Oxide and Chemically Converted Graphene," *Journal of Nanoparticles,* vol. 2014, p. 640281, 2014, doi: 10.1155/2014/640281.

[54] B. R. Putra, K. Szot-Karpińska, P. Kudła, H. Yin, J. A. Boswell, A. M. Squires, M. A. Da Silva, K. J. Edler, P. J. Fletcher, S. C. Parker, and F. Marken, "Bacteriophage M13 Aggregation on a Microhole Poly(Ethylene Terephthalate) Substrate Produces an Anionic Current Rectifier: Sensitivity toward Anionic Versus Cationic Guests," *ACS Applied Bio Materials,* vol. 3, no. 1, pp. 512-521, 2020, doi: 10.1021/acsabm.9b00952.

[55] Y. Xiong, X. Liu, and H. Xiong, "Aggregation Modeling of the Influence of Ph on the Aggregation of Variably Charged Nanoparticles," *Scientific Reports,* vol. 11, no. 1, p. 17386, 2021, doi: 10.1038/s41598-021-96798-3.

[56] B. Králová, "Electrophoretic Methods for the Isolation and Characterization of Enzymes," *Analytica Chimica Acta,* vol. 383, no. 1, pp. 109-117, 1999, doi: 10.1016/S0003-2670(98)00492-9.

[57] F. Fouladvand, P. Bemani, M. Mohammadi, R. Amini, and F. A. Jalilian, "A Review of the Methods for Concentrating M13 Phage," *Journal of Applied Biotechnology Reports,* Review vol. 7, no. 1, pp. 7-15, 2020, doi: 10.30491/JABR.2020.105916.

CHAPTER 4

THERMONANOMECHANICS OF GRAPHAGE13 AEROGELS

This chapter is based on the previously published paper:

K. Stokes, Y. Sun, H. Zhang, P. Passaretti, H. White, and P. Goldberg Oppeneheimer, "Thermonanomechanics of Graphene Oxide-M13 Bacteriophage Nanocomposites -Towards Graphene-Based Nanodevices," *Carbon Trends,* vol. 15, p. 100343, 2024/06/01/ 2024, doi: 10.1016/j.cartre.2024.100343

Author contributions – **K. Stokes**, **P. Passaretti** and **Y. Sun** conceptualised the study. **K. Stokes, H. Zhang** and **Y. Sun** carried out the experimental acquisition and analyses and validated the results. **P. Goldberg Oppenheimer** and **H. White** were responsible for funding acquisition and resources provision. **P. Goldberg Oppenheimer** supervised and administered the study, curated the data and overviewed the developed methodology. **K. Stokes, Y. Sun** and **P. Goldberg Oppenheimer** wrote the original draft and reviewed and edited the final draft.

4.1 Abstract

The self-assembly of graphene oxide (GO) and M13 bacteriophage results in the formation of micro-porous structures, known as GraPhage13 aerogels (GPA). Given the limited applications of aerogels in industry due to their nanomechanical properties, along with the previously observed temperature-dependent characteristics in graphene-based nanocomposites, a thorough exploration of the thermosensitive nanomechanical properties of GPA is essential. Herein, a comprehensive characterisation of the morphology, composition, and spectroscopic analysis of the GPA for a range of temperatures has been conducted and correlated with its nanomechanical properties. Elevated temperatures have been found to lead to gradual removal of oxygen-containing functional groups (OCFGs) from GPA, observed as an increase in the carbon-to-oxygen ratio from 1.19±0.02 at 25°C to 1.57±0.04 at 250°C. The removal of these OCFGs disrupted the GO-M13 bonds, leading to the presence of fewer but larger pores. This resulted in increased structural defects, observed through an increase in the intensity ratio of the D to G Raman peaks (I_D/I_G), and a reduction in stiffness from 82.9 ± 0.6 N/m at 25°C to 36.1 ± 0.4 N/m at 250 °C. Notably, unique nanomechanical behaviours of GPA have been further identified, where the thermal expansion of sp^3 bonds exceeds that of a crystalline sp^3 structure, while the thermal contraction of sp^2 bonds in GPA is found to be between graphite and GO. This underscores the impact of GO functionalisation on the thermal expansion behaviour of GPA. The obtained insights enhance the overall comprehension of the temperature annealing impact on GPA and highlight the tuneability of its nanomechanical properties, showcasing a broad potential of this novel nanocomposite across a diverse range of applications.

4.2 Introduction

Graphene Oxide (GO) is an atomically thin layer of sp^2 - hybridised carbon with oxygen-containing functional groups (OCFGs) such as hydroxyl, carboxyl, carbonyl and epoxide [1]. The presence of the OCFGs enables GO to interact with biomolecules, facilitating its self-assembly into graphene-based nanocomposites [2] One such nanocomposite, GraPhage13 aerogels (GPAs) are formed through the self-assembly of GO and the M13 bacteriophage. GPA's porous structure provides a high surface area and low density, with tuneable properties suitable for a broad range of applications ranging from adsorbents [3, 4], through electrodes [5, 6], and onto sensors [7, 8].

To enable the utilisation of aerogels in these applications, they must exhibit excellent mechanical properties including a high mechanical strength and stability, elasticity, durability, and thermal stability [9, 10]. However, aerogels often suffer from suboptimal mechanical characteristics such as low mechanical stability, brittleness, and poor deformation recovery, thereby limiting their potential in industrial exploitation [11, 12]. Since graphene-based hybrid nanocomposites have previously demonstrated temperature-dependent stability, structure and mechanical properties [13, 14], it is imperative to evaluate the influence of temperature on the morphology, composition and nanomechanical properties of GPA to facilitate the comprehensive understanding of GPA's sensitivity to changes in temperature as well as its inherent tuneability. Understanding the thermomechanical properties of GPA, especially under varying temperature and related mechanical stress conditions, is critical to ensuring their reliability and efficiency in applications such as electronics, where the devices are heated during operation. This knowledge not only aids in optimising their performance

but also opens new possibilities for their use in environments with extreme temperature conditions, e.g., cryogenic applications, or mechanical demands.

In this study, the effects of temperature on the morphology, composition and nanomechanics of GPA were examined. The nanocomposite was annealed at temperatures ranging from 25°C to 300°C, with the specific temperatures dependent on the requirements of each experimental method. This range is aligned with the commonly applied temperatures for various applications including for instance, low temperature thermal energy storage [15, 16], gas sensors [17, 18], and carbon capture [19, 20]. The morphology and composition of GPA have been subsequently analysed via scanning electron microscopy (SEM) and energy-dispersive X-ray spectroscopy (EDX). Furthermore, the nanomechanical properties have been investigated by obtaining force-distance (F-D) curves via atomic force microscopy (AFM) and, to gain an in-depth understanding of the effect of temperature on the structure of GPA, Raman spectroscopy with in-situ annealing has been performed. The annealing of GPA was found to increase the carbon-to-oxygen (C:O) ratio, modify the presence of defects and reduce both the stiffness of the nanocomposite as well as the adhesion force between it and the AFM probe. The thermal expansion rate of sp^3 bonds in GPA were established to exceed these in a crystalline sp^3 structure, while the sp^2 bonds exhibited thermal expansion behaviour between graphite and GO, signifying the impact of GO's functionalisation on the thermal expansion of GPA.

This research highlights the improved understanding of the temperature-dependent properties of GPA and elucidates the potential to manipulate its structure, composition and nanomechanics through the heat exposure. Advancing our understanding of GPA, a carbon-based aerogel, utilising its enhanced thermal and nanomechanical

properties, make it a promising candidate for environmental applications including water purification systems and air filtration as well as in the development of smart materials for sensors and actuators.

The findings collectively not only contribute to the expanding body of knowledge on carbon materials, offering insights pertinent to a broad range of applications ranging from nanotechnology to environmental engineering but also emphasise the ability to fine-tune the GPA, paving the way for the integration of this novel nanocomposite in graphene-based devices for applications in for instance, electromagnetic wave absorption [21, 22], oil-water separation [23, 24] or thermal energy storage [25, 26].

4.3 Results and Discussion

4.3.1 Micronano-morphology and Composition

The morphology of GPA at ambient temperature was compared to GPA annealed at 250°C for 30 min (GPA_{250}) (Figure 4.1). The specific GPAs were selected for comparison since they represent the two extremes of the attainable temperature range. The annealing process has been identified to cause irreversible changes to the micronano-structure of the nanocomposite (Figure 4.1c-d), with the original porous structure remaining intact even at the higher temperature of 250°C. This is most probably due to the strong interactions between the positively charged N-terminus and K_8 residue of M13 and the carboxylic acid groups in GO [27]. These interactions increase its overall structural stability following annealing and consequently, prevent structural changes in the subsequent heating to similar temperatures.

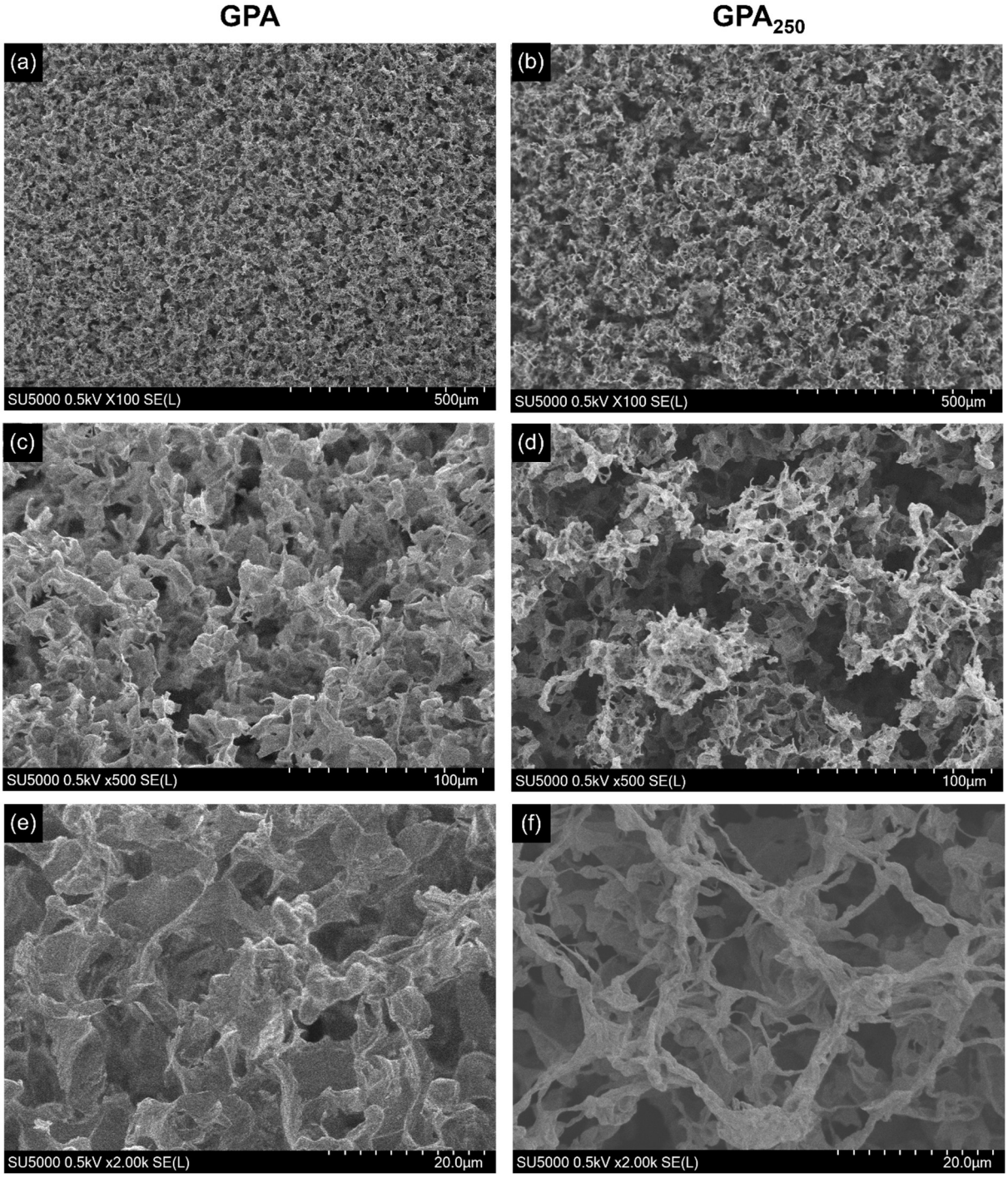

Figure 4.1: SEM images of GPA and GPA_{250}

Characteristic SEM images of the micronano morphology of GPA and GPA_{250} at **(a-b)** 100x, **(c-d)** 500x and **(e-f)** 2000xmagnification.

The morphologies of GPA and GPA_{250} appear similar, however there is a difference in the porosity, with the larger pore sizes identified for GPA_{250} compared to GPA. An in-

depth analysis with SEM imaging enabled the comparison of the average 2D pore size distributions (for further details, please see Section 2.3.5). Although this technique has limitations, such as analysing only a 2D representation of surface pores and the potential subjectivity in image thresholding, it remains an effective method for comparing the porosity of two materials. The results demonstrated consistency across three areas from three different samples of both GPA and GPA_{250}, as reflected in the small error bars observed in the pore size distribution (Figure 4.2).

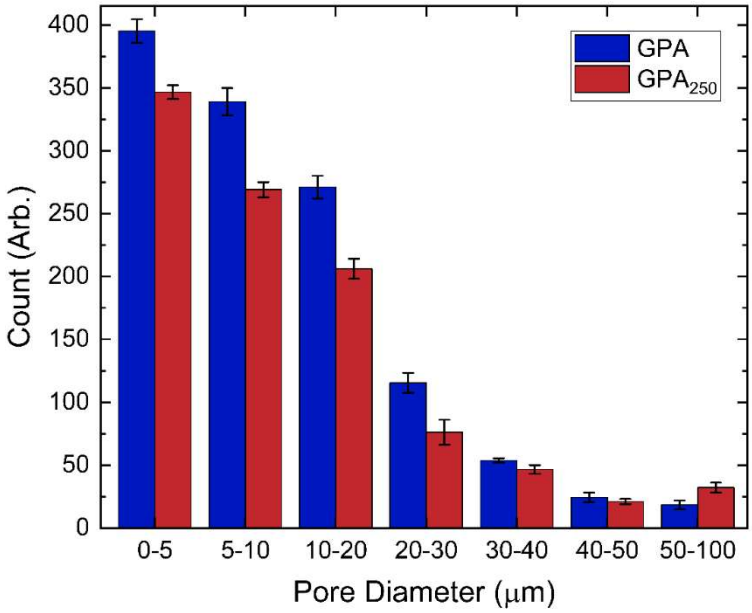

Figure 4.2: Pore size distribution of GPA and GPA_{250}.

The distribution of pore diameter of GPA and GPA_{250}. The count represents the number of pores detected in a SEM image at 100x magnification.

The variation in pore size distribution from SEM images taken over the same area highlights the differences between GPA and GPA_{250}. GPA is found to exhibit a notably higher number (1160 ± 40) of pores with diameter below 30 µm compared to the GPA_{250} (900 ± 30). With the increase in the pore size, the distributions equalize, where both GPA and GPA_{250} exhibit a similar number of pores with diameters in the range of 40–50 µm. For diameters exceeding 50 µm, GPA_{250} exhibits a higher pore count (32 ± 4)

compared to GPA (18 ± 3). This may be attributed to elevated temperatures, which lead to the removal of certain OCGFs through the emission of gases, such as the CO_2, disrupting bonds between GO and M13 and increasing the occurrence of larger pores. Furthermore, differences in the number of pores are observed between the two structures. GPA exhibits a greater number of pores compared to GPA_{250}, with an average of 1220 ± 30 pores detected in the SEM images for GPA, compared to 1000 ± 10 for GPA_{250}. The increase in annealing temperature disrupts the GO-M13 bonds, removing some of the pore walls and resulting in fewer but larger pores, and forming a more fibrous structure [28, 29].

The effect of temperature on the GPA was further investigated using energy dispersive x-ray (EDX) spectroscopy (Section 2.2.4). The representative spectrum of GPA_{250} in comparison to the EDX spectra of GPA (Figure 4.3a) [27, 30] demonstrated a higher ratio of carbon-to-oxygen (C:O) for GPA_{250} relative to GPA. With the increase in annealing temperature from 25 °C to 250 °C, the C:O ratio is found to increase from

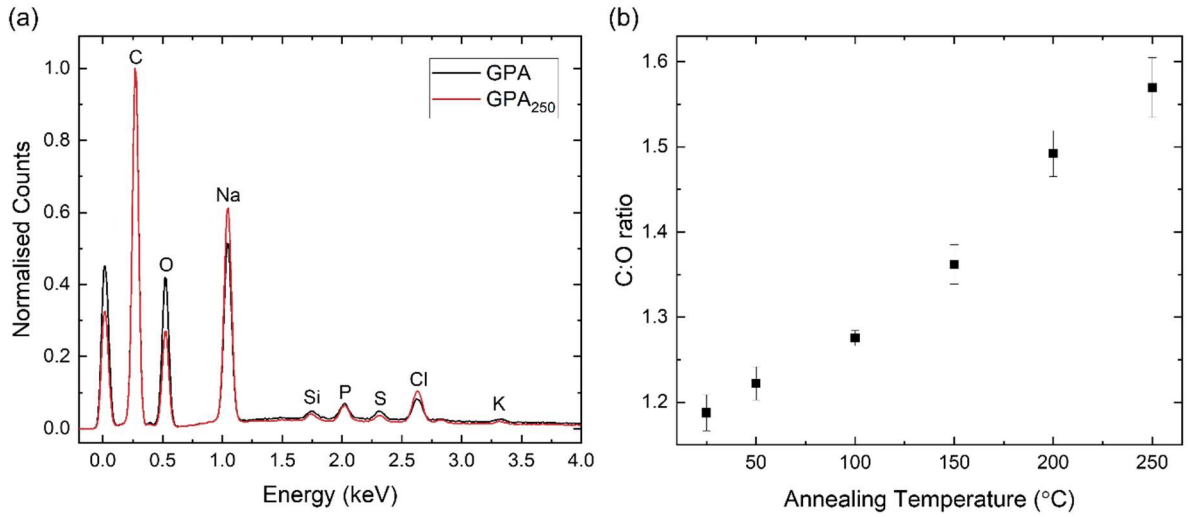

Figure 4.3: Composition of GPA with temperature

(a) Representative EDX spectrum of GPA and GPA_{250}. The spectra have been normalised with respect to the carbon peak. **(b)** Change in carbon-to-oxygen (C:O) ratio of GPA versus annealing temperature.

1.19 ± 0.01 for GPA to 1.58 ± 0.03 for GPA_{250} (Figure 4.3b). This confirms that the higher annealing temperatures progressively reduce GO towards its reduced graphene oxide (rGO) form by removing its OCFGs, leading to an increase in the C:O ratio [31].

4.3.2 Nanomechanics

The nanomechanics of GPA annealed at varying temperatures has been subsequently investigated through the force-distance (F-D) curves (Figure 4.4) obtained via AFM (Section 2.2.7), allowing for a detailed examination of the mechanical response of GPA after being subjected to a range of annealing temperatures. This also provides further insights into the adhesion forces and stiffness of GPA, offering a comprehensive understanding of how this nanomaterial responds to temperature-induced changes.

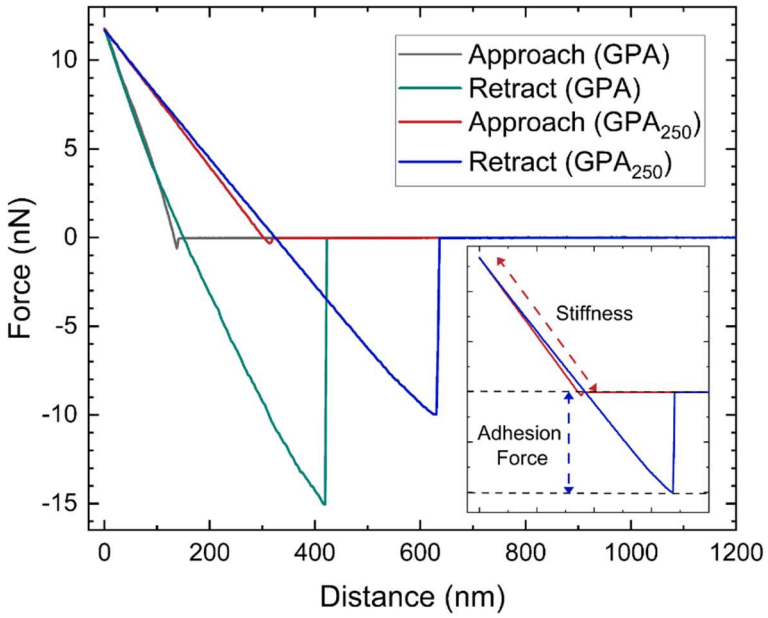

Figure 4.4: F-D curves for GPA and GPA_{250}

Force-distance (F-D) curves for GPA and GPA_{250} obtained through atomic force microscopy. Inset: the stiffness is the gradient of the approach curve in the contact region and the adhesion force is the maximum negative force on the retraction curve.

Following the approach curves from right to left hand side shows an initial absence of contact between GPA and the tip results in zero force. Once the attractive forces between the tip and GPA overcome the spring constant of the cantilever, the tip snaps into contact with the surface of GPA, leading to an observed increase in the force in the negative direction [32]. The tip continues the approach, indenting the GPA and bending the cantilever whilst increasing its deflection, until a set maximum force is obtained. Since the cantilever deflection is proportional to the force applied to the sample, the stiffness of the pore walls can be determined by calculating the force exerted by the AFM tip on the pore walls of GPA as a function of the indentation distance.

The stiffness quantifies the capacity of the sample to withstand external forces without undergoing deformation and can be derived by determining the gradient of the approach curve in the contact region, i.e., above 0 nN [33, 34]. The variation in GPA stiffness versus varying temperatures is shown in Figure 4.5a, where it is evident that the stiffness of GPA decreases with annealing temperature, from 82.9 ± 0.6 N/m at 25°C to 36.1 ± 0.4 N/m at 250 °C, most likely due the morphology. Shown in Figure 4.1 – Figure 4.3, subjecting GPA to higher temperatures increases the distance between surface asperities due to the removal of OCFGs, reducing the stress transfer through the structure, and therefore reducing the stiffness of the pore walls [35, 36]. The decreasing strain with temperature could be also attributed to the defects introduced into the GPA, inducing irregularities in its structure [37].

It is important to distinguish the thermal behaviour of GPA from that of GO. In conventional GO systems, the reduction to rGO typically enhances compressive strength due to the removal of OCFGs and the restoration of sp^2 carbon networks [38].

However, in GPA, the mechanical properties depend on the integrity of the bonds formed between GO and M13, which are mediated by GO's OCFGs. As these functional groups are eliminated with increasing temperature, the GO-M13 bonds are disrupted, leading to a reduction in strength. This mechanism underscores the unique thermonanomechanical behaviour of GPA compared to GO.

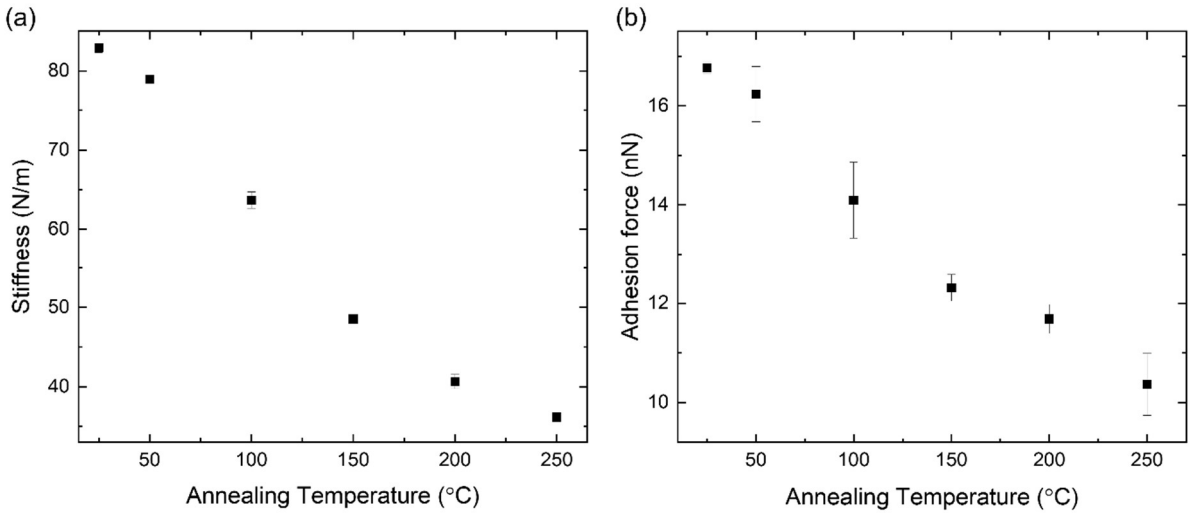

Figure 4.5: Stiffness and adhesion force of GPA with temperature

The change in **(a)** stiffness of GPA and **(b)** the adhesion force between the AFM probe and the GPA, with increasing annealing temperature.

Following the retraction curve (Figure 4.4) from left to right, various attractive forces between the tip and the GPA, e.g., electrostatic, capillary, van der Waals and contact forces, cause the tip to bend towards and adhere to the sample as the tip retracts. The spring constant of the cantilever eventually overcomes the adhesion between the tip and GPA and disengages from the nanocomposite surface, restoring the force to zero. The adhesion force between the AFM probe and GPA is determined by the maximum negative force on the deflection curve [39, 40].

The adhesion forces between the probe and GPAs annealed at different temperatures (Figure 4.5b) indicate that increasing the annealing temperature results in the reduction

of the adhesion force from 16.8 ± 0.1 nN at 25°C to 10.4 ± 0.6 nN at 250°C. This is attributed to structural changes to GPA. The F-D curves were conducted under ambient conditions, with forces arising from the capillary condensation dominating the adhesive forces [41, 42]. Annealing GO leads to its gradual reduction towards the rGO, characterised by fewer OCFGs and more sp^2-hybridised carbon [31, 43]. Since OCFGs interact with water whilst sp^2-hybridised carbon is hydrophobic, the reduction of GO leads to an increased hydrophobicity [44, 45]. Water droplets on the surface of more hydrophobic structures demonstrate larger contact angles and high motilities, leading to a lower adhesion force [46, 47].

Furthermore, the reduction in adhesion force may also relate to alterations in the porous micronano-morphology. Subjecting GPA to increased temperatures changes to pore size distribution, reducing the number of pores between 0 and 40 μm and increasing the number of pores in the range of 50–100 μm (Figure 4.1 – Figure 4.2). Given that the adhesion force is related to the contact area between surface asperities, larger pore sizes result in a smaller contact area, reducing the adhesion force [48]. A reduction in the adhesion force also lowers the strain transfer between materials with a thermal expansion coefficient mismatch, such as GPA and the substrate or applied coatings. Reduced stress transfer primarily results in sliding at the interface, which helps to mitigate stress buildup. This sliding mechanism allows the materials to better

accommodate thermal expansion mismatches, thereby improving the stability and performance of GPA-based devices under varying temperature conditions [49, 50].

4.3.3 Raman Spectroscopy with *Insitu* Heat Treatment

Raman spectroscopy (Section 2.2.8) was applied to study the changes to the structure of GPA with temperature. The insitu thermal treatment setup enabled temperatures up to 300°C to be accomplished. The representative spectra exhibit two prominent peaks at shifts of 1360 cm^{-1} and 1590 cm^{-1}, and signal-to-noise (SNR) ratio noticeably higher for GPA_{250} compared to GPA for the same acquisition time (Figure 4.6a-b). This is attributed to several factors, including the temperature increase, which causes the water absorbed within the GPA to evaporate and subsequently condense on the walls of the heating chamber. Consequently, the laser focus is compromised, leading to a reduction in the number of counts and affecting the SNR. Furthermore, the spectra are affected by thermal background radiation. While the constant component of this radiation can be removed, random thermal fluctuations remain unaccounted for, leading to a decrease in the SNR [51].

The two characteristic peaks identified via Raman spectra for GPA and GPA_{250} could potentially be a superposition of multiple spectral bands. Therefore, to determine the optimal peak fitting, various fits were investigated for GPA and GPA_{250} (Figure 4.6a-b) via the Bayesian Information Criterion (BIC), enabling a statistical comparison, with the fit with the lowest BIC value considered the most suitable for the spectrum analysis (for further details please refer to Section 2.3.2) [52, 53].

BIC values for Raman spectra of GPA fitted with varying numbers of peaks (Table 4.1) show a decrease of 974 from a 2-peak to a 4-peak fit, followed by a subsequent

increase of 20 for a 5-peak fit, indicating that the 4-peak fit (Figure 4.6e) is the optimal choice. An in-depth discussion of the characteristic Raman spectra of GO and GPA is

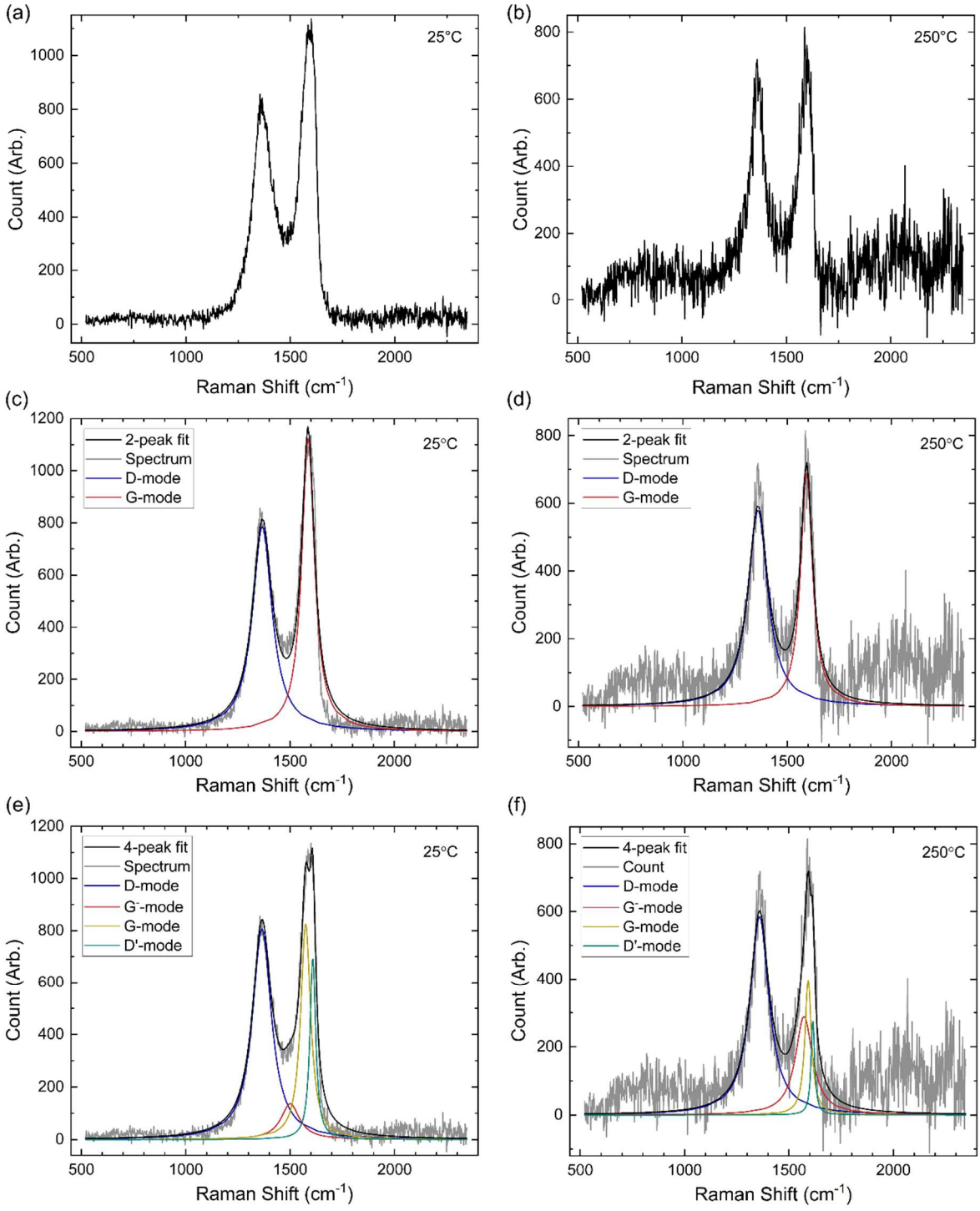

Figure 4.6: Raman spectra of GPA and GPA_{250}

Raman spectra of **(a)** GPA and **(b)** GPA_{250} with the optimal 2-peak fit **(c-d)** and 4-peak fit **(e-f)**, respectively

included in Section 1.4.2. In brief, the G-mode peak (Figure 4.6c-f) originates from the stretching of the sp^2 bonds, the D'-mode and G^- mode are caused by defective sp^2 structures due to the functionalisation of GO [54, 55]. The peak profile over the D-mode range likely includes contributions from defective sp^2 bonds, and amorphous or disordered sp^3-hybridised structures [27, 52, 56].

Table 4.1: Comparing Raman spectra peak fits

Comparison of the BIC values of the 2-peak and 4-peak fits to the Raman spectra of GPA acquired at 25 °C and 250 °C.

Sample	BIC Value			
	2-peak	3-peak	4-peak	5-peak
GPA	7665	7073	6691	6711
GPA_{250}	9186	9190	9202	9223

Conversely, for GPA_{250}, the 2-peak fit exhibits the lowest BIC value (Figure 4.6d), suggesting it is the most suitable peak fit instead of the 4-peak fit (Figure 4.6f). The difference in the optimal fitting between GPA and GPA_{250} can be attributed to structural changes induced by the different temperatures. The D′ peak tends to merge with the G peak at high defect concentrations, suggesting that exposing GPA to elevated temperatures leads to an increase in the number of defects within the structure [57]. However, it should be noted that the G^-, G and D' peaks in the 4-peak fit are all associated with the presence of sp^2 bonds and can be superimposed to form the G-mode peak in the 2-peak fit. Therefore, for the purpose of tracking the effect of

temperature on the Raman spectrum, the two-peak fit with the D-mode and G-mode is sufficient. The two-peak fit for GPA and GPA_{250} is shown in Figure 4.6c-d**,** respectively.

Figure 4.7 illustrates the position of the D and G peaks as the temperature is incrementally increased in-situ within Raman spectrometer. This was compared to the predicted trend of Raman shift caused by the thermal expansion of graphite, GO, and diamond. The predictions were derived by correlating thermal expansion data with the relationship between strain and Raman shift (refs [58-61]), to determine whether the changes in the position of the D- and G-modes are due to the thermal expansion of GPA.

The thermal expansion of a material results from the response of its structure and bonds to changes in temperature. By comparing the temperature-dependent evolution of the Raman D band frequency of diamond, a sp^3 hybridised structure, to that of GPA, allows to discern whether the D peak is predominantly influenced by sp^3 bonds. This would exhibit a downward shift with an increase in temperature. Conversely, if it is influenced by sp^2 bonds, it would demonstrate an upward shift, consistent with a small yet negative thermal expansion coefficient of graphene and in-plane graphite, leading to the stiffening of sp^2 carbon-carbon bonds. Conversely, the G peak represents the sp^2 bonds in GPA, capturing the functionalisation and defects associated with these bonds. However, unlike its constituent GO, exhibits a three-dimensional carbon-based architecture and therefore, the Raman shift caused by the thermal expansion of both GO and graphite was compared to the Raman shift of the G peak [62, 63].

The general trend in Figure 4.7a demonstrates that the D peak position decreases as the temperature increases, with the largest Raman shift of 1369.1 ± 0.7 cm^{-1} at 40°C

and the lowest of 1363 ± 3 cm^{-1} at 300 °C. This redshift with temperature suggests the softening of the carbon-carbon bonds, with the predominant influence being attributed to the sp^3 Raman mode rather than the predicted sp^2 D-mode [62]. On the other hand, the position of the G peak progressively increases with temperature (Figure 4.7b) [52], exhibiting a minimum shift of 1586.5 ± 0.4 cm^{-1} at 25°C and reaching 1592 ± 2 cm^{-1} at 300°C, demonstrating the stiffening of sp^2 bonds and therefore implying that both the stiffening and softening of carbon-carbon bonds occur in GPA, demonstrating the different inherent structures present. Further, the predicted Raman shift for diamond with the D-mode (Figure 4.7a) demonstrates downshift with temperature, indicating that the position of the latter is dependent on the thermal expansion of GPA. Moreover, Figure 4.7a demonstrates that the thermal expansion rate of sp^3 bonds in GPA exceeds that of the crystalline sp^3 structure, revealing a distinctive thermal behaviour. The difference in the thermal expansion rates, with the D-mode showing a downshift of 0.030 ± 0.003 cm^{-1}/°C and diamond a downshift of 0.0093 cm^{-1}/°C, could be because of the differences in the microstructure of GPA and diamond. However, it could also be indicative of presence of defects in the GPA micronano-structure, increasing the distance between neighbouring carbon atoms [62].

Furthermore, comparing the temperature-induced upshift of the GPA G-mode with the thermal expansion of graphite and GO (Figure 4.7b) reveals the in-plane thermal expansion of GPA between graphite and GO. The substantial deviation in the Raman shift trend, in contrast to the thermal contraction behaviour of GO, suggests that the in-plane thermal expansion of GO in GPA is not solely influenced by thermal contraction of the sp^2 bonds, but also by the GPA micronano-structure. The larger shift rates for the GPA G-mode compared to the graphite in-plane thermal expansion

demonstrate complex in-plane thermal expansion of the nanocomposite, determined by the functionalisation of GO. The upshift in the G-mode, lying between the thermal expansion of graphite and GO, indicates that the functionalisation of GPA does impact the thermal expansion coefficient of the sp^2 C-C bonds, highlighting a unique nanomechanical feature in the nanocomposite [58, 64].

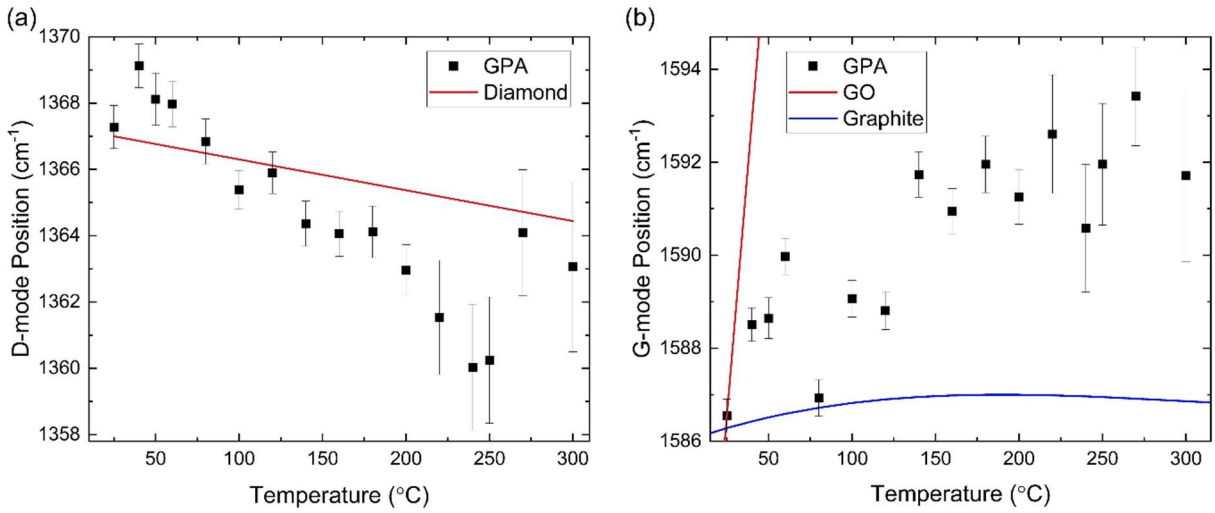

Figure 4.7: Position of GPA Raman peaks with temperature

(a) Position of D-mode compared to the Raman shift resulting from thermal expansion of diamond and **(b)** position of the Raman shift resulting from thermal expansion of graphene oxide and graphite. The error bars represent that standard error in the peak position.

To explore further potential indicators for structural changes of GPA with temperature, the relationship between the temperature and the full width half maximum (FWHM) of the Raman peaks was analysed. Both the D-mode (Figure 4.8a) and the G-mode (Figure 4.8b) FWHM are found to decrease with temperature from 25°C to 200°C, with the D-mode decreasing from 114 ± 2 cm^{-1} to 82 ± 2 cm^{-1} and the G-mode from 74 ± 1 cm^{-1} to 61 ± 2 cm^{-1}. This represents the gradual reduction of GO whilst some of the OCFGs are removed [65, 66]. Beyond the temperature of 200°C, there is a general

increase in the FWHM, with the G-mode increasing to 104 ± 6 cm^{-1} at 300°C and the D-mode increasing to 131 ± 6 cm^{-1} at 270°C.

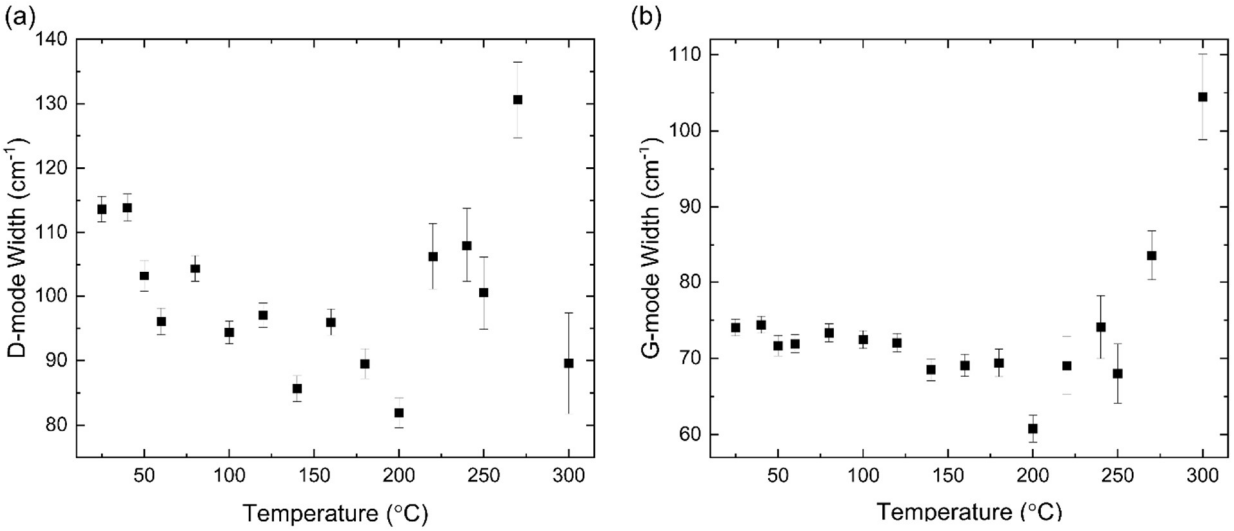

Figure 4.8: FWHM of GPA Raman peaks with temperature

The full width half maximum (FWHM) of the GPA **(a)** D-mode and **(b)** G-mode Raman peaks as function of temperature. The error bars represent the standard error in the peak width.

The significant change in the FWHM observed at temperatures higher than 200°C demonstrates the increase in structural deformation [67]. This corresponds with the observations in SEM images (Figure 4.1) of the structural changes caused by high temperature treatment. Moreover, this is consistent with Figure 4.5a, illustrating a decrease in GPA stiffness with increasing temperature thereby, rendering the GPA more prone to deformation.

To further understand the reduction in the D-mode FWHM to 90 ± 8 cm^{-1} at 300°C and investigate the temperature-induced alterations in the micronano-structure of GPA, the ratio of the D-mode and G-mode intensities (I_D/I_G) was examined (Figure 4.9), which provides a measure of defects in GPA with temperature [65]. Between 25°C and 60°C, I_D/I_G decreases from 1.07 ± 0.02 to 0.90 ± 0.02, whereafter, the I_D/I_G increases with

temperature to 1.3 ± 0.1 at 270°C until a sudden drop-off at 300°C, which has an I_D/I_G value of 0.57 ± 0.04.

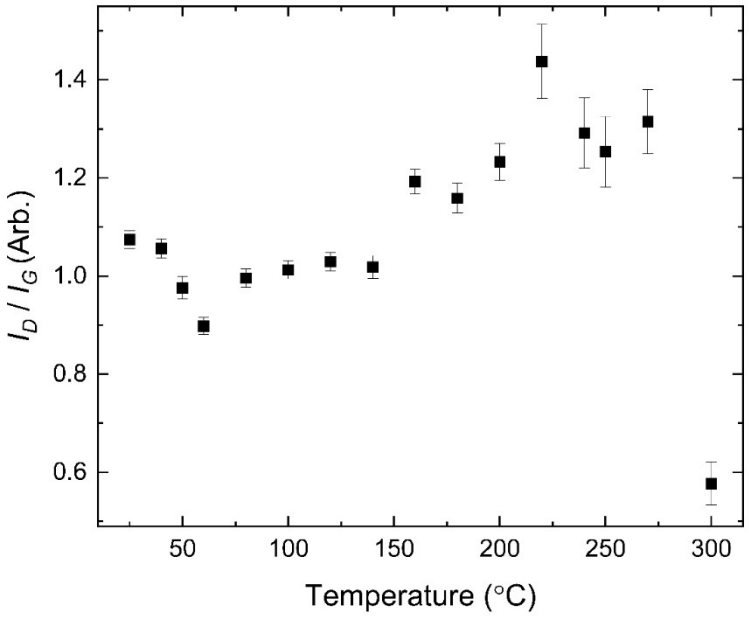

Figure 4.9: I_D/I_G of GPA with temperature

The D-mode/G-mode intensity ratio (I_D/I_G) for GPA versus temperature.

There are two competing mechanisms contributing towards the I_D/I_G ratio with increase in temperature. As GO decomposes, OCFGs are removed from the structure, reducing the number of defects and therefore, lowering the I_D/I_G. However, some of the OCFGs removed may be carbonyl and carboxyl groups, and carbon atoms are removed from the structure through the elimination of these functional groups, in the form of gases such as CO and CO_2. This generates defects in GPA and therefore increases I_D/I_G [29, 68, 69].

GO starts to decompose at temperatures above 60°C, however, a decrease in I_D/I_G is visible below this temperature. This can be attributed to the desorption of water within the GPA structure, which reduces the number of defects. The increase in I_D/I_G between 60°C and 270°C suggests the increased removal of carboxyl and carbonyl groups with

temperature. The sudden decrease in I_D/I_G at 300°C implies that further OCFGs are being removed without the additional carbon atoms and since the epoxy groups are removed at temperatures higher than 400°C, it is likely that the decrease in I_D/I_G signifies the onset of the hydroxyl groups removal from GO [31, 66, 67].

These findings differ from previous Raman studies on GO, which report that I_D/I_G decreases with increasing temperature [70, 71]. This can be attributed to the differences between GO and GPA, specifically the interactions between GO and M13 which enable its self-assembly. The removal of OCFGs with increasing temperature disrupts the GO-M13 bonds, significantly influencing I_D/I_G. This mechanism is unique to GPA and does not occur in systems composed solely of GO.

4.4 Conclusion

The effect of annealing GraPhage13 aerogels (GPA) on their micronano-morphology, composition and nanomechanical properties has been investigated through a suite of SEM, EDX, AFM force measurements and Raman spectrometry. The EDX spectra revealed that annealing GPA increases the carbon-to-oxygen ratio, with the gradual reduction of graphene oxide (GO) through the elimination of its oxygen-containing functional groups (OCFGs). The occurrence of defects in GPA with temperature was also found to depend on the elimination of OCFGs and consequently, the removal of the carbon attached to the carbonyl and carboxyl groups. Annealing GPA also changes its nanomechanical properties, with both the adhesion force between the AFM probe and the GPA as well as the stiffness of the nanocomposite decreasing with an increase in temperature.

The structural changes of GPA with temperature ranging from 25°C to 300°C have been further studied via Raman spectroscopy with an in-situ annealing. The representative spectra of GPA demonstrated two dominant peaks, with the D-mode arising from contribution of sp^3 Raman peak and the peak originating from disordered sp^2 carbon, and the G-mode from the stretching of sp^2 carbon-carbon bonds. The D-mode was found to downshift with the increase in temperature, attributed to the softening of sp^3 bonds and the presence of defects. Conversely, the G-mode was found to upshift, owing to the stiffening of sp^2 bonds due to the negative thermal expansion coefficient of GO. Comparing the D-mode and G-mode Raman shift to the thermal expansion of diamond, GO and graphite demonstrated the unique thermal and nanomechanical behaviours of GPA. The thermal expansion rate of sp^3 bonds in GPA surpasses that observed in a crystalline sp^3 structure and the sp^2 bonds in GPA exhibit a thermal expansion between graphite and GO, indicating that the functionalisation of GO influences the thermal expansion of GPA. GraPhage13 aerogel, derived from the self-assembly of graphene oxide and M13 bacteriophage, presents a micro-porous structure with potential industrial applications. Annealing at elevated temperatures results in the removal of oxygen-containing functional groups from GPA, transforming GO into reduced graphene oxide, and leading to larger pore sizes, smaller contact areas and hence reduced adhesion and stiffness. Notably, GPA exhibits unique thermal behaviours where the sp^3 bonds expand more than in crystalline structures, and sp^3 bonds contract in a range intermediate between graphite and GO. These findings highlight the significant influence of GO functionalisation on GPA's thermal properties. Advanced Raman spectroscopy analysis further reveals consistent defect levels and exceptional thermal-mechanical stability at the nanoscale. The enhanced

understanding of GPA's properties post-annealing indicates its applicability in diverse areas including electronic and photonic devices, energy storage and conversion systems, environmental applications, and smart material systems.

Overall, this study demonstrates the effect of temperature on the micronano-composition and nanomechanics of GPA as well as providing the underpinning insights into the mechanism behind these changes, whilst yielding the temperature-dependent properties and tuneability of GPA and thus, laying the platform towards its exploitation in a range of applications as a versatile material in carbon-based technology. For instance, the tuneable nanomechanical properties of the GPA make it a promising candidate for the development of advanced sensors, capable of detecting subtle environmental changes, whereas its enhanced stability and performance within a broad range of temperatures, indicate its potential as a reliable material for energy storage systems, where thermal fluctuations are common. The overall unveiled unique characteristic of this nanocomposite paves the way for the design and implementation of GPA in miniaturised devices, showcasing its versatility and importance in advancing technological innovations.

4.5 Materials and Methods

Further information on graphene oxide and M13 bacteriophage used in these experiments can found in Sections 2.1.1 and 2.1.2, respectively.

For detailed descriptions of the methods used in this chapter, please refer to Chapter 2,, specifically the following sections:

- 2.2.2 Fabrication of GraPhage13 Aerogels (GPA)

- 2.2.4 Scanning Electron Microscopy (SEM) and Energy Dispersive X-Ray Spectroscopy (EDX)
- 2.2.7 Atomic Force Microscopy
- 2.2.8 Raman Spectroscopy
- 2.3.2 Bayesian Information Criterion (BIC)
- 2.3.3 Peak Fitting
- 2.3.5 Pore Size Analysis

4.6 References

[1] S. C. Ray, "Application and Uses of Graphene Oxide and Reduced Graphene Oxide," in *Applications of Graphene and Graphene-Oxide Based Nanomaterials*, S. C. Ray Ed. Oxford: William Andrew Publishing, 2015, pp. 39-55.

[2] P. Passaretti, "Graphene Oxide and Biomolecules for the Production of Functional 3d Graphene-Based Materials," *Frontiers in Molecular Biosciences,* Review vol. 9, 2022, doi: 10.3389/fmolb.2022.774097.

[3] Y. Qin, C. Xue, H. Yu, Y. Wen, L. Zhang, and Y. Li, "The Construction of Bio-Inspired Hierarchically Porous Graphene Aerogel for Efficiently Organic Pollutants Absorption," *Journal of Hazardous Materials,* vol. 419, p. 126441, 2021, doi: 10.1016/j.jhazmat.2021.126441.

[4] J. Huang, D. Li, L. Huang, S. Tan, and T. Liu, "Bio-Based Aerogel Based on Bamboo, Waste Paper, and Reduced Graphene Oxide for Oil/Water Separation," *Langmuir,* vol. 38, no. 10, pp. 3064-3075, 2022, doi: 10.1021/acs.langmuir.1c02821.

[5] R. Chen, X. Li, Q. Huang, H. Ling, Y. Yang, and X. Wang, "Self-Assembled Porous Biomass Carbon/Rgo/Nanocellulose Hybrid Aerogels for Self-Supporting Supercapacitor Electrodes," *Chemical Engineering Journal,* vol. 412, p. 128755, 2021, doi: 10.1016/j.cej.2021.128755.

[6] Y. Wang, J. Yang, Y. Song, Q. Yang, C. Xiong, and Z. Shi, "Porous and Three-Dimensional Carbon Aerogels from Nanocellulose/Pristine Graphene for High-Performance Supercapacitor Electrodes," *Diamond and Related Materials,* vol. 132, p. 109626, 2023, doi: 10.1016/j.diamond.2022.109626.

[7] X. Yuan, Y. Wei, S. Chen, P. Wang, and L. Liu, "Bio-Based Graphene/Sodium Alginate Aerogels for Strain Sensors," *RSC Advances,* 10.1039/C6RA12469K vol. 6, no. 68, pp. 64056-64064, 2016, doi: 10.1039/C6RA12469K.

[8] H. Liu, T. Xu, C. Cai, K. Liu, W. Liu, M. Zhang, H. Du, C. Si, and K. Zhang, "Multifunctional Superelastic, Superhydrophilic, and Ultralight Nanocellulose-Based Composite Carbon Aerogels for Compressive Supercapacitor and Strain

Sensor," *Advanced Functional Materials,* vol. 32, no. 26, p. 2113082, 2022, doi: 10.1002/adfm.202113082.

[9] E. M. Lucas, M. S. Doescher, D. M. Ebenstein, K. J. Wahl, and D. R. Rolison, "Silica Aerogels with Enhanced Durability, 30-Nm Mean Pore-Size, and Improved Immersibility in Liquids," *Journal of Non-Crystalline Solids,* vol. 350, pp. 244-252, 2004, doi: 10.1016/j.jnoncrysol.2004.07.074.

[10] T. Chen, G. Yang, Y. Li, Z. Li, L. Ma, S. Yang, and J. Wang, "Temperature-Adaptable Pressure Sensors Based on Mxene-Coated Go Hierarchical Aerogels with Superb Detection Capability," *Carbon,* vol. 200, pp. 47-55, 2022, doi: 10.1016/j.carbon.2022.08.002.

[11] S. P. Patil, V. G. Parale, H.-H. Park, and B. Markert, "Molecular Dynamics and Experimental Studies of Nanoindentation on Nanoporous Silica Aerogels," *Materials Science and Engineering: A,* vol. 742, pp. 344-352, 2019, doi: 10.1016/j.msea.2018.11.019.

[12] V. Ramasubbu, F. S. Omar, K. Ramesh, S. Ramesh, and X. S. Shajan, "Three-Dimensional Hierarchical Nanostructured Porous Tio2 Aerogel/Cobalt Based Metal-Organic Framework (Mof) Composite as an Electrode Material for Supercapattery," *Journal of Energy Storage,* vol. 32, p. 101750, 2020, doi: 10.1016/j.est.2020.101750.

[13] Y. Hanzawa, H. Hatori, N. Yoshizawa, and Y. Yamada, "Structural Changes in Carbon Aerogels with High Temperature Treatment," *Carbon,* vol. 40, no. 4, pp. 575-581, 2002, doi: 10.1016/S0008-6223(01)00150-6.

[14] M. M. Atta, E. O. Taha, and A. M. Abdelreheem, "Nitrogen Plasma Effect on the Structural, Thermal, and Dynamic Mechanical Properties of Pva/Starch/Graphene Oxide Nanocomposite," *Applied Physics A,* vol. 127, no. 7, p. 532, 2021, doi: 10.1007/s00339-021-04671-x.

[15] I. Sarbu and C. Sebarchievici, "A Comprehensive Review of Thermal Energy Storage," *Sustainability,* vol. 10, no. 1, p. 191, 2018, doi: 10.3390/su10010191.

[16] H. Zhang, J. Baeyens, G. Cáceres, J. Degrève, and Y. Lv, "Thermal Energy Storage: Recent Developments and Practical Aspects," *Progress in Energy and Combustion Science,* vol. 53, pp. 1-40, 2016, doi: 10.1016/j.pecs.2015.10.003.

[17] J. Zhang, X. Liu, G. Neri, and N. Pinna, "Nanostructured Materials for Room-Temperature Gas Sensors," *Advanced Materials,* vol. 28, no. 5, pp. 795-831, 2016, doi: 10.1002/adma.201503825.

[18] W. Yan, A. Harley-Trochimczyk, H. Long, L. Chan, T. Pham, M. Hu, Y. Qin, A. Zettl, C. Carraro, M. A. Worsley, and R. Maboudian, "Conductometric Gas Sensing Behavior of Ws2 Aerogel," *FlatChem,* vol. 5, pp. 1-8, 2017, doi: 10.1016/j.flatc.2017.08.003.

[19] X. Zhu, S. Li, Y. Shi, and N. Cai, "Recent Advances in Elevated-Temperature Pressure Swing Adsorption for Carbon Capture and Hydrogen Production," *Progress in Energy and Combustion Science,* vol. 75, p. 100784, 2019, doi: 10.1016/j.pecs.2019.100784.

[20] P. Priyadarshini, G. Rim, C. Rosu, M. Song, and C. W. Jones, "Direct Air Capture of Co2 Using Amine/Alumina Sorbents at Cold Temperature," *ACS Environmental Au,* vol. 3, no. 5, pp. 295-307, 2023, doi: 10.1021/acsenvironau.3c00010.

[21] X. Huang, G. Yu, Y. Zhang, M. Zhang, and G. Shao, "Design of Cellular Structure of Graphene Aerogels for Electromagnetic Wave Absorption,"

Chemical Engineering Journal, vol. 426, p. 131894, 2021, doi: 10.1016/j.cej.2021.131894.

[22] B. Zhao, Y. Li, H. Ji, P. Bai, S. Wang, B. Fan, X. Guo, and R. Zhang, "Lightweight Graphene Aerogels by Decoration of 1d Coni Chains and Cnts to Achieve Ultra-Wide Microwave Absorption," *Carbon,* vol. 176, pp. 411-420, 2021, doi: 10.1016/j.carbon.2021.01.136.

[23] K. Ji, Y. Gao, L. Zhang, S. Wang, Q. Yue, X. Xu, W. Kong, B. Gao, Z. Cai, and Y. Chen, "A Tunable Amphiphilic Enteromorpha-Modified Graphene Aerogel for Oil/Water Separation," *Science of The Total Environment,* vol. 763, p. 142958, 2021, doi: 10.1016/j.scitotenv.2020.142958.

[24] Y. Mu, L. Wang, R. Zhang, R. A. Pashameah, E. Alzahrani, Z. Li, A. K. Alanazi, H. Algadi, M. Huang, Z. Guo, T. Wan, and H. Wei, "Rapid and Facile Fabrication of Hierarchically Porous Graphene Aerogel for Oil-Water Separation and Piezoresistive Sensing Applications," *Applied Surface Science,* vol. 613, p. 155982, 2023, doi: 10.1016/j.apsusc.2022.155982.

[25] T. Yan, T. Li, J. Xu, J. Chao, R. Wang, Y. I. Aristov, L. G. Gordeeva, P. Dutta, and S. S. Murthy, "Ultrahigh-Energy-Density Sorption Thermal Battery Enabled by Graphene Aerogel-Based Composite Sorbents for Thermal Energy Harvesting from Air," *ACS Energy Letters,* vol. 6, no. 5, pp. 1795-1802, 2021, doi: 10.1021/acsenergylett.1c00284.

[26] D. Wei, C. Wu, G. Jiang, X. Sheng, and Y. Xie, "Lignin-Assisted Construction of Well-Defined 3d Graphene Aerogel/Peg Form-Stable Phase Change Composites Towards Efficient Solar Thermal Energy Storage," *Solar Energy Materials and Solar Cells,* vol. 224, p. 111013, 2021, doi: 10.1016/j.solmat.2021.111013.

[27] P. Passaretti, Y. Sun, I. Khan, K. Chan, R. Sabo, H. White, T. R. Dafforn, and P. G. Oppenheimer, "Multifunctional Graphene Oxide-Bacteriophage Based Porous Three-Dimensional Micro-Nanocomposites," *Nanoscale,* 10.1039/C9NR03670A vol. 11, no. 28, pp. 13318-13329, 2019, doi: 10.1039/C9NR03670A.

[28] A. F. Betancur, A. García, and F. R. Pérez, "Thermal Stability and Chemical Analysis of Hybrid Materials Reinforced with Graphene Oxide," *Journal of Physics: Conference Series,* vol. 1219, no. 1, p. 012003, 2019, doi: 10.1088/1742-6596/1219/1/012003.

[29] C. Li, Y. Lu, J. Yan, W. Yu, R. Zhao, S. Du, and K. Niu, "Effect of Long-Term Ageing on Graphene Oxide: Structure and Thermal Decomposition," *R Soc Open Sci,* vol. 8, no. 12, p. 202309, 2021, doi: 10.1098/rsos.202309.

[30] K. Stokes, Y. Sun, P. Passaretti, H. White, and P. Goldberg Oppenheimer, "Optimisation of Graphage13 Macro-Dispersibility Via Understanding the Ph-Dependent Ionisation During Self-Assembly: Towards the Manufacture of Graphene-Based Nanodevices," *Nanoscale,* 10.1039/D3NR00778B vol. 15, no. 32, pp. 13304-13312, 2023, doi: 10.1039/D3NR00778B.

[31] I. Sengupta, S. Chakraborty, M. Talukdar, S. K. Pal, and S. Chakraborty, "Thermal Reduction of Graphene Oxide: How Temperature Influences Purity," *Journal of Materials Research,* vol. 33, no. 23, pp. 4113-4122, 2018, doi: 10.1557/jmr.2018.338.

[32] T. Hassenkam, L. Skovbjerg, and S. Stipp, "Probing the Intrinsically Oil-Wet Surfaces of Pores in North Sea Chalk at Subpore Resolution," *Proceedings of*

the National Academy of Sciences of the United States of America, vol. 106, pp. 6071-6, 2009, doi: 10.1073/pnas.0901051106.

[33] E. I. Rivin and E. I. Rivin, "Introduction and Definitions," in *Handbook on Stiffness &Amp; Damping in Mechanical Design*: ASME Press, 2010, p. 0.

[34] G. Thomas, N. A. Burnham, T. A. Camesano, and Q. Wen, "Measuring the Mechanical Properties of Living Cells Using Atomic Force Microscopy," *J Vis Exp,* no. 76, 2013, doi: 10.3791/50497.

[35] G. Jayatilaka, W. Ntsoane, M. Mohammadi, and M. Tehrani, "Correlating Structure to Damping and Stiffness in Graphene Oxide Films," in *American Society for Composites-Thirty-Seventh Technical Conference*, Arizona, USA, O. Zhupanska and E. Madenci, Eds., 2022: DEStech Publications, Inc., doi: 10.12783/asc37/36445OSTI-MSA. [Online]. Available: https://par.nsf.gov/biblio/10416976

[36] S. Iswar, S. Galmarini, L. Bonanomi, J. Wernery, E. Roumeli, S. Nimalshantha, A. M. Ben Ishai, M. Lattuada, M. M. Koebel, and W. J. Malfait, "Dense and Strong, but Superinsulating Silica Aerogel," *Acta Materialia,* vol. 213, p. 116959, 2021, doi: 10.1016/j.actamat.2021.116959.

[37] D. G. Papageorgiou, I. A. Kinloch, and R. J. Young, "Mechanical Properties of Graphene and Graphene-Based Nanocomposites," *Progress in Materials Science,* vol. 90, pp. 75-127, 2017, doi: 10.1016/j.pmatsci.2017.07.004.

[38] Ö. G. Karaca, B. Moran, M. Türk, A. Bal-Öztürk, B. İzbudak, Y. A. Aydin, G. Utkan, and N. Alemdar, "The Comparison of Contribution of Go and Rgo Produced by Green Synthesis to the Properties of Cmc-Based Wound Dressing Material," *International Journal of Biological Macromolecules,* vol. 271, p. 132521, 2024, doi: 10.1016/j.ijbiomac.2024.132521.

[39] H.-J. Butt, B. Cappella, and M. Kappl, "Force Measurements with the Atomic Force Microscope: Technique, Interpretation and Applications," *Surface Science Reports,* vol. 59, no. 1, pp. 1-152, 2005, doi: 10.1016/j.surfrep.2005.08.003.

[40] B. Cappella, "Physical Principles of Force–Distance Curves by Atomic Force Microscopy," in *Mechanical Properties of Polymers Measured through Afm Force-Distance Curves*. Cham: Springer International Publishing, 2016, pp. 3-66.

[41] D. L. Sedin and K. L. Rowlen, "Adhesion Forces Measured by Atomic Force Microscopy in Humid Air," *Analytical Chemistry,* vol. 72, no. 10, pp. 2183-2189, 2000, doi: 10.1021/ac991198c.

[42] X. Zeng, Y. Peng, M. Yu, H. Lang, X. a. Cao, and K. Zou, "Dynamic Sliding Enhancement on the Friction and Adhesion of Graphene, Graphene Oxide, and Fluorinated Graphene," *ACS Applied Materials & Interfaces,* vol. 10, no. 9, pp. 8214-8224, 2018, doi: 10.1021/acsami.7b19518.

[43] R. Muzyka, S. Drewniak, T. Pustelny, M. Sajdak, and Ł. Drewniak, "Characterization of Graphite Oxide and Reduced Graphene Oxide Obtained from Different Graphite Precursors and Oxidized by Different Methods Using Raman Spectroscopy Statistical Analysis," *Materials (Basel),* vol. 14, no. 4, 2021, doi: 10.3390/ma14040769.

[44] R. Zulkharnay, O. Ualibek, O. Toktarbaiuly, and P. W. May, "Hydrophobic Behaviour of Reduced Graphene Oxide Thin Film Fabricated Via Electrostatic

Spray Deposition," *Bulletin of Materials Science,* vol. 44, no. 2, p. 112, 2021, doi: 10.1007/s12034-021-02381-x.

[45] T. He, B. Lu, Y. Chen, Y. Wang, Y. Zhang, J. L. Davenport, A. P. Chen, C.-W. Pao, M. Liu, Z. Sun, A. Stram, A. Mordaunt, J. Velasco, Y. Ping, Y. Zhang, and S. Chen, "Nanowrinkled Carbon Aerogels Embedded with Fenx Sites as Effective Oxygen Electrodes for Rechargeable Zinc-Air Battery," *Research,* vol. 2019, 2019, doi: 10.34133/2019/6813585.

[46] J. V. Escobar, C. Garza, and R. Castillo, "Measuring Adhesion on Rough Surfaces Using Atomic Force Microscopy with a Liquid Probe," *Beilstein Journal of Nanotechnology,* vol. 8, pp. 813-825, 2017, doi: 10.3762/bjnano.8.84.

[47] J. Dawson, S. Coaster, R. Han, J. Gausden, H. Liu, G. McHale, and J. Chen, "Dynamics of Droplets Impacting on Aerogel, Liquid Infused, and Liquid-Like Solid Surfaces," *ACS Applied Materials & Interfaces,* vol. 15, no. 1, pp. 2301-2312, 2023, doi: 10.1021/acsami.2c14483.

[48] H. Kang, X. Qian, L. Guan, M. Zhang, Q. Li, A. Wu, and M. Dong, "Studying the Adhesion Force and Glass Transition of Thin Polystyrene Films by Atomic Force Microscopy," *Nanoscale Research Letters,* vol. 13, no. 1, p. 5, 2018, doi: 10.1186/s11671-017-2426-9.

[49] S.-C. Her and C.-Y. Huang, "The Effects of Adhesive and Bonding Length on the Strain Transfer of Optical Fiber Sensors," *Applied Sciences,* vol. 6, no. 1, p. 13, 2016, doi: 10.3390/app6010013.

[50] K.-K. Hung and I. Chasiotis, "Control of Substrate Strain Transfer to Thin Film Photovoltaics Via Interface Design," *Solar Energy,* vol. 225, pp. 643-655, 2021, doi: 10.1016/j.solener.2021.07.016.

[51] A. A. Osipov, "High-Temperature Raman Spectroscopy," *Pure and Applied Chemistry,* vol. 91, no. 11, pp. 1749-1756, 2019, doi: 10.1515/pac-2019-0115.

[52] Y. Sun, P. Passaretti, I. Hernandez, J. Gonzalez, W. Liu, F. Rodriguez, D. J. Dunstan, P. Goldberg Oppenheimer, and C. J. Humphreys, "Nanomechanics of Graphene Oxide-Bacteriophage Based Self-Assembled Porous Composites," *Scientific Reports,* vol. 10, no. 1, p. 15618, 2020, doi: 10.1038/s41598-020-72372-1.

[53] Z. E. Brubaker, J. J. Langford, R. J. Kapsimalis, and J. L. Niedziela, "Quantitative Analysis of Raman Spectral Parameters for Carbon Fibers: Practical Considerations and Connection to Mechanical Properties," *Journal of Materials Science,* vol. 56, no. 27, pp. 15087-15121, 2021, doi: 10.1007/s10853-021-06225-1.

[54] A. C. Ferrari and J. Robertson, "Interpretation of Raman Spectra of Disordered and Amorphous Carbon," *Physical Review B,* vol. 61, no. 20, pp. 14095-14107, 2000, doi: 10.1103/PhysRevB.61.14095.

[55] S. Claramunt, A. Varea, D. López-Díaz, M. M. Velázquez, A. Cornet, and A. Cirera, "The Importance of Interbands on the Interpretation of the Raman Spectrum of Graphene Oxide," *The Journal of Physical Chemistry C,* vol. 119, no. 18, pp. 10123-10129, 2015, doi: 10.1021/acs.jpcc.5b01590.

[56] V. Georgakilas, M. Otyepka, A. B. Bourlinos, V. Chandra, N. Kim, K. C. Kemp, P. Hobza, R. Zboril, and K. S. Kim, "Functionalization of Graphene: Covalent and Non-Covalent Approaches, Derivatives and Applications," *Chemical Reviews,* vol. 112, no. 11, pp. 6156-6214, 2012, doi: 10.1021/cr3000412.

[57] A. Eckmann, A. Felten, A. Mishchenko, L. Britnell, R. Krupke, K. S. Novoselov, and C. Casiraghi, "Probing the Nature of Defects in Graphene by Raman Spectroscopy," *Nano Letters,* vol. 12, no. 8, pp. 3925-3930, 2012, doi: 10.1021/nl300901a.

[58] Y. Su, H. Wei, R. Gao, Z. Yang, J. Zhang, Z. Zhong, and Y. Zhang, "Exceptional Negative Thermal Expansion and Viscoelastic Properties of Graphene Oxide Paper," *Carbon,* vol. 50, no. 8, pp. 2804-2809, 2012, doi: 10.1016/j.carbon.2012.02.045.

[59] A. Tardieu, F. Cansell, and J. P. Petitet, "Pressure and Temperature Dependence of the First-Order Raman Mode of Diamond," *Journal of Applied Physics,* vol. 68, no. 7, pp. 3243-3245, 1990, doi: 10.1063/1.346375.

[60] A. E. Mag-isa, J.-H. Kim, and C.-S. Oh, "Measurements of the in-Plane Coefficient of Thermal Expansion of Freestanding Single-Crystal Natural Graphite," *Materials Letters,* vol. 171, pp. 312-314, 2016, doi: 10.1016/j.matlet.2016.02.110.

[61] T. M. G. Mohiuddin, A. Lombardo, R. R. Nair, A. Bonetti, G. Savini, R. Jalil, N. Bonini, D. M. Basko, C. Galiotis, N. Marzari, K. S. Novoselov, A. K. Geim, and A. C. Ferrari, "Uniaxial Strain in Graphene by Raman Spectroscopy: G Peak Splitting, Gruneisen Parameters, and Sample Orientation," *Physical Review B,* vol. 79, no. 20, p. 205433, 2009, doi: 10.1103/PhysRevB.79.205433.

[62] H. Zhang and J. Horvat, "Temperature Dependence of Raman Scattering Spectroscopy in Aerographite and Single-Walled Carbon Nanotube Aerogel," *Applied Physics A,* vol. 127, no. 6, p. 434, 2021, doi: 10.1007/s00339-021-04566-x.

[63] Y. Sun, P. Passaretti, I. Hernandez, J. Gonzalez, W. Liu, F. Rodriguez, D. J. Dunstan, P. Goldberg Oppenheimer, and C. J. Humphreys, "Nanomechanics of Graphene Oxide-Bacteriophage Based Self-Assembled Porous Composites," *Sci Rep,* vol. 10, no. 1, p. 15618, 2020, doi: 10.1038/s41598-020-72372-1.

[64] D. G. Trikkaliotis, A. K. Christoforidis, A. C. Mitropoulos, and G. Z. Kyzas, "Graphene Oxide Synthesis, Properties and Characterization Techniques: A Comprehensive Review," *ChemEngineering,* vol. 5, no. 3, p. 64, 2021, doi: 10.3390/chemengineering5030064.

[65] V. Scardaci and G. Compagnini, "Raman Spectroscopy Investigation of Graphene Oxide Reduction by Laser Scribing," *C,* vol. 7, no. 2, p. 48, 2021, doi: 10.3390/c7020048.

[66] N. G. de Barros, A. C. Gonzaga Neto, K. B. Vaccioli, H. R. V. Angulo, L. G. de Andrade e Silva, S. M. Toffoli, and T. S. Valera, "Graphene Oxide: A Comparison of Reduction Methods," *C,* vol. 9, no. 3, p. 73, 2023, doi: 10.3390/c9030073.

[67] C. Neumann, S. Reichardt, P. Venezuela, M. Drögeler, L. Banszerus, M. Schmitz, K. Watanabe, T. Taniguchi, F. Mauri, B. Beschoten, S. V. Rotkin, and C. Stampfer, "Raman Spectroscopy as Probe of Nanometre-Scale Strain Variations in Graphene," *Nature Communications,* vol. 6, no. 1, p. 8429, 2015, doi: 10.1038/ncomms9429.

[68] J. A. Quezada Renteria, C. Ruiz-Garcia, T. Sauvage, L. F. Chazaro-Ruiz, J. R. Rangel-Mendez, and C. O. Ania, "Photochemical and Electrochemical Reduction of Graphene Oxide Thin Films: Tuning the Nature of Surface

Defects," *Physical Chemistry Chemical Physics,* 10.1039/D0CP02053B vol. 22, no. 36, pp. 20732-20743, 2020, doi: 10.1039/D0CP02053B.

[69] H. Ramamoorthy, K. Buapan, T. Chiawchan, K. Thamkrongart, and R. Somphonsane, "Exploration of the Temperature-Dependent Correlations Present in the Structural, Morphological and Electrical Properties of Thermally Reduced Free-Standing Graphene Oxide Papers," *Journal of Materials Science,* vol. 56, no. 27, pp. 15134-15150, 2021, doi: 10.1007/s10853-021-06262-w.

[70] D. López-Díaz, J. A. Delgado-Notario, V. Clericò, E. Diez, M. D. Merchán, and M. M. Velázquez, "Towards Understanding the Raman Spectrum of Graphene Oxide: The Effect of the Chemical Composition," *Coatings,* vol. 10, no. 6, p. 524, 2020, doi: 10.3390/coatings10060524.

[71] M. J. Kim, Y. Jeong, S. Sohn, S. Y. Lee, Y. J. Kim, K. Lee, Y. H. Kahng, and J.-H. Jang, "Fast and Low-Temperature Reduction of Graphene Oxide Films Using Ammonia Plasma," *AIP Advances,* vol. 3, no. 1, 2013, doi: 10.1063/1.4789545.

CHAPTER 5

SORPTION PROPERTIES OF GRAPHAGE13 AEROGELS

This chapter is based on the previously published paper:

K. Stokes, Y. Sun, H. Zhang, P. Passaretti, H. White, and P. Goldberg Oppeneheimer, " Unveiling the Sorption Properties of Graphene Oxide-M13 Bacteriophage Aerogels for Advanced Sensing and Environmental Applications," *ACS Applied Materials and Interfaces,* 2024, doi: 10.1021/acsami.4c16202

Author contributions – **K. Stokes**, **P. Passaretti** and **Y. Sun** conceptualised the study. **K. Stokes** and **Y. Sun** carried out the experimental acquisition and analyses and validated the results. **P. Goldberg Oppenheimer** and **H. White** were responsible for funding acquisition and resources provision. **P. Goldberg Oppenheimer** supervised and administered the study, curated the data and overviewed the developed methodology. **K. Stokes**, **Y. Sun** and **P. Goldberg Oppenheimer** wrote the original draft and reviewed and edited the final draft.

5.1 Abstract

GraPhage13 aerogels (GPAs) are ultralow density, porous structures fabricated through the self-assembly of graphene oxide (GO) and M13 bacteriophage. Given GPA's high surface area and extensive porous network, properties typically associated with highly adsorbent materials, it is essential to characterise its sorption capabilities, Herein, the water, ethanol, and acetone sorption properties of GPA were explored using dynamic vapor sorption (DVS) to evaluate its potential for advanced applications, including water sorption for humidity control, freshwater generation, and moisture-enabled electric generation, as well as ethanol and acetone sorption for biomedical sensing and environmental monitoring. GPA was found to be highly hygroscopic, with a sorption capacity of 0.68 ± 0.02 g/g at 90% relative humidity, double that of conventional desiccant silica gels and 20% higher than GO laminates. This remarkable sorption capacity, along with its sorption kinetics, was influenced by both GPA's morphology and the strong interactions between the water molecules and the functional groups on the GO within GPA. The low hysteresis and stability of GPA during repeated sorption–desorption cycles highlight the reversibility of water sorption. While GPA shows lower capacity for ethanol and acetone, its tuneability presents opportunities for improving acetone sorption, and its ethanol sorption capacity exceeds that of similar carbon-based materials. These findings underscore GPA's capability and versatility in vapor adsorption, paving the way toward its integration into graphene-based devices for sensing applications.

5.2 Introduction

The development of novel adsorbents with high sorption capacities and selective affinities for a range of vapours has been of an increasing interest due to the broad range of applications. For instance, highly hygroscopic materials capable of absorbing water from the environment have found applications in humidity control [1], moisture-enabled electric generation [2] and freshwater generation [3], and adsorbents with an affinity for volatile organic compounds (VOCs) such as ethanol and acetone, have found applications in environmental monitoring [4, 5] and biomedical sensors [6, 7]. Activated carbon has been widely used as an adsorbent due to its high absorption capacity, resulting from its porosity, large surface area and hydrophilic functionalities, which can interact with the water and VOC molecules. However, it is known to exhibit certain limitations, including unwanted reactions which can limit its porosity and the mass loss which occurs during the regeneration of exhausted activated carbon [8]. These drawbacks have highlighted the continued unmet need for developing novel carbon-based absorbents capable of retaining the advantages of activated carbon while simultaneously delivering cost-effectiveness and reusability.

Graphene oxide (GO) is an atomic layer of sp^2 hybridized carbon atoms incorporating various oxygen-containing functional groups including carboxyl, carbonyl, epoxy and hydroxyl. Assembling GO into an aerogel combines the functional group interactions via GO with the porous, low density and high surface area of aerogel, enhancing the capabilities in adsorption and sensing [9, 10]. However, methods for producing aerogels with a GO precursor often rely on toxic and environmentally harmful reagents, or high-temperature and high-pressure conditions, which significantly increase production costs. In contrast, the self-assembly of GO with biomolecules presents a

cost-effective, scalable and environmentally sustainable alternative [11]. Existing graphene-based composites, such as graphene aerogels, reduced graphene oxide (rGO) aerogels, and graphene foams, have shown promise in adsorption applications due to their high surface areas and adsorption capacities. However, they face notable limitations that underscore the need for developing alternative materials. These challenges include cost-inefficient and toxic synthesis methods, limited scalability, and poor stability during cyclic use. For instance, graphene oxide foams demonstrate good adsorption of volatile organic compounds like acetone and ethanol but often exhibit hysteresis and lower water sorption capacities. Furthermore, traditional graphene-based composites are less environmentally friendly, relying on energy-intensive processes that limit their widespread adoption. In this regard, in a pioneering study, Passaretti et al. fabricated GO-based aerogels through the self-assembly of GO and the filamentous M13 bacteriophage [12]. The self-assembly process has been shown to generate the GraPhage13 aerogels (GPAs), which are macro-porous nanocomposites with an ultralow density (8.8 mg/cm^3) and high surface area (325 m^2/g) (Figure 5.1) [12]. Their self-assembly does not require high temperatures, pressures, or toxic reagents, and both GO and M13 can be generated on a large scale. The modular and self-assembling nature of GPA is inherently scalable. As demonstrated in our earlier work, the compatibility of GPA synthesis with standard chemical engineering techniques allows for its production at various scales without significant alterations to the process. This scalability makes GPA well-suited for adoption in commercial manufacturing. Furthermore, the low-cost precursors (GO and M13), combined with the absence of extreme conditions during synthesis, significantly reduce production costs. Our past studies also noted that the use of aqueous media

and ambient conditions eliminates the need for expensive equipment, aligning GPA production with sustainable manufacturing practices. This enables the cost-effective, scalable, and environmentally friendly production of GPA, positioning it as a promising material for large-scale industrial applications [13, 14]. Furthermore, through the functionalisation of GO, chemical/genetical modifications of M13, and incorporation of additional nanomaterials such as carbon nanotubes and gold nanoparticles into the porous structure, the characteristics of GPA could be effectively tailored for specific applications [15, 16]. These unique properties, combined with the low-cost, scalable and environmentally friendly production, renders the GPA an attractive, novel prospect for absorbents.

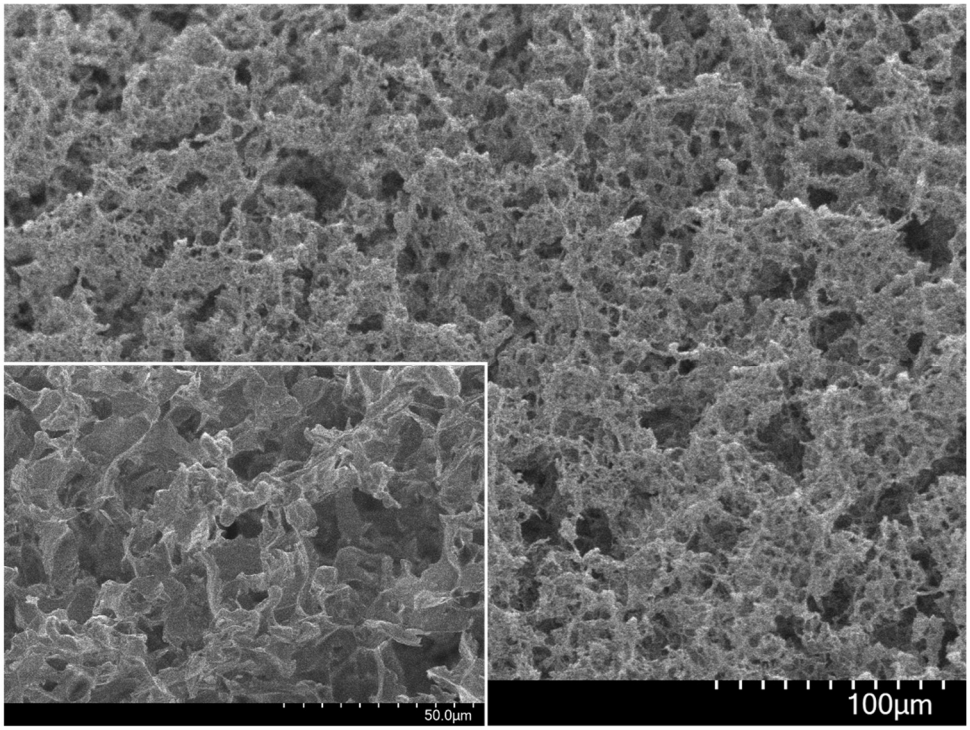

Figure 5.1: SEM images of GraPhage13 aerogel

Scanning electron microscopy images of GraPhage13 aerogels showcasing the macro-porous structure. Inset: a zoomed-in view highlighting the ultralow density and high surface area of the structure.

Herein, the sorption behaviour of GPA for water, ethanol and acetone is comprehensively investigated through a series of in-depth dynamic vapor sorption (DVS) studies. GPA is found to exhibit a notably high water sorption capacity, surpassing that of conventional adsorbents. This performance is subsequently attributed to its extensive porous network, large surface area, multilayer adsorption and the strong interactions between water molecules and GO's functional groups. While GPA's sorption capacity for ethanol and acetone is lower than water, due to the finite nature of their multilayer adsorption and its weaker interactions with these solvents, its ethanol sorption capacity is highly competitive with similar carbon-based materials and the tuneable properties of GPA offer a unique potential route for enhancing its acetone sorption capabilities. This exceptional sorption property of GPA further lay the platform for diverse applications including for instance, biomedical sensors and environmental monitoring. The study also paves the way for future research into exploring GPA's affinity for different vapours for additional potential end uses such as environmental security [17] and wastewater treatment [18]. Moreover, the ability to fine-tune the properties of GPA provides avenues to optimize and enhance its sorption capabilities. This adaptability further underscores the versatility and potential of GPA in addressing a broad spectrum of environmental and technological challenges.

5.3 Results and Discussion

5.3.1 Water Sorption

The water sorption characteristics of GPA were investigated with DVS (Section 2.2.9) by monitoring the change in mass over time under varying partial pressures (PP),

ranging from 0% to 90% in 10% increments (Figure 5.2a). At each PP step, the mass of GPA initially increased while it adsorbed water until either attaining the stop criterion, defined by a mass change below 0.002% per minute for a 10 min period, or reaching the maximum time limit of 12 h. For the PP steps between 10 and 80%, the stop criterion was achieved, indicating that the moisture content within the GPA had equilibrated with the surrounding environment [19, 20]. At 90% PP, GPA exhibited an average mass change of 68 ± 2% across three different samples, clearly demonstrating the excellent repeatability of both the fabrication process and the sorption measurements. This is equivalent to a sorption capacity of 0.68 ± 0.02 g/g, more than double the capacity of conventional desiccant silica gels and exceeds that of GO laminates by approximately 20% [21].

It is likely that GO is the primary absorbent in GPA. The functional groups on GO within GPA provide specific binding sites for the water molecules through hydrogen bonding and electrostatic interactions, leading to stronger and more extensive interactions with the adsorbate, thereby enhancing its sorption capacity [21, 22]. The M13 acts as a structural component, with the GO-M13 interactions generating its extensive pore network and high specific surface area, creating a large volume for adsorption [23, 24]. The combination of these factors leads to the highly hygroscopic nature of GPA.

Additionally, the stop criterion was not achieved at 90% PP and the maximum time limit was reached, suggesting that its sorption capacity of GPA may even exceed 0.68 ± 0.02 g/g, providing an avenue for future investigations. Throughout the experiments, no condensation or dripping of liquid water was observed. This confirms that the adsorption processes involve vapor-phase adsorption within the porous structure of GPA, rather than surface condensation leading to liquid formation.

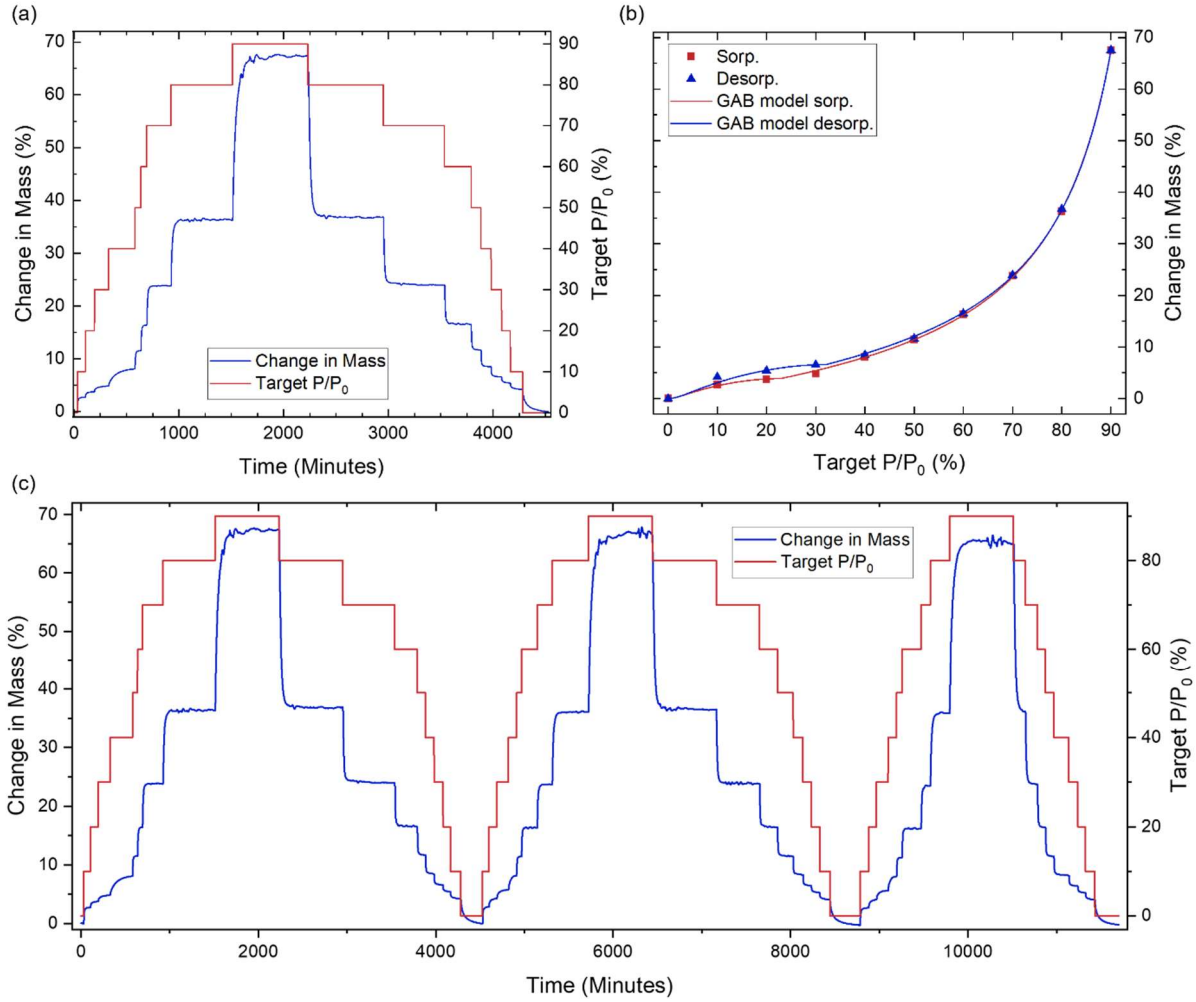

Figure 5.2: Water sorption characteristics of GPA

(a) Percentage change in mass of GPA over time as a function of the partial water vapor pressure variation between 0 and 90%. **(b)** Resulting isotherm illustrating the adsorption behaviour. **(c)** Effect of subjecting GPA to three consecutive sorption–desorption cycles. The data facilitate the investigation of the kinetics, isotherms and hysteresis behaviours of water sorption on GPA.

Direct comparisons with other graphene-based aerogels are not possible, as previous studies primarily employed liquid immersion techniques, which involve submerging the material in liquid and comparing weights before and after [25, 26]. In contrast, DVS dynamically controls partial pressure between 0% and 90%. Consequently, direct comparisons with similar graphene-based aerogels are not possible. On the other

hand, the sorption capacity of GO laminates is specified at 90% PP, making it a meaningful benchmark. The structural differences between laminates and aerogels, particularly the extensive porous network of GPA, likely contribute to its superior sorption performance relative to laminates. However, in comparison to similar studies on other porous carbon-based materials, GPA exhibits a comparable or superior water sorption capacity, demonstrating its potential in water sorption-based applications [27, 28].

The equilibrium mass recorded at the end of each PP step was subsequently used to generate the sorption–desorption isotherms (Figure 5.2b). Various models, including the Langmuir, Freundlich, Temkin, Brunauer–Emmett–Teller (BET), Guggenheim–Anderson–de Boer (GAB), and dual-site Langmuir–Freundlich (DLR) models, were applied to the isotherm data. The optimal fit was determined by the model with the lowest Bayesian information criterion (BIC) value [29, 30]. For water sorption by GPA, the Guggenheim–Anderson–de Boer (GAB) model was established as the most suitable for the isotherm representation.

The isotherm was classified as type II, characteristic of sorption by macroporous adsorbents with unrestricted monolayer–multilayer adsorption. Type II isotherms typically show an initial rapid increase in mass, reflecting the progressive formation of a monolayer of adsorbate on the adsorbent. This is followed by an inflection point, signalling the completion of monolayer sorption and the onset of multilayer adsorption. A more gradual curve suggests a smoother, overlapping transition between monolayer and multilayer adsorption. As adsorption continues, the mass increases as the multilayer thickness grows, with no apparent saturation point [31].

The initial increase in mass between 0 and 10% suggests the formation of a monolayer of water on the surface of GPA, driven by adsorbent–adsorbate interactions. Specifically, the strongest interactions arise from the hydrogen bonding between the water molecules and the polar hydroxyl groups on GO [32]. This is followed by a gradual increase in mass between 10% and 30% PP, indicating the gradual transition from monolayer to multilayer adsorption. The latter is facilitated by hydrogen bonds between water molecules in the environment and those adsorbed onto GPA. Beyond 40% PP, the mass of GPA increases more rapidly, suggesting that sorption becomes dominated by indefinite multilayer adsorption [33, 34]. To note, deriving an activation energy for the multilayer adsorption process is not feasible with the current data. Activation energy determination requires temperature-dependent kinetic measurements to relate the rate of adsorption to temperature. Since our study was conducted at a constant temperature and without kinetic measurements over a range of temperatures, the activation energy was not extracted from the data. Future studies involving temperature-dependent kinetic measurements could provide further insights into the energetics of the multilayer adsorption process.

Between 10 and 30% PP, during the transition between monolayer and multilayer sorption, a low level of hysteresis was observed. This can be attributed to the strong hydrogen bonds between the water molecules and hydroxyl groups on GPA, possessing a high binding energy. Breaking these bonds during desorption requires more energy than forming them during sorption, leading to the observed hysteresis [35]. However, this hysteresis is minimal and only observed in the 10–30% PP range, reflecting the reversibility of the water sorption and suggesting that the overall sorption–desorption processes induce little structural change to GPA [36].

To further investigate this, GPA was subjected to three consecutive sorption–desorption cycles (Figure 5.2c), where it exhibited excellent repeatability and stability. The most significant difference between the cycles is observed at 90% PP, where the mass decreases by 1.20% from cycle 1 to cycle 2 and by 1.51% from cycle 2 to cycle 3. This most probably originates from small structural changes, such as the stresses and strains exerted on the GPA during sorption–desorption, causing a fraction of the pores to collapse, or volumetric shrinkage due to the attractive bridging of the water molecules across the pores.

The third sorption–desorption cycle in Figure 5.2c appears shorter than the preceding cycles. This observation is attributed to the material's behaviour under repeated cycling rather than experimental inconsistency. Each stage's stop criterion was defined as a mass change of less than 0.002% per minute, stable over 10 min. With each cycle, minor structural changes such as slight pore collapse or volumetric shrinkage may occur due to the stresses exerted during sorption–desorption [37]. These changes can result in a quicker attainment of equilibrium in subsequent cycles, leading to shorter cycle durations. At the highest partial pressure (90% PP), the mass change during the third cycle exhibits increased noise and a subtle slope during the hold time. This is attributed to the gradual water sorption of GPA toward an equilibrium, which is not achieved before the maximum time limit and the increased sensitivity of the balance at high humidity levels. The fluctuations are minimal and stop before the transition to the subsequent partial pressure stage, thus not significantly affecting the overall adsorption capacity or data interpretation. While we observed excellent repeatability and stability over three cycles, we acknowledge that assessing mass loss over only three cycles provides a limited view of long-term cycling stability. However, our primary

focus has been on investigating the kinetics and isotherm behaviours of GPA. In applications such as gas or molecular sensing in medical devices, where components are often disposable or intended for single use, extensive long-term cycling may not be critical. Future studies will explore the durability of GPA over a larger number of cycles to evaluate its potential for reusable applications.

To gain insights into the sorption kinetics, a range of kinetic models such as the Langmuir, pseudo-second-order, Avrami, Weibull and intraparticle diffusion models, were applied to each sorption and desorption stage (for further details on each model, please refer to Section 1.5.3). [38]. The model with the lowest BIC value was considered the best fit, allowing for the analysis of the mechanisms driving water sorption kinetics in GPA. When the difference in BIC values was below 6, indicating that the models were statistically close, the preferable model was selected based on the physical significance of the fitted values and their consistency with the parameters of preceding or subsequent segments (for further details please see Section 2.3.2) [39, 40]. Given the complexity of GPA sorption characteristics, arising from its porous structure and GPA-water interactions, no single model provided an optimal fit across many of the PP stages. Instead, hybrid models combining two different kinetic sorption models were required [41].

When subjecting GPA to PPs between 10 and 30%, the kinetics were best described by a hybrid of the pseudo-second order (PSO) and the Avrami models (Figure 5.3a,b, Table 5.1). The Avrami model exhibited a rapid initial sorption, while the PSO model showed a more gradual sorption process. The PSO model typically describes sorption dominated by interactions between the adsorbent and adsorbate. In this context, the PSO model represents the gradual formation of strong hydrogen bonds between the

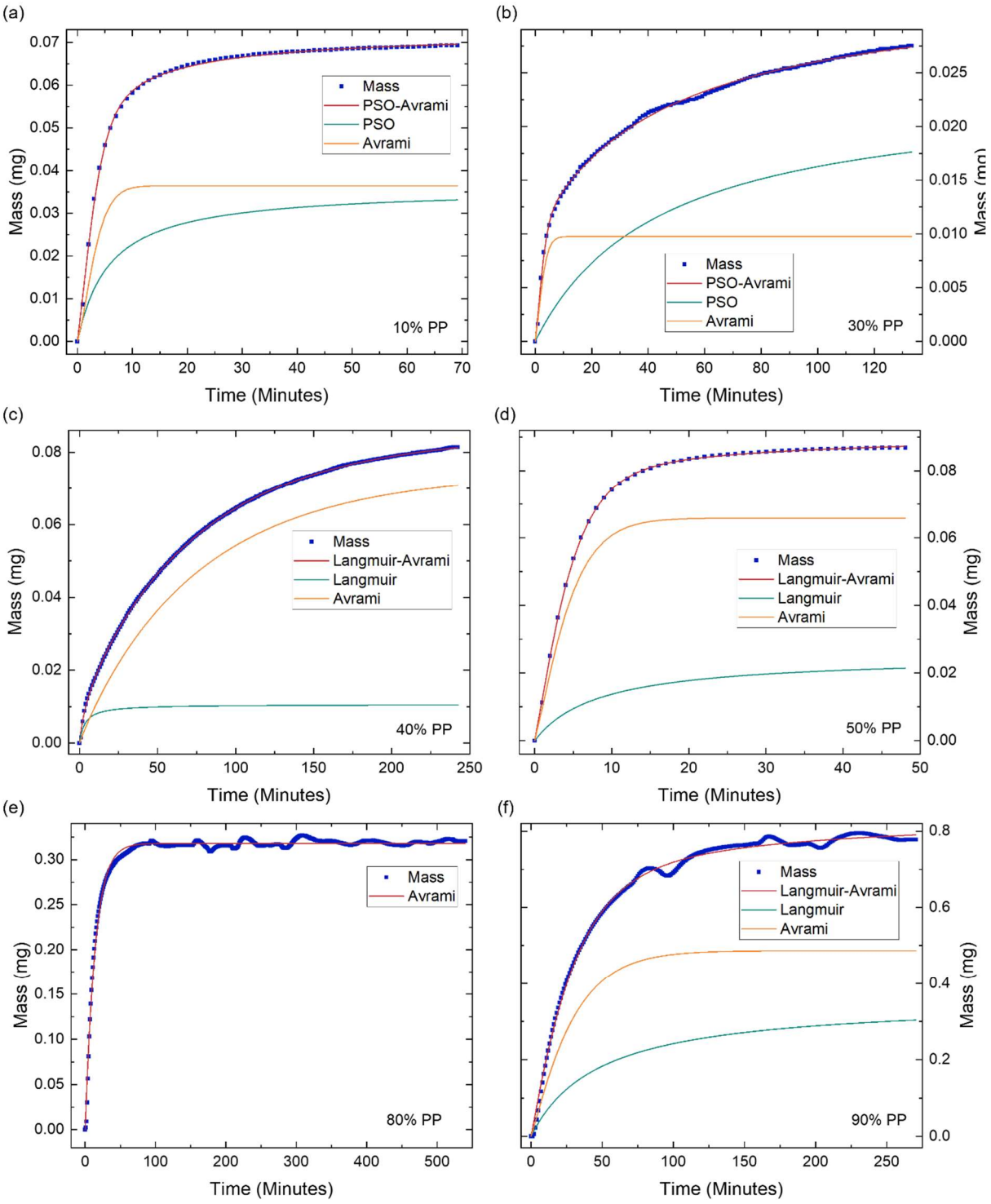

Figure 5.3: Water sorption kinetics for GPA

Water sorption kinetics of GPA demonstrating the increase in mass over time at different partial pressures (PP) of **(a)** 10% PP, **(b)** 30% PP, **(c)** 40% PP, **(d)** 50% PP, **(e)** 80% PP and **(f)** 90% PP. The starting mass and time are shifted to zero. The fit of the hybrid models and their individual components are displayed.

Table 5.1: BIC values for GPA water sorption kinetic models

Bayesian information criterion (BIC) values for kinetic models (PSO, intra-particle diffusion, Avrami, Langmuir, hybrid PSO-Avrami, and hybrid Langmuir-Avrami) fit to GPA water sorption data. The optimal model is indicated by the lowest BIC value. When the difference in BIC is less than 6, the optimal model is assessed based on the physical significance and consistency of the fitted parameters

	BIC value					
Partial pressure (%)	**PSO**	**Intra-particle**	**Avrami**	**Langmuir**	**PSO-Avrami**	**Langmuir-Avrami**
10	-888	-591	-924	-888	-1070	-875
20	-1279	-936	-1361	-1279	-1570	-1558
30	-1875	-1543	-2090	-1874	-2271	--2222
40	-3406	-2592	-37768	-3406	-3662	-4154
50	-562	-408	-686	-562	-799	-799
60	-437	-324	-492	-437	-532	-532
70	-685	-462	-830	-685	-893	-893
80	-2595	-5009	-5878	-5009	-4990	-4990
90	-2069	-1170	-2347	-2069	-2405	-2405

water molecules and the highly polar functionalities on GO, particularly its hydroxyl groups [30, 32]. As the PP increases from 10% to 30%, the contribution of the PSO component increases. The rising PP allows the water vapor to penetrate deeper into the porous structure, exposing more functional groups for the water molecules to bind with [42, 43]. The Avrami model is associated with the nucleation and growth of different phases. The Avrami equation, which describes the dependence of the nucleation and growth of new phases, can be employed to gain insights into the sorption mechanism. The Avrami exponent, n, is a representation of the dimensionality of the growth of the new phase and generally lies between $1 \leq n \leq 4$, with $1 \leq n \leq 2$ representing one-dimensional (1D) growth, $2 \leq n \leq 3$ representing two-dimensional (2D) growth, and $3 \leq n \leq 4$ representing three-dimensional (3D) growth

[44]. Throughout the water sorption process, the Avrami exponent consistently lies within the $1 \leq n \leq 2$ range, with an average value of 1.1 ± 0.1. This suggests that water sorption is 1D and homogeneous across GPA, with the likelihood of adsorption occurring being uniform across all areas within a given time interval [45].

At 40% PP, the optimal model shifts to the Langmuir-Avrami model (Figure 5.3c), which describes monolayer sorption of the adsorbate onto the surface and within the pores of the adsorbent, with sorption kinetics proportional to the concentration of adsorbed molecules. The shift from the PSO model to the Langmuir model, and its low contribution toward the sorption kinetics, indicates the saturation of GO's hydroxyl groups, the completion of monolayer sorption and the transition to multilayer sorption, consistent with Figure 5.2b [46, 47]. The significant contribution of the Avrami model indicates the presence of homogeneous layer-by-layer water sorption, facilitated by hydrogen bonds between the water molecules already adsorbed on the surface of GPA and those in the surrounding environment [45, 48]. Between 50% and 70% PP, the Langmuir-Avrami model remains optimal (Figure 5.3d), however the contribution of the Langmuir component increases with PP, due to the increasing water–water interactions as sequential layers of water molecules form. At 80% PP, the Avrami model alone best represents the sorption kinetics (Figure 5.3e), reflecting a more consistent, organized growth of multilayers, where each layer adsorbs at a similar rate. However, at 90% PP, the optimal model transitions back to the Langmuir–Avrami hybrid model (Figure 5.3f). The renewed dependence of the sorption kinetics on the concentration of water previously adsorbed onto GPA suggests that the sorption is becoming constrained by the diffusion into the porous structure, reflecting the progressive occupation of water within the pores [46]. The fluctuations of mass observed at 90% PP (Figure 5.3f) are

not a result of partial pressure instability at high humidities, as the DVS system maintained consistent control of the partial pressure throughout the experiment. Instead, these fluctuations are likely due to dynamic adsorption-desorption behaviour within the aerogel's porous structure as it approaches equilibrium at high humidity. At 90% PP, local saturation and re-equilibration of water molecules within the pore network or on the aerogel's surface may occur, leading to small and transient mass changes. Additionally, water sorption at high partial pressures could induce structural adjustments, such as swelling or contraction of the aerogel, further contributing to the observed fluctuations.

Following the in-depth examination of the adsorption kinetics, the desorption process was subsequently analysed to interpret the underlying mechanisms governing the release of adsorbed water. The desorption stages between 80 and 50% PP are best described by the Weibull–Avrami hybrid model (Figure 5.4a,b) (Table 5.2). The Weibull component exhibits rapid desorption which rapidly plateaus, whereas the Avrami component demonstrates more gradual desorption. The Weibull model is often applied to describe the kinetics of water desorption, representing it as a series of probabilistic events and effectively captures desorption from heterogeneous surfaces [49]. The heterogeneity arises from water being confined within pores of varying depths and volumes within the porous structure. As a result, water molecules exhibit different probabilities of desorption based on their varying capacities to diffuse out of these pores. On the other hand, the Avrami component represents the uniform release of water molecules, indicating the gradual desorption of water layers from the multilayer structure on GPA’s surface.

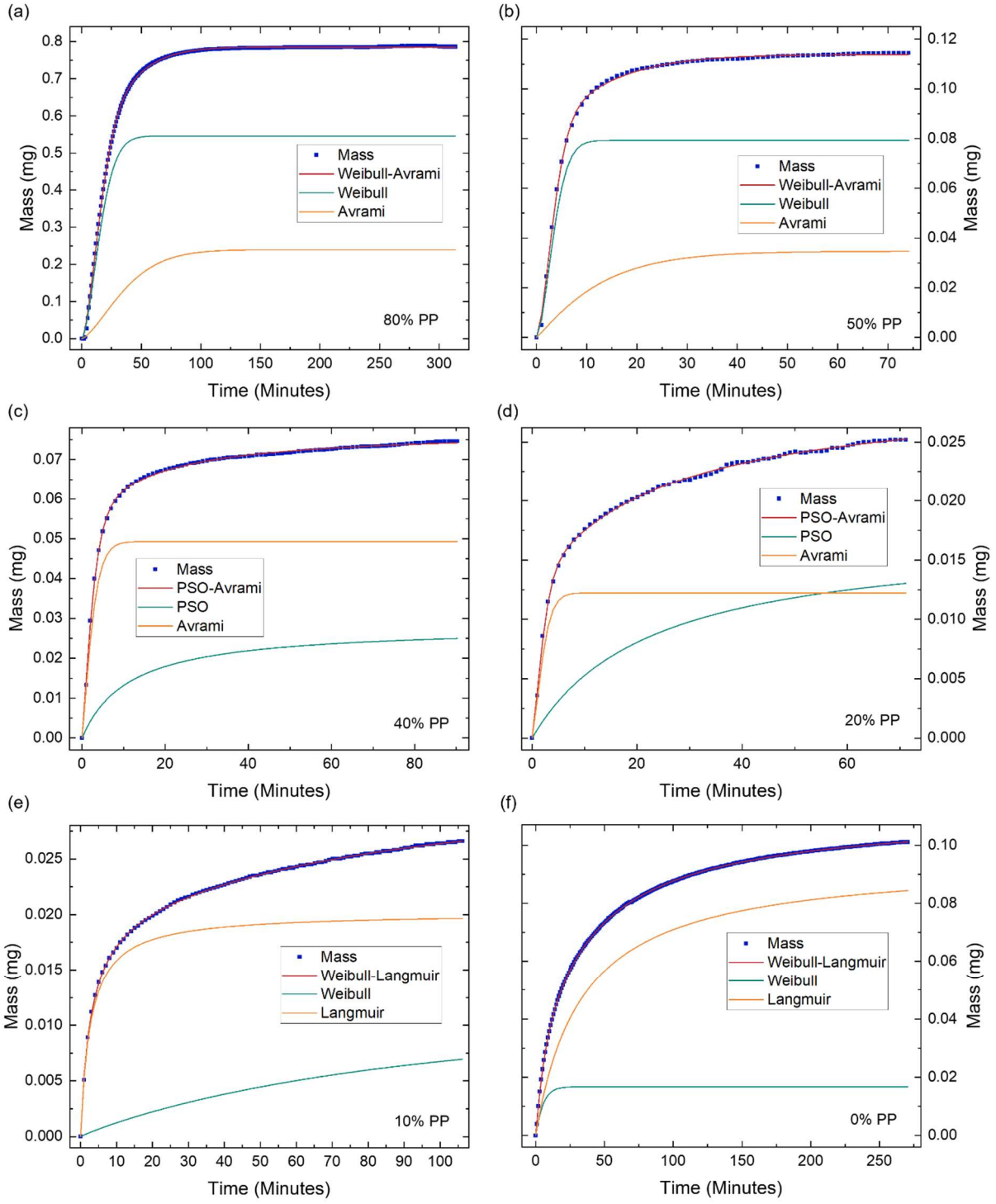

Figure 5.4: Water desorption kinetics for GPA

Water desorption kinetics of GPA, illustrating the mass decrease over time at different partial pressures of **(a)** 80% PP, **(b)** 50% PP, **(c)** 40% PP, **(d)** 20% PP, **(e)** 10% PP and **(f)** 0% PP. The initial mass and time are shifted to zero and the mass values are multiplied by (−1) for easier comparison with the adsorption kinetics. The fit of the hybrid models is displayed along with the individual components.

Table 5.2: BIC values for GPA water desorption kinetic models

Bayesian information criterion (BIC) values for kinetic models (PSO, intra-particle diffusion, Avrami, Langmuir, Weibull, hybrid PSO-Avrami, hybrid Langmuir-Avrami, hybrid Weibull-Avrami and hybrid Weibull-Langmuir) fit to GPA water desorption data. The optimal model is indicated by the lowest BIC value. When the difference in BIC is less than 6, the optimal model is assessed based on the physical significance and consistency of the fitted parameters

	BIC value								
Partial pressure (%)	**PSO**	**Intra-particle**	**Avrami**	**Langmuir**	**Weibull**	**PSO-Avrami**	**Langmuir-Avrami**	**Weibull-Avrami**	**Weibull-Langmuir**
80	-2011	-1097	-3039	-2011	-3039	-3261	-1994	-3635	-1994
70	-1289	-789	-1591	-1289	-1591	-1788	-1274	-1895	-1788
60	-928	-642	-1084	-928	-1084	-1221	-914	-1262	-1221
50	-890	-608	-993	-890	-993	-1125	-1125	-1163	-1125
40	-1327	-796	-1248	-1327	-1248	-1556	-1556	-1523	-1556
30	-2131	-1453	-2104	-2131	-2104	-2515	-2345	-2508	-2515
20	-1377	-1027	-1422	-1377	-1422	-1679	-1546	-1661	-1679
10	-1530	-1172	-1698	-1530	-1698	-1966	-2012	-1966	-1966
0	-3773	-2316	-3909	-3773	-3909	-4723	-4723	-4527	-4822

Between 40% and 30% PP, desorption is best described by the hybrid PSO-Avrami model (Figure 5.4c), where the Avrami component dominates, exhibiting a more rapid desorption. The transition from the Weibull model to the PSO model suggests that the water molecules with lower binding affinities have desorbed. The desorption of the water molecules with higher binding energies, such as those bound to GO's hydroxyl groups, are better captured by the PSO model. However, the desorption is dominated by the layer-by-layer release of water molecules. At 20% PP, the PSO component gradually becomes more dominant than the Avrami component (Figure 5.4d), indicating that the desorption of the strongly bound water molecules becomes the primary desorption mechanism.

Lowering the PP further to 10%, the optimal model transitions to the Weibull–Langmuir model (Figure 5.4e). The Langmuir component is the faster and more dominant component, while the Weibull component shows a more gradual increase. The Langmuir model describes the desorption of the water molecules from the few remaining occupied energetically favourable states, with the probability of desorption governed by the occupancy of these sites. The Weibull model, on the other hand, accounts for the variability in binding site strengths, originating from some of the less energetically favourable sites still being occupied, and water remaining constrained within the porous structure. At 0%, the Weibull–Langmuir model remains optimal. However, the Weibull component rapidly plateaus (Figure 5.4f), indicating that the desorption is dominated by the release of water molecules from the high-energy binding sites. Despite the distinct kinetic pathways of adsorption and desorption, the close agreement between equilibrium points and the minimal hysteresis observed (Figure 5.2b), together with the demonstrated stability of GPA under consecutive sorption–desorption cycles (Figure 5.2c), suggest that these differences in kinetics do not adversely affect the reversibility of water sorption by GPA.

5.3.2 Ethanol Sorption

Following the investigations into the water sorption in GPA, the ability of GPA to adsorb organic solvents, specifically ethanol and acetone, was further studied. GPA shows a reduced capacity for ethanol compared to water, with a sorption capacity of 4.2 ± 0.2% (0.042 ± 0.002 g/g) at 90% PP (Figure 5.5a). The bonding of the ethanol molecules to GO via their hydroxyl groups leaves the nonpolar alkyl groups on the surface of GPA. Bonding between the adsorbed and introduced ethanol molecules is predominately governed by weak van der Waals forces, reducing the probability of strong bonding or

strong bonding or interactions between the ethanol molecules and reducing its sorption capacity [32, 50].

The lower sorption capacity for ethanol compared to water also leads to the stop criterion being attained more rapidly, hence the shorter hold times consistently observed across all samples. However, GPA exhibits a similar or improved ethanol sorption capacity compared to other porous carbon-based materials [51, 52]. This can

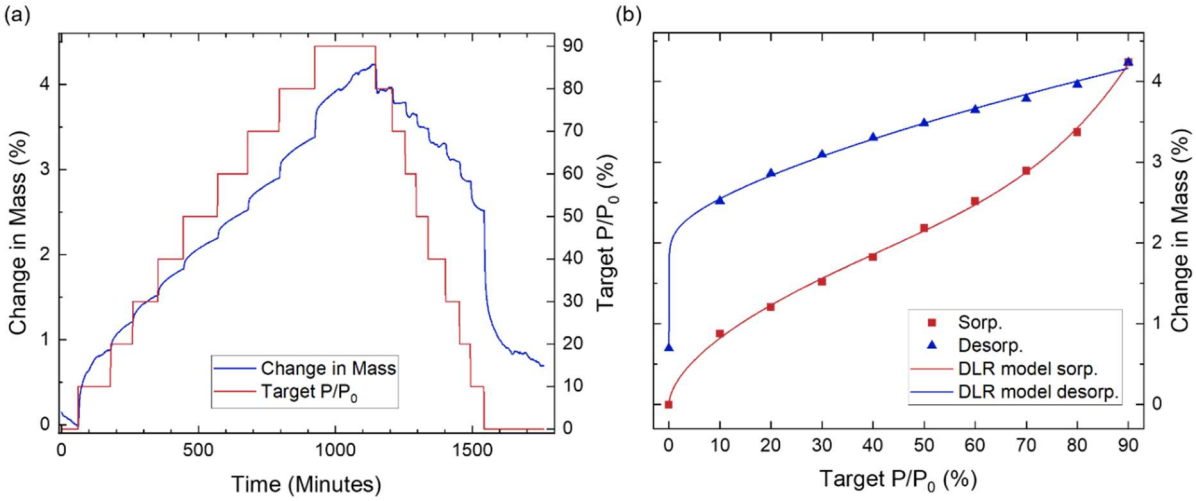

Figure 5.5: Ethanol sorption characteristics for GPA

(a) Percentage change in mass of GPA over time as the partial pressure of ethanol vapor is varied between 0 and 90%. **(b)** Resulting isotherm illustrating the adsorption behaviour.

be attributed to the combination of high surface area and the presence of oxygen-containing functional groups, which facilitate strong interactions with ethanol molecules. Unlike traditional activated carbons, which rely primarily on physical adsorption, GPA's structure supports both physical and chemical interactions, leading to more efficient sorption [53].

The ethanol sorption behaviour of GPA exhibits a type IVa isotherm, typically observed in mesoporous adsorbents (Figure 5.5b). Type IV isotherms are indicative of sorption behaviour driven by adsorbent–adsorbate interactions and capillary condensation,

where the high PP initiates the condensation of vapor within the pores [54]. For type IVa isotherms in particular, capillary condensation leads to hysteresis between the sorption and desorption curves and irreversible sorption of the adsorbate, shown by the 0.7% mass change between the beginning of the sorption cycle and the end of the desorption cycle. This occurs when the pores exceed a critical width. Modelling the pores as cylinders open at both ends, the meniscus during adsorption is cylindrical, while during desorption it becomes hemispherical. Since the radius of curvature for the hemispherical meniscus is half that of the cylindrical meniscus, the evaporation pressure is much lower than the condensation pressure, leading to the observed hysteresis. This likely occurs for GPA as its pores are macro-porous in nature rather than mesoporous [12, 31, 55]. Furthermore, by minimising the BIC, the dual-site Langmuir–Freundlich (DLR) model was identified as the best fit for the isotherm. This model captures the nonideal monolayer adsorption stemming from the complex interactions between GPA and ethanol, leading to the formation of nonpolar alkyl groups on GPA's surface that inhibit multilayer adsorption [56].

Analysing the sorption kinetics at 80% PP and below, ethanol sorption is best modelled with a PSO-Avrami hybrid model (Table 5.3). The gradual sorption shown by the PSO model demonstrates the gradual chemisorption of the adsorbent to the adsorbate, specifically hydrogen bonding between the hydroxyl groups on GO with the hydroxyl group on ethanol [32]. Unlike with water sorption, the Avrami exponent does not remain constant throughout the sorption process. Between 10 and 20% PP (Figure 5.6a), n = 1.2 ± 0.1, suggesting a 1D growth mechanism. This is facilitated by the nucleation of GO's functional groups through its interaction with ethanol, shown by the PSO component dominating the sorption mechanism. However, at 30% PP (Figure 5.6b),

there is a sudden decrease in the contribution of the PSO component, with the Avrami component dominating sorption, and the corresponding exponent decrease to 0.5, indicating no nucleation and instead, the sorption is driven by the diffusion of ethanol into the porous structure [57]. Between 40 and 80% PP (Figure 5.6c), the PSO component yields the slower, but more dominant sorption mechanism and the Avrami exponent gradually increases from n = 0.74 to n = 0.95. The gradual diffusion of

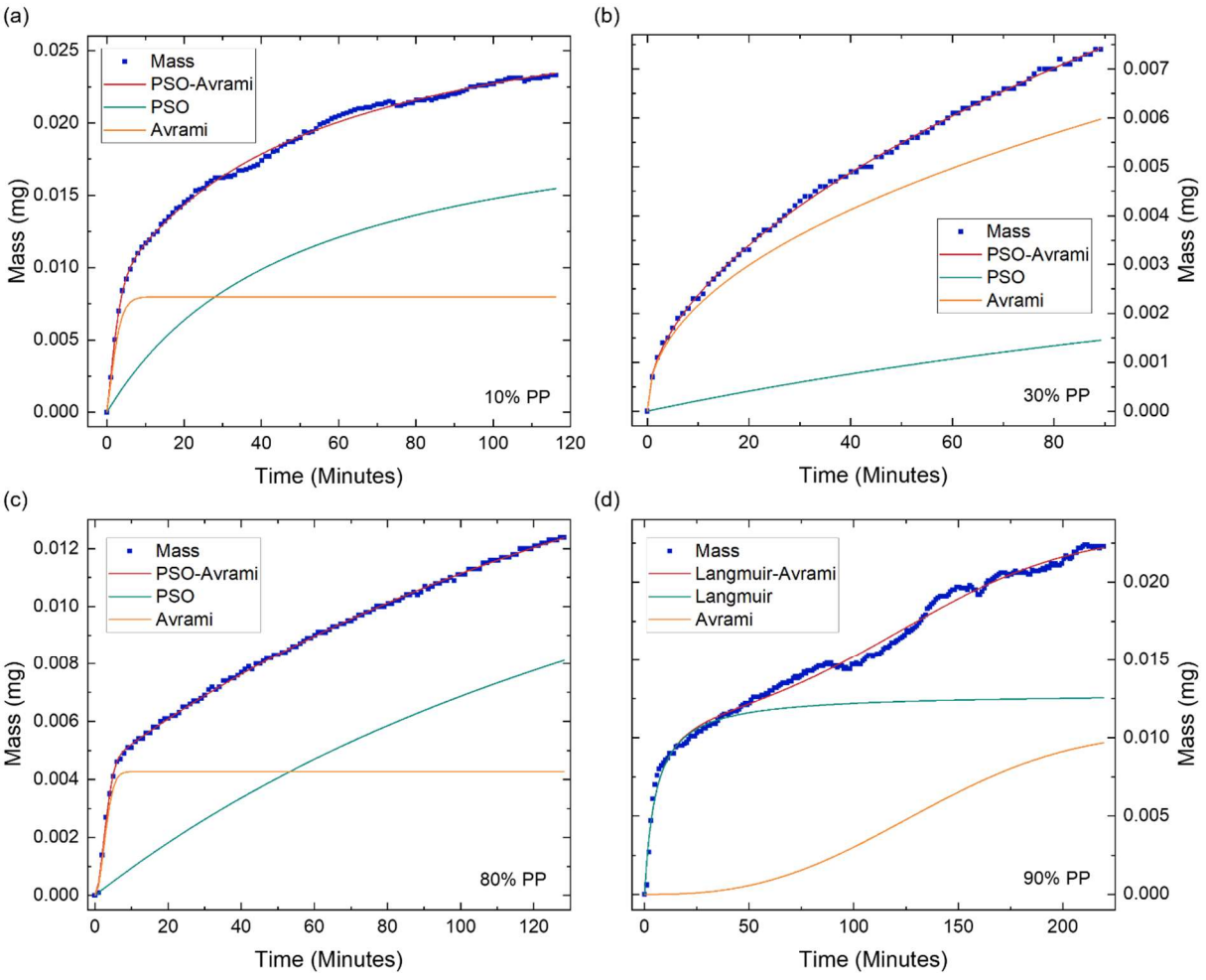

Figure 5.6: Ethanol sorption kinetics for GPA

Ethanol sorption kinetics of GPA, showing the increase in mass over time at different partial pressures (of **(a)** 10% PP **(b)** 30% PP **(c)** 80% PP and **(d)** 90% PP. The starting mass and time have been shifted to zero and the fit of the hybrid models and their individual components is displayed.

ethanol into GPA enables the vapor to interact with more functional groups, increasing GO-ethanol interactions in an inhomogeneous, time-dependent manner [57, 58].

Table 5.3: BIC values for GPA ethanol sorption kinetics

Bayesian information criterion (BIC) values for kinetic models (PSO, intra-particle diffusion, Avrami, Langmuir, hybrid PSO-Avrami, and hybrid Langmuir-Avrami) fit to GPA ethanol sorption data. The optimal model is indicated by the lowest BIC value. When the difference in BIC is less than 6, the optimal model is assessed based on the physical significance and consistency of the fitted parameters.

	BIC value					
Partial pressure (%)	**PSO**	**Intra-particle**	**Avrami**	**Langmuir**	**PSO-Avrami**	**Langmuir-Avrami**
10	-1695	-1448	-1766	-1695	-1924	-1838
20	-1318	-1399	-1410	-1318	-1534	-1462
30	-1507	-1644	-1652	-1507	-1741	-1696
40	-1499	-1649	-1648	-1499	-1777	-1718
50	-1986	-2225	-2218	-1986	-2408	-2313
60	-1723	-1871	-1909	-1723	-2109	-2019
70	-1741	-1828	-1951	-1741	-2209	-2089
80	-1877	-1895	-2095	-1877	-2451	-2236
90	-2810	-2910	-3100	-2810	-3363	-3397

At 90% PP, the optimal model shifts to the Langmuir–Avrami model (Figure 5.6d). The Langmuir model shows initial rapid sorption which plateaus rapidly, suggesting the occupation of GPA's functional groups. As the Langmuir component plateaus, the contribution of the Avrami component starts to increase. The Avrami exponent of n = 2.2 indicates a more complex, 2D growth mechanism [59]. As the functional groups have now been occupied, the continued sorption of ethanol relies on ethanol–ethanol bonding. High concentrations of ethanol in the vapor phase are known to initiate increased association between ethanol molecules and create clusters of ethanol molecules [60]. These complex sorption kinetics, and the absence of any observed

liquid condensation, indicates that the GPA continues to function as an absorber at high partial pressures, rather than a condensation surface.

Analysing the desorption characteristics, the PP between 80 and 60% are best represented by the Avrami model (Figure 5.7a) (

), which can be attributed to the release of ethanol molecules from the ethanol clusters

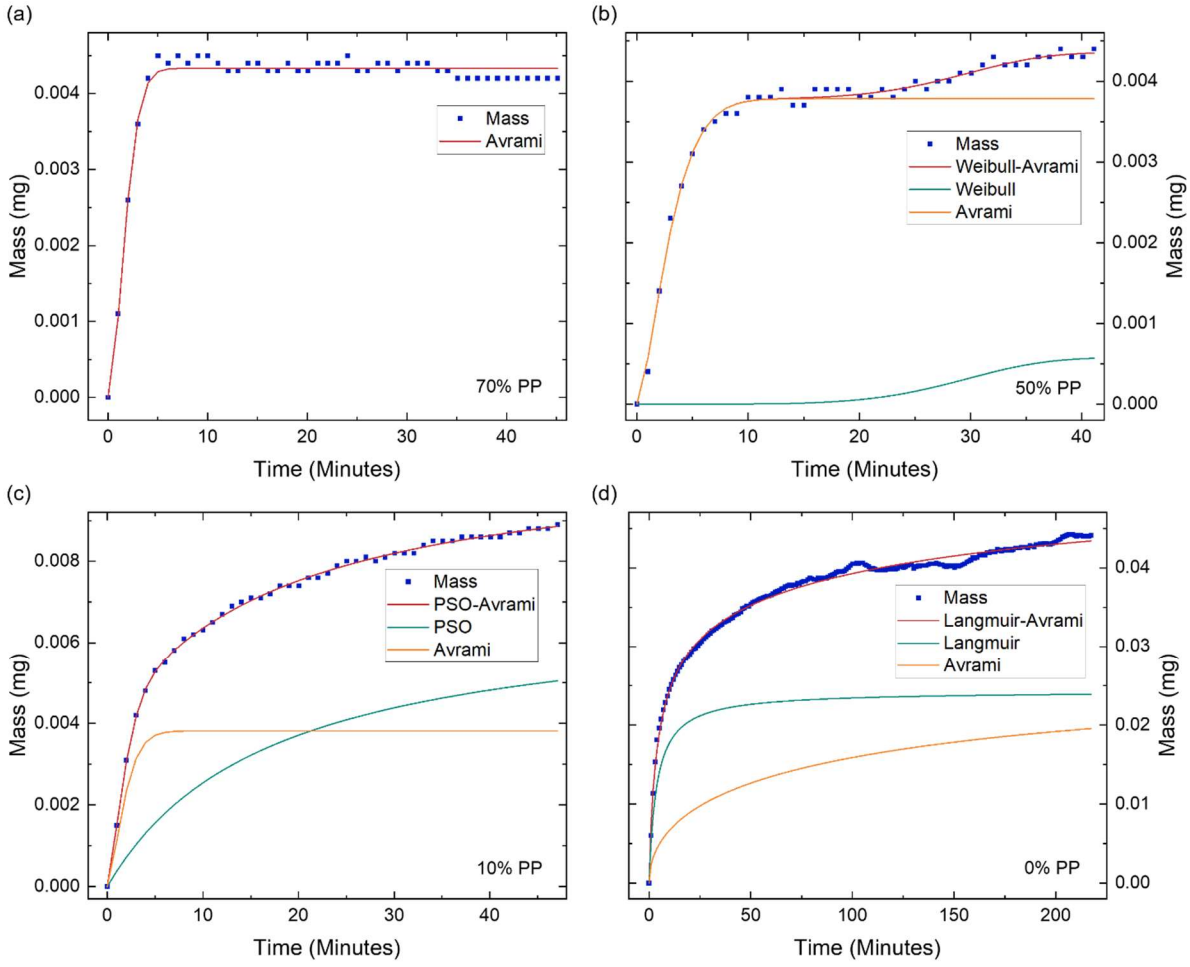

Figure 5.7: Ethanol desorption kinetics for GPA

Ethanol desorption kinetics of GPA, illustrating the mass decrease over time at different partial pressures of **(a)** 70% PP **(b)** 50% PP **(c)** 10% PP and **(d)** 0% PP. The initial mass and time have been shifted to zero. The mass values are multiplied by −1 for easier comparison with the adsorption kinetics. The fit of the hybrid models is displayed along with the individual components.

and denucleation [61].

Between 50 and 20% PP, the optimal desorption model is the Weibull–Avrami, with the Avrami model remaining dominant (Figure 5.7b). The Weibull component does not contribute toward desorption until the latter half of each desorption stage, where its influence gradually increases before plateauing, though it remains less significant than the Avrami component.

Table 5.4: BIC values for GPA ethanol desorption kinetics

Bayesian information criterion (BIC) values for kinetic models (PSO, intra-particle diffusion, Avrami, Langmuir, Weibull, hybrid PSO-Avrami, hybrid Langmuir-Avrami, hybrid Weibull-Avrami and hybrid Weibull-Langmuir) fit to GPA ethanol desorption data. The optimal model is indicated by the lowest BIC value. When the difference in BIC is less than 6, the optimal model is assessed based on the physical significance and consistency of the fitted parameters.

	BIC value								
Partial pressure (%)	**PSO**	**Intra-particle**	**Avrami**	**Langmuir**	**Weibull**	**PSO-Avrami**	**Langmuir-Avrami**	**Weibull-Avrami**	**Weibull-Langmuir**
80	-849	-725	-918	-849	-918	-910	-910	-907	-910
70	-719	-629	-857	-719	-857	-849	-849	-848	-849
60	-583	-537	-623	-583	-623	-616	-616	-612	-616
50	-689	-626	-717	-689	-717	-777	-678	-775	-777
40	-992	-867	-1001	-992	-1001	-992	-992	-1009	-998
30	-822	-727	-832	-822	-832	-874	-874	-880	-874
20	-652	-560	-673	-652	-673	-725	-725	-746	-725
10	-804	-667	-781	-804	-781	-906	-794	-900	-906
0	-2913	-2087	-3038	-2913	-3038	-3227	-3196	-3205	-3227

The delayed activation of the Weibull component reflects the heterogeneity of desorption. The weaker bound ethanol molecules at easily accessible sites desorb first, followed by the desorption of more tightly bound ethanol molecules or those from deeper within the porous structure. At 10% PP, desorption is best modelled by the PSO-Avrami model (Figure 5.7c). The Avrami model continues to drive rapid

desorption, however, the contribution of the slower PSO component gradually increases and overtakes the Avrami component by the end of the PP stage, showing the influence of the ethanol molecules desorbing from GO's hydroxyl groups. At 0% PP, the optimal model changes to the Langmuir–Avrami model (Figure 5.7d), suggesting that the rate of desorption is proportional to the concentration of ethanol adsorbed.

5.3.3 Acetone Sorption

Acetone sorption exhibits a similar maximum capacity to ethanol, reaching 4.3 ± 0.1% (0.043 ± 0.001 g/g) at 90% PP (Figure 5.8a). The bonding of the acetone to GPA, attributed to dipole–dipole interactions between the hydroxyl groups on GO with the carbonyl groups on acetone, leaves alkyl groups on the surface of GPA, such that further sorption of acetone is reliant on weak van der Waals forces between the adsorbed acetone molecules and the additional acetone molecules [62]. This maximum sorption capacity is lower than that of other porous carbon-based materials [63, 64]. Previous studies have shown that the optimal pore size for acetone sorption falls within the micropore range, specifically between 2 and 5 times the diameter of an acetone molecule [62]. Despite this, there is potential to modify GPA to enhance its properties for acetone sorption applications through nitrogen doping and reducing the pore size to the micropore range [65, 66].

Counterintuitively, Figure 5.8a also shows that the mass of GPA increases when the PP reduces to 80%. This can be attributed to the mass not reaching equilibrium at 90% PP. With such small mass changes at each PP, a more stringent stop criterion than less than 0.002% mass change per minute for 10 min is required. Similar to ethanol sorption, the resulting isotherm demonstrates type IVa behaviour, with hysteresis, due to the capillary condensation and the DLR model, showing the best fit (Figure 5.8b). The lower mass variation of 0.4% between the start of the sorption cycle and the end of the desorption cycle originates from the weaker GO-acetone bonds compared to GO-ethanol bonds, allowing the more reversible acetone sorption.

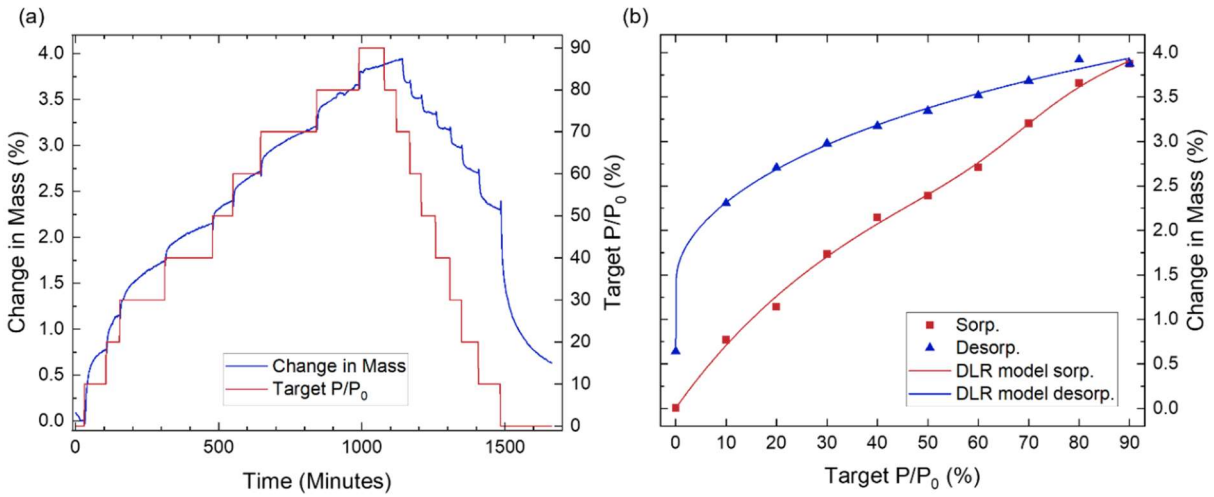

Figure 5.8: Acetone sorption characteristics for GPA

(a) Percentage change in mass of GPA over time as the partial pressure of acetone vapor is varied between 0 and 90%. **(b)** Resulting isotherm illustrating the adsorption behaviour.

The sorption of acetone up to 80% PP is similar to ethanol sorption and is best represented by the PSO-Avrami model (Table 5.5). The PSO model remains dominant throughout, showing the significant influence of the interactions between GPA and acetone, facilitated by dipole–dipole interactions between acetone and GO's functional groups [67]. Between 10 and 30% PP (Figure 5.9a), n = 1.2 ± 0.1, suggesting a 1D

growth mechanism from the nucleation of GO's functional groups. This reduces to 0.54 at 40% PP (Figure 5.9b), indicating the diffusion of acetone into GPA without any nucleation. The Avrami exponent then increases to 0.96 ± 0.07 between 50 and 80% PP (Figure 5.9c), implying the heterogeneous, time-dependent nucleation of GO's functional groups.

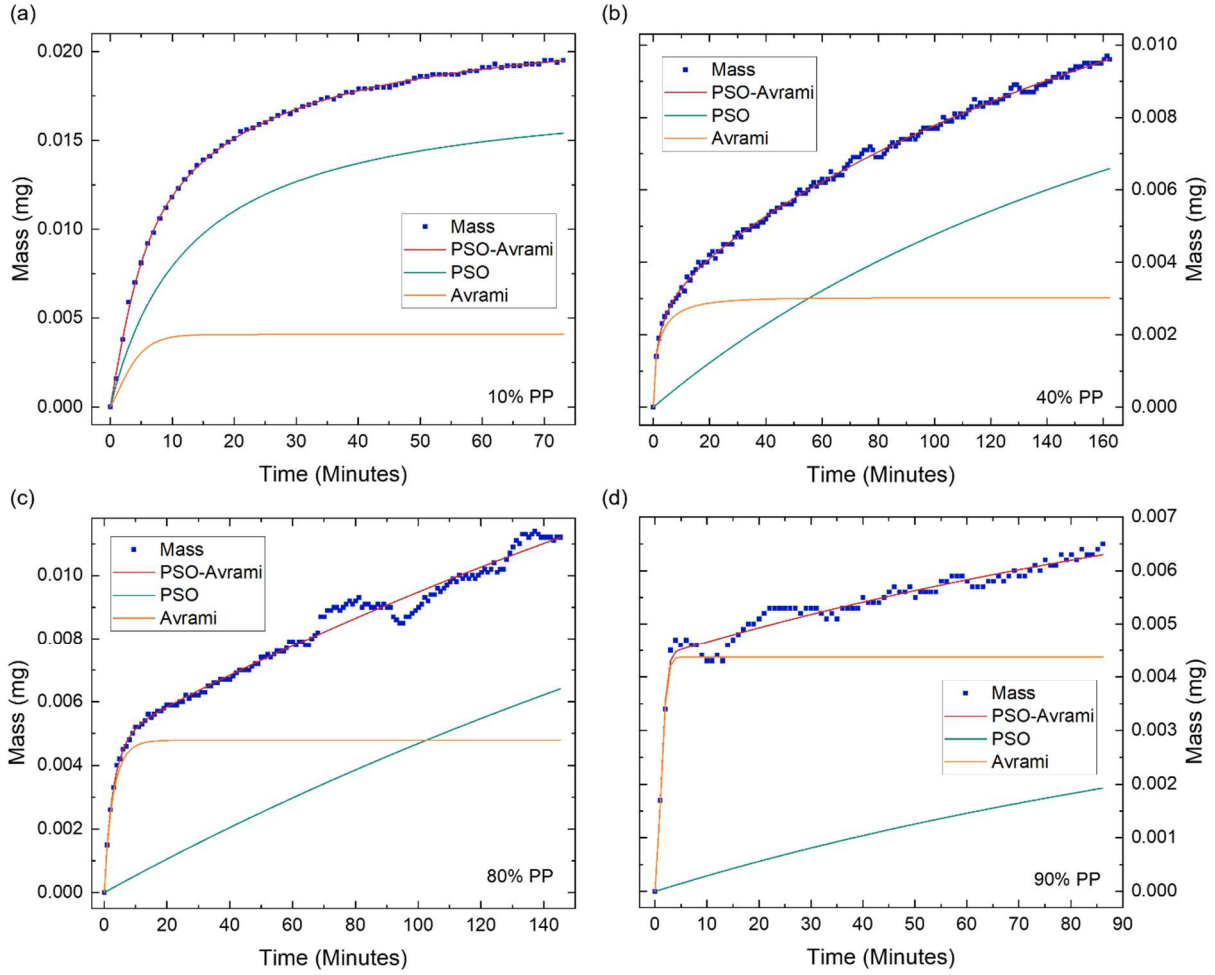

Figure 5.9: Acetone sorption kinetics for GPA

Acetone sorption kinetics of GPA, showing the increase in mass over time at different partial pressures (PP): **(a)** 10% PP **(b)** 50% PP **(c)** 80% PP and **(d)** 90% PP. The starting mass and time have been shifted to zero, and the fit of the hybrid models and their individual components are displayed.

The sorption behaviour of ethanol and acetone differ at 90% PP, where the optimal fit for acetone remains the PSO-Avrami model (Figure 5.9d), suggesting that monolayer sorption has not been achieved, due to the weak GO-acetone interactions [32]. Although the Avrami component does increase at 90% PP, it only reaches n = 1.8. This reflects the ongoing nucleation of GO's functional groups as the acetone molecules continue to diffuse through the structure [57]. Acetone clusters are much less likely to form compared to ethanol clusters, as they rely on weaker van der Waals forces and methyl-carbonyl group interactions [68].

Table 5.5: BIC values for GPA acetone sorption kinetics

Bayesian information criterion (BIC) values for kinetic models (PSO, intra-particle diffusion, Avrami, Langmuir, hybrid PSO-Avrami, and hybrid Langmuir-Avrami) fit to GPA acetone sorption data. The optimal model is indicated by the lowest BIC value. When the difference in BIC is less than 6, the optimal model is assessed based on the physical significance and consistency of the fitted parameters.

	BIC value					
Partial pressure (%)	**PSO**	**Intra-particle**	**Avrami**	**Langmuir**	**PSO-Avrami**	**Langmuir-Avrami**
10	-1094	-945	-1112	-1094	-1185	-1185
20	-710	-678	-708	-710	-727	-700
30	-2423	-2448	-2550	-2423	-2613	-2608
40	-2545	-2583	-2664	-2545	-2819	-2722
50	-1120	-1076	-1115	-1120	-1187	-1129
60	-1499	-1502	-1518	-1499	-1623	-1550
70	-2887	-3065	-3181	-2887	-3407	-3311
80	-2153	-2152	-2252	-2153	-2370	-2316
90	-1376	-1242	-1366	-1376	-1490	-1391

Negating the increase in mass observed as the PP is decreased to 80%, due to an equilibrium not being reached, acetone desorption shows similar characteristics to ethanol desorption. At 70% PP, the optimal fit is the Avrami model (Figure 5.10a) (Table

5.6), originating from denucleation. This transitions to the Weibull–Avrami model between 60 and 40% PP (Figure 5.10b), with the Avrami component being the dominant sorption mechanism and the low, delayed contribution of the Weibull model representing the heterogeneity of desorption from different binding sites and different locations in the porous structure.

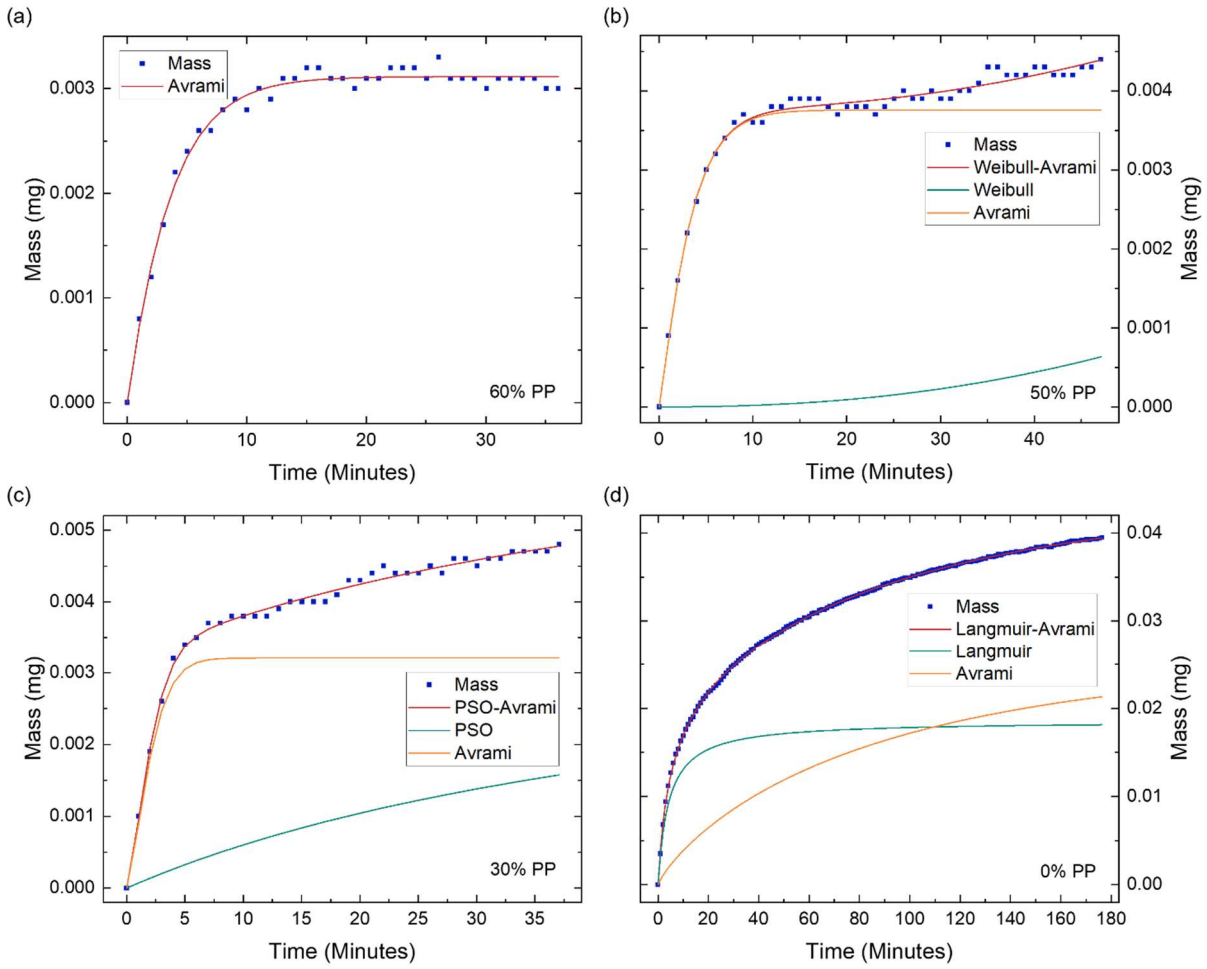

Figure 5.10: Acetone desorption kinetics for GPA

Acetone desorption kinetics of GPA, illustrating the mass decrease over time at different partial pressures of **(a)** 60% PP **(b) 5**0% PP **(c)** 30% PP and (**d)** 0% PP. The initial mass and time have been shifted to zero. The mass values are multiplied by −1 for easier comparison with the adsorption kinetics. The fit of the hybrid models is displayed along with their individual components.

As the PP drops to 30%, the optimal model transitions to the PSO-Avrami model (Figure 5.10c). The PSO model shows the gradual dechemisorption of the acetone molecules from GPA, which becomes more significant as the PP is further reduced to 10%. Finally, once the PP decreases to 0% (Figure 5.10d), the optimal model becomes the Langmuir–Avrami model, implying that the rate of desorption is proportional to the concentration of acetone molecules adsorbed.

Table 5.6: BIC values for GPA acetone desorption kinetics

Bayesian information criterion (BIC) values for kinetic models (PSO, intra-particle diffusion, Avrami, Langmuir, Weibull, hybrid PSO-Avrami, hybrid Langmuir-Avrami, hybrid Weibull-Avrami and hybrid Weibull-Langmuir) fit to GPA acetone desorption data. The optimal model is indicated by the lowest BIC value. When the difference in BIC is less than 6, the optimal model is assessed based on the physical significance and consistency of the fitted parameters.

	BIC value								
Partial pressure (%)	**PSO**	**Intra-particle**	**Avrami**	**Langmuir**	**Weibull**	**PSO-Avrami**	**Langmuir-Avrami**	**Weibull-Avrami**	**Weibull-Langmuir**
80	-	-	-	-	-	-	-	-	-
70	-607	-581	-694	-607	-757	-595	-687	-680	-595
60	-617	-574	-687	-617	-687	-682	-682	-691	-606
50	-785	-724	-825	-785	-825	-859	-774	-857	-859
40	-765	-721	-823	-765	-823	-839	-754	-836	-754
30	-627	-580	-638	-627	-638	-703	-616	-626	-616
20	-941	-825	-925	-941	-925	-1046	-929	-1042	-929
10	-1183	-1045	-1161	-1183	-1161	-1292	-1174	-1292	-1170
0	-2459	-1963	-2527	-2459	-2527	-2855	-2675	-2789	-2855

Our findings highlight that the sorption capacities of GPA for ethanol and acetone vapours observed in this study represent only a fraction of its potential total capacity. The slow, continuous adsorption process, which remained unsaturated within the experimental time frame, indicates that GPA may possess a significantly higher

capacity than initially apparent. Fully quantifying this capacity would require longer experimental durations tailored to specific application timeframes, which was beyond the scope of this work. Therefore, while GPA exhibits promising sorption behaviour, a direct comparison with existing adsorbent materials was not undertaken. Future research would aim to determine the equilibrium capacities over extended periods and evaluate GPA's performance against other adsorbents under standardised conditions to comprehensively assess its effectiveness for specific applications.

5.3.4 Water Sorption of GPA_{250}

In the previous chapter (Chapter 4), it was demonstrated that annealing GPA at 250°C (GPA_{250}) removes some OCFGs and alters the GO-M13 bonds, resulting in fewer but larger pores. These structural changes are expected to influence its sorption properties. Consequently, the effect of annealing on the water sorption behaviour of GPA_{250} was investigated and compared with GPA.

The maximum water sorption capacity of GPA_{250} at 90% PP was 70 ± 2%, comparable to GPA (Figure 5.11a). Annealing at 250°C initiates the removal of carboxyl and carbonyl groups from GO but does not reach the temperature needed to eliminate hydroxyl groups. Since hydroxyl groups play a primary role in bonding with water molecules during the initial stages of sorption, this minimally affects the sorption capacity of GPA_{250} relative to GPA.

However, the sorption-desorption cycle duration increases significantly, from 3800 ± 300 minutes for GPA to 4700 ± 300 minutes for GPA_{250}. Moreover, while GPA and GPA_{250} both exhibit type II isotherms, there is a noticeable increase in the observed hysteresis for GPA_{250} (Figure 5.11b). With fewer functional OCFGs available for water

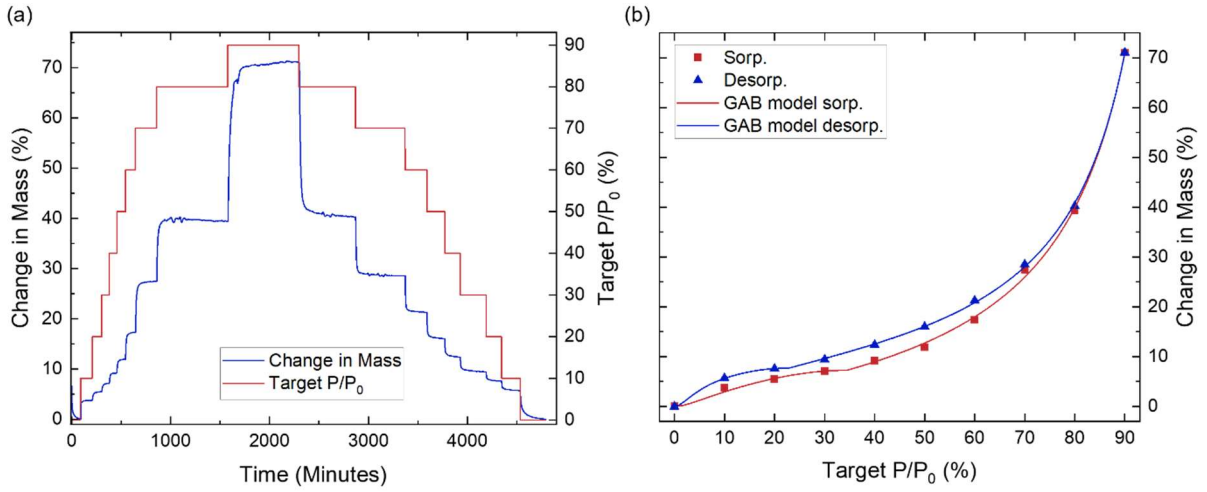

Figure 5.11: Water sorption characteristics of GPA_{250}

(a) Percentage change in mass of GPA over time as a function of the partial water vapor pressure variation between 0 and 90%. **(b)** Resulting isotherm illustrating the adsorption behaviour.

binding during sorption, water molecules tend to cluster and form metastable states through strong hydrogen bonding among themselves. These metastable states require additional energy to overcome during desorption, delaying the system's return to equilibrium. This behaviour accounts for the increased hysteresis and prolonged cycle duration observed for GPA_{250} [69, 70].

Both the sorption and desorption kinetics of GPA_{250} closely resemble GPA. The optimal models for the sorption kinetics of GPA_{250} remain consistent with those identified for GPA: the PSO-Avrami model between 10-30% PP, Langmuir-Avrami for 40-70%, Avrami at 80% and Langmuir-Avrami at 90% (Table 5.7). Similarly, the optimal desorption models align with those of GPA: Weibull Avrami between 80-50% PP, PSO-Avrami between 40-20%, and Weibull-Langmuir between 10-0% (Table 5.8). These findings suggests that temperature-induced changes to the morphology (Figure 4.1 - Figure 4.2) and composition (Figure 4.3) may not be substantial enough to significantly affect its water sorption characteristics. Future studies into annealing GPA at higher

temperatures could provide deeper insights into the relationship between thermal treatment and the water sorption dynamics, revealing the potential threshold where the morphological and compositional changes become impactful.

Table 5.7: BIC values for GPA_{250} water sorption kinetics

Bayesian information criterion (BIC) values for kinetic models (PSO, intra-particle diffusion, Avrami, Langmuir, hybrid PSO-Avrami, and hybrid Langmuir-Avrami) fit to GPA_{250} water sorption data. The optimal model is indicated by the lowest BIC value. When the difference in BIC is less than 6, the optimal model is assessed based on the physical significance and consistency of the fitted parameters.

	BIC value					
Partial pressure (%)	**PSO**	**Intra-particle**	**Avrami**	**Langmuir**	**PSO-Avrami**	**Langmuir-Avrami**
10	-1193	-836	-1198	-1193	-1378	-1378
20	-1734	-1258	-1762	-1734	-2002	-1938
30	-3511	-2978	-4535	-3511	-4649	-4676
40	-2329	-1523	-2376	-2329	-2475	-2475
50	-1182	-797	-1290	-1182	-1633	-1633
60	-2077	-1171	-1942	-2077	-2558	-2558
70	-2460	-1412	-2620	-2460	-2444	-2966
80	-5553	-3041	-5896	-5553	-5534	-5534
90	-6020	-2911	-7698	-6020	-7682	-7685

Table 5.8: BIC values for GPA_{250} water desorption kinetics

Bayesian information criterion (BIC) values for kinetic models (PSO, intra-particle diffusion, Avrami, Langmuir, Weibull, hybrid PSO-Avrami, hybrid Langmuir-Avrami, hybrid Weibull-Avrami and hybrid Weibull-Langmuir) fit to GPA_{250} water desorption data. The optimal model is indicated by the lowest BIC value. When the difference in BIC is less than 6, the optimal model is assessed based on the physical significance and consistency of the fitted parameters

	BIC value								
Partial pressure (%)	**PSO**	**Intra-particle**	**Avrami**	**Langmuir**	**Weibull**	**PSO-Avrami**	**Langmuir-Avrami**	**Weibull-Avrami**	**Weibull-Langmuir**
80	-1405	-916	-1876	-1405	-1876	-2065	-2065	-2281	-2065
70	-1257	-804	-1478	-1257	-1478	-1605	-1243	-1766	-1243
60	-1040	-672	-1173	-1040	-1173	-1324	-1324	-1374	-1324
50	-2799	-1712	-2646	-2799	-2646	-3484	-2864	-3492	-3484
40	-2070	-1231	-1932	-2070	-1932	-2471	-2134	-2455	-2471
30	-2003	-1272	-1883	-2003	-1883	-2289	-2029	-2249	-2289
20	-1724	-1141	-1677	-1724	-1677	-2002	-1911	-1979	-2002
10	-1752	-1233	-1725	-1752	-1725	-2022	-1895	-1978	-2022
0	-4042	-2711	-4604	-4042	-4604	-6003	-5533	-5334	-6003

5.4 Conclusion

The sorption characteristics of GraPhage13 aerogels with water, ethanol and acetone have been comprehensively characterised through in-depth DVS studies with the detailed analysis of isotherms and sorption–desorption kinetics. GPA demonstrates a remarkably high sorption capacity of 0.68 g/g, twice that of traditional silica gel adsorbents and 20% higher than GO laminates. This superior performance is attributed to its high surface area, extensive porous network and the strong interactions between water molecules and the functional groups on the GO within GPA, along with water–water interactions that enable indefinite multilayer adsorption. The low level of hysteresis and the stability of GPA under consecutive sorption–desorption cycles underscore the reversibility of water sorption and the reusability of GPA. GPA exhibits a lower sorption capacity for ethanol and acetone. This is largely due to the finite nature of multilayer adsorption, slower sorption kinetics resulting from the lower affinity of ethanol and acetone for GPA and the significant hysteresis as result of the capillary

condensation. Nevertheless, the tuneability of GPA offers substantial potential for enhancing acetone sorption capacity and its ethanol sorption capacity is comparable or superior to that of similar porous carbon-based materials, highlighting GPA's versatility in adsorbing a wide range of vapours.

This study underscores the remarkable sorption characteristics of GPA, demonstrating both its capability and versatility. Collectively, the findings pave the way for the development and integration of GPA into advanced graphene-based devices for environmental monitoring, freshwater generation and miniaturized biomedical sensors. Realising these applications on an industrial scale will require advancing the production process from laboratory methods to efficient and cost-effective industrial techniques. Moreover, integrating GPA into graphene-based devices will be critical for unlocking its potential across a diverse range of applications. While challenges remain in transitioning from laboratory-scale processes to industrial settings, ongoing advancements in bioengineering (e.g., enhancing M13 bacteriophage yield) and material processing (e.g., continuous flow systems for GO reduction) are promising. These innovations align with the principles of green chemistry, which are central to GPA production, and support its industrial feasibility.

5.5 Material and Methods

Further information on graphene oxide and M13 bacteriophage used in these experiments can found in Sections 2.1.1 and 2.1.2, respectively.

For detailed descriptions of the methods used in this chapter, please refer to Chapter 2, specifically the following sections:

- 2.2.2 Fabrication of GraPhage13 Aerogels (GPA)

- 2.2.9 Dynamic Vapor Sorption (DVS)
- 2.3.2 Bayesian Information Criterion (BIC)

5.6 References

[1] H. Lee, A. Ozaki, M. Lee, and T. Yamamoto, "Humidity Control Effect of Vapor-Permeable Walls Employing Hygroscopic Insulation Material," *Indoor Air,* vol. 30, no. 2, pp. 346-360, 2020, doi: 10.1111/ina.12622.

[2] T. Xu, X. Ding, H. Cheng, G. Han, and L. Qu, "Moisture-Enabled Electricity from Hygroscopic Materials: A New Type of Clean Energy," *Advanced Materials,* vol. 36, no. 12, p. 2209661, 2024, doi: 10.1002/adma.202209661.

[3] Q. Bai, W. Zhou, W. Cui, and Z. Qi, "Research Progress on Hygroscopic Agents for Atmospheric Water Harvesting Systems," *Materials (Basel),* vol. 17, no. 3, 2024, doi: 10.3390/ma17030722.

[4] R. Ramanathan, S. Nagarajan, S. Sathiyamoorthy, B. Manavaimaran, H. C. Barshilia, and R. C. Mallik, "A Highly Sensitive and Room Temperature Ethanol Gas Sensor Based on Spray Deposited Sb Doped Sno2 Thin Films," *Materials Advances,* 10.1039/D3MA00696D vol. 5, no. 1, pp. 293-305, 2024, doi: 10.1039/D3MA00696D.

[5] A. A. Baharuddin, B. C. Ang, A. S. M. A. Haseeb, Y. C. Wong, and Y. H. Wong, "Advances in Chemiresistive Sensors for Acetone Gas Detection," *Materials Science in Semiconductor Processing,* vol. 103, p. 104616, 2019, doi: 10.1016/j.mssp.2019.104616.

[6] X. Fan, J. Wang, S. Yang, and C. Ma, "Ce Enhanced Humidity-Independent Acetone-Sensing Properties of Co3o4 at a Low Operating Temperature," *Materials Science and Engineering: B,* vol. 298, p. 116924, 2023, doi: 10.1016/j.mseb.2023.116924.

[7] T. Arakawa, T. Aota, K. Iitani, K. Toma, Y. Iwasaki, and K. Mitsubayashi, "Skin Ethanol Gas Measurement System with a Biochemical Gas Sensor and Gas Concentrator toward Monitoring of Blood Volatile Compounds," *Talanta,* vol. 219, p. 121187, 2020, doi: 10.1016/j.talanta.2020.121187.

[8] B. Zieliński, P. Miądlicki, and J. Przepiórski, "Development of Activated Carbon for Removal of Pesticides from Water: Case Study," *Sci Rep,* vol. 12, no. 1, p. 20869, 2022, doi: 10.1038/s41598-022-25247-6.

[9] I. Ali, A. A. Basheer, X. Y. Mbianda, A. Burakov, E. Galunin, I. Burakova, E. Mkrtchyan, A. Tkachev, and V. Grachev, "Graphene Based Adsorbents for Remediation of Noxious Pollutants from Wastewater," *Environment International,* vol. 127, pp. 160-180, 2019, doi: 10.1016/j.envint.2019.03.029.

[10] Y. He, N. Zhang, F. Wu, F. Xu, Y. Liu, and J. Gao, "Graphene Oxide Foams and Their Excellent Adsorption Ability for Acetone Gas," *Materials Research Bulletin,* vol. 48, no. 9, pp. 3553-3558, 2013, doi: 10.1016/j.materresbull.2013.05.056.

[11] G. Nassar, E. Daou, R. Najjar, M. Bassil, and R. Habchi, "A Review on the Current Research on Graphene-Based Aerogels and Their Applications," *Carbon Trends,* vol. 4, p. 100065, 2021, doi: 10.1016/j.cartre.2021.100065.

[12] P. Passaretti, Y. Sun, I. Khan, K. Chan, R. Sabo, H. White, T. R. Dafforn, and P. G. Oppenheimer, "Multifunctional Graphene Oxide-Bacteriophage Based Porous Three-Dimensional Micro-Nanocomposites," *Nanoscale,* 10.1039/C9NR03670A vol. 11, no. 28, pp. 13318-13329, 2019, doi: 10.1039/C9NR03670A.

[13] R. Ikram, B. M. Jan, and W. Ahmad, "An Overview of Industrial Scalable Production of Graphene Oxide and Analytical Approaches for Synthesis and Characterization," *Journal of Materials Research and Technology,* vol. 9, no. 5, pp. 11587-11610, 2020, doi: 10.1016/j.jmrt.2020.08.050.

[14] C. M. Warner, N. Barker, S. W. Lee, and E. J. Perkins, "M13 Bacteriophage Production for Large-Scale Applications," *Bioprocess Biosyst Eng,* vol. 37, no. 10, pp. 2067-72, 2014, doi: 10.1007/s00449-014-1184-7.

[15] Y. Sun, P. Passaretti, I. Hernandez, J. Gonzalez, W. Liu, F. Rodriguez, D. J. Dunstan, P. Goldberg Oppenheimer, and C. J. Humphreys, "Nanomechanics of Graphene Oxide-Bacteriophage Based Self-Assembled Porous Composites," *Scientific Reports,* vol. 10, no. 1, p. 15618, 2020, doi: 10.1038/s41598-020-72372-1.

[16] K. Stokes, Y. Sun, J. L. Thomas, P. Passaretti, H. White, and P. Goldberg Oppenheimer, "Conductivity Optimisation of Graphene Oxide-M13 Bacteriophage Nanocomposites: Towards Graphene-Based Gas Micronano-Sensors," *Discover Nano,* vol. 19, no. 1, p. 152, 2024, doi: 10.1186/s11671-024-04101-w.

[17] N. Sattar, H. Sajid, S. Tabassum, K. Ayub, T. Mahmood, and M. A. Gilani, "Potential Sensing of Toxic Chemical Warfare Agents (Cwas) by Twisted Nanographenes: A First Principle Approach," *Science of The Total Environment,* vol. 824, p. 153858, 2022, doi: 10.1016/j.scitotenv.2022.153858.

[18] K. Rana, H. Kaur, N. Singh, T. Sithole, and S. S. Siwal, "Graphene-Based Materials: Unravelling Its Impact in Wastewater Treatment for Sustainable Environments," *Next Materials,* vol. 3, p. 100107, 2024, doi: 10.1016/j.nxmate.2024.100107.

[19] L.-O. Nilsson, "Durability Concept; Pore Structure and Transport Processes," in *Advanced Concrete Technology*, J. Newman and B. S. Choo Eds. Oxford: Butterworth-Heinemann, 2003, ch. 8, pp. 3-29.

[20] S. Glass, C. Boardman, and S. Zelinka, "Short Hold Times in Dynamic Vapor Sorption Measurements Mischaracterize the Equilibrium Moisture Content of Wood," *Wood Science and Technology,* vol. 51, pp. 243-260, 2017, doi: 10.1007/s00226-016-0883-4.

[21] B. Lian, S. De Luca, Y. You, S. Alwarappan, M. Yoshimura, V. Sahajwalla, S. C. Smith, G. Leslie, and R. K. Joshi, "Extraordinary Water Adsorption Characteristics of Graphene Oxide," *Chemical Science,* 10.1039/C8SC00545A vol. 9, no. 22, pp. 5106-5111, 2018, doi: 10.1039/C8SC00545A.

[22] M. Bermeo, N. El Hadri, F. Ravaux, A. Zaki, L. Zou, and M. Jouiad, "Adsorption Capacities of Hygroscopic Materials Based on Nacl-Tio₂ and Nacl-Sio₂ Core/Shell Particles," *Journal of Nanotechnology,* vol. 2020, p. 3683629, 2020, doi: 10.1155/2020/3683629.

[23] Y. Zhuang, F. Yu, J. Ma, and J. Chen, "Facile Synthesis of Three-Dimensional Graphene–Soy Protein Aerogel Composites for Tetracycline Adsorption,"

Desalination and Water Treatment, vol. 57, no. 20, pp. 9510-9519, 2016, doi: 10.1080/19443994.2015.1029530.

[24] Y. Jin, Q. Du, Y. Li, Y. Zhang, B. Chen, M. Wang, K. Chen, Y. Sun, S. Zhao, and Z. Jing, "Removal of Methylene Blue by Crosslinked Egg White Protein/Graphene Oxide Bionanocomposite Aerogels," *Nanomaterials,* vol. 12, no. 15, p. 2659, 2022, doi: 10.3390/nano12152659.

[25] M. A. Riaz, P. Hadi, I. H. Abidi, A. Tyagi, X. Ou, and Z. Luo, "Recyclable 3d Graphene Aerogel with Bimodal Pore Structure for Ultrafast and Selective Oil Sorption from Water," *RSC Advances,* 10.1039/C7RA02886E vol. 7, no. 47, pp. 29722-29731, 2017, doi: 10.1039/C7RA02886E.

[26] H. Lu, X. Jiang, J. Wang, and R. Hu, "Degradable Composite Aerogel with Excellent Water-Absorption for Trace Water Removal in Oil and Oil-in-Water Emulsion Filtration," *Frontiers in Materials,* Original Research vol. 9, 2022, doi: 10.3389/fmats.2022.1093164.

[27] U. Legrand, D. Klassen, S. Watson, A. Aufoujal, B. Nisol, R. Boudreault, K. E. Waters, J.-L. Meunier, P.-L. Girard-Lauriault, M. R. Wertheimer, and J. R. Tavares, "Nanoporous Sponges as Carbon-Based Sorbents for Atmospheric Water Generation," *Industrial & Engineering Chemistry Research,* vol. 60, no. 35, pp. 12923-12933, 2021, doi: 10.1021/acs.iecr.1c02248.

[28] L. Liu, S. Tan, T. Horikawa, D. D. Do, D. Nicholson, and J. Liu, "Water Adsorption on Carbon - a Review," *Advances in Colloid and Interface Science,* vol. 250, pp. 64-78, 2017, doi: 10.1016/j.cis.2017.10.002.

[29] S. Yanniotis and J. Blahovec, "Model Analysis of Sorption Isotherms," *LWT - Food Science and Technology,* vol. 42, no. 10, pp. 1688-1695, 2009, doi: 10.1016/j.lwt.2009.05.010.

[30] J. Wang and X. Guo, "Adsorption Kinetic Models: Physical Meanings, Applications, and Solving Methods," *Journal of Hazardous Materials,* vol. 390, p. 122156, 2020, doi: 10.1016/j.jhazmat.2020.122156.

[31] M. Thommes, K. Kaneko, A. Neimark, J. Olivier, F. Rodriguez-Reinoso, J. Rouquerol, and K. Sing, "Physisorption of Gases, with Special Reference to the Evaluation of Surface Area and Pore Size Distribution (Iupac Technical Report)," *Pure and Applied Chemistry,* vol. 87, 2015, doi: 10.1515/pac-2014-1117.

[32] V. V. Neklyudov, N. R. Khafizov, I. A. Sedov, and A. M. Dimiev, "New Insights into the Solubility of Graphene Oxide in Water and Alcohols," *Physical Chemistry Chemical Physics,* 10.1039/C7CP02303K vol. 19, no. 26, pp. 17000-17008, 2017, doi: 10.1039/C7CP02303K.

[33] G. Sang, S. Liu, and D. Elsworth, "Water Vapor Sorption Properties of Illinois Shales under Dynamic Water Vapor Conditions: Experimentation and Modeling," *Water Resources Research,* vol. 55, no. 8, pp. 7212-7228, 2019, doi: 10.1029/2019WR024992.

[34] C. Buttersack, "Modeling of Type Ii High-Resolution Sorption Isotherms: Evaluation of Different Approaches," *Colloids and Surfaces A: Physicochemical and Engineering Aspects,* vol. 650, p. 129489, 2022, doi: 10.1016/j.colsurfa.2022.129489.

[35] V. Kutarov, Y. Tarasevich, E. Aksenenko, and R. Dlubovskiy, "Thermodynamics of Irreversible Adsorption of Water Vapours by Montmorillonite," *Adsorption*

Science & Technology, vol. 35, no. 5-6, pp. 458-463, 2017, doi: 10.1177/0263617417696086.

[36] K. S. W. Sing and R. T. Williams, "Physisorption Hysteresis Loops and the Characterization of Nanoporous Materials," *Adsorption Science & Technology,* vol. 22, no. 10, pp. 773-782, 2004, doi: 10.1260/0263617053499032.

[37] Z. P. Bažant and M. Z. Bazant, "Theory of Sorption Hysteresis in Nanoporous Solids: Part I: Snap-through Instabilities," *Journal of the Mechanics and Physics of Solids,* vol. 60, no. 9, pp. 1644-1659, 2012, doi: 10.1016/j.jmps.2012.04.014.

[38] J. Rojas, D. Suarez, A. Moreno, J. Silva-Agredo, and R. A. Torres-Palma, "Kinetics, Isotherms and Thermodynamic Modeling of Liquid Phase Adsorption of Crystal Violet Dye onto Shrimp-Waste in Its Raw, Pyrolyzed Material and Activated Charcoals," *Applied Sciences,* vol. 9, no. 24, p. 5337, 2019, doi: 10.3390/app9245337.

[39] J. P. Vareda, "On Validity, Physical Meaning, Mechanism Insights and Regression of Adsorption Kinetic Models," *Journal of Molecular Liquids,* vol. 376, p. 121416, 2023, doi: 10.1016/j.molliq.2023.121416.

[40] S. I. Vrieze, "Model Selection and Psychological Theory: A Discussion of the Differences between the Akaike Information Criterion (Aic) and the Bayesian Information Criterion (Bic)," *Psychol Methods,* vol. 17, no. 2, pp. 228-43, 2012, doi: 10.1037/a0027127.

[41] V. V. Santana, E. Costa, C. M. Rebello, A. M. Ribeiro, C. Rackauckas, and I. B. R. Nogueira, "Efficient Hybrid Modeling and Sorption Model Discovery for Non-Linear Advection-Diffusion-Sorption Systems: A Systematic Scientific Machine Learning Approach," *Chemical Engineering Science,* vol. 282, p. 119223, 2023, doi: 10.1016/j.ces.2023.119223.

[42] A. Afzalifar, G. C. Shields, V. R. Fowler, and R. H. A. Ras, "Probing the Free Energy of Small Water Clusters: Revisiting Classical Nucleation Theory," *The Journal of Physical Chemistry Letters,* vol. 13, no. 34, pp. 8038-8046, 2022, doi: 10.1021/acs.jpclett.2c01361.

[43] M. P. Andersson, "The Shape of Water – How Cluster Formation Provides a Unifying Explanation of Water's Anomalous Properties," *Journal of Molecular Liquids,* vol. 383, p. 122169, 2023, doi: 10.1016/j.molliq.2023.122169.

[44] N. A. Oladoja, "A Critical Review of the Applicability of Avrami Fractional Kinetic Equation in Adsorption-Based Water Treatment Studies," *Desalination and Water Treatment,* vol. 57, no. 34, pp. 15813-15825, 2016, doi: 10.1080/19443994.2015.1076355.

[45] Y. Liu and X. Yu, "Carbon Dioxide Adsorption Properties and Adsorption/Desorption Kinetics of Amine-Functionalized Kit-6," *Applied Energy,* vol. 211, pp. 1080-1088, 2018, doi: 10.1016/j.apenergy.2017.12.016.

[46] T. A. Saleh, "Isotherm Models of Adsorption Processes on Adsorbents and Nanoadsorbents," in *Interface Science and Technology*, vol. 34, T. A. Saleh Ed.: Elsevier, 2022, ch. 4, pp. 99-126.

[47] S. Azizian and S. Eris, "Adsorption Isotherms and Kinetics," in *Interface Science and Technology*, vol. 33, M. Ghaedi Ed.: Elsevier, 2021, ch. 6, pp. 445-509.

[48] A. V. Muthachikavil, B. Peng, G. M. Kontogeorgis, and X. Liang, "Distinguishing Weak and Strong Hydrogen Bonds in Liquid Water—a Potential of Mean Force-Based Approach," *The Journal of Physical Chemistry B,* vol. 125, no. 26, pp. 7187-7198, 2021, doi: 10.1021/acs.jpcb.1c02816.

[49] A. Marabi, S. Livings, M. Jacobson, and I. S. Saguy, "Normalized Weibull Distribution for Modeling Rehydration of Food Particulates," *European Food Research and Technology,* vol. 217, no. 4, pp. 311-318, 2003, doi: 10.1007/s00217-003-0719-y.

[50] P. O. Bedolla, G. Feldbauer, M. Wolloch, S. J. Eder, N. Dörr, P. Mohn, J. Redinger, and A. Vernes, "Effects of Van Der Waals Interactions in the Adsorption of Isooctane and Ethanol on Fe(100) Surfaces," *The Journal of Physical Chemistry C,* vol. 118, no. 31, pp. 17608-17615, 2014, doi: 10.1021/jp503829c.

[51] A. Silvestre-Albero, J. Silvestre-Albero, A. Sepúlveda-Escribano, and F. Rodríguez-Reinoso, "Ethanol Removal Using Activated Carbon: Effect of Porous Structure and Surface Chemistry," *Microporous and Mesoporous Materials,* vol. 120, no. 1, pp. 62-68, 2009, doi: 10.1016/j.micromeso.2008.10.012.

[52] P. Huo, Y. Zhang, L. Zhang, M. Yang, W. Wei, X. Zhang, J. Yang, and Y. Zhang, "Insight into the Adsorption Process of Ethanol and Water on the Pore Structure and Surface Chemistry Properties Engineered Activated Carbon Fibers," *Industrial & Engineering Chemistry Research,* vol. 60, no. 30, pp. 11141-11150, 2021, doi: 10.1021/acs.iecr.1c02005.

[53] A. H. Berger and A. S. Bhown, "Comparing Physisorption and Chemisorption Solid Sorbents for Use Separating Co2 from Flue Gas Using Temperature Swing Adsorption," *Energy Procedia,* vol. 4, pp. 562-567, 2011, doi: 10.1016/j.egypro.2011.01.089.

[54] G. Sang, S. Liu, D. Elsworth, Y. Yang, and L. Fan, "Evaluation and Modeling of Water Vapor Sorption and Transport in Nanoporous Shale," *International Journal of Coal Geology,* vol. 228, p. 103553, 2020, doi: 10.1016/j.coal.2020.103553.

[55] Y. Hattori, K. Kaneko, and T. Ohba, "Adsorption Properties," in *Comprehensive Inorganic Chemistry Ii (Second Edition)*, J. Reedijk and K. Poeppelmeier Eds. Amsterdam: Elsevier, 2013, ch. 5.02, pp. 25-44.

[56] C. Zheng, H. Song, Y. Xie, X. Yang, L. Lan, K. Kang, and S. Bai, "Modeling of Multi-Temperature Iv and V-Type Water Vapor Adsorption Isotherms on Activated Carbons for Chemical Protection," *Colloids and Surfaces A: Physicochemical and Engineering Aspects,* vol. 670, p. 131486, 2023, doi: 10.1016/j.colsurfa.2023.131486.

[57] J. S. Blázquez, F. J. Romero, C. F. Conde, and A. Conde, "A Review of Different Models Derived from Classical Kolmogorov, Johnson and Mehl, and Avrami (Kjma) Theory to Recover Physical Meaning in Solid-State Transformations," *Physica status solidi (b),* vol. 259, no. 6, p. 2100524, 2022, doi: 10.1002/pssb.202100524.

[58] N. X. Sun, X. D. Liu, and K. Lu, "An Explanation to the Anomalous Avrami Exponent," *Scripta Materialia,* vol. 34, no. 8, pp. 1201-1207, 1996, doi: 10.1016/1359-6462(95)00657-5.

[59] P. Bruna, D. Crespo, R. González-Cinca, and E. Pineda, "On the Validity of Avrami Formalism in Primary Crystallization," *Journal of Applied Physics,* vol. 100, no. 5, 2006, doi: 10.1063/1.2337407.

[60] A. A. Manka, J. Wedekind, D. Ghosh, K. Höhler, J. Wölk, and R. Strey, "Nucleation of Ethanol, Propanol, Butanol, and Pentanol: A Systematic

Experimental Study Along the Homologous Series," *The Journal of Chemical Physics,* vol. 137, no. 5, 2012, doi: 10.1063/1.4739096.

[61] K. H. Nielsen, K. Wondraczek, U. S. Schubert, and L. Wondraczek, "Large-Area Wet-Chemical Deposition of Nanoporous Tungstic Silica Coatings," *Journal of Materials Chemistry C,* 10.1039/C5TC02045J vol. 3, no. 38, pp. 10031-10039, 2015, doi: 10.1039/C5TC02045J.

[62] R. Shi, B. Liu, H. Chen, L. Yu, Y. Guo, Z. Zeng, and L. Li, "Synthesis of Porous Carbon for Acetone Adsorption: Specific Surface Area, Porous Structure and Oxygen Functional Groups," *ChemistrySelect,* vol. 7, no. 7, p. e202103992, 2022, doi: 10.1002/slct.202103992.

[63] C. Cheng, F. Liu, Z. Shao, S. Dou, L. Zhong, and Y. Zheng, "Sago Cycas–Based Hierarchical–Structured Porous Carbon for Adsorption of Acetone Vapour: Preparation, Characterization and Performance," *Environmental Science and Pollution Research,* vol. 29, no. 13, pp. 19165-19175, 2022, doi: 10.1007/s11356-021-17158-2.

[64] X. Ma, T. Qi, R. Chen, R. Su, Z. Zeng, L. Li, and S. Wang, "Experimental and Theoretical Calculations Insight into Acetone Adsorption by Porous Carbon at Different Pressures: Effects of Pore Structure and Oxygen Groups," *Journal of Colloid and Interface Science,* vol. 646, pp. 67-77, 2023, doi: 10.1016/j.jcis.2023.04.156.

[65] J. Gao, L. Li, Z. Zeng, X. Ma, R. Chen, C. Wang, and K. Zhou, "Superior Acetone Uptake of Hierarchically N-Doped Potassium Citrate-Based Porous Carbon Prepared by One-Step Carbonization," *Journal of Materials Science,* vol. 54, no. 8, pp. 6186-6198, 2019, doi: 10.1007/s10853-018-03300-y.

[66] O. O. Oghenetega, P. Fulvio, N. S. Bobbitt, and K. S. Walton, "Single-Component Adsorption Equilibria of Co(2), Ch(4), Water, and Acetone on Tapered Porous Carbon Molecular Sieves," *J Chem Eng Data,* vol. 69, no. 3, pp. 1411-1422, 2024, doi: 10.1021/acs.jced.3c00368.

[67] V. S. Dave, S. Hepburn, and S. W. Hoag, "Physical States and Thermodynamic Principles in Pharmaceutics," in *Pharmaceutics (Second Edition)*, A. K. Dash and S. Singh Eds.: Academic Press, 2024, ch. 2, pp. 23-65.

[68] B. Apicella, X. Li, M. Passaro, and C. Russo, "Insights on Clusters Formation Mechanism by Time of Flight Mass Spectrometry. 2. The Case of Acetone–Water Clusters," *Journal of the American Society for Mass Spectrometry,* vol. 27, no. 11, pp. 1835-1845, 2016, doi: 10.1007/s13361-016-1464-3.

[69] E. A. Müller, L. F. Rull, L. F. Vega, and K. E. Gubbins, "Adsorption of Water on Activated Carbons: A Molecular Simulation Study," *The Journal of Physical Chemistry,* vol. 100, no. 4, pp. 1189-1196, 1996, doi: 10.1021/jp952233w.

[70] A. Tóth and K. László, "Water Adsorption by Carbons. Hydrophobicity and Hydrophilicity," in *Novel Carbon Adsorbents*, J. M. D. Tascón Ed. Oxford: Elsevier, 2012, ch. 5, pp. 147-171.

CHAPTER 6

OPTIMISING THE CONDUCTIVITY OF GRAPHAGE13 AEROGELS

This chapter is based on the previously published paper:

K. Stokes, Y. Sun, J. L. Thomas, P. Passaretti, H. White, and P. Goldberg Oppeneheimer, “Conductivity Optimisation of Graphene Oxide-M13 Bacteriophage Nanocomposites: Towards Graphene-Based Gas Micronano-sensors”, *Discover Nano,* vol. 19, p. 152, 2024, doi: 10.1186/s11671-024-04101-w

Author contributions – **K. Stokes, P. Passaretti** and **Y. Sun** conceptualised the study. **K. Stokes**, **J. L. Thomas** and **Y. Sun** carried out the experimental acquisition and analyses and validated the results. **P. Goldberg Oppenheimer** and **H. White** were responsible for funding acquisition and resources provision. **P. Goldberg Oppenheimer** supervised and administered the study, curated the data and overviewed the developed methodology. **K. Stokes**, **Y. Sun** and **P. Goldberg Oppenheimer** wrote the original draft and reviewed and edited the final draft.

6.1 Abstract

Graphene oxide (GO) and M13 bacteriophage can self-assemble to form ultra-low density porous structures, known as GraPhage13 aerogels (GPA). Due to the insulating nature of GPA and the challenges in producing highly conductive aerogels, it is paramount to explore ways to enhance the conductivity of GPA. Herein, we have developed a method to enhance the conductivity of GPA, via the integration and optimisation of 5 nm and 20 nm diameter gold nanoparticles (AuNPs) into the aerogel structure and systematically analysed the morphology, composition and spectroscopic properties of the resulting GPA-Au nanocomposite.

It was found that the AuNPs formed electronic interactions with GO, enabling their integration within GPA, with the concentration of AuNPs within GPH saturating at 0.59±0.01 mg/mL. The resulting GPA-Au maintained its porous micronano-structure, and a discrete distribution of AuNPs within the optimised GPA-Au was observed with SEM imaging. The insulating nature of GPA was initially confirmed with a typical conductance of 0.34 ± 0.02 nA and conductivity of 6.8 nS/cm. The integration of 20 nm and 5 nm AuNPs into GPA yielded increased conductivities of 190 nS/cm and 360 nS/cm, respectively, well within the range of semiconducting materials for applications including antistatic coatings and electromagnetic interference (EMI) shielding. SEM and Raman spectral analysis revealed that the mechanism behind the enhanced conductivity is due to the formed electronic interactions between GO and AuNPsincreasing the carrier concentration in GPA. The AuNPs interact with the sp^2 domains in GO, lowering the activation energy for electron hopping by introducing localised states near the Fermi level, and reducing the distance between hopping sites. These findings demonstrate the potential of functionalised AuNPs to tune and

significantly improve the electrical properties of GPA, paving the way for their application in EMI shielding and antistatic coatings.

6.2 Introduction

The development of highly conductive graphene-based aerogels is imperative given their immense applied potential for energy storage [1, 2], pressure sensors [3, 4], gas sensors [5, 6], and electromagnetic interference (EMI) shielding [7, 8]. However, achieving high conductivity in these aerogels remains challenging. Their inherently porous nature often results in an amorphous structure with numerous defects, impeding efficient electron transfer within the material [9]. Additionally, for GO-based aerogels, the oxygen-containing functional groups (OCFGs) in GO act as scattering sites, reducing the carrier mobility and leading to a low conductivity [10].

For instance, GraPhage13 aerogels (GPAs) – porous nanocomposites generated through the self-assembly of GO and the filamentous M13 bacteriophage – exhibit insulating properties, with their low conductivity of 0.2 nS/cm falling outside of the range required for semiconductors (10^{-8} – 10^{2} S/cm) [11, 12]. However, through the functionalisation of GO and M13, it is possible to incorporate various nanomaterials into the GPA structure, offering means to modulate the conductivity. Previous studies demonstrated a 30-fold increase in conductance though the incorporation of carbon nanotubes, highlighting the potential of this approach to tune the conductivity of GPAs [11].

In this study, we develop and establish a route to enhance the conductivity of GPA by integrating gold nanoparticles (AuNPs) into its micronano-structure. The interaction between GO, M13 and carboxylic acid functionalised AuNPs with diameters of 5 nm

and 20 nm were investigated with ultraviolet-visible (UV-Vis) spectroscopy and the composition optimised via energy-dispersive X-ray (EDX) spectroscopy. Changes in the morphology and microstructure of the GPAs with integrated 5 nm AuNPs (GPA-Au_{5nm}) and 20 nm AuNPs (GPA-Au_{20nm}) were observed with scanning electron microscopy (SEM) and Raman spectroscopy, and their I-V characteristics were measured to determine if the integration of AuNPs significantly enhances conductivity.

It was determined that the electronic interactions between GO and the carboxylic acid groups on the AuNPs allowed for their incorporation into GPA, with the addition of 20 nm and 5 nm AuNPs increasing the conductivity to 190 nS/cm and 360 nS/cm respectively. These results demonstrate the tuneability of GraPhage13 aerogels, paving the way for the integration of additional nanomaterials to enhance their properties for specific applications. The significant improvement in GPA conductivity achieved through the incorporation of AuNPs underscores the potential of these materials for advanced technologies. By enhancing conductivity while maintaining structural integrity, this study advances the understanding of nanomaterial interactions within aerogels and lays a solid foundation for the development of high-performance, multifunctional materials. The demonstrated improvements in conductivity position GPAs as promising candidates for practical applications such as antistatic coatings [13, 14] and EMI shielding [14, 15], with the scalable, cost-effective, and environmentally-friendly nature of GPA production enhancing its commercial potential [16]. Furthermore, these findings emphasise the potential for further exploration of integrating additional nanomaterials into GPAs to tailor the intrinsic properties such as various types of nanoparticles to achieve even greater conductivity and other functional properties. The overall insights gained from this study provide constructive guidance,

paving the way toward realising the full potential of graphene-based aerogels across a wide range of applications.

6.3 Results and Discussion

6.3.1 Incorporation of Gold Nanoparticles

The interactions between AuNPs and GPAs were investigated via the UV-Vis spectroscopy (Section 2.2.3). In the initial stages of GPA production, GO and M13 are introduced into a buffer, enabling their self-assembly. Following this, centrifugation separates and isolates the components from solution. Through removing 90% of the supernatant and re-suspending the pellet, the GraPhage13 hydrogel (GPH) is generated (Section 2.2.2). However, the supernatant itself provides valuable insights. By combining GO and AuNPs (GO-AuNPs), M13 and AuNPs (M13-AuNPs) and all the components (GPH-AuNPs), followed by centrifugation, supernatant analysis and comparison with the UV-Vis spectra of the individual components within the solution, we determine whether the components interacted or eliminated from the solution or whether they remain unreactive and remain present in solution (Figure 6.1).

The UV-Vis spectra (Figure 6.1a) illustrate the characteristics of the supernatants produced after centrifugation of GO, M13 and GPH, compared to the combined spectra of GO and M13 (GO+M13). In the GO supernatant spectrum, a peak at 230 nm indicates the $\pi \rightarrow \pi^*$ transition of C=C bonds, while a shoulder at 310 nm suggests $n \rightarrow \pi^*$ transitions of C=O bonds [17]. The M13 spectrum exhibits a prominent absorption band between 200-230 nm, attributed to the $\pi \rightarrow \pi^*$ transitions of peptide bonds, with a distinct peak at 269 nm resulting from the major coat protein PVIII and viral DNA [16]. The GPH supernatant spectra resembles the spectrum for GO with a more pronounced

peak at 269 nm due to the presence of the M13. When comparing GPH to GO+M13, the absorption notably decreases, e.g., the peak at 269nm decreases from 1.1 to 0.12. This indicates that the interactions between GO and M13, namely the pH-dependent electrostatic interactions between the negatively charged carboxylic acids on GO and the positively charged groups of the N-terminus and K_8 residues of the M13, produce GO-M13 pellet, which precipitates from solution to produce GPH (Chapter 3).

The UV-Vis spectra of 5 nm and 20 nm AuNPs supernatants (Figure 6.1b) display characteristic peaks around 524 nm and 522 nm, respectively, corresponding to localised surface plasmon resonance. While both AuNPs exhibit similar absorption behaviour, their interaction with M13 is negligible, as indicated by consistent M13 peak absorbance in the presence and absence of AuNPs (Figure 6.1c). Conversely, the combination of GO and AuNPs leads to a significant reduction in AuNP absorption (Figure 6.1d), indicating their interaction and subsequent precipitation [18]. Similarly, AuNPs integrate into GPH, resulting in decreased absorption peaks for both AuNPs and GPH components compared to their individual spectra (Figure 6.1e). This reduction in absorbance upon mixing with GPH signifies the interactions between AuNPs and GO, facilitating their precipitation from the solution. This hybridisation, involving the carboxyl groups on the AuNPs and the oxygen-containing functional groups on GO [19, 20], creates a new composite material where the electronic and structural properties of GO are significantly modified by the presence of AuNPs.

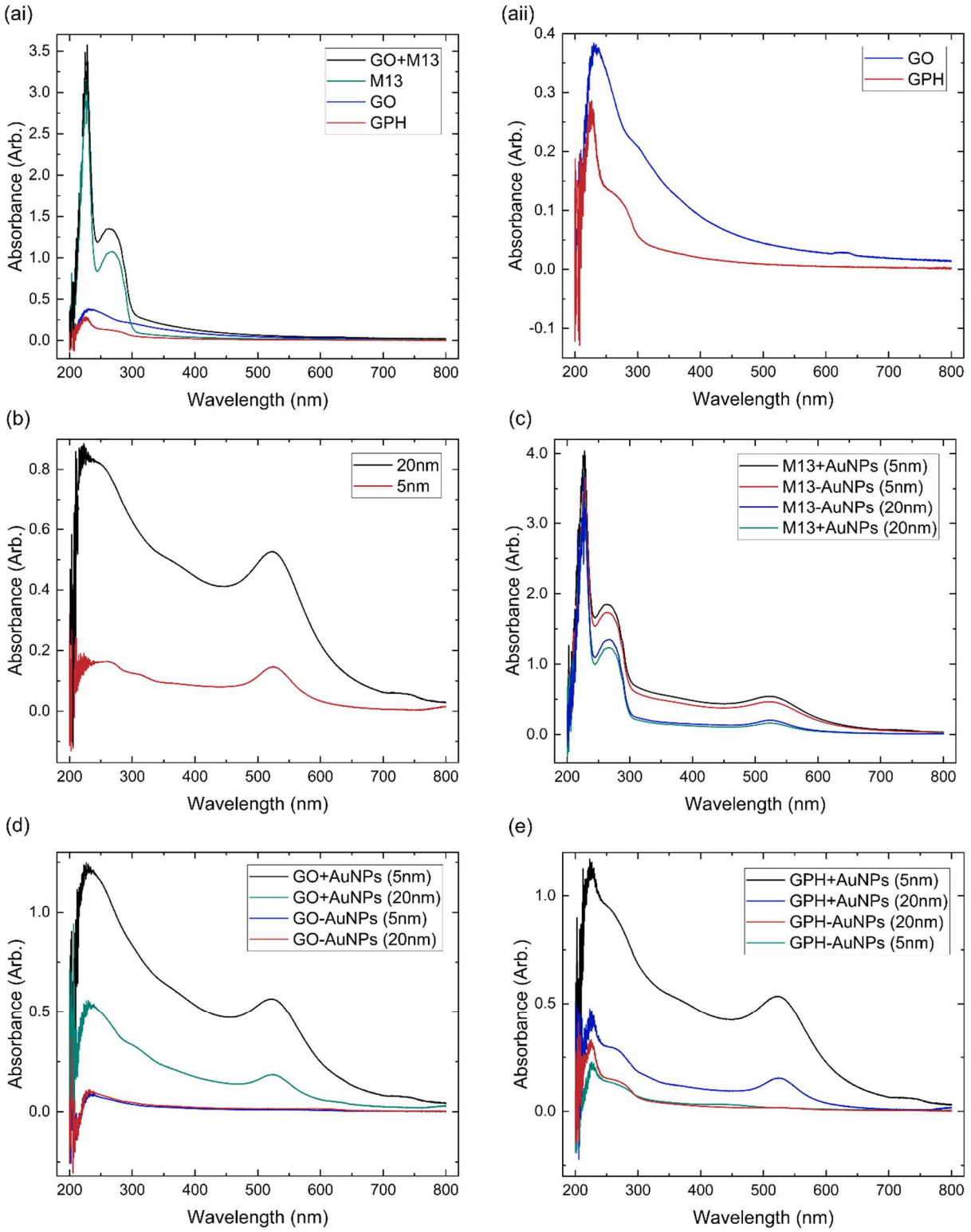

Figure 6.1: UV-Vis spectra of GO, M13, GPH and AuNPs supernatants

UV-Vis spectra of the supernatants generated from mixtures of graphene oxide (GO), M13 bacteriophage and carboxylic acid functionalised gold nanoparticles (AuNPs) with diameters of 5 nm and 20 nm. The spectrum of GO, M13 and GPH supernatants in comparison to the addition of the GO

and M13 spectra, are shown in **(ai)** with **(aii)** zoom-in on the features of the GO and GPH spectra. **(b)**, The supernatants produced by centrifuging 5 nm and 20 nm AuNPs**. (c)** Comparison of the addition of M13 and Au supernatants (M13+AuNPs) after mixing M13 and Au (M13-AuNPs) with 5 nm and 20 nm AuNPs. **(d)** The supernatants from the addition and mixtures of graphene oxide (GO) with 5 nm and 20 nm AuNPs and **(e)** the UV-Vis spectrum of mixing GraPhage13 hydrogel (GPH) and 20 nm and 5 nm AuNPs.

6.3.2 Optimisation of GPA-Au

To determine the optimal concentration of the 5 nm and 20 nm AuNPs for integration into GPA, GPH-Au with varying concentrations of AuNPs were synthesised and the resulting GPA-Au analysed using energy dispersive x-ray spectroscopy (EDX) (Section 2.2.4). The weight percentage of gold incorporated into GPA, in comparison to overall weight of GPA, was studied across different AuNP concentrations (Figure 6.2a).

As the concentration of AuNPs increases, the wt% Au also increases until reaching a plateau, indicating saturation of GPH and no further increase in AuNP concentration within GPA. For GPA-Au_{20nm}, saturation occurs at approximately 0.61 mg/mL, resulting in 50 ± 2 wt% Au, while for GPA-Au_{5nm}, saturation occurs at approximately 0.58 mg/mL, yielding 56 ± 1 wt% Au. The higher maximum wt% Au for GPA-Au_{5nm} compared to GPA-Au_{20nm} may be attributed to the larger size of 20 nm AuNPs blocking some of the binding sites on GO, resulting in lower Au content. Additionally, the smaller 5 nm AuNPs may integrate more effectively within the micro-nanostructure. A representative spectrum of optimised GPA-Au is shown in Figure 6.2b, with SEM images of resulting GPA-Au in Figure 6.3, where the presence of 20 nm AuNPs is clearly visible (Figure 6.3e-f).

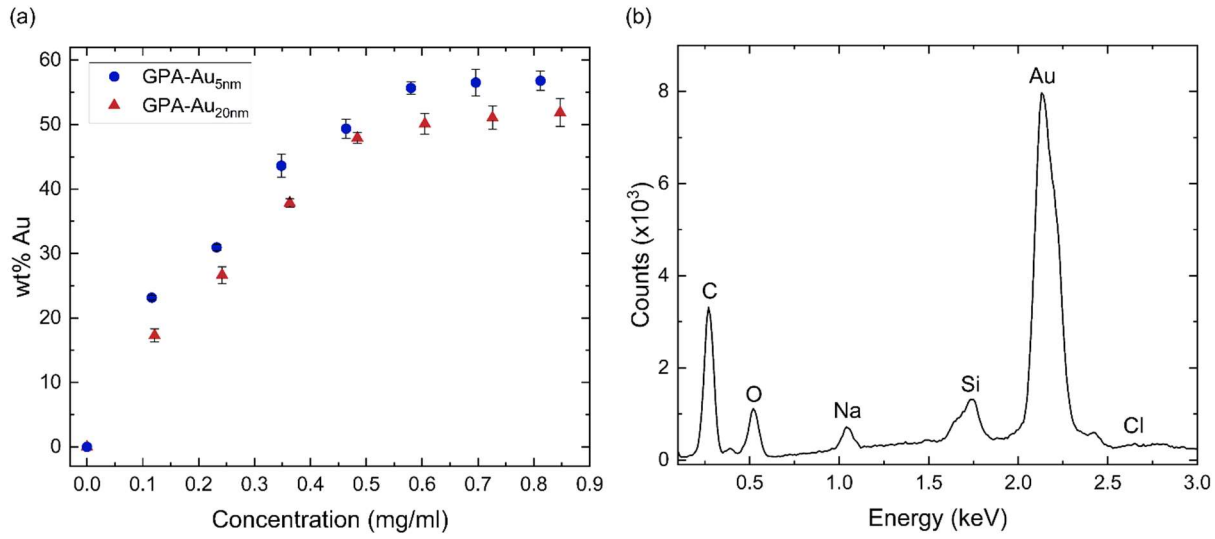

Figure 6.2: Composition of GPA-Au

(a) The relationship between the concentration of gold nanoparticle (AuNPs) solution utilised to produce the GraPhage13 hydrogel (GPH), subsequently dried to form the GraPhage13 aerogel (GPA) and the resulting weight percentage of Au in the aerogel containing AuNPs with diameters of 5nm (GPA-Au_{5nm}) and 20nm (GPA-Au_{20nm}). The data points represent the mean wt % of Au across three GPAs fabricated with each given concentration of Au, and the error bars represent the standard error on the mean **(b)** Representative EDX spectrum of GPA-Au.

6.3.3 In-Depth Raman Spectroscopy

From our previous Raman analyses of GPA, detailed in Section 4.3.3, at least two distinctive peaks were expected. These are the D-mode, which has contributions from both defective sp^2 carbon, and sp^3 amorphous or disordered carbon, and the G-mode, stemming from the sp^2 bond stretching. Other peaks which may be present for GPA are the G^- and D' modes, arising from the functionalisation of the sp^2 bonds in GO.

Herein, Raman spectroscopy (Section 2.2.8) was conducted on GPA, GPA-Au_{5nm} and GPA-Au_{20nm} using excitation wavelengths of 514 nm and 633 nm (Figure 6.4). The purpose of using two lasers was to identify whether the observed Raman features in

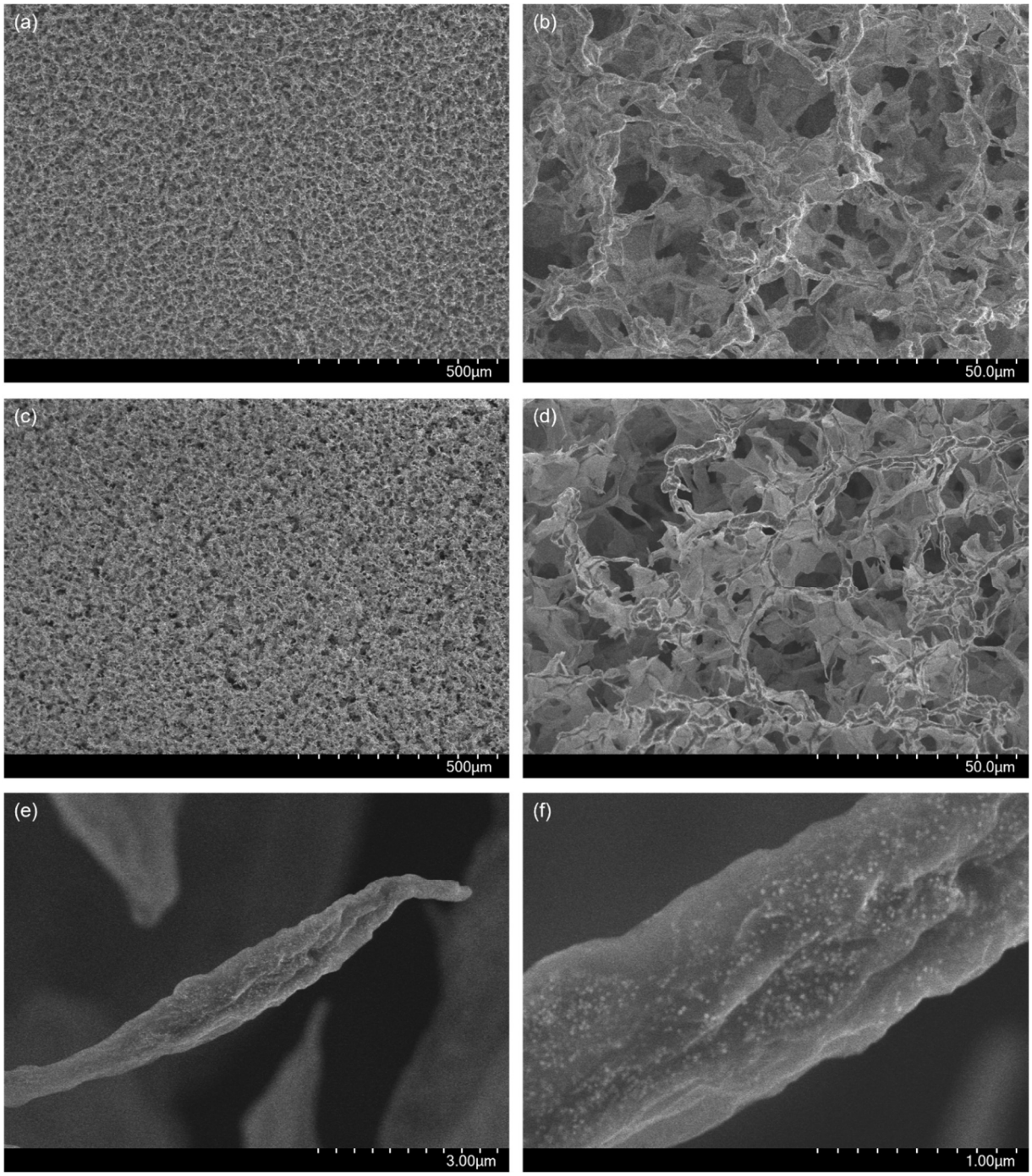

Figure 6.3: SEM images of GPA-Au

SEM images of GraPhage13 aerogels functionalised with **(a-b)** 5 nm AuNPs and **(c-f)** 20 nm AuNPs.

the D mode range originated from the D mode associated with C-C sp^2 bonds or the sp^3 Raman mode, as the D mode frequency shifts with laser excitation, whereas a sp^3 Raman peak is non-dispersive peak [21-23]. The Bayesian information criterion (BIC)

was utilised to determine the optimal objective models for fitting each spectrum (for further details on peak fitting and BIC, please see Section 2.3.2 and 2.3.3) [11].

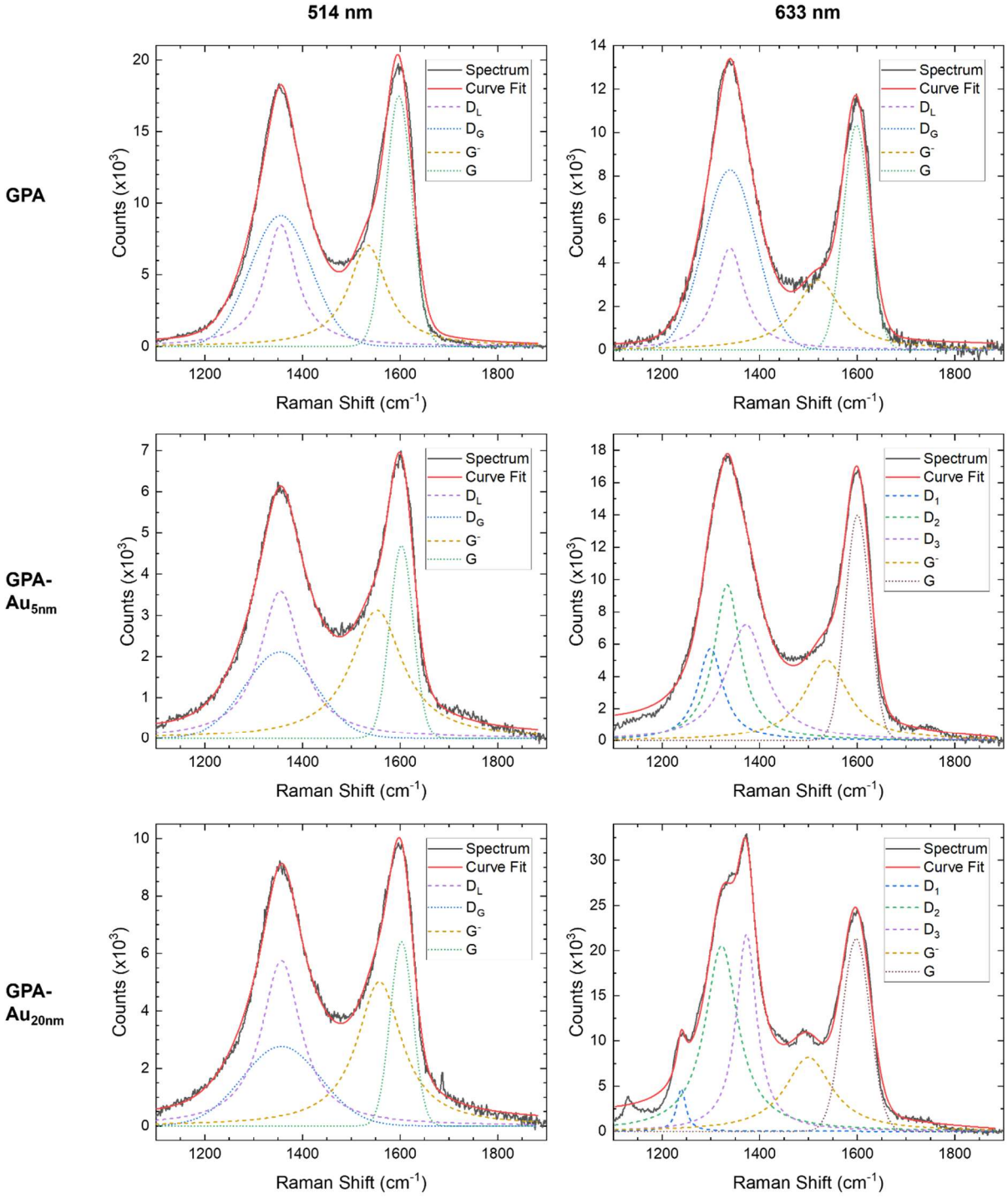

Figure 6.4: Raman spectra of GPA, GPA-Au_{5nm} and GPA-Au_{20nm}

Raman spectra of GPA, GPA-Au_{5nm} and GPA-Au_{20nm} at wavelengths of 514nm and 633nm, with the overall curve fit. The Lorentzian and Gaussian fits are given by dashed and dotted lines, respectively.

Under 514 nm excitation, the D features of all three samples consist of a single peak at 1355 cm^{-1} (Table 6.1), despite changes in peak shape and frequency shifts. This peak is approximately 20 cm^{-1} higher than the sp^3 peak, with its expected Raman shift of 1332 cm^{-1}, hence attributed to the D mode. The optimal peak fit for the D-mode was generated by fitting one Lorentzian and one Gaussian peak, termed D_L and D_G respectively, at the same Raman shift of 1355 cm^{-1}, generating a mixed Gaussian-Lorentzian line-shape [24, 25].

Table 6.1: 514nm Raman peaks for GPA, GPA-Au_{5nm} and GPA-Au_{20nm}

Raman shift, full width half maximum (FWHM) and intensity of the Raman peaks present in spectra of GPA, GPA-Au_{5nm} and GPA-Au_{20nm}, obtained at a wavelength of 514nm.

Peak	GPA			GPA-Au_{5nm}			GPA-Au_{20nm}		
	Raman Shift (cm^{-1})	FWHM (cm^{-1})	Intensity (cm^{-1})	Raman Shift (cm^{-1})	FWHM (cm^{-1})	Intensity (cm^{-1})	Raman Shift (cm^{-1})	FWHM (cm^{-1})	Intensity (cm^{-1})
D_L	1356.5±0.4	39±2	(1.1±0.1) x 10^6	1354.6±0.3	50±2	(7.0±0.4) x 10^5	1355.7±0.3	48±2	(9.3±0.6) x 10^5
D_G		62±1	(9.6±0.6) x 10^3		74±1	(2.9±0.2) x 10^3		73±2	(3.3±0.2) x 10^3
G^-	1539±3	44±3	(1.1±0.1) x 10^6	1553±4	62±3	(8.2±0.8) x 10^5	1550±2	53±1	(8.2±0.2) x 10^5
G	1598.3±0.6	26.3±0.5	(1.84±0.03) x 10^3	1602.4±0.5	24.1±0.5	(6.3±0.2) x 10^3	1601.6±0.4	24.5±0.4	(8.2±0.1) x 10^3

Under 633 nm excitation, GPA also exhibits a single D peak similar to that observed under 514 nm, however its position downshifts to 1338.7 cm^{-1} (Table 6.2). The D mode is activated by a defect-induced double resonance process, involving the energy of the LO phonon at the K point in the Brillouin zone. The presence of a Kohn anomaly at the K point causes the highly dispersive nature of the D peak [26]. The splitting of the D

profile into three peaks, D_{1-3}, is clearly visible for GPA-Au_{20nm} under 633 nm and becomes evident for GPA-Au_{5nm} through comparing BIC values. This split appears following the introduction of AuNPs and is more pronounced with 20 nm AuNPs.

Table 6.2: 633nm Raman peaks for GPA, GPA-Au_{5nm} and GPA-Au_{20nm}

Raman shift, full width half maximum (FWHM) and intensity of the Raman peaks for GPA, GPA-Au_{5nm} and GPA-Au_{20nm}, obtained at a wavelength of 633 nm.

Peak	GPA			Peak	GPA-Au_{5nm}			GPA-Au_{20nm}		
	Raman Shift (cm^{-1})	FWHM (cm^{-1})	Intensity (cm^{-1})		Raman Shift (cm^{-1})	FWHM (cm^{-1})	Intensity (cm^{-1})	Raman Shift (cm^{-1})	FWHM (cm^{-1})	Intensity (cm^{-1})
D_L	1338.7±0.5	38±2	(7±1) x 10^5	D_1	1229±4	32±4	(6.4±0.4) x 10^5	1239.5±0.8	11±1	(1.9±0.3) x 10^5
D_G		53.7±0.8	(1.1±0.1) x 10^4	D_2	1335±2	33±8	(1.1±0.6) x 10^6	1321±1	40±1	(3.0±0.2) x 10^6
-	-	-	-	D_3	1374±8	50±4	(1.1±0.4) x 10^5	1372.5±0.5	26.6±0.9	(2.1±0.1) x 10^6
G^-	1522±3	64±4	(9.6±0.8) x 10^6	G^-	1537±4	53±5	(9±1) x 10^5	1501±2	58±3	(1.8±0.1) x 10^6
G	1598.3±0.3	27.0±0.4	(1.4±0.2) x 10^4	G	1600.5±0.5	25.1±0.4	(1.52±0.03) x 10^4	1597.3±0.3	28.6±0.4	(2.44±0.03) x 10^4

Meanwhile, this split does not appear under 514 nm. These observations indicate that the split peaks are likely modified D peaks, becoming visible due to being in resonance under 633 nm. The integration of AuNPs into GPA modifies the sp^2-network, altering the phonon dispersion curve, particularly the LO branches. This results in a significant shift in the G^- mode (LO at the Gamma point) and an obvious splitting of the D mode (LO at the K point), as captured by the 633 nm laser. The modification of the dispersion

curve, indicative of perturbations to the sp^2 network of GPA, is more substantial with 20 nm AuNPs than with 5 nm AuNPs [27, 28].

Additionally, the 633 nm Raman spectrum of GPA-Au_{20nm} shows the highest peak intensities, with a maximum intensity of (3.7 ± 0.2) x 10^4 counts, in comparison to (1.9 ± 0.1) x 10^4 counts for GPA-Au_{5nm}. This might be attributed to the localised surface plasmon resonance (LSPR) exhibited by AuNPs. When electromagnetic radiation interacts with the conduction electrons on the surface of the AuNPs, it causes the electrons to oscillate at the same frequency as the incident light. At the resonant frequency, this results in an amplified local electromagnetic field, leading to an increased Raman signal [29]. For AuNPs with diameters smaller than 50 nm, collisions between the electrons and the particle surface decreases their mean free path. This dampens the LSPR proportionally to the particle diameter, thereby reducing the Raman intensity [30].

To gain further insight into Raman spectra, the intensity ratio of D to G peaks (I_D/I_G) was calculated (Table 6.3), to give a measure of the concentration of defects and disorder within a sample [31]. At the 633 nm laser excitation, the integration of AuNPs into GPA increases I_D/I_G due to an increase in the intensity of the D-profile, as many modified D modes become resonant. This D-profile splitting indicates that the AuNPs introduce defects into the structure, likely resulting from interactions between GPA and the AuNPs [32, 33]. Furthermore, I_D/I_G appears to be independent of the diameter of the AuNPs. This may be attributable to the GPA-Au composites being produced using the same fabrication process, ensuring similar chemical and structural properties. Additionally, the defects are intrinsic to the GPA structure and the interactions between GO and the carboxylic groups on the AuNPs, making them independent of the AuNP

diameter. Moreover, the increase in I_D/I_G through the integration of AuNPs suggests an increase in the electrical conductivity [34]. These trends are not observed at the 514 nm laser excitation. There is little change in I_D/I_G between GPA and GPA-Au_{5nm}, and only a slight increase for GPA-Au_{20nm}. The 514 nm laser is not able to induce resonance in the modified D modes and therefore, structural changes to GPA due to the presence of AuNPs are less detectable [27].

Table 6.3: I_D/I_G for Raman spectra of GPA, GPA-Au_{5nm} and GPA-Au_{20nm}

The intensity ratio of D-peak to G-peak (I_D/I_G) of Raman peaks for GPA, GPA-Au_{5nm} and GPA-Au_{20nm}, at wavelengths of 514 nm and 633 nm.

Parameter	GPA		GPA-Au_{5nm}		GPA-Au_{20nm}	
	514nm	633nm	514nm	633nm	514nm	633nm
I_D/I_G	0.91±0.08	0.81±0.08	0.86±0.07	3.1±0.6	1.15±0.05	2.9±0.1

6.3.4 Conductivity of GPA and GPA-Au

The conductivity of GPA, compared to GPA-Au_{5nm} and GPA-Au_{20nm}, generated with the saturation concentration of AuNPs (0.58 mg/mL for GPA-Au_{5nm} and 0.61 mg/mL for GPA-Au_{20nm}), was measured as detailed in Section 2.2.10. Three of each aerogel were fabricated and their I-V characteristics were recorded. The mean current at each voltage, and the standard error on the mean, is shown in Figure 6.5. The small error bars in these measurements demonstrate the consistency in fabricating GPAs with reproducible conductivities, underscoring its potential for scalable commercial manufacture.

The I-V characteristic of GPA (Figure 6.5a) aligns closely with previous findings [11] and confirms the insulating nature of GPA, with a maximum current of 3.4±0.2 nA at 10 V. This leads to a conductance of 0.34 nS and a conductivity of 6.8 nS/cm, two orders of magnitude below the minimum conductivity for semiconducting materials for antistatic coatings and EMI shielding. GPA-Au_{20nm} (Figure 6.5b) exhibits a significantly enhanced conductivity, reaching 90±8 nA at 10 V, marking a 26-fold increase over GPA and generating a conductivity of 190 nS/cm, achieving a value within the range for semiconducting materials in these applications. The conductivity was enhanced further through the integration of 5 nm AuNPs, with GPA-Au_{5nm} demonstrating a current of 180±4 nA at a bias of 10 V, twice that of GPA-Au_{20nm} and representing a 53-fold increase compared to GPA. This is equivalent to a conductance of 18 nS and a conductivity of 360 nS/cm, representing a significant step towards use of GPA in EMI shielding and antistatic coatings.

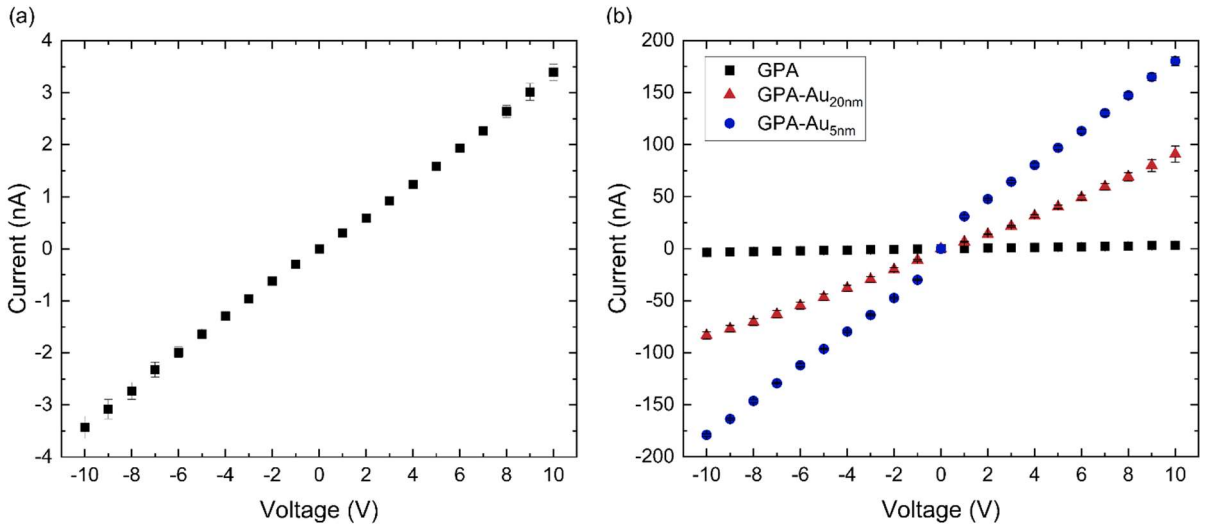

Figure 6.5: Conductivity of GPA, GPA-Au_{20nm} and GPA-Au_{5nm}

(a) I-V characteristic of GPA and **(b)** comparison of the I-V characteristics of GPA, GPA-Au_{20nm} and GPA-Au_{5nm}. GPA-Au_{5nm} and GPA-Au_{20nm} were generated with the saturation concentration of AuNPs (0.58 mg/mL for GPA-Au_{5nm} and 0.61 mg/mL for GPA-Au_{20nm}

There are two mechanisms by which the AuNPs interacting with GO-M13 could enhance the conductivity of the resulting GPA, either by increasing the carrier density or by increasing the carrier mobility [35]. The presence of scattering at functional sites within GO significantly reduces its carrier mobility. Reducing GO to reduced graphene oxide eliminates some of the functional groups and aids in the dispersion of the free carriers, increasing their mobility [10]. This would be evident in Raman spectra via a redshift in the G-mode position as the concentration of sp^2 bonds increases and a reduction in I_D/I_G resulting from a reduced level of defects [36]. Similarly, the bonding of the AuNPs to GO would reduce the concentration of available functional groups and therefore the G-mode position and I_D/I_G would be expected to decrease. Conversely, a significant increase in I_D/I_G is observed and the G-mode remains relatively constant when comparing GPA to GPA-Au_{5nm} and GPA-Au_{20nm}. Therefore, an increase in the carrier density is most probable mechanism behind the conductivity enhancement.

The electrical properties of GO are governed by variable range hopping, a mechanism in which electrons move between localised conductive sp^2 regions separated by sp^3 domains. The disorder in GO, caused by its OCFGS, disrupts the delocalised π-electron network, isolating the conductive regions and creating a mobility gap. This hopping-based transport is influenced by factors such as the density of localised states, the distance between hopping sites, and the activation energy required for hopping [37, 38]. The AuNPs introduced into GPA interact with the sp^2 domains in GO, altering the local electronic environment. These interactions reduce the activation energy for electron hopping by introducing new localised states near the Fermi level, effectively enhancing carrier concentration. The AuNPs can also provide additional pathways for conduction by reducing the spatial separation between hopping sites [39].

Smaller AuNPs possess a higher surface-to-volume ratio, which increases the available surface area for interaction with GO, leading to a more stable dispersion of the AuNPs within the solution. This stable dispersion promotes a higher density of GO-Au interactions, which is essential for enhancing the carrier density through the previously discussed mechanism, thereby improving the conductivity. Consequently, GPA-Au_{5nm} exhibits a higher conductivity compared to GPA-Au_{20nm} [40, 41].

Given the mechanism by which AuNPs enhance the conductivity of GPA, a positive correlation between the amount of AuNPs incorporated into GPA and the resulting conductivity is expected. The conductivity improvement depicted in Figure 6.5 corresponds to the maximum saturation of Au wt% in GPA. This implies that increasing the AuNP loading beyond this saturation point will not result in further conductivity gains. Conversely, reducing the AuNP load decreases the Au wt% in GPA, thereby diminishing the conductivity enhancement. If the AuNP load is sufficiently reduced, the GPA will eventually return to its insulating state in the absence of AuNPs.

6.4 Conclusion

A novel method has been developed and validated for transforming insulating graphene oxide-based aerogels into semiconducting materials suitable for EMI shielding and antistatic coatings. This advancement paves the way for future integration into electronic systems and the development of advanced graphene-based sensors. The integration of 5 nm and 20 nm diameter carboxylic acid-functionalised gold nanoparticles (AuNPs) into GraPhage13 aerogels (GPA) was systematically investigated using UV-Vis spectroscopy and EDX. UV-Vis spectra revealed interactions between graphene oxide (GO) and AuNPs, facilitating their integration into

the GraPhage13 hydrogel (GPH), the precursor for GPA. EDX measurements determined the saturation concentration of AuNPs within GPH. The optimal GPA-Au with the maximum concentration of AuNPs was further analysed using SEM, Raman spectroscopy, and conductivity measurements. SEM analysis confirmed the integration of AuNPs into the GPA micro-nanostructure, with Raman spectra showing distinct changes in the D-mode and G-mode due to the presence of AuNPs. These changes were more pronounced in GPA-Au_{20nm} compared to GPA-Au_{5nm}, indicating that AuNPs modify the sp^2 carbon network and phonon dispersion in GO. Conductivity measurements revealed a significant increase in GPA conductivity, transitioning from an insulator with a conductivity of 6.8 nS/cm to 190 nS/cm and 360 nS/cm for GPA-Au_{20nm} and GPA-Au_{5nm}, respectively. This study highlights the potential to tune GPA properties through nanoparticle integration, offering possibilities for further customisation with various nanomaterials and modifications of M13 viral building blocks. The significant enhancement of GPA conductivity through AuNP integration makes it a promising candidate for integration into miniaturised devices for applications such as antistatic coatings and EMI shielding.

6.5 Materials and Methods

Further information on graphene oxide and M13 bacteriophage used in these experiments can found in Sections 2.1.1 and 2.1.2, respectively.

For detailed descriptions of the methods used in this chapter, please refer to Chapter 2, specifically the following sections:

- 2.2.2 Fabrication of GraPhage13 Aerogels (GPA)

- 2.2.4 Scanning Electron Microscopy (SEM) and Energy Dispersive X-Ray Spectroscopy (EDX)
- 2.2.8 Raman Spectroscopy
- 2.2.10 Electrical Conductivity
- 2.3.2 Bayesian Information Criterion (BIC)
- 2.3.3 Peak Fitting

6.6 References

[1] J. Orangi, H. Tetik, P. Parandoush, E. Kayali, D. Lin, and M. Beidaghi, "Conductive and Highly Compressible Mxene Aerogels with Ordered Microstructures as High-Capacity Electrodes for Li-Ion Capacitors," *Materials Today Advances,* vol. 9, p. 100135, 2021, doi: 10.1016/j.mtadv.2021.100135.

[2] Y. B. Pottathara, H. R. Tiyyagura, Z. Ahmad, and K. K. Sadasivuni, "Graphene Based Aerogels: Fundamentals and Applications as Supercapacitors," *Journal of Energy Storage,* vol. 30, p. 101549, 2020, doi: 10.1016/j.est.2020.101549.

[3] S. Wei, X. Qiu, J. An, Z. Chen, and X. Zhang, "Highly Sensitive, Flexible, Green Synthesized Graphene/Biomass Aerogels for Pressure Sensing Application," *Composites Science and Technology,* vol. 207, p. 108730, 2021, doi: 10.1016/j.compscitech.2021.108730.

[4] C. Long, X. Xie, J. Fu, Q. Wang, H. Guo, W. Zeng, N. Wei, S. Wang, and Y. Xiong, "Supercapacitive Brophene-Graphene Aerogel as Elastic-Electrochemical Dielectric Layer for Sensitive Pressure Sensors," *Journal of Colloid and Interface Science,* vol. 601, pp. 355-364, 2021, doi: 10.1016/j.jcis.2021.05.116.

[5] A. Bibi, C.-Y. Chen, K.-N. Huang, N. Sathishkumar, H.-T. Chen, Y.-F. Lin, J.-M. Yeh, and K. S. Santiago, "Comparative Study on the H2s Gas-Sensing Properties of Graphene Aerogels Synthesized through Hydrothermal and Chemical Reduction," *Journal of the Taiwan Institute of Chemical Engineers,* vol. 154, p. 105155, 2024, doi: 10.1016/j.jtice.2023.105155.

[6] Q. Li, D. Chen, J. Miao, S. Lin, Z. Yu, Y. Han, Z. Yang, X. Zhi, D. Cui, and Z. An, "Ag-Modified 3d Reduced Graphene Oxide Aerogel-Based Sensor with an Embedded Microheater for a Fast Response and High-Sensitive Detection of No2," *ACS Applied Materials & Interfaces,* vol. 12, no. 22, pp. 25243-25252, 2020, doi: 10.1021/acsami.9b22098.

[7] Z. Cheng, R. Wang, Y. Wang, Y. Cao, Y. Shen, Y. Huang, and Y. Chen, "Recent Advances in Graphene Aerogels as Absorption-Dominated Electromagnetic Interference Shielding Materials," *Carbon,* vol. 205, pp. 112-137, 2023, doi: 10.1016/j.carbon.2023.01.032.

[8] S. Singh, P. Tripathi, A. Bhatnagar, C. R. Prakash Patel, A. P. Singh, S. K. Dhawan, B. K. Gupta, and O. N. Srivastava, "A Highly Porous, Light Weight 3d

Sponge Like Graphene Aerogel for Electromagnetic Interference Shielding Applications," *RSC Advances,* 10.1039/C5RA19273K vol. 5, no. 129, pp. 107083-107087, 2015, doi: 10.1039/C5RA19273K.

[9] L. dos Santos-Gómez, J. R. García, M. A. Montes-Morán, J. A. Menéndez, S. García-Granda, and A. Arenillas, "Ultralight-Weight Graphene Aerogels with Extremely High Electrical Conductivity," *Small,* vol. 17, no. 41, p. 2103407, 2021, doi: 10.1002/smll.202103407.

[10] S. Gupta, P. Joshi, and J. Narayan, "Electron Mobility Modulation in Graphene Oxide by Controlling Carbon Melt Lifetime," *Carbon,* vol. 170, pp. 327-337, 2020, doi: 10.1016/j.carbon.2020.07.073.

[11] Y. Sun, P. Passaretti, I. Hernandez, J. Gonzalez, W. Liu, F. Rodriguez, D. J. Dunstan, P. Goldberg Oppenheimer, and C. J. Humphreys, "Nanomechanics of Graphene Oxide-Bacteriophage Based Self-Assembled Porous Composites," *Scientific Reports,* vol. 10, no. 1, p. 15618, 2020, doi: 10.1038/s41598-020-72372-1.

[12] S. M. Sharaf, "Smart Conductive Textile," in *Advances in Functional and Protective Textiles*, S. ul-Islam and B. S. Butola Eds.: Woodhead Publishing, 2020, ch. 7, pp. 141-167.

[13] W. Fei, J. Cui, Y. Sun, J. Yang, S. Gao, and J. Li, "Anti-Corrosion and Electrically Conductive Inorganic Conversion Coatings Based on Aligned Graphene Derivatives by Electrodeposition," *Nano Materials Science,* vol. 4, no. 3, pp. 244-250, 2022, doi: 10.1016/j.nanoms.2021.07.011.

[14] H. D. Shetty, G. V. Ashok Reddy, V. Ramasamy, C. S. Kaliprasad, B. Daruka Prasad, H. S. Yogananda, R. Naik, V. Prasad, G. Koyyada, and Y. Anil Kumar, "Electrical Conductivity and Electromagnetic Interference Shielding Effectiveness of Elastomer Composites: Comparative Study with Various Filler Systems," *Inorganic Chemistry Communications,* vol. 151, p. 110578, 2023, doi: 10.1016/j.inoche.2023.110578.

[15] W. Ghafoor, M. Ahmad, M. Raffi, and S. U. Awan, "Role of Electrical Conductivity in the Shielding Effectiveness of Composite Polyvinyl Alcohol/Multiwall Carbon Nanotube Nanofibers for Electromagnetic Interference Applications," *ACS Omega,* vol. 9, no. 3, pp. 3070-3077, 2024, doi: 10.1021/acsomega.3c04120.

[16] P. Passaretti, Y. Sun, I. Khan, K. Chan, R. Sabo, H. White, T. R. Dafforn, and P. G. Oppenheimer, "Multifunctional Graphene Oxide-Bacteriophage Based Porous Three-Dimensional Micro-Nanocomposites," *Nanoscale,* 10.1039/C9NR03670A vol. 11, no. 28, pp. 13318-13329, 2019, doi: 10.1039/C9NR03670A.

[17] R. Mittal, A. Kumar, and S. K. Awasthi, "Practical Scale up Synthesis of Carboxylic Acids and Their Bioisosteres 5-Substituted-1h-Tetrazoles Catalyzed by a Graphene Oxide-Based Solid Acid Carbocatalyst," *RSC Advances,* 10.1039/D1RA01053K vol. 11, no. 19, pp. 11166-11176, 2021, doi: 10.1039/D1RA01053K.

[18] X. Xia, S. Guo, W. Zhao, P. Xu, H. Yu, T. Xu, and X. Li, "Carboxyl Functionalized Gold Nanoparticles in Situ Grown on Reduced Graphene Oxide for Micro-Gravimetric Ammonia Sensing," *Sensors and Actuators B: Chemical,* vol. 202, pp. 846-853, 2014, doi: 10.1016/j.snb.2014.06.029.

[19] Q. Gou, X. Cai, Z. Yan, Y. Gao, J. Tang, W. Xiao, and J. Cai, "Highly Selective Pb(Ii) Adsorption by Dtpa-Functionalized Graphene Oxide/Carboxymethyl Cellulose Aerogel," *Langmuir,* vol. 40, no. 15, pp. 8002-8014, 2024, doi: 10.1021/acs.langmuir.3c03954.

[20] H. Pan, S. Low, N. Weerasuriya, B. Wang, and Y.-S. Shon, "Morphological Transformation of Gold Nanoparticles on Graphene Oxide: Effects of Capping Ligands and Surface Interactions," *Nano Convergence,* vol. 6, no. 1, p. 2, 2019, doi: 10.1186/s40580-018-0171-0.

[21] A. C. Ferrari, "Raman Spectroscopy of Graphene and Graphite: Disorder, Electron–Phonon Coupling, Doping and Nonadiabatic Effects," *Solid State Communications,* vol. 143, no. 1, pp. 47-57, 2007, doi: 10.1016/j.ssc.2007.03.052.

[22] C. Pardanaud, G. Cartry, L. Lajaunie, R. Arenal, and J. G. Buijnsters, "Investigating the Possible Origin of Raman Bands in Defective Sp2/Sp3 Carbons Below 900 Cm−1: Phonon Density of States or Double Resonance Mechanism at Play?," *C,* vol. 5, no. 4, p. 79, 2019, doi: 10.3390/c5040079.

[23] A. C. Ferrari, J. Robertson, A. C. Ferrari, and J. Robertson, "Raman Spectroscopy of Amorphous, Nanostructured, Diamond–Like Carbon, and Nanodiamond," *Philosophical Transactions of the Royal Society of London. Series A: Mathematical, Physical and Engineering Sciences,* vol. 362, no. 1824, pp. 2477-2512, 2004, doi: 10.1098/rsta.2004.1452.

[24] A. Tagliaferro, M. Rovere, E. Padovano, M. Bartoli, and M. Giorcelli, "Introducing the Novel Mixed Gaussian-Lorentzian Lineshape in the Analysis of the Raman Signal of Biochar," *Nanomaterials,* vol. 10, no. 9, p. 1748, 2020, doi: 10.3390/nano10091748.

[25] A. C. Ferrari and J. Robertson, "Interpretation of Raman Spectra of Disordered and Amorphous Carbon," *Physical Review B,* vol. 61, no. 20, pp. 14095-14107, 2000, doi: 10.1103/PhysRevB.61.14095.

[26] A. C. Ferrari and D. M. Basko, "Raman Spectroscopy as a Versatile Tool for Studying the Properties of Graphene," *Nat Nanotechnol,* vol. 8, no. 4, pp. 235-46, 2013, doi: 10.1038/nnano.2013.46.

[27] J.-B. Wu, M.-L. Lin, X. Cong, H.-N. Liu, and P.-H. Tan, "Raman Spectroscopy of Graphene-Based Materials and Its Applications in Related Devices," *Chemical Society Reviews,* 10.1039/C6CS00915H vol. 47, no. 5, pp. 1822-1873, 2018, doi: 10.1039/C6CS00915H.

[28] R. Kar and N. Maiti, "Observation of D Band Splitting in Vertically Aligned Graphene Nanowalls and Their Evolution with Laser Power During Raman Spectroscopy," *Journal of Nanoparticle Research,* vol. 23, no. 1, p. 4, 2021, doi: 10.1007/s11051-021-05147-y.

[29] J. H. Lee, H. Y. Cho, H. K. Choi, J. Y. Lee, and J. W. Choi, "Application of Gold Nanoparticle to Plasmonic Biosensors," *Int J Mol Sci,* vol. 19, no. 7, 2018, doi: 10.3390/ijms19072021.

[30] S. Link and M. A. El-Sayed, "Size and Temperature Dependence of the Plasmon Absorption of Colloidal Gold Nanoparticles," *The Journal of Physical Chemistry B,* vol. 103, no. 21, pp. 4212-4217, 1999, doi: 10.1021/jp984796o.

[31] T. Palaniselvam, H. B. Aiyappa, and S. Kurungot, "An Efficient Oxygen Reduction Electrocatalyst from Graphene by Simultaneously Generating Pores and Nitrogen Doped Active Sites," *Journal of Materials Chemistry,*

10.1039/C2JM35128E vol. 22, no. 45, pp. 23799-23805, 2012, doi: 10.1039/C2JM35128E.

[32] L. E. G. Armas, V. M. Zamarion, L. T. Quispe, E. P. U. Otero, J. W. Menezes, L. B. R. Zegarra, A. Rahim, K. Araki, H. E. Toma, C. Jacinto, C. Valsechi, and A. C. Seabra, "Effect of Gold Nanoparticles and Unwanted Residues on Raman Spectra of Graphene Sheets," *Brazilian Journal of Physics,* vol. 48, no. 5, pp. 477-484, 2018, doi: 10.1007/s13538-018-0596-2.

[33] P. Nancy, A. K. Nair, R. Antoine, S. Thomas, and N. Kalarikkal, "In Situ Decoration of Gold Nanoparticles on Graphene Oxide Via Nanosecond Laser Ablation for Remarkable Chemical Sensing and Catalysis," *Nanomaterials,* vol. 9, no. 9, p. 1201, 2019, doi: 10.3390/nano9091201.

[34] V. Balaji Mohan, Stamm, M. Debes Bhattacharyya, D. Liu, and K. Jayaraman, "Improvements in Electronic Structure and Properties of Graphene Derivatives," *Advanced Materials Letters,* vol. 7, no. 6, pp. 421-429, 2016, doi: 10.5185/amlett.2016.6123.

[35] X. Wang, X. Zhang, L. Sun, D. Lee, S. Lee, M. Wang, J. Zhao, Y. Shao-Horn, M. Dincă, T. Palacios, and K. K. Gleason, "High Electrical Conductivity and Carrier Mobility in Ocvd Pedot Thin Films by Engineered Crystallization and Acid Treatment," *Sci Adv,* vol. 4, no. 9, p. eaat5780, 2018, doi: 10.1126/sciadv.aat5780.

[36] S. Perumbilavil, P. Sankar, P. R. Thankamani, and R. Philip, "White Light Z-Scan Measurements of Ultrafast Optical Nonlinearity in Reduced Graphene Oxide Nanosheets in the 400–700 Nm Region," *Applied Physics Letters,* vol. 107, p. 051104, 2015, doi: 10.1063/1.4928124.

[37] A. Ubah, N. Zakeri, M. Cerruti, and T. Szkopek, "High Resistivity Free-Standing Crosslinked Graphene Oxide Substrates: Hopping Conduction Mechanism and Application to Recyclable Electronics," *Flexible and Printed Electronics,* vol. 8, no. 3, p. 034002, 2023, doi: 10.1088/2058-8585/acf8d5.

[38] N. G. A. Pereira, M. E. L. Gonzaléz, A. A. A. d. Queiroz, A. F. Oliveira, and E. Tavares Wanderley Neto, "Higher Electrical Conductivity of Functionalized Graphene Oxide Doped with Silver and Copper (Ii) Ions," *Energies,* vol. 16, no. 20, p. 7019, 2023, doi: 10.3390/en16207019.

[39] I. Dhanya, S. Heera, S. Samuel M, and S. K. Pisharady, "Electrical Conductivity Studies and Correlated Barrier Hopping Transport in Europium-Doped Graphene Oxide Nanocomposites," *New Journal of Chemistry,* 10.1039/D1NJ04443E vol. 46, no. 1, pp. 352-358, 2022, doi: 10.1039/D1NJ04443E.

[40] H. Laroui, S. Wilson, G. Dalmasso, K. Salaita, N. Murthy, S. Sitaraman, and D. Merlin, "Nanomedicine in Gi," *American journal of physiology. Gastrointestinal and liver physiology,* vol. 300, pp. G371-83, 2010, doi: 10.1152/ajpgi.00466.2010.

[41] Y. Wang, J. E. Q. Quinsaat, T. Ono, M. Maeki, M. Tokeshi, T. Isono, K. Tajima, T. Satoh, S.-i. Sato, Y. Miura, and T. Yamamoto, "Enhanced Dispersion Stability of Gold Nanoparticles by the Physisorption of Cyclic Poly(Ethylene Glycol)," *Nature Communications,* vol. 11, no. 1, p. 6089, 2020, doi: 10.1038/s41467-020-19947-8.

CHAPTER 7

SUMMARY AND FUTURE OUTLOOK

7.1 Summary

This thesis explored the development, characterisation, and applications of GraPhage13 aerogels (GPA), an ultra-low density porous bionanocomposite fabricated through the self-assembly of graphene oxide (GO) and M13 bacteriophage.

The interaction between GO and M13 was found to be dependent on pH (Chapter 3). Between pH 2-6, the concentration of deprotonated functional groups on GO was minimised. This reduced the electrostatic repulsion between these negatively charged groups and the negatively charged amino acids on M13, enabling their interaction. The generated GO-M13 aggregate possessed a lower surface charge than the sum of its components, and the main contributor towards this surface charge was the M13 bacteriophage.

Chapter 4 described the investigations into the temperature-dependent properties of GPA. Monitoring the carbon-to-oxygen (C:O) ratio revealed that higher temperatures led to the increased removal of GO's oxygen-containing functional groups (OCFGs). This resulted in varying properties such as larger pore sizes and a reduced stiffness and adhesion force. Through Raman spectroscopy, the presence of both sp^3 and sp^2 carbon-carbon bonds was observed. The sp^3 in GPA exhibited a thermal expansion greater than the sp^3 bonds in diamond. The sp^2 bonds in GPA demonstrated a thermal expansion that falls between the known thermal expansion of sp^2 bonds in GO and graphite, demonstrating the impact of the GPA micro-nanostructure and the functionalisation of GO with M13 on its thermal properties.

The capacity of GPA to adsorb water, ethanol and acetone as explored in Chapter 5. GPA was found to be highly hygroscopic due to its extensive porous network, high

surface area, and strong GPA-water and water-water hydrogen bonds. The stability of GPA under multiple sorption-desorption cycles highlights its potential applications such as freshwater generation and humidity sensing. For ethanol and acetone sorption, a lower sorption capacity and a greater sorption-desorption hysteresis was observed. This was attributed to weaker adsorbent-adsorbate bonds, and the resulting alkyl groups on the surface of GPA preventing multilayer sorption and promoting capillary condensation. Nevertheless, there is the possibility of tuning the properties of GPA to enhance its acetone sorption characteristics. Additionally, GPA's ethanol sorption capacity is competitive with other porous carbons, offering promise in applications such as biomedical sensing and environmental applications.

However, GPA's integration into graphene-based devices for applications such as EMI shielding was limited by its insulating nature. Taking advantage of the functionalisation of GO, Chapter 6 explored the integration of carboxylic acid functionalised gold nanoparticles (AuNPs) to improve its conductivity. The AuNPs were incorporated into GPA through electronic interactions between GO and the AuNPs, resulting in a 53-fold increase in conductivity. This enhancement originates from an increase in the carrier density, with the GO-AuNP interactions lowering the activation energy for electron hopping by introducing localised states near the Fermi level, and reducing the distance between hopping sites.

The insights gained through this research not only contribute to the fundamental understanding of GPA but also pave the way for the development of next-generation graphene-based materials and devices for a diverse range of applications.

7.2 Future Outlook

The unique morphology of GPA, coupled with its cost-effective, scalable, and environmentally friendly production, positions it as a versatile bionanocomposite for a wide range of applications. Additional exploration of GPA's tuneability could further highlight its adaptability. Since the self-assembly of GPA is governed by interactions between the functional groups on the amino acids of M13 and the OCFGs on GO, modifying the oxygen content of GO or chemically and genetically engineering M13 to display different functional groups could significantly influence its resulting morphology and properties. Furthermore, engineering M13 to bind specific materials, such as target analytes or various nanomaterials, could pave the way for the development of highly specialised GPAs tailored for specific applications.

Future studies into the microstructure of GPA are necessary to fully understand the contributions of GO and M13 to its stability and functionality. While SEM analysis demonstrates that GO forms a structured network within the aerogel, it remains unclear whether this network is fully percolating throughout the material. Determining the continuity of the GO network is critical, as a percolating structure could significantly enhance the mechanical, thermal, and electrical properties of GPA. Techniques such as X-ray tomography or conductive atomic force microscopy could provide deeper insights into the connectivity of GO flakes within the network. Additionally, while most GO flakes appear to interact with M13, there is a possibility that some flakes are not fully covered. This raises questions about the presence and role of GO-GO interactions within the aerogel. GO-GO interactions may complement GO-M13 bonds in contributing to the structural stability and mechanical integrity of GPA. Advanced

imaging techniques such as high-resolution TEM could provide detailed visualisations of these interactions.

While Chapter 3 focused on the role of pH in GPA self-assembly, other factors such as stirring speed, temperature, and the concentration of GO and M13 may also influence the assembly process. Future studies should systematically examine these parameters both individually and in combination to understand their collective influence on GPA self-assembly.

Extended explorations into the versatility of its sorption capabilities, such as its ability to adsorb oils, hazardous organic pollutants and gases, could open up applications in environmental remediation and clean energy storage. Additionally, future studies could focus on obtaining SEM images and conducting mechanical testing of aerogels post-sorption experiments to evaluate the structural and mechanical integrity of the material under operational conditions. Such data would provide valuable insights into how repeated sorption and desorption cycles affect the aerogel's microstructure and durability.

The investigations into the temperature-induced changes in the morphology, composition, and sorption properties of GPA were constrained by the currently achievable temperature range. Expanding the temperature range in future studies could provide a comprehensive understanding of the structural integrity of GPA across higher temperatures, which is crucial for high-temperature applications. Elevated temperatures could also further reduce the GO in GPA to rGO, enhancing its hydrophobicity and conductivity. Exploring a broader temperature range would offer

valuable insights into the effects on GPA's morphology, composition, nanomechanical properties, as well as its sorption and electrical characteristics.

Future studies should also include a Life Cycle Assessment (LCA) to evaluate the overall environmental impact of GPA production compared to alternative materials. This would provide a quantitative assessment of its sustainability by considering factors such as energy consumption, emissions, and waste generation throughout its lifecycle. Such an analysis would be essential in determining the feasibility of GPA for large-scale, environmentally friendly applications. However, the industrial applications of GPA are limited by its lack of integration into functional devices. Successfully integrating GPA into proof-of-concept graphene-based devices, followed by the potential scaling up and mass-production of these platforms, could pave the way for its widespread use in a versatile range of applications.

The successful self-assembly of GO with M13 to form GPA raises the intriguing possibility that other bacteriophages could similarly interact with GO to create novel structures. This study serves as a foundation for future research into GO-phage interactions, potentially leading to the development of diverse GO-phage composites with unique properties and a broad range of applications.